Experimental design to evaluate the impact of precipitation regimes on the rates of dissolution of sedimentary building stones and implications for predictive modeling

Noemi Giovelli (MSc)

University of Strathclyde

Faculty of Engineering | Department of Architecture

Thesis Submitted in Fulfilment of the Requirements for the Degree of Doctor of Philosophy

2024

DECLARATION

This thesis is the result of the author's original research. It has been composed by the author and has not been previously submitted for examination which has led to the award of a degree.

Noemi Giovelli

(08/01/2024)

The results presented in Chapter 4 were included in a paper presented to the CHNT 2021 conference, titled “Built heritage and Climate Chane: performance evaluation of natural building stone exposed to rainfall through a combination of image analysis and laboratory leaching tests”. The paper is currently scheduled for publication.

Abstract

Sedimentary stone represents one of the main materials used in construction since ancient times, whose durability can be greatly affected by environmental exposure. Water represents a major factor of stone degradation and, as a consequence, building stones exposed to high precipitation environments, such as Scotland, are highly vulnerable. Assessing the durability of the stone is crucial to plan for appropriate conservation strategies and interventions. This requires the identification of the factors that control the decay progression and their respective contribution to the rate of degradation.

This research explored the influence of rainfall patterns variability on the rates of mineral dissolution of different sedimentary stones containing variable concentrations of carbonate minerals. Samples were subject to artificial weathering employing an exposure apparatus specifically designed to meet the project requirements. Multiple trials of different duration were conducted to examine the performance of the samples under both stable and variable exposure conditions.

The samples' performance was assessed from the concentration of dissolved Ca, Mg, K, Na, and Fe in the stones leachates that were collected at regular intervals of time. A dissolution profile was obtained for each stone by plotting the dissolution rate of each analyte at each sampling point.

Results showed that alterations in the duration of the rainwater cycle corresponded to a variation of the rate of mineral dissolution. The carbonate mineral content of the stone appeared to control the relationship between the dissolution rates of Ca and Mg and the rainfall event duration. These two variables were found to be inversely correlated in samples containing higher concentrations of carbonate minerals.

The results provide an insight into the parameters that control the rates of dissolution of sedimentary building stone dissolution by rainfall and support the estimation of the effects of future alterations in the precipitation patterns on the stone rate of degradation.

Acknowledgments

This study has been completed thanks to the help and contribution of numerous people, to whom I express my deepest and most sincere gratitude.

Luis Albornoz-Parra (British Geological Survey) provided help for the selection of the stones employed in this study. His support dates long before the present research started, and still continues today.

John Brown (City of Glasgow College) offered his skills and time for the preparation of the samples. His help was fundamental for the progression of the project during the interruption of campus-based activities caused by the Covid-19 pandemic.

James Francis (University of Strathclyde) also helped with the preparation of the samples, by extracting the cores from the stone samples to be analysed by X-ray computed tomography.

Kate Dobson (University of Strathclyde) was fundamental for the X-ray computed tomography work. Her support and contribution to the present research relate to both the analysis of the samples and the processing of the results.

James Minto (University of Strathclyde) also supported the X-ray computed tomography work and provided valuable input on the processing of the scans.

Alexander Clunie, Jessica Bame and Graeme Anderson (University of Strathclyde) directed the analysis on the leachate samples by inductively coupled

plasma mass spectrometry and provided important advices on the preparation of the samples prior to analysis.

Lindsey Whiteford (University of Strathclyde) assisted with the 3D printing of the exposure apparatus components and assisted with the selection of the most appropriate materials.

A big thank you also to Blockstone, Carlo Bernasconi, Casone Group, Denfind Stone, Drumhead Quarry, for providing the samples and offering support for the samples selection and delivery.

My gratitude also goes to Ombretta Romice (University of Strathclyde), for assisting with the arrangements in preparation of the thesis submission.

A very special thanks goes to my supervisors, Cristina Gonzalez-Longo (University of Strathclyde, department of Architecture) and Christine M. Davidson (University of Strathclyde, department of Pure and Applied Chemistry).

Cristina-Gonzalez Longo has followed my journey at the University of Strathclyde since my master's degree. I wish to thank her for the constant support and unconditional trust, and especially for always motivating me. Throughout the years she has been a firm point in the progression of my career.

I am deeply grateful to Cristine M. Davidson, for the invaluable support to the project in each of its phases, from the planning of the experimental stage to the interpretation of results and reviewing of the thesis. I wish to thank her for always finding the time to help me, even when she didn't have any.

A major thank you to the University of Strathclyde, for funding this research and offering me this opportunity.

To my friends, the old and the new ones, that do not know how important they have been just with their presence. Thanks to my family, which was with me since the very start.

And ultimately, to my friend and husband, Alessandro, who was by my side for every step backwards and every step forward. I dedicate this piece of work to him. I owe him every bit of strength that moved me though this journey.

Table of Contents

Terms and Definitions

Ageing exposure: procedure that involves the exposure of samples to environmental agents by natural-field or accelerated-laboratory testing.

Damage function: function that expresses the relationship between a decay indicator and one or more properties of the stone to quantify damage caused by degradation.

Decay: process that involves a decrease of the original properties of the stone by chemical or physical mechanisms.

Decay Indicator: property or mechanism that is representative of the damage caused by a degradation process.

Degradation: progressive decline of the stone condition and functional capacity.

Dose-Response function: function that expresses the relationship between a decay indicator and one or more degradation agents.

Durability: capacity of a stone to withstand degradation and perform its function over a period of time when exposed to decay agents.

Weathering: chemical or physical degradation caused by the stone exposure to weathering agents.

1. Introduction and Literature Review

1.1 Research Context

Stone is one of the main construction materials used since ancient times and thereafter its study is vital for the conservation of built heritage. The most appropriate conservation strategies and actions can be designed by assessing the future performance of the stone in accordance with the specific climatic and environmental characteristics of its location and exposure.

In countries such as Scotland, the vast majority of built heritage is made of sedimentary stone, which can present different levels of vulnerability when exposed to the environment. Historically, the type of stone used for construction depended on availability and resources, as well as on the culture of builders and communities. Until the development of the railway system in the nineteenth-century, mainly local stones were used. Nevertheless, stone remained a primary building material until the turn of the twentieth century.

The study of building stone requires multi- and interdisciplinary research in order to determine critical aspects for its conservation. Stone degradation is a natural manifestation produced by a disequilibrium between the stone formation environment and in-service conditions (Bauer and Velde, 2014). As such, it represents an inevitable and irreversible process. However, intensity and rate of

degradation can vary greatly, due to the wide range of factors that control the decay progression. Decay processes are related to the material response to the environment. An important indicator for the stone expected performance is its durability, concerning the expected level of susceptibility to exposure and the potential consequences over the stone element integrity. This factor is strongly connected to the inherent properties of the stone, such as its composition and structure, and is subject to variation based on the nature of the environmental stressors.

As for other materials, water represents the main cause of stone degradation. Thereafter building stones exposed to high precipitation environments are highly vulnerable. Scotland, along with mountain areas of central Europe and Scandinavia, has been identified as one of the areas in which carbonate building stones have a higher risk of surface recession (Bonazza et al., 2009).

The influence of water on building stone degradation and the related processes was well described by Torraca (2009). A recent study has provided a detailed review of Its effects on natural stone used in the built environment (Alves et al., 2021). Multiple deterioration processes are connected to the presence of water, whose potential damage is often aggravated by the synergic interaction with additional factors. In 1872, the term *acid rain* was adopted for the first time to describe atmospheric deposition of acidic compounds by means of rain, snow or vapour. This phenomenon was proved to cause a significant increase in the rates of stone degradation, with the most severe effects registered among calcareous stones, due to the highest instability of carbonate minerals to acid precipitation (De la Fuente et al., 2013). Today, the rise in CO_2 atmospheric concentration is

expected to be one of the main contributors to the stone decay caused by atmospheric pollution (Bonazza et al., 2009).

Climate Change adds complexity to the study of the impact of exposure on building stone. The risk of increased precipitations and extreme rainfall events will likely intensify the dissolution rates of carbonate stones (Basu et al., 2020). Potential variations in relative humidity are also expected to produce considerable damage to materials, due to their influence over reaction processes and deposition mechanisms of pollutants (Brimblecombe et al., 2007).

Water is not only a direct agent of decay but also causes other types of deterioration, such as biological soiling, which is expected to experience an increase in species with higher adaptation capacity to the new expected climatic conditions (Jamison et al., 2010). Location and exposure are also critical; for example, changes in wind direction and speed can cause an increase in surface erosion (Sabbioni et al., 2009). Variation in temperature and frequency of cycles are likely to increase damage due to the physical stress induced by freezing-thawing and wetting-drying cycles and salts crystallization (Torraca, 2009).

Research on the implications of climate change on Cultural Heritage has been increasing over the past few years (Siegesmund et al., 2008; Bonazza et al., 2009; Bonazza et al., 2009; Smith et al., 2008, 2010; Brimblecombe, 2014; Sesana et al., 2019, Sesana et al., 2020; Sesana et al., 2021). Although some authors suggest that changing climatic conditions will not necessarily induce changes in the mechanisms influencing the stone deterioration, it is agreed that it will likely have an impact on how quickly deterioration will progress (Phillipson et al., 2016).

The most appropriate preventive measures and conservation strategies can be chosen by estimating the stone future performance based on the factors that contribute to its degradation. An effective way to collect this information is to model the stone degradation according to the relevant climatic and environmental parameters. However, some of the factors influencing the stone rate of degradation remain relatively unexplored.

The influence of the duration of the rainfall event over the dissolution rate of building stone is not yet well-established, although it has been widely accepted as a controlling factor (Schuster et al., 1994; Siegesmund and Snethlage, 2011; Bauer and Velde, 2014). Additionally, the effect of the stone properties over the rate of mineral dissolution remains relatively unexplored. Considering these variables is a critical step to enhance our comprehension of stone vulnerability and ultimately contribute to the improvement of models for the prediction of the stone performance under future climatic conditions.

1.2 Sedimentary stone

Sedimentary rocks are predominant in the earth surface, accounting for the 75% of outcrops (Morbidelli, 2014). Based on their formation mechanisms, sedimentary stones can be classified as clastic/detrital or chemical/biochemical. Clastic rocks are formed from the transport and deposition of minerals and rock fragments of pre-existing rocks. Deposition is followed by the compaction and cementation of the grains by cementing minerals, that act as a binder between the particles (Siegesmund and Snethlage, 2011). This process is known as *diagenesis*, a term

used to refer to the range of mechanisms that lead to the stone lithification. During this stage of the rock formation, the mineralogy, texture and structure of the rock are defined. Clastic rocks are most frequently classified on the basis on their average grain size: rudites (coarse grain size; > 2mm), arenites (medium grain size; 2 – 0.05 mm) and lutites (fine grain size; 0.05 mm – 0.0005 mm).

Sandstone is the most common detrital sedimentary type of rocks used in buildings and belongs to the arenite's family. The composition of sandstone is determined by the deposition conditions and origin of the deposited material. Its main components are the framework grains, the matrix, the cement and the pore fraction. Framework grains usually consist of quartz, which is often associated with feldspars and lithic grains. Sandstones can be characterized by plotting the percentage amounts of these three main components in QLF (quartz, lithic fragments and feldspars) diagrams. The sandstone matrix is composed by the fraction of fine minerals that occupies the pore spaces. Framework grains are bonded by the cement, usually consisting of silica, calcite or additional minerals including clays, Fe-oxides and oxyhydroxides (Potysz et al., 2022).

Chemical or biochemical sedimentary rocks are formed after precipitation from solution by chemical or biological processes. The majority of chemically or biologically precipitated rocks are formed from seawater. The supersaturation of the solution is the pre-requisite for precipitation, which is followed by cementation. The composition of chemical or biochemical sedimentary rocks is the criteria used for their classification. Carbonates account for the vast majority of chemical or biological sedimentary rocks composition, followed by siliceous sediments, evaporites and phosphates (Siegesmund and Snethlage, 2011).

Limestone and dolomites are two of the most common carbonates used in construction.

1.3 Key factors in the process of degradation by rainwater

1.3.1 Environmental stressors

The presence of water is one of the dominant factors controlling the stone degradation (Alves et al., 2020). Combined with temperature, its role is linked to most weathering processes. As shown by Peltier's diagram (figure 1-1), chemical processes are favoured by higher temperatures and rainfall amounts, while physical mechanisms are prevalent in areas with lower temperatures and precipitation. However, the role of temperature with respect to most decay mechanisms is not as straightforward and can be actively influenced by factors as the magnitude and rate of the temperature fluctuations and the presence of thermal gradients (Hall, 1997). Furthermore, factors such as orientation can greatly affect the type of heating regime and determine whether the stone is subject to convective or cyclic radiative heating (Gomez-Heras and Fort, 2007). Temperature controls many of the aspects that govern the interaction with rainwater, as it influences the frequency and direction of moisture transfer, as well as the nature and rate of chemical, physical and biological processes (McAllister et al., 2017).

In the absence of pollution, the capacity of rainfall to dissolve calcite depends on the levels of atmospheric CO_2. In this respect, the natural solubility of the stone has been reported as having the highest influence over the stone deterioration in

areas characterized by low and moderate levels of pollution (Yerrapragada et al., 1996; Lipfert, 1989; Baedecker et al., 1992; Reddy et al., 1989). The contribution of clean rain to the stone deterioration was found to account for the 70% (Baedecker et al., 1992) and 50% to 90% (Jaynes and Cooke, 1986) of the total erosion by dissolution.

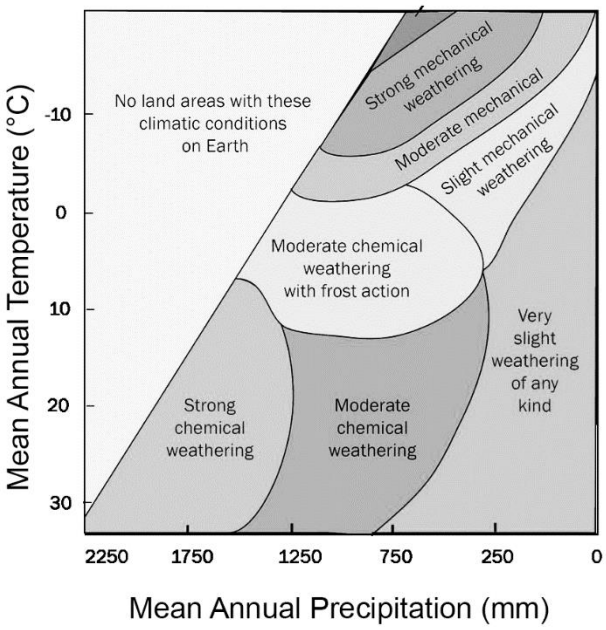

Figure 1-1: Peltier diagram illustrating the type of decay mechanism for stone as a function of Mean Annual Temperature and Mean Annual Precipitation

The consequences of rising atmospheric CO_2 concentrations were investigated to support the prediction of potential effects of climate change over the recession of calcareous stone in Europe (Bonazza et al., 2009). The projected increase in the level of carbon dioxide under the A2 emission scenario was found to be connected

to a rise in solubility of about 16% between 2070 and 2099 for the 750 ppm. This will likely contribute to a significant rise in the rates of carbonate stone recession caused by rainwater in equilibrium with CO_2, which is expected to increase of about 30% in areas with high annual precipitation as Scotland.

The formation of acid rain is connected to the transport and solubilization of gases produced by industrial emissions. Historically, atmospheric sulphur dioxide was the primary pollutant; however, these days, carbon dioxide and nitrogen oxides are the most frequent sources of acidity (Watt, 2009). This is the reason why the presence of atmospheric pollution represents an acceleration factor for the decay process of unsheltered stone elements. Nonetheless, the incremental impact of hydrogen ions in rainwater on the rate of dissolution of carbonate stones at pH 4 is relatively low. The equilibrium solubility of calcite is mainly controlled by its reaction with carbonic acid, formed after the interaction of rainfall with atmospheric CO_2. The deposition of hydrogen ions was found to contribute to the erosion of carbonate stones by 10% to 17% (Baedecker, 1993), 1 to 7% (Delalieux et al., 2002) and 0.3 to 3.2% (Webb et al., 1992).

In contrast, rainwater amounts appeared to have a higher influence over surface recession of marble and limestone samples compared to rainwater acidity (Reddy et al., 1989). Calcium concentrations in runoff-water was reported to vary inversely with rainfall amounts at each episode (Lipfert, 1989). The same was observed in relation to the concentration of excess of sulphur compounds in the run-off water, resulting from the dissolution of reaction products (Reddy et al., 1989). Wind also represents an important controlling factor in the penetration process of rainwater and is one of the leading factors for the presence of moisture in masonry walls (López-González et al., 2022). Comparably to other environmental agents, as

solar radiation, wind-driven rain is subject to directionality and therefore its impact is substantially influenced by exposure (Martínez-Martínez et al., 2022).

Other forms of wet deposition, as soft drizzle, fog and dew, also referred to as “occult precipitation”, can potentially contribute to the decay process by supplying the necessary moisture to initiate a chemical action and activate dry deposit (Charola and Ware, 2002). Stone durability is equally influenced by water vapour, which is transported by diffusion in unsaturated pore spaces due to the tendency to equilibrium that is established between concentration gradients (Pichler et al., 2022). The water diffusion coefficient measures the rate of transfer in a porous material. Water vapor diffusion resistance is a measurement of the degree to which vapor diffusion in the material is inhibited and is defined as the ratio between the water vapor diffusion coefficient in the air and within the stone (Keppert et al., 2006).

The time of wetness, a term designed to indicate how long the stone stays wet, is associated with the presence of moisture. The term has been applied within multiple contexts and in relation to its influence over different factors, as dry deposition and biological colonization (McCabe, 2013). Time of wetness was reported as having a positive correlation with temperature, above which value the correlation assumes a negative form (report n. 30, UNECE). The influence of both parameters on the stone deterioration is likely to increase due to increasingly warmer winters, as projected by climatic models (Bonazza et al., 2009). More recently the concept of “‘time of deep wetness” was proposed to express the impact of moisture at a depth not influenced by surface cycles (McCabe, 2013).

1.1.1 Stone properties

The range of characteristics that define a stone, as the structure, texture and composition, can have a direct impact on its vulnerability to exposure. Porosity is widely accepted as one of the main controlling factors of the stone decay. Higher porosity was found to be correlated with higher degradation rates caused by water freezing, salt crystallization (Benavente et al., 2018; Carvalho et al., 2018) and exposure to acid solutions (Gibeaux et al., 2018). The characteristics of the pore fraction regulate the stone water absorption properties and, therefore, the decay progression.

The relationship with the rate of degradation is mostly defined by the morphological characteristics, which is commonly described by two parameters: total porosity and effective porosity. Effective porosity measures the volume of pores that can be accessed by gases or liquids, whereas the first is connected to the overall amount of empty spaces (Molina et al., 2011) (figure 1-2). Unconnected pores do not allow the flow of water and therefore do not play an active role in the process of degradation. On the other hand, effective porosity is connected to the stone permeability, which is directly connected to multiple degradation mechanisms.

Pores can present variable dimensions. Large pores can have a diameter above 10 µm, while smaller pores, also known as capillary pores, usually have a diameter between 1 and 0.1 µm (Torraca, 2009). Additional factors involve the level of interconnection and tortuosity, a parameter used to describe the path between connected spaces (Amoroso, 2002).

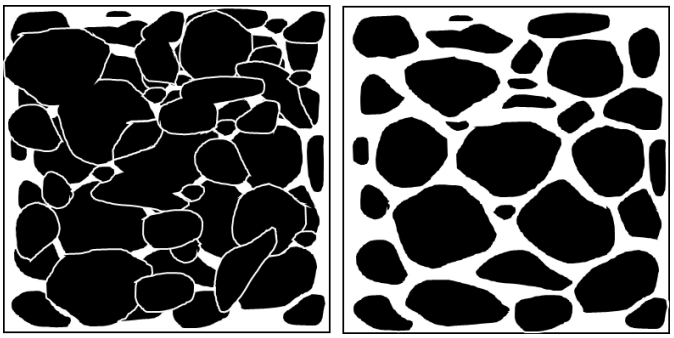

Figure 1-2: schematic representation of unconnected (left) and connected (right) pore spaces in a clastic rock.

The dimension of the pores, the pores size distribution and their level of interconnection were reported as a fundamental parameter of the deterioration progression (Benavente, 2011; Germinario et al., 2019; Gibeaux et al., 2018; Uğur et al., 2020). The ratio between large and capillary pores represents a key element of the stone vulnerability to degradation. Stones with low porosity and a high amount of micropores are more susceptible to degradation compared to stones with high porosity and high average pore radius if the pore network is characterised by low connectivity and high tortuosity (Buj et al., 2010).

Capillarity describes the absorption of water by a porous medium by means of molecular interactions between the solid and the liquid phase (figure 1-3). This mechanism is highly influenced by the size of the pores and represents the main driving force for the absorption of water by pores between 1 μm and 1 mm (Siegesmund and Snethlage, 2014). The water transport within a porous medium is defined by the water absorption (WA) coefficient, a parameter usually negatively correlated with the stone durability (Ozcelik and Ozguven, 2014).

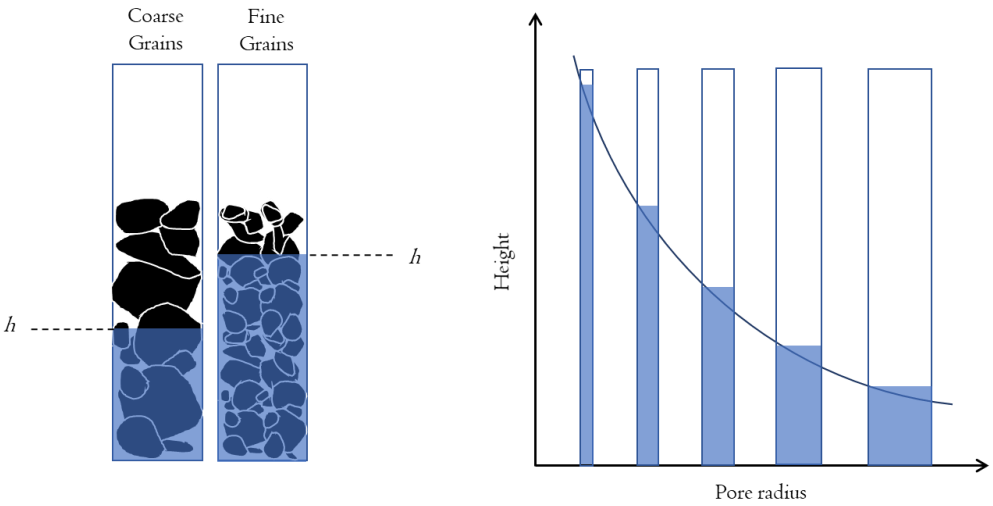

Figure 1-3: schematic representation of the capillary action in porous mediums.

This parameter is highly influenced by the size, type, orientation and distribution of the clastic fraction (Tomasic et al., 2011).

The mineral composition of the stone represents a controlling factor for both chemical and physical degradation. For instance, the presence of carbonate minerals and feldspars is one of the most important contributors to the stone vulnerability to chemical dissolution (Bauer and Velde, 2014). On the other hand, dolomite was reported to increase the stone resistance to dissolution (Heidari et al., 2017) and salt crystallization (Alves et al., 2020). Calcite is also at the centre of physical degradation mechanisms. Effects of heat exposure are often correlated to the volumetric variation of calcite (Torabi-Kaveh et al., 2019). Similarly to carbonates, the presence of some clay minerals is often associated

with a volumetric variation that accompanies the hydration process (Jiménez-González et al., 2008). The presence of phyllosilicates was reported to be associated with a higher susceptibility of arenaceous stones to salts weathering and wetting-drying processes (Alves et al., 2020).

Texture describes the mutual relationship between the minerals size, shape and their spatial arrangement. Although the influence of these factors to the weathering process is relatively less addressed, their importance was confirmed by several studies. For instance, the orientation of calcite minerals, as well as the crystals dimension, was reported to impact the resistance to pollution (De Kock et al., 2017; Martínez-Martínez et al., 2019). Tuff samples presenting different granularity showed different responses when subject to freeze-thaw and salt crystallization (Alves et al., 2020). The presence of stratification and bedding planes appeared to promote localized weathering caused by salt crystallization (Stück et al., 2018).

1.4 Main deterioration mechanisms caused by environmental exposure

1.4.1 Chemical degradation

Chemical process are the group of mechanisms that induce an alteration of the stone original composition. When determining a stone's resistance to chemical weathering, its mineral composition is a key factor. Minerals can become

thermodynamically unstable when exposed to the environment. Less stable ones are usually under-saturated and have a natural tendency to convert into more stable phases (Okrusch and Frimmel, 2020). This process is known as weathering. Hydration, hydrolysis, oxidation and dissolution are common processes involved in the chemical weathering of the stone (Bauer and Velde, 2014).

Hydration involves the incorporation of H_2O into the structure of a mineral. This reaction usually concerns minerals that are either anhydrous or more anhydrous than the reaction product. A common example is represented by the hydration of the mineral hematite into goethite.

Fe_2O_3 (hematite) + H2O → 2FeOOH (goethite)

A further example is the absorption of water by anhydrite, which results in the formation of gypsum (Bauer and Velde, 2014):

$CaSO_4$ (anydrite) + $2H_2O \leftrightarrow CaSO_4 \cdot 2H_2O$ (gypsum)

A common consequence of the hydration process is the expansion of mineral volume, which can lead to internal stress. The swelling of expandable clays is one example of this process; it was found that hydration of expandable clays was linked to tensile failure, scaling and detachment of parts of the stone. (Jiménez-González et al., 2008). Furthermore, a higher level of hydration of a mineral usually corresponds to a higher susceptibility to dissolution.

The reaction of hydrolysis involves the replacement of cations with H^+ ions and release into solution of a chemically equivalent number of cations. It differs from the hydration process, which involves the full incorporation of the water molecule.

Minerals that undergo the process of hydrolysis are K-feldspars, which upon contact with an acid solution form the clay mineral kaolinite. During the reaction, K^+ is replaced by H^+ through ionic exchange, forming hydrous phases, i.e., clay minerals (Bauer and Velde, 2014):

$2\ KAlSi_3O_8$ (K-feldspar) + $H_2O + 2H^+ \rightarrow Al_2SiO_5(OH)_4$ (kaolinite) + $2K^+ + 4SiO_2$ (acqueous silica)

Primary minerals are often formed under reducing conditions and therefore they can be oxidised at the surface. Oxidation involves the combination of oxygen to the mineral structure with a formation of a new phase. The process involves the presence of water and results in hydrated oxides and minerals containing Fe and Mg. Iron is an example of the oxidation reaction. In the mineral fayalite, iron is in the divalent state and is covalently linked to silicon and oxygen. Upon reaction with oxygen in its elemental state insoluble Fe_2O_3 is produced, which precipitates from the hematite:

Fe_2SiO_4 (fayalite) + ½ $O_2 + 2H_2O \rightarrow Fe_2O_3$ (hematite) + H_4SiO_4

The same reaction occurs in clinopyroxenes, with the production of Fe oxides and release of Ca in solution:

$2CaFeSi_2O_6$ (clinopyroxene) + ½ $O^2 + 10H_2O + 4CO_2 \rightarrow Fe_2O_3$ (hematite) + $4H_4SiO_4$ + $2Ca^{+2} + 4HCO_3^-$

A common consequence of the oxidation processes is the weakening of the stone, which can induce a progressive breakdown.

Mineral dissolution represents one of the most important mechanisms at the base of the progressive degradation of stone upon contact with rainwater. The action

of acid solutions is connected to the activity of hydrogen ions (H^+), which are extremely active and can diffuse easily into the chemical structures of minerals.

Minerals can present variable tendency to dissolution. The geochemical form of the element, indicating the type of mineral in which the element is incorporated, regulates the tendency to dissolution (Potysz et al., 2022). Minerals dominated by ionic bonds are susceptible to simple dissolution in the presence of water. For instance, halite (NaCl), dissolve in pure water (1), while others, as calcite ($CaCo_3$) dissolve more easily in acidic solution (2).

$NaCl_{(s)}$ (halite) + $H_2O \rightarrow Na^+_{(aq)} + Cl^-_{(aq)}$ (1)

$CaCO_{3\ (s)}$ (calcite) + $H_2O_{(l)} + CO_{2\ (aq)} \leftrightarrow Ca^+_{\ (aq)} + 2HCO_3^-{}_{(aq)}$ (2)

Some of the most common dissolution process involve carbonate minerals (3), felspars (4) and clay minerals (5):

$CaCO_3 + 2H^+ \leftrightarrows Ca^{2+} + CO_2 + H_2O$ (3)

$2KAlSi_3O_8 + 2H^+ + 9H_2O \leftrightarrow 2K^+ + Al_2Si_2O_5(OH)_4 + 4Si(OH)_4$ (4)

$Mg_5Al_2Si_3O_{10}(OH)_8 + 10H^+ \leftrightarrow 5Mg^{2+} + Al_2Si_2O_5(OH)_4 + 4Si(OH)_4 + 5\ H_2O$ (5)

When the parent mineral contains Fe (II), the process of dissolution usually involves an oxidation step (6):

$Fe_2SiO_4 + ½\ O_2 + 3H_2O \leftrightarrows 2FeOOH + Si(OH)_4$ (6)

The rate of mineral dissolution depends on the amount/contact time of liquid water, solubility of the mineral phase and pH of the aqueous solution (Siegesmund and Snethlage, 2011). The process is controlled by the ion exchange between hydrogen ions and cations of the minerals, a sequential bond breaking reaction,

and the inward diffusion of reactants and/or outward diffusion of hydrolysis products (Yuan et al., 2019). The dissolution rate is also influenced by temperature (Crundwell, 2015).

1.4.2 Physical degradation

Physical mechanisms commonly induce an alteration of the original mechanical properties of the stone, influencing its resistance and often limiting its capacity to perform its intended function. There are four main types of physical degradation processes, i.e., freezing-thawing, heating-cooling, wetting-drying and salt crystallization. Freeze-thaw processes are connected to the internal stress induced by the volume increase associated with the phase transition of water from liquid to ice (Ruedrich J. et al., 2011). This process can have a significant impact over density and porosity, and affect the overall compressive, tensile and impact strength of the stone (Wang et al., 2016).

Similarly, the dimensional change of some mineral phases caused by heat exposure can also result in internal stress. Because different minerals have varying coefficients of thermal expansion, these effects are magnified in heterogeneous rocks (Hall K., 1999). Artificial exposure of granite samples to heating and cooling cycles has resulted in an increase in the values of porosity, in conjunction to a decline of the bulk density, surface hardness and Young modulus (Freire-Lista et al., 2016). The presence of water appears to be a co-factor in the decrease of the mechanical properties when combined to heat exposure (Ghobadi and Babazadeh, 2014).

As covered in the previous section, the process of water absorption by hydrophilic minerals can be linked to an increase in porosity, mass-loss and water absorption capacity (Sumner et al., 2009), with a corresponding decrease in density, P-Wave velocity and slake durability index (Zhou *et al.*, 2017). The applied pressure resulting from mineral swelling caused by interaction with water induces the development and expansion of internal micro-cracks (Xu et al., 2020), detachment of portions of stone and consequential reduction of the tensile strength (Jimenez-Gonzalez and Scherer, 2008), dynamic compressive strength and elastic modulus (Zhou et al., 2017).

A further common source of damage is related to the pressure associated with the crystallization of salts, a process linked to the solubility and movement of salts within the stone pores. In this case, the type of salt, the degree of supersaturation and the location of the crystallization are key aspects of the weathering process (Rodriguez-Navarro & Doehne 1999). An experimental study carried by Angeli et al., (2007) identified three stages in the development of damage caused by salts, i.e., an initial weight increase cause by salts accumulation, a weight variation resulting from the competition between salt supply and stone damage, and a weight decrease, caused by the evolution of the damage (Angeli et al., 2007).

1.5 Testing of stone durability

Different methods are adopted to test the stone resistance to decay and acquire information over the influence of factors and processes. Natural outdoor climate exposure and accelerated artificial weathering represent common approaches.

Field exposure is particularly relevant when investigating the effects of atmospheric pollution, where the complexity of the interactions can be difficult to replicate in a laboratory setting. Field testing involves the exposure of samples to the environment, often for years, during which the stone performance is monitored alongside the relevant environmental parameter. Exposure programs became common procedures in the 1980's, when the damaging effects of pollution on stone buildings became evident, along with the economic consequences of new deterioration processes and increased rates (Jaynes and Cooke, 1986). The absence of a common protocols for field testing resulted in a wide range of variations of the methodological approach (figure 1-4). In most cases, stone samples were placed in a fixed position facing the prevailing wind direction to a certain inclination (Reddy et al., 1989). Other studies adopted a freely rotating apparatus to eliminate the bias caused by a preferential exposure (Jaynes and Cooke, 1986; Butlin et al., 1995). Likewise, programs presents variable geographical distribution, from a urban (Delalieux et al., 2002), to a national (Butlin et al., 1995) and international context (Kucera et al., 2001).

The testing of building stone susceptibility to chemical weathering is also frequently conducted under controlled laboratory conditions. Immersion represents the most common approach to explore the effects of acid rain to the stone dissolution and can be conducted under passive or active conditions.

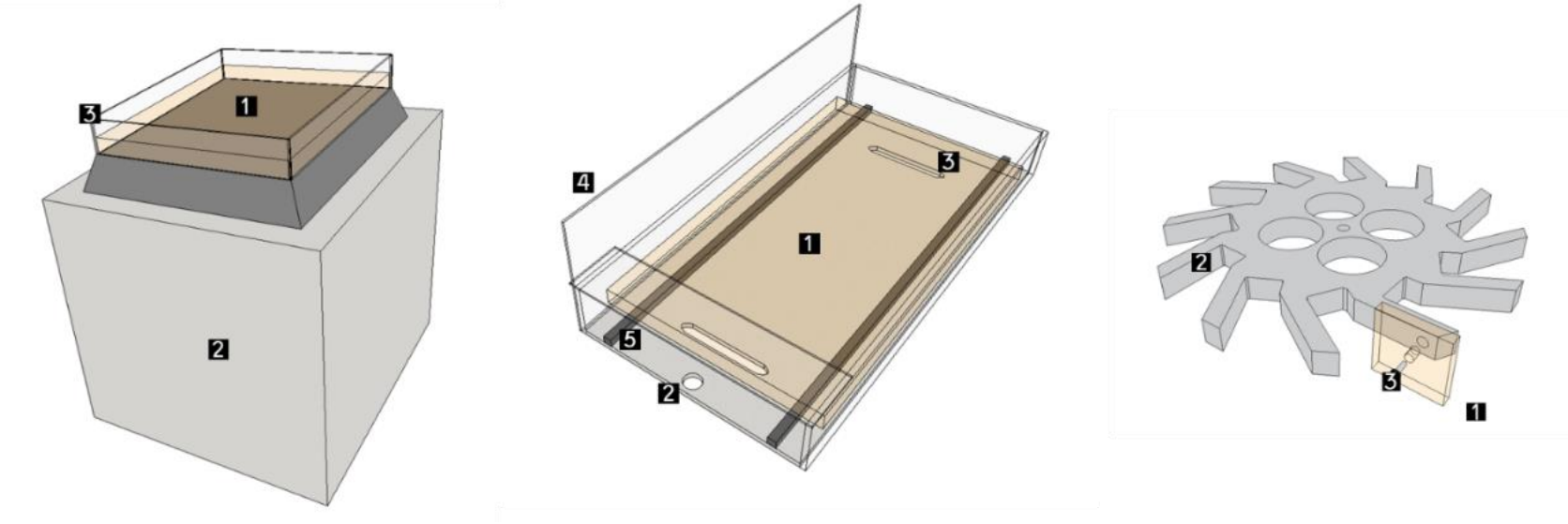

a b c

Figure 1-4: different types of set-ups used for field exposure testing of stone samples. Figure 4a.: setting used for the exposure of stone samples used by Delalieux et al. (2002). A sample of dimension 25 x 25 cm is mounted on top of a polystyrene box at an angle of 15°. 1: sample, 2: polystyrene box, 3: glass shield. Figure 4b.: setting used for the exposure of stone samples used by NAPAP program. A sample of dimension 30 x 60 x 5.1 cm is placed at a 30 ° angle in a rack fabricated from polypropylene. 1: sample, 2: run-off outlet, 3: ventilation opening, 4: water splash shield, 5: rubber strips to elevate the sample. Figure 4c.: setting used for the exposure of stone samples used by the ICP Materials program. A sample of dimension 5 x 5 x 0.80 cm is mounted on a freely rotating carousel at 120 °. 1: sample, 2: carousel arms for the fixing of the sample, 3: nylon screw.

With active immersion, a shaker is used to simulate the mechanical effect of rainfall. Passive and active immersion was adopted to investigate the resistance of carbonate stone to carbonic acid solutions (Thornbush and Viles, 2007), nitric and sulphuric acid solutions (Holynska et al., 2003; Franzoni and Sassoni, 2011, Eyssautier-Chuine et al, 2016; Gibeaux et al., 2018;), carbonic acid brine (Dawson et al., 2014), nitric, sulphuric, hydrochloric and acetic acid (Kryza et al., 2009). Artificial weathering by immersion was also combined to gas exposure obtained from the acid solution evaporation (Gibeaux et al., 2018), to simulate the influence of dry deposition.

An alternative to immersion for laboratory accelerated exposure is represented by the spraying of the solution. This method was adopted to evaluate the mineral dissolution (Baedecker and Reddy, 1993) and mass loss (Labus and Bochen, 2012; Fereidooni and Khajevand, 2017; Tecer, 1999) of carbonate stones at different concentrations of sulphuric and nitric acid. A common approach to investigate the effect of polluted atmospheres involves the use of climatic chambers. Climatic chambers allow the contemporaneous exposure of the samples to multiple factors. Conditions adopted to simulate natural weathering in climatic chambers involved different concentrations of SO_2, NO_2, O_3, HCl and variable relative humidity and temperature values (Ausset et al., 1995; Johnson et al., 1990; Lisci et al., 2022; Sitzia et al., 2021; Unterwurzacher and Mirwald, 2008).

Artificial exposure in a controlled laboratory setting is also the most common procedure for the investigation of physical mechanisms. Standardised procedures are available, allowing a systematic study of the effects of different stressors in a replicable and comparable way (Cerfontaine et al., 2018). However, the intensity of the applied parameters, as well as the duration of each single cycle often

changes between studies (Jelle, 2012). Similarly, can present varying dimensions and shape depending on the properties being tested.

Freezing-thawing are among the most studied physical processes and are usually carried by immersion (Jamshidi, 2024). The thawing process can be conducted under dry (Ke et al., 2020) or, more frequently, wet conditions by transferring the samples into a water bath (Altindag et al., 2004; Aral et al., 2020; Chen et al., 2004; Jamshidi et al., 2015; Mutlutürk et al., 2004; Ruedrich et al., 2011; Salvini et al., 2023; Yavuz, 2010). Similarly, the resistance of the stone to heat exposure is tested at variable temperatures by means of ovens (Hale and Shakoor, 2003; Mutluturk et al., 2004; Brotons et al. 2013) or infrared lamps (Warke and Smith, 1998), followed by a cooling phase at room temperature.

The effects of wetting-drying cycles are most frequently evaluated by immersion, similarly to the laboratory study of chemical processes. Zhao et al. (2017) showed that the methodological approach can differ considerably between studies. The immersion time for the wetting cycle was found to vary from 1 day (Hale and Shakoor, 2003; Lin et al., 2005; Khanlari and Abdilor, 2015) to 30 days (Deng et al., 2012). The drying procedure is equally variable, involving air-drying (Sumner and Loubser, 2008; Deng et al., 2012) and oven-drying (Hale and Shakoor 2003; Hua et al., 2015; Khanlari and Abdilor, 2015).

The same procedures are often used to study salt-induced decay, i.e., immersion in saturated salt solution followed oven drying or room temperature cooling. Testing is usually conducted against the action of two of the most common salts found in masonry buildings, i.e., sodium sulphate (;Angeli et al., 2007; Buj and Gisbert 2010; Ghobadi and Babazadeh 2015; López-Arce et al., 2010; Rodriguez-

Navarro and Doehne, 1999; Ruedrich and Siegesmund, 2007) and sodium chloride (Ludovico-Marques and Chastre, 2016; Rodriguez-Navarro and Doehne, 1999). The temperature regime was also found to be a key factor in controlling the outcome of the simulated weathering by salt crystallization, in relation to its influence on the thermal expansion of the salt, the depth of penetration of the solution and the time and rate for its evaporation (Smith et al., 2005). It was also determined that the use of convective and radiative heating for the drying process provides different results, with only radiative heating affecting the material's integrity (Gomez-Heras and Fort, 2007).

Some constraints in the simulation of the stone performance by artificial weathering stands in the methodological approach, which examines degradation in relation to a specific stressor, without accounting for the holistic effect of multiple agents that are normally found in service conditions (Silva et al., 2011). When multiple processes were investigated simultaneously, as in the case of heating-cooling-wetting, a significant increase in the rate of degradation was observed (Ghobadi et al., 2014).

1.5.1 Modelling of the stone performance

In the last years, statistical models have been developed from field and laboratory exposure data to assess the response of building stone under future scenarios. Both methodologies represent the two main approaches to the modelling of the stone performance. Field exposure was used to inform the development of dose-response functions (DRFs). These models are based upon the regression of the

dependent variable, represented by an indicator of the sample performance, against one or more environmental factors. In contrast, damage functions are most often developed from artificial accelerated ageing of stone samples to physical stressors. Unlike DRFs, damage models usually integrate the stone mechanical/physical properties as predictors of the stone performance, while the environmental stressor is not directly expressed.

Dose-response functions and Damage Models were adopted within the context of different studies to evaluate the impact of future climatic conditions on the Architectural Heritage in Europe, by mapping areas at risk of surface recession for carbonate stones (Bonazza et al., 2009a), conducting a surface recession risk assessment of architectural buildings in Italy (Gaddi et al., 2022) and predicting the effects of thermal stress on Carrara marble (Bonazza et al., 2009b). Different dose-response functions were developed in the past from a wide range of climatic and environmental data, exposure conditions and methodological approaches (figure 1-5).

Their progress reflects a timeline that adapts to the variations in environmental conditions and the progressively improved understanding of the factors at the base of stone degradation. One of the first attempts to model the performance of stone was conducted by the Regional Air Pollution Study (RAPS), promoted by the Environmental Protection Agency (EPA) (F. Mansfeld, 1980). Reddy et Al. (1986) investigated the effects of precipitation on marble and limestone by chemical analysis of the samples run-off water (Reddy et al., 1986). Models increased in the level of complexity and accuracy of the output with the UK National Materials Exposure Program (NMEP), conducted between 1987 and

1991, with the integration of atmospheric SO_2, total rainfall and rainfall acidity (Butlin et al., 1995).

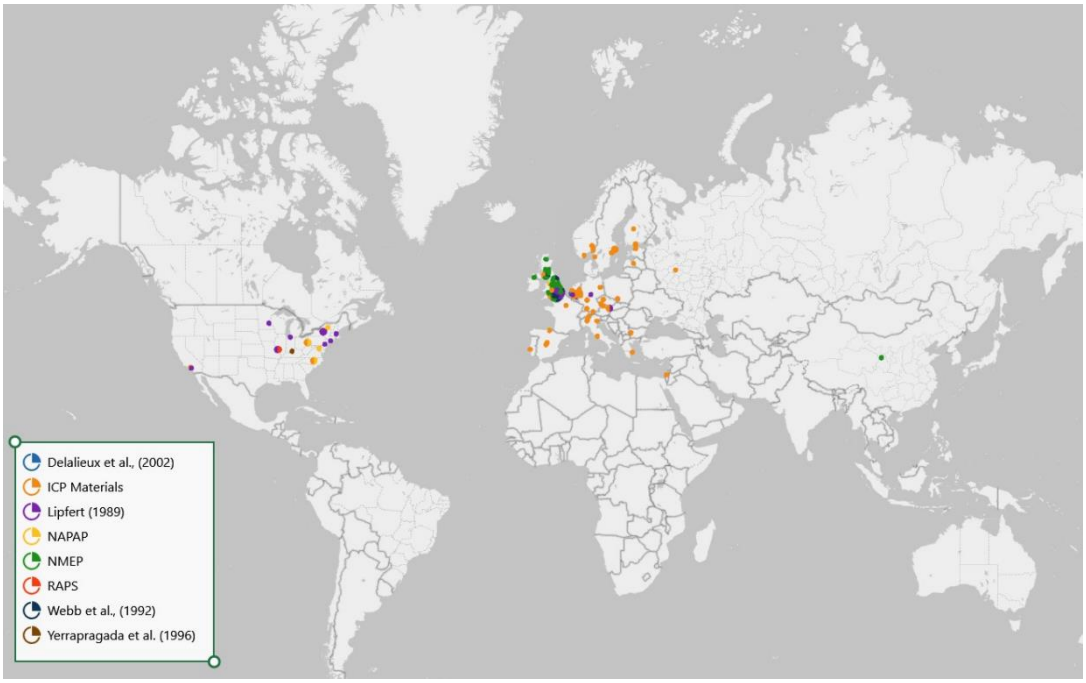

Figure 1-5: test-sites locations adopted by the different field exposure programs for the development of dose-response functions.

The first theoretical support to the development of DRFs for stone materials came from the work of Lipfert (1989), who accounted for the contribution of three main mechanisms to the stone deterioration, i.e., dissolution in clean rain, acceleration of dissolution caused by rain acidity, and attack by gaseous air pollutants. Most DRFs that followed Lipfert's study comply with the same theoretical structure, integrating terms for the dry deposition of gaseous pollutants and rainfall data (Webb et al., 1992; Yerrapragada et al., 1996; Delalieux et al, 2002).

Although the integration of these three terms represented the prevalent approach to most DRFs, there are some exceptions, as the models derived from the

National Acid Precipitation Assessment Program (NAPAP), which integrated temperature as a predictor (Baedecker and Reddy, 1993b) and the theoretical model developed by Livingstone, where the relative contribution of the main processes involved in calcium dissolution was based upon the electrolyte theory and carbonate equilibria (Livingstone, 1992).

Similarly, several damage models were developed from the accelerated exposure of stone samples. Mutlutürk et al (2004) developed one of the first damage models from the artificial exposure to freeze-thawing and heating-cooling of 10 different rock typologies. Other types of indicators of the stone durability were subsequently integrated to Mutlutürk model to quantify the degradation process on a variety of stone types and decay processes (Mohamed Aly Abdelhamid, 2020; Jamshidi et al., 2013). Akin and Özan (2011) employed Mutlutürk's model to express the stone durability against several environmental processes on yellow travertine samples and examined the contribution of porosity to the stone damage. Ghobadi et al. (2014) adopted a similar approach, where half-life and decay constant values were determined by UCS measurements of nine sandstone typologies with different levels of porosity.

Mutlutürk model was also applied to express the stone mechanical performance under both static and dynamic conditions (Wang et al., 2016a). The same approach was followed by Wang et al. (2016b), to estimate the integrity loss after thermal shock, and Bin Du et al., (2019), for the long-term prediction of dynamic compression strength after wetting and drying exposure. Further developments involved its integration into multivariate models, to predict the properties of carbonate and travertine stones (Jamshidi et al., 2015; Yavuz et al., 2006). Porosity values or correlated variables were often incorporated as predictors to

damage functions, to improve the statistical significance of models (Amirkiyaei et al., 2021; Bayram et al., 2012; Jamshidi et al., 2015). A first attempt to predict the stone resistance to freeze-thaw in relation to the petrographic characteristics of the stone was recently conducted on granitic rocks (Jamshidi et al., 2020).

1.6 Aims and Objectives

An accurate representation of the mechanisms and factors controlling the rate of weathering at the base of the interaction of stone with rainwater is still to be achieved. To ensure the full representation of the complexity of the underlying the process there is a clear need to evaluate the integration of more comprehensive information into the modelling process. Most of the available predictive models do not integrate information that has a crucial role in controlling the rate of the weathering progression. Such information refers to the characteristic of the rainfall regimes, as well as to the properties of the stone that control the interaction.

The aim of the thesis is to research the rates of mineral dissolution under variable precipitation regimes, making a comparison between the performance trend of different types of sedimentary stones used in construction when exposed to equivalent conditions. The study aims to advance fundamental research on the modelling of the stone performance by expanding the understanding of the factors that influence the rate of degradation. At the same time, it aims at supporting the development of a new methodological approach for the acquisition of exposure data by accelerated laboratory weathering.

The objectives of the research are:

- To design and test an apparatus for the artificial accelerated exposure of stone samples and study of the process of mineral dissolution.
- To explore the rates of dissolution for the different stone types in relation to their properties.
- To explore the mineral dissolution trend of different stone typologies subject to artificial weathering under equivalent conditions.
- To investigate the influence of the rainfall event duration over the rate of mineral dissolution.
- To verify the correlation between mineral dissolution rate and mass-loss.

As pointed out by Saba et al., (2018) no mathematical model has yet been taken as regulatory by national and international authorities, showing the need for further advances in this research area. The aim is to enable an evaluation of the decay potential rate of progression to establish a management strategy based on prevention. As research proceeds, improved information is made available through updated climate projections with consistently higher spatial resolution, enabling the possibility for increasingly accurate determinations of the potential effects over specific sites.

1.7 Research methodology

The present research makes use of accelerated weathering to evaluate the performance of different stone types when exposed to the action of rainwater. A

total of four test-set was assembled by combining different sedimentary stone types presenting variable amounts of carbonate minerals and different structural properties. Additionally, samples were selected based on their past use as construction material or current use as replacement stones. The selection of the samples was conducted from literature information, followed by their morphological and compositional characterization by X-ray computed tomography.

Each test-set was tested during four rounds of artificial weathering using an exposure apparatus specifically designed to fit to the project requirements. The experimental conditions involved the cyclic exposure of the samples to surrogate acidic rainwater and UVA/UVB lamps to promote the water evaporation. Variable timeframes of exposure and/or conditions were applied to explore different aspects of the weathering process. The following conditions were investigated:

Exposure of triplicate specimens of three stone types to surrogate rainwater by a stable cyclic regime. This test trial was aimed at assessing the variability of the dissolution trend among replicate samples exposed to equivalent conditions.

Exposure of 10 samples to surrogate rainwater and UVA/UVB lamps by a short-term cyclic stable regime. The test trial was aimed at evaluating the short-term dissolution under stable conditions.

Exposure of 10 samples to surrogate rainwater and UVA/UVB lamps by a long-term cyclic and stable regime. The test trial was aimed at evaluating the long-term dissolution process under stable conditions and provide a control for the comparative assessment of the dissolution trends obtained from variable exposure conditions.

Exposure of 10 samples to surrogate rainwater and UVA/UVB lamps by a long-term cyclic variable regime. This test trial was aimed at assessing the influence of the rainfall event duration over the rate of mineral dissolution. The samples were exposed to a total of 5 consecutive water delivery regimes.

The weathering process was monitored from the elemental analysis of the run-off water sampled at regular intervals of time throughout the full duration of the exposure. The mass-loss experienced by each sample was recorded at the end of each exposure trial. The data analysis process involved the extrapolation of the dissolution rate from the of the concentration of different elements (Ca, Mg, K, Na and Fe) dissolved in the leachate at each sampling point. The rate of dissolution of each analyte at each sampling point was plotted to investigate the overtime trend and verify the presence of variations. The comparative evaluation between different exposure trials supported the interpretation of the results in relation to variable exposure conditions and allowed for the interpretation of the factors involved in the dissolution progression.

Multivariate analysis was adopted as part of the data treatment process to support the interpretation at different levels. Principal component analysis was applied to verify the relationship between variables, identify the discriminatory power of the dissolved elements between different samples and explore the existence of underlying patterns in the dataset. The technique was also used to test the functionality of the artificial apparatus, to identify potential malfunctions or defects of the experimental process from the identification of outliers.

Ultimately, multivariate regression analysis and principal component regression were used to investigate the correlation between dissolution rate and duration of

the rainfall cycle and the possibility of predicting the dissolution rate of Ca based on the duration of the rainfall event.

1.8 Research limitations

Stone degradation is a complex process involving the simultaneous interaction of multiple factors (Gomez-Heras and Fort, 2007). The acquisition of accurate prediction data relies upon the possibility of reproducing, with an acceptable margin of error, the mechanisms and processes that the stone would experience in a natural type of setting. Still, the reproducibility of the natural process under laboratory conditions is limited.

In this respect, the present work aims at expanding the understanding of the control factors at the base of the mechanism of degradation, and not necessarily at replicating the complexity of natural exposure conditions. Instead, it is based upon the selective evaluation of the influence of individual parameters.

The data provided by this study does not account for factors that can significantly influence the processes investigated. The effects of the time of wetness, wind directionality, relative humidity and atmospheric pollution are known to control the progression and rate of the stone degradation. The same applies to temperature, which will be included as a parameter during the accelerated weathering process only on the basis of its accessory function to water evaporation. Additionally, It is important to take into account how orientation influences the effects of climatic agents that are subject to directionally, as wind and solar radiation.

The stone degradation is not only controlled by the environment. Factors that can cause an acceleration of the decay progression can derive from inappropriate manufacturing methods of the building element, the incorrect placement with respect to the stone bedding, any previous intervention including the replacement of stone elements and adoption of an unproper mortar.

Nonetheless, the alternative option of natural field exposure to fully represent the combination of factors that contribute to the stone decay is in contrast with the following experimental requirements:

- The selective variation of the parameters of interest is necessary to determine the potential influence of variables such as the duration of the rainfall event over the mineral dissolution trend. This condition is necessary to exclude the impact of any additional parameter when analysing the dissolution process variation. This requirement is not achievable in a natural setting, due to the wide range of variables that can influence the stone performance.
- Comparability with a control trial is necessary to evaluate the impact of changes in the experimental conditions. This requirement relies on the experimental process being repeatable, which is unachievable under natural conditions.

Therefore, the results presented within the context of this study should inform about the influence of specific factors and must be read in connection to the wider context that characterise an element in service. These considerations highlight the need to interpret the data obtained from the proposed methodology as a partial information of a much more complex process.

1.9 Thesis structure

The thesis is divided into nine chapters.

Chapter 1 introduces the research and describes its aims, objectives, methodology and limitations. A review of the existing literature covering the main decay factors and mechanisms of degradation affecting sedimentary building stone are also presented in Chapter 1, along with an overview of the state of the art of the modelling of stone degradation, ending with a summary of the main findings and the overall design of the research.

Chapter 2 presents the Materials and Methods, which include a description of the exposure apparatus, including its design and operating principles, the specifications of the accelerated exposure procedure. It also presents the samples test-set, providing an overview of the historical significance and current use, along with a petrographic description obtained from literature. The methodologies applied for the sample's characterization and the investigation of their performance during accelerated exposure are also presented in this chapter.

Chapter 3 reports the information obtained from the characterization of the samples employed in the study by X-ray computed tomography analysis.

The experimental results are presented in chapter 4 and 5, 6 and 7.

Chapter 4 introduces the findings of the trial test and variability test. The trial test sub-section provides details over the performance of the exposure apparatus and reports the post-exposure mass loss of the samples. For the variability test, the

chapter introduces the observation conducted over the samples performance from the dissolution trends, mean dissolution rates and weight change values. It also presents the results of the principal component analysis conducted on the dissolution rates of the analytes.

Chapter 5 reports the results of the short-term performance test with stable water delivery cycles. The chapter is structured similarly to Chapter 3, presenting the dissolution trends of the samples, mean dissolution rates, post-exposure weight change and principal component analysis. It also includes observations over the comparison with the dissolution trends obtained from the variability test.

The results of the long-term performance tests under stable and variable exposure conditions are reported in Chapter 6 and 7, respectively. Chapter 6 follows a similar structure to Chapters 4 and 5. Chapter 7 also introduces the results of the comparative assessment between the dissolution rates obtained from different rainfall patterns and presents the observation conducted from the comparison of the stones performance under stable and variable exposure conditions.

The discussion of the results and modelling of Ca dissolution rate are introduced in Chapter 8, and the conclusions and recommendation for future work are presented in Chapter 9.

2. Materials, Methods and Instruments

This chapter includes description of the criteria followed for the selection of the stones samples, together with a comprehensive review of the techniques and methodologies applied. Details are given about the full test-set of stone samples, the exposure apparatus design and operating principles, and settings for each experimental trial. It also describes the techniques and procedures applied for the characterization of samples and the assessment of their performance during the experimental trial.

2.1 Materials

2.1.1 Samples Selection and description

The stone types were selected from the sedimentary class. Sedimentary stone is the type of stone most extensively used in Scotland, the UK and the rest of Europe for building construction. It is also characterised by an overall higher susceptibility to weathering.

The test-set selection was conducted based on information acquired from literature and after consultation with building stone specialists from the British

Geological Survey at the Lyell centre in Edinburgh. Several criteria were established to select the stone samples, as follows:

a. The structural and compositional properties; the main benchmarks for selection were the concentration of carbonate minerals and the total amount of porosity. Further intrinsic parameters that were taken into consideration were the dimension of the clasts and the presence and amount of feldspars and clay minerals.
b. The frequency in the use of the stone throughout history as construction material.
c. The current use as matching stone in replacement interventions.
d. The geographical area of use, and thereafter the environmental conditions, with preference given to regions identified as at higher risk of surface recession by rainfall based on existing hazard maps.
e. The previous use of the stone in controlled exposure experiments involving the action of surrogate rainwater solution.

The test-set was assembled from three categories of sedimentary stone, i.e.: arenites (identified by the suffix -SS), calcarenites (identified by the suffix -CA and -BC) and limestone (identified by the suffix -LM). The samples were gathered from different quarries in Scotland, England, Switzerland and Italy. The complete test-set consisted of 10 specimens, with a carbonate minerals content ranging from 0 to 100% and values of total porosity from 1 to 20%. As already mentioned, conservation should prioritise the preservation of the original stone, but there are certain instances when this is not possible and stone-matching is required. This involves the identification of the specimen with the closest characteristics to a

sample that could not be acquired due to the closure of the quarry. The information over the selected stones was mainly acquired from Franzoni and Sassoni (2011), Bläuer (1985), Lott and Cooper (2005) and Duthie (2011). The final objective of the test-set selection was to obtain a wide range of properties, so to enable a proper evaluation of the dissolution process based on the stone characteristics. The stone types selected for the present research are presented here and listed in table 2-1.

Bearl Sandstone (BL-SS)

Figure 2-1: BL-SS (actual size)

Bearl sandstone (England) (figure 2-1) is quarried near Corbridge, Northumberland. The stone has been mainly used locally as construction material for houses, churches, and bridges, as well as replacement stone for conservation works. It is a medium-grained Carboniferous sandstone, with a moderately well sorted uniform fabric. The clastic fraction is mainly composed of quartz grains.

The stone contains relatively high amounts of feldspars (c. 4%) and clay minerals (c. 7%) and presents a relatively high porosity.

Bernese Sandstone (BL-SS)

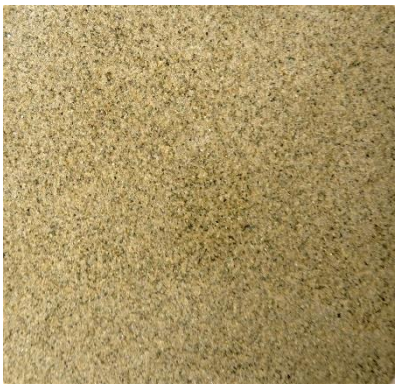

Figure 2-2: BN-SS (actual size)

Bernese sandstone (Switzerland) (figure 2-2) is from the Upper Marine Molasse, formed by material transported from the erosion of the Alps. Bernese sandstone has a high cultural and historical significance for Switzerland, due to its extensive employment in numerous buildings in the Bern area, especially in the old part of the city. The extraction of Bernese sandstone started in the 15th century from the south of Bern, in Ostermundigen and Gurten, although evidence exists of its use in the Roman period. If originally it was only used locally, later its employment as building stone spread to other regions of Switzerland, as a result of the development of new transport facilities.

Bernese sandstone can be classified as a soft stone, which is why it was widely used as carving stone for elaborated building façades. For this same reason, the

stone is highly susceptible to weathering and today its conservation poses considerable challenges. Examples of buildings in Bern where the stone was employed are Bern minster, the Kornhaus (1711), the Heilig-Geist-Kirche (1496), the Zytglogge (1218), the Burgerspital (1307) and the Bundeshaus (1902). Today there are three active quarries, Gurten, Krauchthal and Ostermundigen, mostly supplying Bernese sandstone as a replacement stone in conservation works. It is a fine to medium grained arkose sandstone mainly composed of quartz and feldspars (20-30%). The cement is mainly formed by calcite, less often by Dolomite, for a total amount of carbonate minerals of 30-40%. Clay minerals (illite, chlorite, smectite) are also present. The stone has high porosity and level of interconnections.

Cadeby limestone (CB-LM)

Figure 2-3: CB-LM (actual size)

Cadeby limestone (England) (figure 2-3) is a late Permian dolomitic limestone, extensively quarried for several centuries for construction purposes. Due to the mineral composition rich in magnesium carbonate, it was previously known as

Lower Magnesian Limestone. The outcrop extends from north Nottinghamshire to the Northumberland coast and there are currently three active quarries supplying Cadeby limestone, i.e., Highmoor, Hazel Lane and Cadeby quarries. The stone has high historical and cultural significance, due to its widespread use as construction material throughout history. The earliest evidence of its use dates back to Roman times, with the presence of several historical sites located along the outcrop. The stone remained in use for several centuries, with many valuable examples in the Yorkshire area, which include Beverley minster (1188) and Southwell minster (1108), the castles of Conisborough and Pontefract, the abbeys of Selby, Thornton, Welbeck and Roche and the House of Parliament. The limestone is mainly composed of calcite (c. 54 %) and dolomite (c. 45 %). It can present a large variety of textures, ranging from loosely compact and highly porous specimens to very compact and less porous typologies. Some varieties still maintain intact a bioclastic texture.

Crema Fiorito Biocalcarenite (CF-BC)

Figure 2-4: CF-BC (actual size)

Crema Fiorito (Italy) (figure 2-4) is a calcarenite used for interior and exterior applications in wall and paving applications. It is a fine-grained sandstone with a high degree of porosity (19.5%). Crema Fiorito Biocalcarenite is mainly composed of carbonate granules of algal fragments, shells, fragments of bivalves and micro-crystalline calcite. It presents a low content of siliceous granules and grains are bonded by carbonate cement. Calcite and dolomite are the dominant mineral fraction and constitute about 80% of the stone composition.

Dunhouse Buff sandstone (DH-SS)

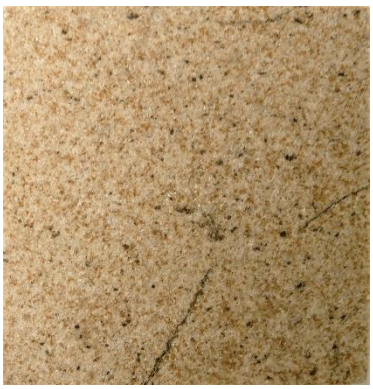

Figure 2-5: DH-SS (actual size)

Dunhouse Buff sandstone (Scotland) (figure 2-5) is a popular carboniferous sandstone widely employed as building material in Edinburgh, Glasgow and Newcastle. The quarry is located near Darlington and has been active since the early 1900s. Besides its extensive use in contemporary constructions, it was also

used as replacement stone in several conservation projects of significant buildings, including Durham castle (1072), Edinburgh castle (1103) and Castle Howard (1701). It is a fine grained non-calcareous sandstone with a high level of porosity (c. 17%). The clastic fraction is mainly composed of sub-rounded quartz crystals (c. 70%) and of K-feldspars (c. 4 %). Kaolinite is also present filling the pores (5 %).

Drumhead sandstone (DM-SS)

Figure 2-6: DM-SS (actual size)

Drumhead sandstone (Scotland) (figure 2-6) was quarried near Denny, Falkirk, since the early 18th century and throughout the following century. Its early employment in construction was restricted to the Falkirk and Stirling area, until the opening of the Union Canal allowed its transportation to Glasgow, Linlithgow and Edinburgh. The stone has been employed for the construction of many historically significant buildings, such as Craigs House (early 19th century) and Dunipace Parish Church, Stirling (1834). The importance of the stone also relates to its

matching characteristics to sandstone typologies which are no longer available, due to the closure of the quarries that supplied construction stone in central Scotland. These include the sandstone from Giffnock and Bishopbriggs, which provided building stone for many prestigious buildings in the UK.

The stone is from the Upper Limestone Formation of the Clackmannan Group, of late carboniferous age. The quarry supplies two different types of building stones, one characterized by a pale creamy buff colour and frequent lamination, the other consisting of a white uniform variety. The white and uniform variety was the sandstone typology obtained for the purpose of the present research. The stone is mainly composed of monocrystalline quartz (c. 65%). A small fraction of feldspars (c. 2%), in the form of K-feldspars and plagioclase, is still well preserved. The sandstone also contains a small amount of carbonate minerals (c. 3%), which form the matrix along with clay minerals, partially resulting from the alteration of feldspars, and silica overgrowth on quartz grains (c. 6%). The stone presents high porosity, with a good level of interconnection between pores.

Grigio Perla Calcarenite (GP-CA)

Figure 2-7: GP-CA (actual size)

Grigio Perla (Italy) (figure 2-7) is a fine-grained light grey calcarenite with medium porosity, extracted from the Maremma area of Tuscany. It is mostly used for internal and external paving and cladding. Grigio Perla is mainly composed of calcium carbonate (74.2%) and has a low content of quartz, feldspars, fragments of magmatic and metamorphic rocks. The fine grains are bonded by carbonate cement. The stone presents moderate to high porosity.

Pietra Serena sandstone (PS-SS)

Figure 2-8: PS-SS (actual size)

Pietra serena sandstone (Italy) (figure 2-8) has very high historical significance. Its citation in historical records dates back to 1568, although its employment as construction stone goes back to much earlier times. It was first employed by the Etruscans during the Archaic period and successively in Roman times. Throughout history the stone was extracted from numerous quarries in Tuscany, in the areas surrounding Florence. Today Pietra Serena is mostly known for its

employment during the Renaissance period, especially in relation to the work of Filippo Brunelleschi.

Some of the most prominent examples of buildings where Pietra Serena was used are the basilica of San Lorenzo (1470), basilica of Santo Spirito (1481), basilica of Santissima Annunziata (1250) and Spedale degli Innocenti (1419). Pietra Serena strongly influenced the aesthetic of the renaissance architecture, for the contrast derived by the combination of the grey colour of the stone and the white rendering of the masonry. Although the stone is typically associated with the name of Filippo Brunelleschi, other prominent architects and engineers employed it, including Michelangelo Buonarroti and Giuseppe Poggi. The stone has a distinct grey colour, the framework grains are fine-grained and homogeneous in size. It is mainly composed of angular to sub-angular monocrystalline and polycrystalline quartz, a much lower amounts of feldspars, and fragments of silicate and carbonate rocks. The grains are bonded by carbonate cement (c. 12%), that almost completely fills the pores.

Pietra Serena Extradura (PSX-SS)

Figure 2-9: PSX-SS (actual size)

Pietra Serena Extradura (Italy) (figure 2-9) represents a more compact variety of Pietra Serena. It is a fine-grained grey sandstone, with grains displaying parallel orientation to the bedding planes. The framework grains are bonded by carbonate cement (c. 15%) that completely fills the interstices. The mineralogical composition resembles that of Pietra Serena, and it is mainly composed by quartz, feldspars, mica and fragments of silicate and carbonate rocks.

Pitairlie sandstone (PT-SS)

Figure 2-10: PT-SS (actual size)

Pitairlie sandstone (Scotland) (2-10) has been quarried since the mid-19th century near Monikie in Angus, before operations ceased in 1915. The quarry was reopened by the Denfind Stone company and is still in operation. Its employment in construction is largely related to paving, although the stone has found recent use in conservation works as well.

It is a fine-grained sublithic arenite dominated by quartz and lithic grains. Feldspars are present in relatively high amounts, along with accessory minerals, such as biotite, iron oxide and chlorite. The intergranular component consists of silica overgrowths and calcite. Clays are also present filling the pore space. The stone presents low porosity.

Table 2-1: list of selected stone types and identification

Bearl sandstone	BL-SS
Bernese sandstone	BN-SS
Cadeby limestone	CB-LM
Crema Fiorito biocalcarenite	CF-BC
Dunhouse sandstone	DH-SS
Drumhead sandstone	DM-SS
Grigio Perla calcarenite	GP-CA
Pietra Serena sandstone	PS-SS
Pietra Serena extradura sandstone	PSX-SS
Pitairlie sandstone	PT-SS

2.1.2 Samples preparation

The samples preparation for the accelerated artificial exposure was carried with the support of the City of Glasgow College. The samples were cut into small slabs of 5 x 5 x 1 cm in replicates of four. This dimension was chosen based on the specifications previously adopted by site-exposures programs involving stone specimens, e.g., the International Co-operative Programme on Effects of Air Pollution on Materials, including Historic and Cultural Monuments (ICP Materials).

A total of four test-sets, corresponding to a total amount of 48 samples, were prepared. For some specimens, a higher number of replicates was prepared, to allow for some preliminary tests to be conducted. One test-set was used to determine the fresh stone characteristics (test-set 0), while the remaining three (test-set 1; test-set 2; and test-set 3) were subject to accelerated weathering.

The morphological analysis was conducted on cylindrical cores measuring 5 mm in diameter sampled from each stone using an 8 mm drill bit on test-set 0. The core extraction was performed at the Department of Civil and Environmental Engineering (CEE) of the University of Strathclyde.

2.1.3 Exposure apparatus

A customized exposure apparatus was designed to replicate the action of a standard environmental chamber, with the addition of some specific elements to fit the purposes of the research. The design of the apparatus was based upon

exposure systems adopted for field and laboratory exposure. Some specifications, as the use of plants irrigators for the spraying of the solution, were gathered from the laboratory exposure system introduced by Baedecker (1993). Adjustments to the procedure illustrated by the study were carried regarding the use of 60 x 30 cm slabs, to enable the contemporaneous exposure of multiple samples within a limited space. The possibility of altering the samples dimension was sustained within the same study. The dimension of the stone samples was instead informed by the samples' specification adopted by the UNECE/ICP program.

The design was partially inspired by some of the systems adopted by field exposure programs, as the ones developed by Reddy et al., (1993), Cardell et al., (2002) and Delalieux et al., (2002), to conform to specific experimental necessities, including the collection of the leachate for analysis. The materials where selected to ensure compatibility with the solution and prevent contamination of the run-off water. The design process was carried using the open access 3D modelling software pCon.Planner (EasternGraphics GmbH; Thuringia, Germany).

The apparatus consisted of a series of independent exposure units (figure 2-11), each accommodating one sample slab of 5 x 5 x 1 cm. A single unit (figure 2-12) is composed of a stand (9) which provides a 15˚ inclination to the sample; acrylic glass shields on three sides (8); a shelf for support (5); two rubber strips (4) to elevate the sample from the base and allow proper ventilation; a percolation tray for the collection of the run-off water (7); three neoprene strips (1) to hold the sample (3) in place and isolate the sides, restricting the contact of the water to the stone surface. The adoption of the neoprene strips was preferred to the sealing of the samples into the exposure units to facilitate their removal and repositioning.

The strips positioned on the back of the sample had the additional purpose of pushing the slab beyond the base, so as to avoid any barrier to the water flow towards the collection tray. Brackets (6) were used to assemble the glass shields, to allow any required adjustment and enable the quick removal/addition of units.

The exposure units were assembled into racks (figure 2-13) and positioned on the shelf of an enclosed “plant shed” of dimension 50 cm (width) x 44.5 cm (depth) x 134 cm (height) (figure 2-14) to avoid contamination with ambient dust. On a lower shelf were placed the bottles for the water collection. Water was conveyed from the tray by means of a PVC tube inserted in the containers. To minimize contamination, the bottles’ openings were sealed with cling film. Contamination of the samples was prevented by also sealing the upper part of the plant shed with cling film. Battery-operated pumps (Landrip HZ-DT01) were used to convey the surrogate rainwater to the samples through a series of nozzle. The channel of each tray was connected to a tube where the nozzles connectors are inserted in correspondence to the exposure units. The water supply was stored in a tank, placed at a lower level than the pump. The development of the exposure apparatus involved the design of some elements, namely the stand (9) and the gutters for the collection of water (7). The design process was conducted using the software Autodesk 123D Design. The stand was designed to provide a 15˚ angle slope to the samples and offer support to the exposure units (figure 2-15a). This inclination was chosen based on previous work for the field exposure of stone samples. The exposure units were kept in place by a raised edge on the front of the stand, which prevented the necessity of securing both parts together and allowed a quick replacement in case of necessity.

The collection gutter was designed to collect the runoff water from the samples and deliver it to the containers through the insertion of plastic tubes (figure 2-15b). In this case the main necessity was the stability of the component's constituent material upon contact with water. The trays were not fixed to the individual units but were instead secured in place by the pressure applied by the lateral shields. A gasket was applied between the collection trays and the lateral shields for higher stability. The design of both components was followed by their 3D printing at the Fab-Lab at the University of Strathclyde. At a first stage, two preliminary models were printed in Polylactic Acid Filament (figure 2-15c and 2-15d) to check the suitability of the design to 3D printing and correct any potential flaws.

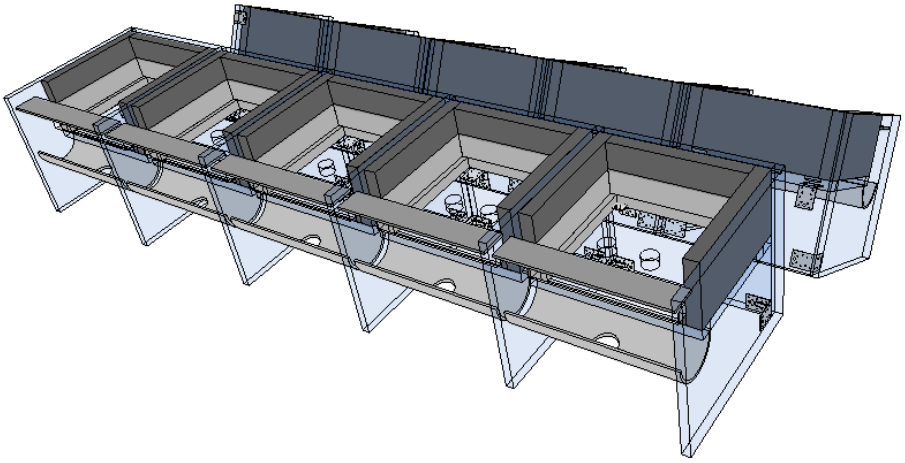

Figure 2-11: 3D model showing the design of the exposure set-up and its components.

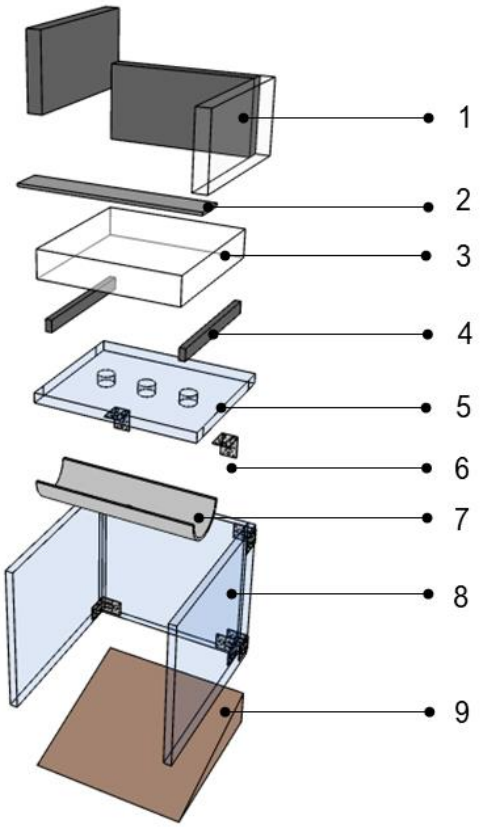

Figure 2-12: exploded view of a single exposure unit displaying the individual components.

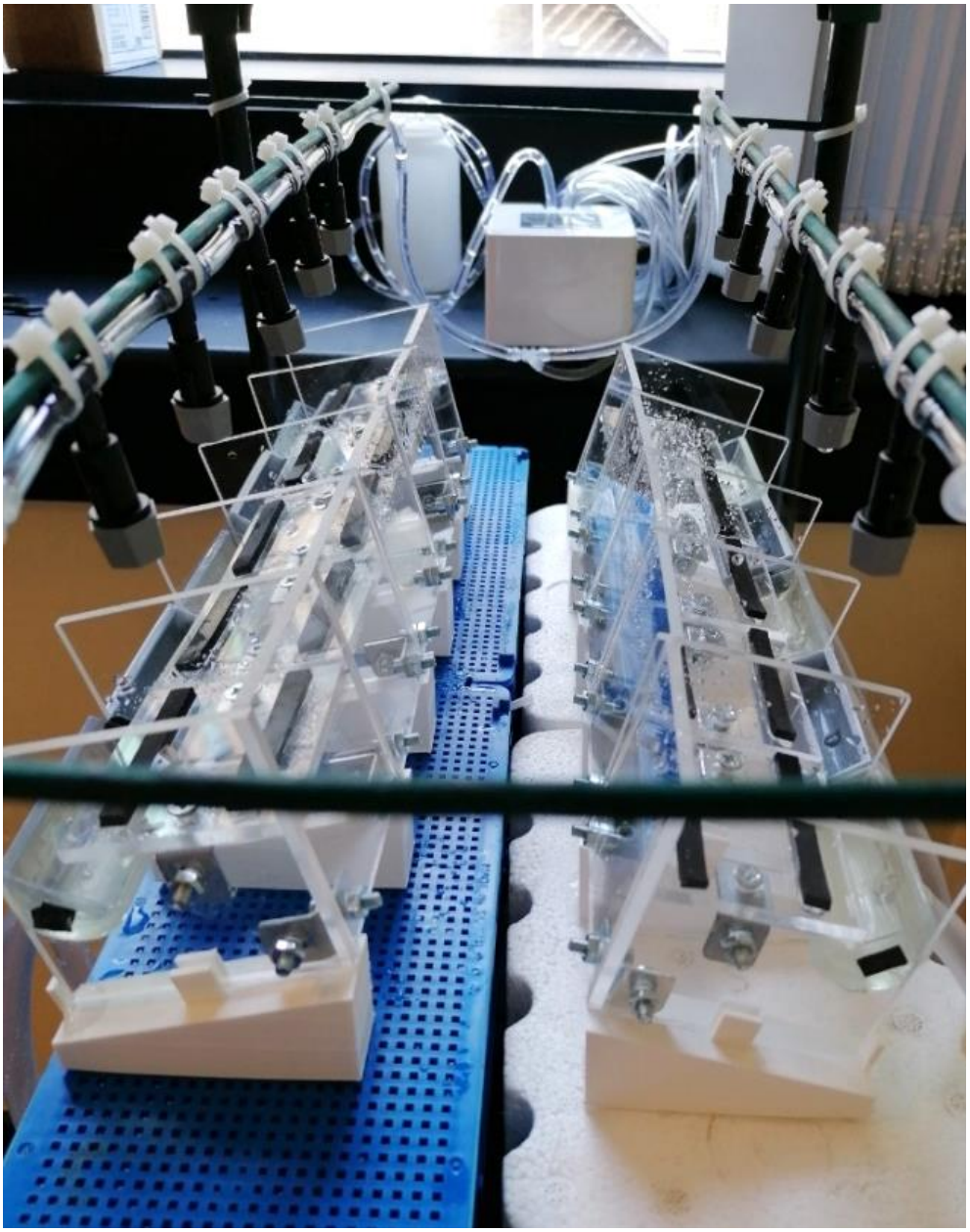

Figure 2-13: the assembled exposure units within the exposure set-up.

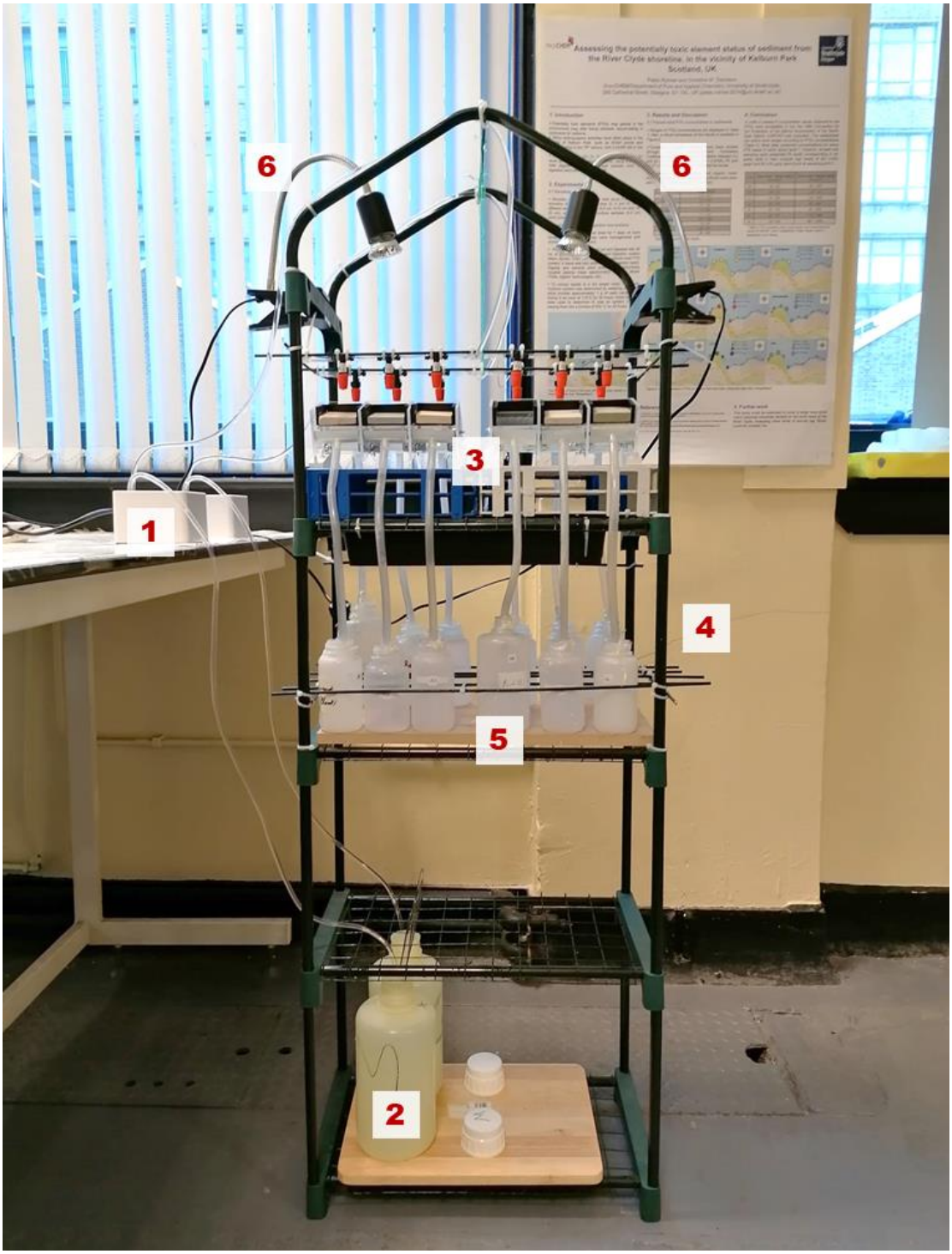

Figure 2-14: full exposure apparatus consisting of pumps (1), bottles containing the surrogate rainwater solution (2), the assembled exposure units with the samples (3), the collection bottles (4) placed on a shelve (5) of the plant shed, and UVA/UVB lamps.

An adjustment to the design of the stand was necessary to improve its stability and increase support. The final components were printed using different materials, whose selection was based on the specific purpose of each element.

To avoid any interaction with the water solution, the collection trays were printed with a UV waterproof resin, while the stands were printed in polylactic acid (PLA). The collection trays were produced in two separate rounds, during which two different types of resin were used, i.e., a clear one and a coloured one, which was employed due to a shortage of the first type.

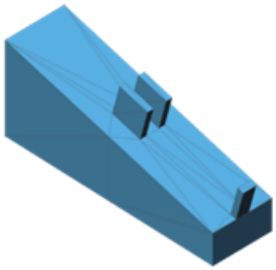

a

c

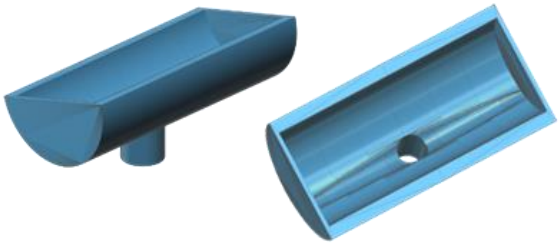

b

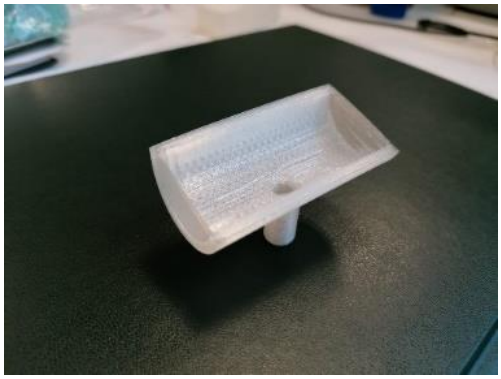

d

Figure 2-15: 3D model of the stand. Figure 4b: 3D model of the gutter for the leachate collection. Figure 4c: Polylactic Acid Filament model of the stand 3D. Figure 4d: Polylactic Acid Filament model of the gutter.

2.2 Artificial accelerated exposure

The testing was based over the controlled exposure of the different stone types to accelerated weathering. Samples were subject to the action of a surrogate rainwater solution to artificially replicate the effects of outdoor exposure to high-rainfall environments under polluted conditions. The artificial ageing process was designed to acquire information over the stone performance in a replicable way.

The leaching experiments were designed to simulate natural climatic strains and obtain data representative of a natural setting. The methodology was based on the cyclic exposure of the samples to individual stressors. The procedure for the artificial accelerated exposure was developed by partly following the guidelines of standards procedure for the testing of Building components.

The overall approach and planning of the experimental stage, including the selection of the degradation agents, was informed by the Joint CIB W080 / RILEM TC 140 protocol – *Prediction of Service Life of Building Materials and Components*. Further specifications regarding the type of stressors adopted and the scheduling of the exposure cycles were sourced from the NORDTEST method NTBUILT 495 – *Building materials and components in the vertical position: exposure to accelerated climatic strains*. Some modifications to the procedure adopted by standard protocols were necessary, because of the specific requirements of the experimental process, for instance in relation to the sampling of the leachate, and the impossibility of acquiring some of the cited components.

The testing comprised several exposure tests of different duration and was designed to evaluate different aspects of the mineral dissolution process. These

included: the comparison of dissolution data between stone samples of the same typology under equivalent conditions; the long and short-term trends in dissolution for samples subject to stable exposure settings; and the presence of variations in the rate of dissolution resulting from the application of variable rainfall patterns.

The stressors that were selected for investigation were:

a. Surrogate rainwater solution, to replicate the effect of rainwater in contemporary urban environments, where nitrogen-containing compounds represent one of the dominant atmospheric pollutants. The present pH values of rainwater in highly polluted urban settings were taken as a reference.

b. UVA/UVB light, by using fluorescent UVA/UVB lamps (50 watt) with a relative spectral distribution in the UV band similar to that of global solar irradiance.

c. Heat, provided by the UVA/UVB lamps, whose action controls different aspects of the weathering process when associated with rainwater.

Each exposure round was based upon a wetting-drying alternation pattern. The full experimental process involved a total of two preliminary rounds of exposure involving a limited number of stone typologies and three rounds of exposure of the full test-set of stone samples (table 2-3). The duration of each exposure trial was decided to gain a progressive understanding of the stone performance and acquire a representative description of the different stages of the decay progression.

Table 2-2: stone types used for each round of accelerated exposure.

EXPOSURE TEST	SAMPLES	STRESSORS	DURATION
Trial Test	BN-SS; PT-SS	- Surrogate rainwater (sulphuric acid solution)	10 days
Variability Test	BN-SS (x3); PT-SS (x3); CB-LM (x3)	- Surrogate rainwater (nitric acid solution)	2 weeks
Short-term performance test	BL-SS; BN-SS; CB-LM; CF-BC; DH-SS; DM-SS; GP-CA; PS-SS; PSX-SS; PT-SS	- Surrogate rainwater (nitric acid solution) - UVA/UVB lamps	1 month
Long-term performance test with stable spray patterns	BL-SS; BN-SS; CB-LM; CF-BC; DH-SS; DM-SS; GP-CA; PS-SS; PSX-SS; PT-SS	- Surrogate rainwater (nitric acid solution) - UVA/UVB lamps	4 months and 10 days
Long-term performance test with variable spray patterns	BL-SS; BN-SS; CB-LM; CF-BC; DH-SS; DM-SS; GP-CA; PS-SS; PSX-SS; PT-SS	- Surrogate rainwater (nitric acid solution) - UVA/UVB lamps	3 months and 10 days

2.2.1 Preliminary tests

2.2.1.1 Trial Test

A trial test was conducted with the aim of testing the exposure apparatus and determine the most appropriate experimental procedure. The preliminary test was carried on 2 stone samples, Cadeby limestone (CB-LM) and Bernese sandstone (BN-SS) (figure 2-16). The samples were selected to compare the response between a limestone and sandstone containing high amount of carbonate minerals. A procedural blank (plexiglass) was included to monitor contamination. The test involved the periodic exposure of the stone slabs to surrogate rainwater, consisting of a sulphuric acid solution with a concentration of the order of 10^{-5} mol L^{-1}, for a period of 10 days. Before the exposure trial, the specimens were dried at 60°C for 5 hours. This temperature was set to avoid any damage to the minerals that can be induced by higher temperatures. In one day, a total number of 6 wetting-drying cycles was completed, corresponding to 60 cycles for an exposure trial of 10 days.

Each cycle was characterized by the following exposure conditions:

a) Surrogate rainwater (4 seconds; water flow rate: 1.5 ml/sec).

b) Ambient laboratory climate, for the remaining time, to complete a cycle of 4 hours.

After the exposure trial, the samples were washed and oven dried at 60°C for 5 hours to determine the weight variation.

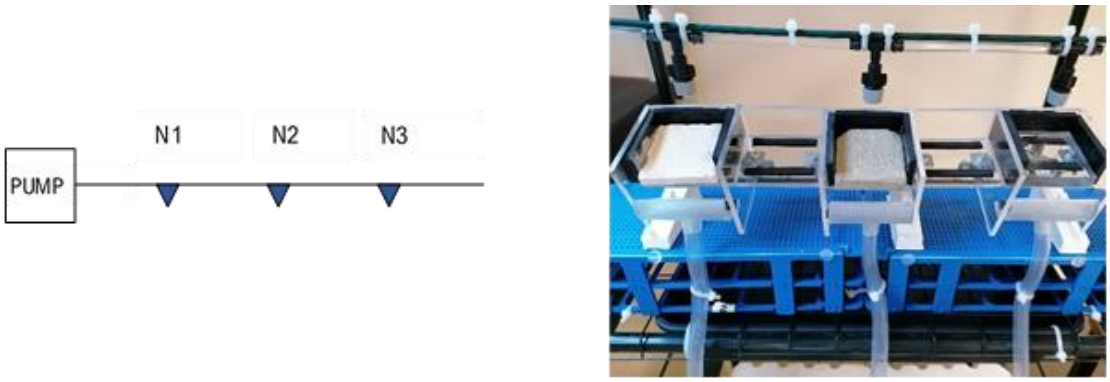

Figure 2-16: set-up of the trial test, with the pump connected to the three nozzles. Two samples and 1 procedural blank were exposed.

2.2.1.2 Variability Test

The trial test was followed by another preliminary test to determine the variability in the response of replicate samples to the leaching action of surrogate rainwater. The test was conducted on triplicate specimens of three stone types, i.e., Bernese sandstone (BN-SS), Pitairlie sandstone (PT-SS) and Cadeby limestone (CB-LM) (figure 2-17). The samples used for the variability test were selected from the initial test-set based on their respective concentrations of carbonate minerals.

The total number of samples used in the leaching test was 10, which included 3 replicates for each of the three selected stone typologies, + 1 procedural blank (plexiglass) to monitor contamination. The test involved the samples periodic exposure to the surrogate rainwater solution for a period of 14 days, with the purpose of assessing the variability between replicates in the amount of the ionic species (Ca, Mg, K, Na and Fe) present in the run-off water.

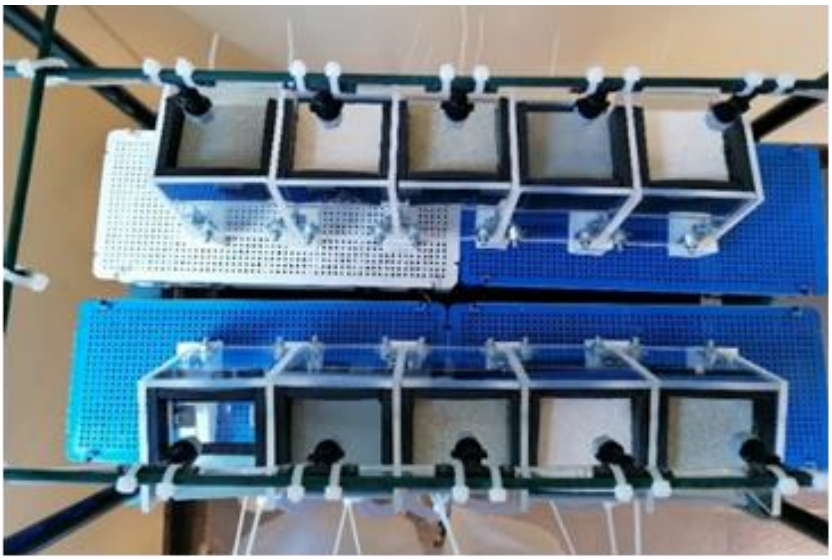

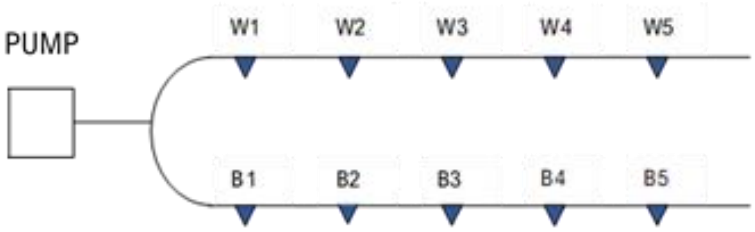

Figure 2-17: exposure set-up for the variability test. One pump was connected to two series of nozzles by a T connector. The samples arrangement was established based on the volumes of water delivered to each sample during the test preparatory stage.

Prior to accelerated exposure, the samples were oven dried for 24 hours at 60˚C. Before starting the test, a preliminary exposure test without the samples was performed to determine the volume of water delivered by each nozzle of the exposure apparatus. Due to minor divergences between the volumes of water supplied by each nozzle (± 0.5 mL of surrogate rainwater per cycle), the individual

exposure units were divided into three groups based on the respective volumes of surrogate rainwater delivered. Each group consisted of three exposure units that distributed similar amounts of solution. Each stone typology was allocated to a group, so that the replicates would be subject to comparable exposure conditions.

For this and the following tests, sulphuric acid was replaced by nitric acid to better simulate the atmospheric composition of contemporary urban environments. Artificial rainwater was prepared by single dilution of 6.30 µL of concentrated nitric acid/L, with a final concentration of the acid of the order of 10^{-4} mol L^{-1}. The surrogate rainwater was delivered to the samples at regular intervals of time during the course of 14 days.

Each exposure cycle consisted of a total duration of 4 hours for each cycle:

a. Surrogate acidic rainwater (7 seconds; water flow rate: 1.5 ml/sec)
b. Laboratory conditions for the remaining time

Six wetting-drying cycles per sample were completed within 24 hours, corresponding to a total of 84 cycles for the whole exposure trial of 14 days. On working days, the leachate for each of the 10 samples were collected every 12 cycles; after weekends the samples were collected every 18 cycles, making a total of six collection times during the 14 days. A total of 60 leachate samples was gathered by the end of the experiment. Leachates were filtered with a 45 µm membrane filter, and 30 mL of leachate was sampled and placed in a 50 mL volumetric flask. Samples were acidified with nitric acid (70%) to a 5% concentration, brought to volume by adding deionized water and stored in a

refrigerator until analysis. During the test, some of the gutters, which were printed using a coloured type of resin due to a shortage of the clear one, started to degrade with swelling and flaking off of the resin (figure 2-18). To avoid the interruption of the test, they were temporarily sealed with insulating tape. After the test, all the faulty components were replaced with new components that were printed using the clear type of resin, which displayed a higher stability upon contact with the leachate solution.

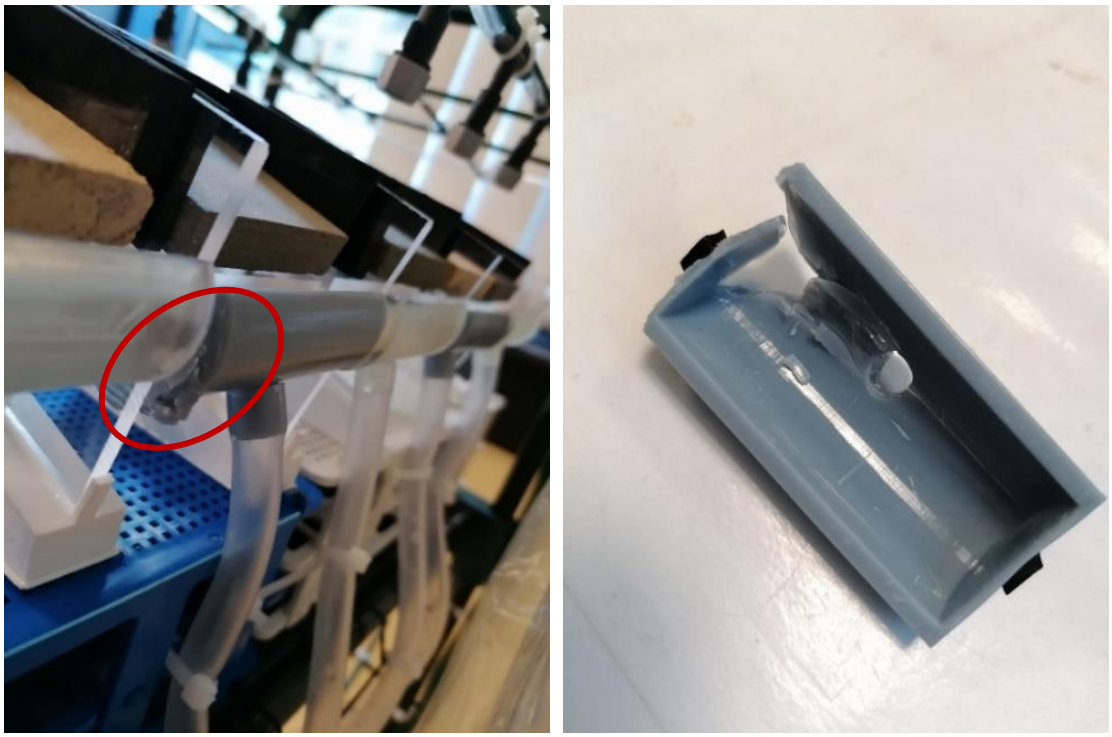

Figure 2-18: detail of the exposure apparatus showing the failure of one of the coloured resin gutters.

2.2.2 Short term exposure

2.2.2.1 Short term performance test (test-set 1)

A test-set consisting of 10 samples was subject to the leaching action of surrogate rainwater (figure 2-19). The tested samples were Crema Fiorito biocalcarenite (CF-BC), Pietra Serena sandstone (PS-SS), Pietra Serena Extradura sandstone (PSX-SS), Pitairlie sandstone (PT-SS), Dunhouse sandstone (DH-SS), Grigioperla calcarenite (GP-CA), Cadeby limestone (CB-LM), Bearl sandstone (BL-SS), Drumhead sandstone (DM-SS), and Bernese sandstone (BN-SS).

The nozzles that had been previously used for the trial and variability tests were replaced with adjustable ones, to allow the regulation of the water flow and ensure equal volumes of water to each sample. The gutters that exhibited a negative interaction with the leachate solution during the previous test were substituted with the clear resin, which proved to be stable upon contact with the samples' leachate. Artificial rainwater was prepared by single dilution of 6.30 µL of concentrated nitric acid (70%), to give a final concentration of the acid in the rainwater of the order of 10^{-4} mol L^{-1}. UVA/UVB lamps were incorporated into the exposure apparatus to promote the evaporation of water.

The specifications adopted for each rainfall pattern are listed in table 2-4. Compared to the variability test, the duration of the surrogate rainwater spraying was increased by 1 second, to compensate for the decrease in water flow rate caused by the higher number of channels connected to the nozzles. A total of 6 cycles were completed in 24 hours, giving a total of 180 cycles for each sample during the full exposure time. The leachate collection for each of the 10 samples

was carried out approximately every 18 cycles, with a total of 11 collection points during the 30 days. The sampling procedure was similar to the one adopted in the previous test, except that this time 40 mL of leachate was collected.

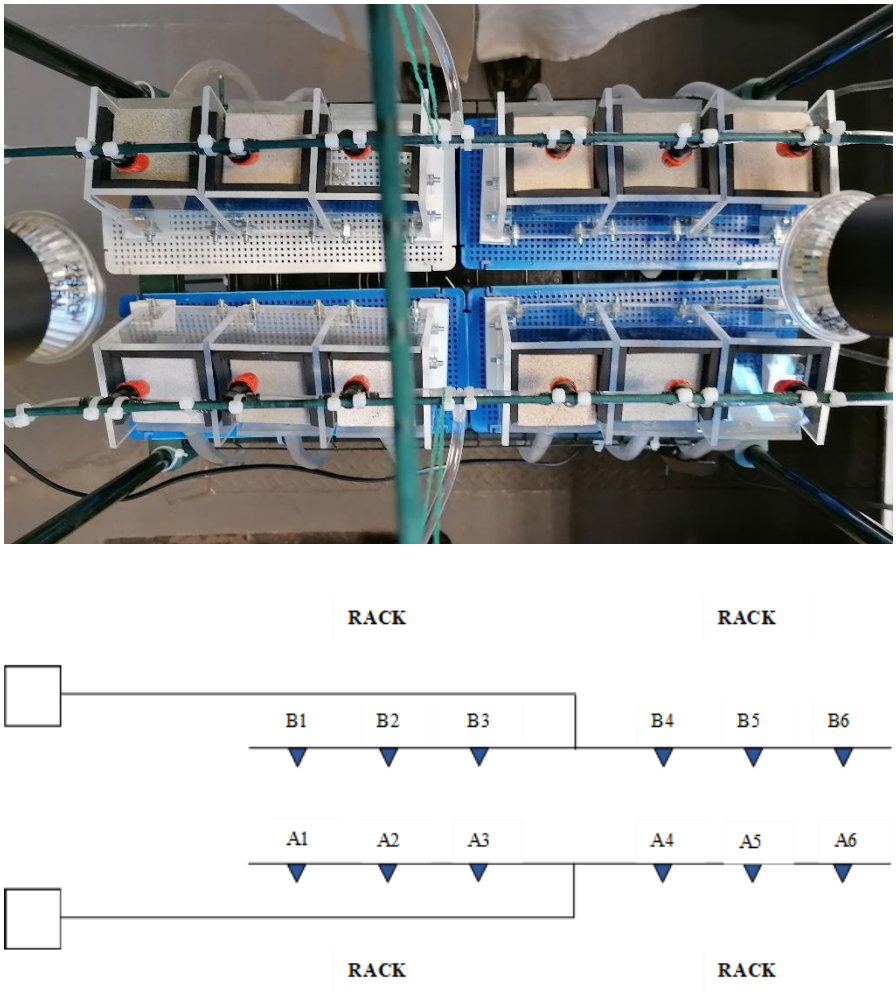

Figure 2-19: set up of the short-term exposure test (test-set 2). Two pumps were employed, each connected to a series of 6 samples though a T connector placed in a central position.

Table 2-3: specifications of each exposure stage adopted during the long-term exposure of test-set 3.

	RP1
Tot duration of cycle	4 hrs
Surrogate rainwater	8 sec
Laboratory Conditions	30 min
UVA/UVB lamps	45 min
Laboratory conditions	For the remaining time

2.2.3 Long-term exposure

2.2.3.1 Long-term performance tests with stable exposure patterns (test-set 2)

The test-set of 10 samples was employed for the long-term exposure test (figure 2-20). The samples employed in test-set 2 were the same used for the short-term exposure of test-set 1.

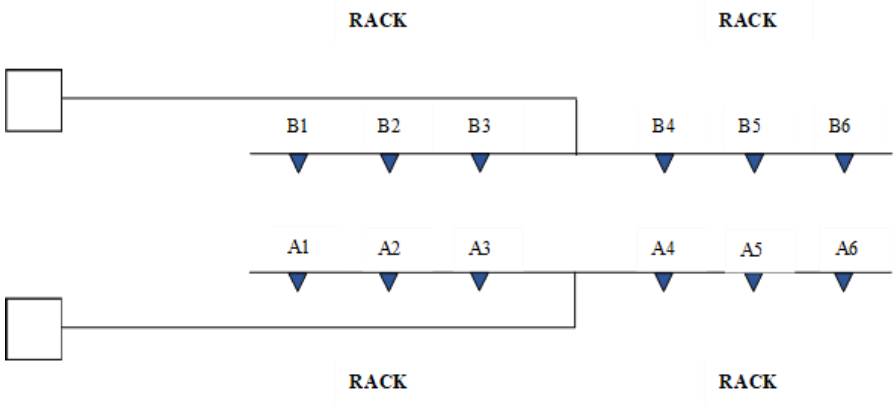

Figure 2-20: set-up the long-term exposure test (test-set 2). Each pump was connected to a series of 6 samples through a T connector placed in a central position.

Artificial rainwater was prepared by single dilution of 6.30 µL of concentrated nitric acid/L, with a final concentration of the acid in the rainwater of the order of 10^{-4} mol L^{-1}. A in the previous tests, UVA/UVB lamps were also incorporated into the exposure apparatus to promote the evaporation of water. The accelerated exposure consisted of the same specifications employed in test-set 1, with a total duration of 4 hours for each single cycle. The total duration of the test was 4

months and 10 days, or a total of 792 exposure cycles. The leachate was collected weekly.

The primary objectives of the test were the evaluation of the long-term performance of the samples in response to stable intervals and volumes of surrogate rainwater, and the acquisition of a benchmark trend to compare the progression of the final exposure (test-set 3), where variable rainfall patterns were tested. The sampling procedure was similar to previous tests. However, the volume sampled from the leachates was brought back to 30 mL. After filtration, each sample was placed in a volumetric flask, acidified with nitric acid (70%) to a 5% concentration, brought to volume to 50 mL adding deionized water and stored in a refrigerator until analysis.

2.2.3.2 Long-term performance test with variable exposure patterns (test-set 3)

Test-set 3 consisted of the same number and typology of samples used in test-set 2. Artificial rainwater was prepared as in the exposure of test-set 1 and test-set 2. The experiment involved the exposure of the 10 samples for a total exposure duration of 3 months and 10 days, during which different rainfall patterns were tested (figure 2-21).

The rainfall patterns were changed at preselected intervals of time, while the UVA/UVB exposure was kept constant throughout the entire test.

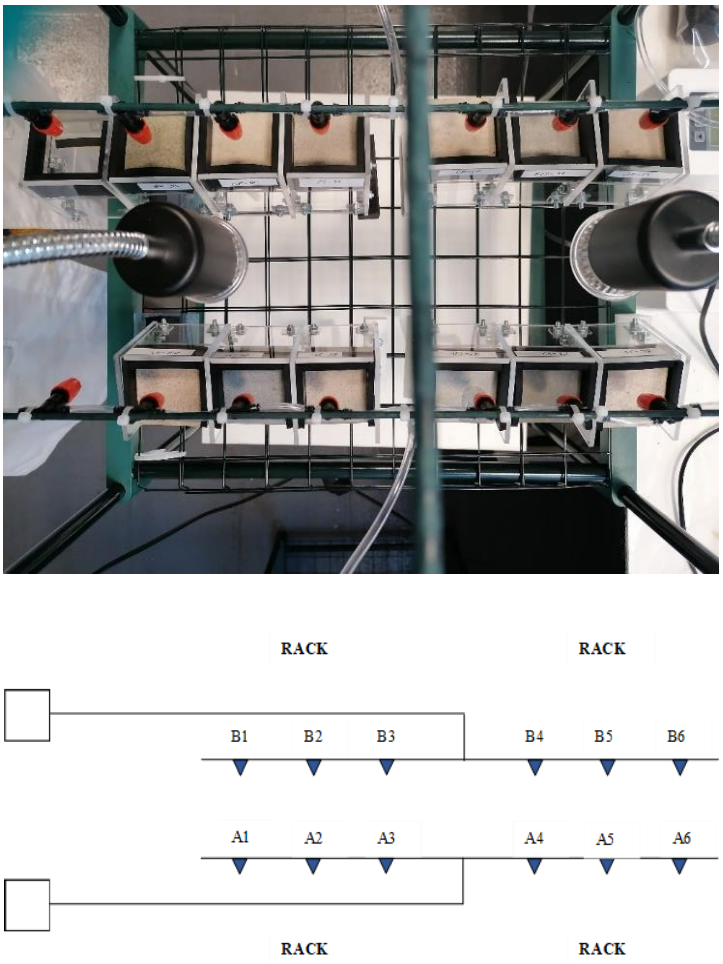

Figure 2-21: set-up of the long-long term exposure test with variable spray patterns (test-set 4). The set-up was the same used for test-set 3.

This test was designed to investigate variations in the dissolution rate of the different stone types by comparison with the results of test-set 3, which was employed as a control (figure 2-22). To improve compatibility between results of the two test-sets, only the cycle duration was changed, while the total volumes of surrogate rainwater delivered to each sample within the 24 hours was kept constant. The only exception was rainfall pattern 1, where the volumes of

surrogate rainwater delivered within 24 hours corresponded to 48 hours of test-set 2. The specifications adopted for each rainfall pattern are listed in table 2-5.

The surrogate rainwater volumes used in rainfall pattern 1 corresponded to the volumes applied during the 1st and 2nd month of exposure of test-set 2. The aim of this exposure condition was to evaluate the stones response to heavy rainfall events and longer drying periods.

Table 2-4: specifications of each exposure stage adopted during the long-term exposure of test-set 3.

	RP1	RP2	RP3	RP4	RP5
Duration of one cycle	12 hrs	12 hrs	8 hrs	4 hrs	2 hrs
Surrogate rainwater	48 sec	24 sec	16 sec	8 sec	4 sec
Laboratory Conditions	30 min	30 min	30 min	30 min	30 min
UVA/UVB lamps	45 min	45 min	45 min	45 min	45 min
Laboratory conditions	For the remaining time				

The surrogate rainwater volumes used in rainfall pattern 2 corresponded to the volumes applied during the 3rd month of exposure of test-set 2. The aim of this test was to assess the effect of a reduction in water supply by half maintaining unaltered the drying period. The surrogate rainwater volumes used in rainfall pattern 3 corresponded to the volumes applied during the 4th month of exposure of test-set 2. The aim of the test was to assess the effect of a further reduction in

both water volumes and drying period. At the end of the three-months exposure, two further rainfall patterns were tested, each of a duration of 5 days.

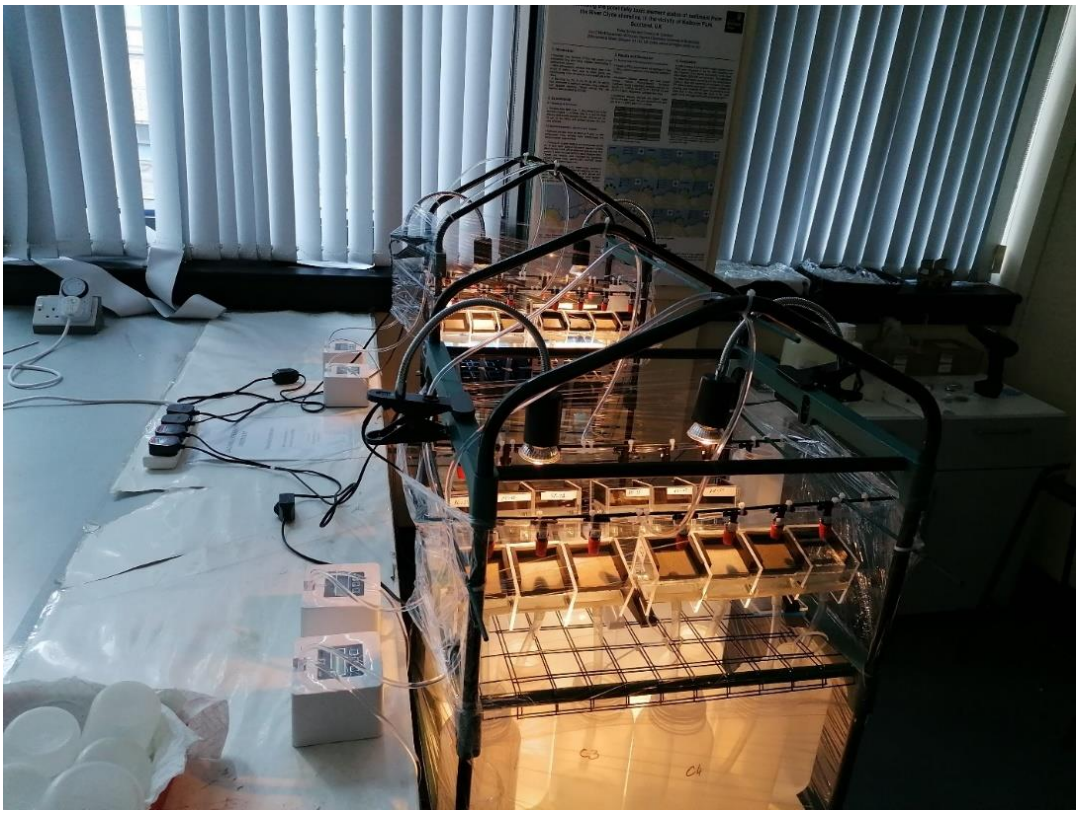

Figure 2-22: exposure apparatus for test-set 2 and test-set 3. Test-set 2 was used as a control for test-set 3.

The surrogate rainwater volumes used in rainfall pattern 4 corresponded to the volumes applied during 5 days of exposure of test-set 2. The aim of the test was to evaluate the correspondence between test-set 3 with test-set 2 when equal exposure conditions are applied and determine if the rainfall pattern variation during the previous three-months influenced the progression of the dissolution process.

The surrogate rainwater volumes used in rainfall pattern 5 corresponded to the volumes applied during 5 days of exposure of test-set 2. The final rainfall pattern 5 was aimed at testing the effects of frequent and short rainfall events. Both rainfall patterns 4 and 5 involved a single sampling point, carried at the end of the 5-days exposure. The sampling procedure was similar to the one adopted in the previous test. At the end of both exposures, the total volume of surrogate rainwater was equal between test-set 2 and test-set 3, making mass-losses values comparable between samples of different test-sets.

2.3 Characterization of samples

2.2.4 X-ray Computed Microtomography

2.2.4.1 Operating Principles

Computed microtomography (CT) is a non-destructive technique used for the structural analysis of materials. X-ray µCT employs X-rays to obtain a series of two-dimensional radiographs of the object under analysis, usually with resolution in the micrometre (µm) range.

An XµCT scanner consists of three main components, the X-ray source, a detector and the sample stage. The X-rays are generated from the source, transmitted through the sample and recorded by the detector as a projected image. This process is repeated until the sample has completed a full rotation. The data is then reconstructed using an algorithm that creates a stack of the cross-sections

obtained from the scan. The process of reconstruction provides a three-dimensional digital greyscale representation of the object and its internal structure.

2.2.4.2 Data acquisition

The X-ray µCT analysis were conducted on 5.5 mm cylindrical core samples extracted from 10 stone typologies of the test-set, as described in section 2.1.2 (figure 2-13). Before carrying the XµCT analysis, the core cylinders were oven-dried at a temperature of 60 °C for a period of 24 hours. Information about the samples microstructure and composition was acquired by X-ray µCT (Nikon XT H 225 LC, Nikon corp., Tokyo, Japan) at the department of Civil and Environmental Engineering of the University of Strathclyde. The scanning was conducted at a resolution of 8 µm, with a scan time of 105 minutes for each sample.

Figure 2-23: the 10 core cylinders were stack in a glass tube for X-ray µCT analysis.

2.2.5 Image processing

Information about the intrinsic structural and compositional characteristics of the unaltered samples was acquired through the image analysis of the reconstructed X-ray µCT data. The reconstructed data represents the attenuation of X-rays at each point within the sample. Attenuation is controlled by the density of the material and is encoded in greyscale images. The data processing is based upon the discrimination of the sample's different components based on their difference in density.

2.2.5.1 Fiji ImageJ

ImageJ is a public domain image processing software. Fiji ImageJ was used to analyse images obtained from the X-ray µCT scans to obtain information about the samples' pores and its compositional properties. This is usually done through the segmentation process, which isolates individual features of an image based on the characteristics of the pixel to extract the relevant information.

The procedure included the following steps:

1) Extraction of a single image from the stack for analysis; Fiji-Image-J software was mainly used to process single images extracted from the X-ray µCT stack. Images were selected based on a subjective evaluation of how representative they were of the overall sample.

2) Image importing and conversion; Single images were imported into the software and the RGB image converted into a greyscale image using a *weighted conversion*. The image type was then converted to an 8-bit format by linearly scaling from min-max values to 0 (pure white) – 255 (pure black).
3) Image calibration was performed based on the included scale bar to define the spatial scale of the active image and allow measurements to be carried in calibrated units.
4) Histogram equalization is a contrast enhancement operation, which was conducted to prepare the image for segmentation.
5) Image filtering can help to reduce noise that would interfere with the image segmentation. For the filtering of the X-ray µCT images, a median filter was applied, which reduces noise in the image by replacing each pixel with the median of the neighbour pixel value.
6) Noise adjustment involved two further steps, i.e., despeckle and remove outliers. Despeckle is a median filter that replaces each pixel with the median value in its 3 × 3 neighbourhood. Remove Outliers is an operation that is carried out to remove certain types of elements based on their size.
7) Thresholding is an operation applied to conduct the image segmentation and create a binary image from the greyscale image, from which quantitative information can be extracted.

2.2.5.2 Avizo

Avizo is a commercial software for interactive data visualization and analysis of 3D datasets developed by Thermo Fischer Scientific.

Avizo was employed for the 3-dimensional image processing of the reconstructed data from the X-ray CT scans with the main purpose of extracting information on the characteristics of the pore network, such as the level of interconnection between pores and the sample overall permeability. The procedure to conduct the quantitative analysis involves the segmentation of each element based on the grey values of the image data. The applied workflow followed two main stages:

1. Quantification of pore size distribution
2. Determination of permeability

The procedure followed to isolate porosity from the samples involved the following steps:

1) Extraction of a sub volume from the cylindrical core. The sub-volume was selected visually based on its representativity of the full sample.
2) Noise reduction by applying the *anisotropic diffusion* filter.
3) Segmentation of the pores by *interactive thresholding*.
4) Separation of the connected pores from the isolated unconnected ones through the *axis connectivity* module.
5) Quantification of the connected pores by *label analysis.*
6) Total permeability computation through *generation of the pore network* operation.

2.4 Investigation of the samples performance

Except for the initial trial test, the samples' performance in each artificial exposure round was assessed in terms of mineral dissolution and mass-loss. The leachate solutions from each sample were analysed by inductively coupled plasma mass spectrometry to determine the concentration of major ions from the samples.

2.5 Investigation of the samples performance

Except for the initial trial test, the samples' performance in each artificial exposure round was assessed in terms of mineral dissolution and mass-loss. The leachate solutions from each sample were analysed by inductively coupled plasma mass spectrometry to determine the concentration of major ions from the samples.

2.5.1 Analysis of the stone leachates by inductively coupled plasma mass-spectrometry

2.5.1.1 Operating Principles

Inductively coupled plasma mass spectrometry (ICP-MS) is a well-established analytical technique, used for multi-elemental analysis at trace and ultra-trace levels and the determination of isotopic ratios (figure 2-24).

The fundamental components of an ICP-MS are the sample introduction system, consisting of a nebulizer and spray chamber, an inductively coupled plasma (ICP), an interface, ion optics to guide the ions into the mass spectrometer (usually a quadrupole), which sorts ions by their mass-to-charge ratio, and a detection system, counting individual ions exiting the quadrupole. The liquid sample is nebulized before entering the spray chamber. In the spray chamber the aerosol droplets are selectively filtered based on their size, with only the smaller ones (<10 μm diameter) being transferred to argon plasma. The sample atoms are ionized after the solvent evaporation. The degree of ionization depends on the temperature of the plasma and the ionization potential of the element.

The resulting ions are conveyed into the mass-analyser where they are sorted based on their mass-to-charge ratio (m/z). The analyte concentration is obtained from comparison of the signals generated by the sample with the signals generated by a series of standards solutions containing known quantities of the elements under analysis (external calibration). Internal calibration is also used, along with external calibration, to correct for possible variations in the instrument response during the course of the analysis.

2.5.1.2 Analysis of leachates

Mineral dissolution was estimated by trace element analysis of the cations in the run-off water. The chemical analysis was conducted by ICP-MS (Agilent 7700x, Agilent Technologies Ltd., Cheshire, UK) and the concentration of the cations Ca^{2+}, Fe^{2+}, K^{+}, Mg^{2+}, Na^{+} and were determined. Calibration standards matching

the leachate matrix (i.e., in 10^{-4} mol L^{-1} HNO_3) were prepared from commercially available stock solutions (from Qmx Laboratories, Thaxted, UK).

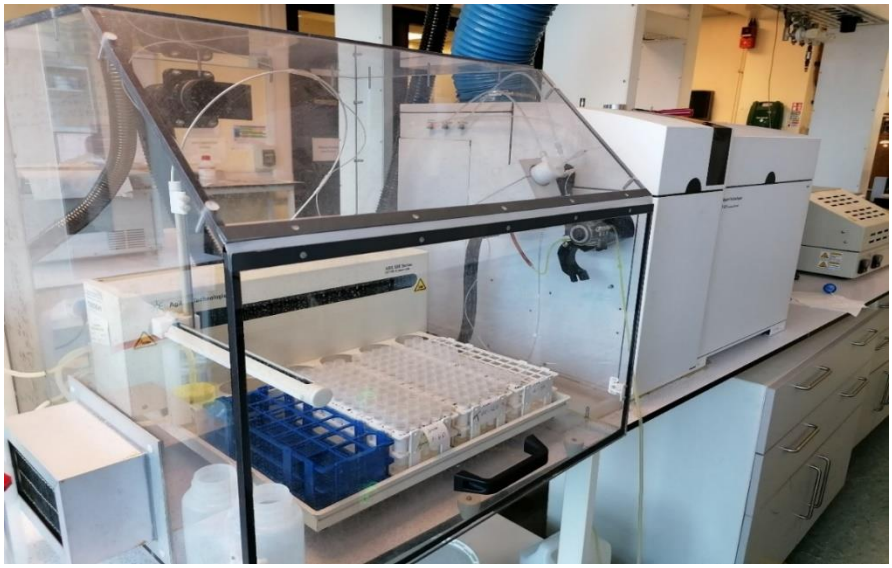

Figure 2-24: leachate samples from the short term-exposure of test-set 1 during ICP-MS analysis.

2.5.1.3 Scaling of leachates concentrations

The ICP-MS measurements of the analyte concentrations at different points in time were converted into amount of analytes released per mL of surrogate rainwater applied. The conversion was carried by scaling the analytes concentrations by the total volume of leachate collected and the recorded volume of surrogate rainwater delivered to each sample, as follows:

$$Dissolution\ rate = \frac{\left(C\ \cdot \frac{V^{diluted}}{1000}\right) \cdot \frac{V^{collected}}{V^{sampled}} \cdot C^{50}}{V^{delivered}}$$

Where C stands for the analyte concentration; $V^{diluted}$ stands for the volume of the diluted leachate solution (50 mL); $V^{collected}$ stands for the total volume of leachate collected; $V^{sampled}$ stands for the volume of leachate collected for analysis; C^{50} stands for the analyte concentration in 50 mL; and $V^{delivered}$ stands for the total volume of surrogate rainwater delivered to the sample.

Monitoring of the volumes of solution delivered to each stone was carried out by collecting surrogate rainwater at regular intervals of time for the whole duration of the tests. This step was conducted by placing beakers under each nozzle and collecting the water delivered by a single cycle (figure 2-25).

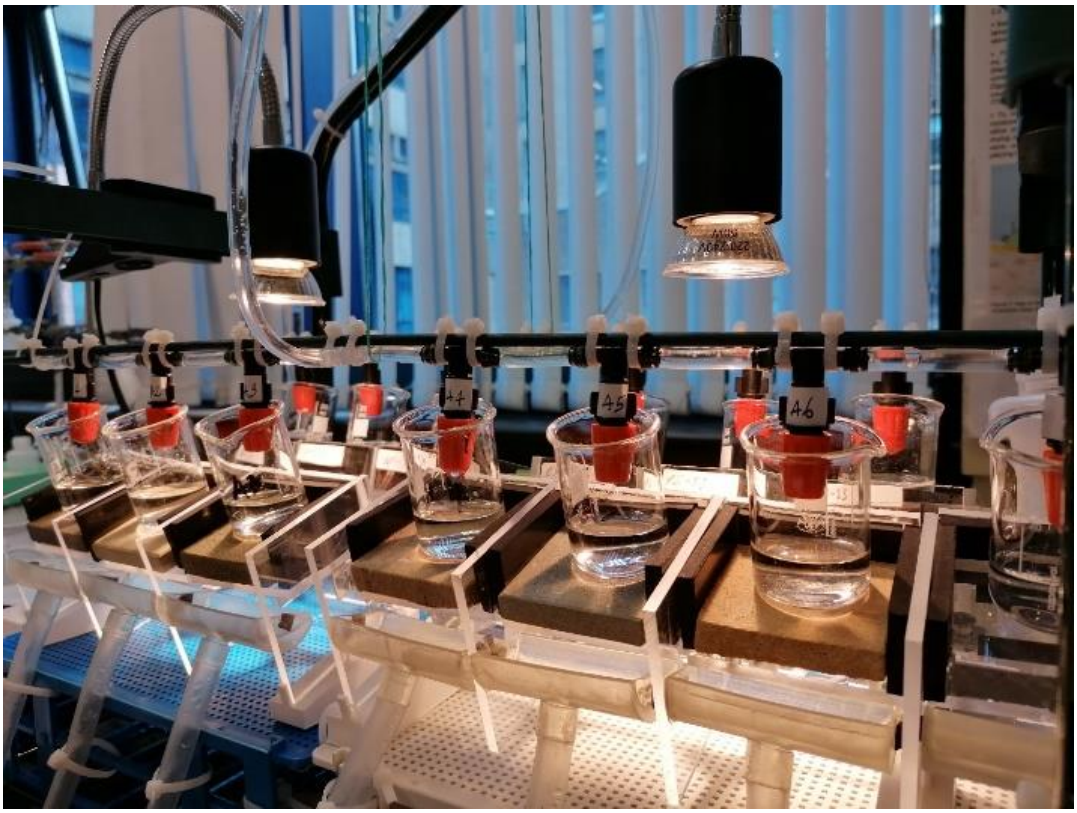

Figure 2-25: collection of the surrogate rainwater solution to record the volumes delivered to each sample and ensure equal distribution. The volumes were recorded at regular intervals throughout the full duration of the exposure trials and used to scale the analytes concentrations.

2.5.2 Weight change

The weight change was recorded to quantify the stone damage after each exposure trial. This metric represents an indicator of the weathering effect complementary to the mineral dissolution data. The leachate analysis provides partial information on the effects of weathering, as the dissolution process can reduce the contact between grains and investigate a loss of cohesion, prior to the grain detachment. The recording of the weight variation of each sample was used to study the physical mechanism of the stone progressive erosion resulting from the process of mineral dissolution. Mass loss information for each sample was calculated from the following equation:

$$\left(\frac{initial\ weight\ -\ exposed\ weight}{initial\ weight}\right) \cdot 100$$

Pre- and post-exposure weights were recorded with a balance (Mettler Toledo UM3), after the samples were washed with deionized water and oven dried for 24 hours. The drying temperature was kept under 100°C to prevent heat damage to the minerals. For the trial- and variability test, the drying temperature was 60°C, while for test-set 1, 2 and 3 the drying temperature was set to 70°C, in accordance with the guidelines provided by NORDTEST method NTBUILT 495 – *Building materials and components in the vertical position: exposure to accelerated climatic strains*.

2.5.3 Percentage variation of dissolution rates

The change in dissolution rate was investigated to assess the influence of the exposure conditions to the dissolution rates of the samples during the long-term exposure trial with variable rainfall patterns (RP).

The percentage change was applied with the following objectives:

- Quantify the influence of the rainfall cycle duration over the rate of dissolution by acquiring the percentage variation in dissolution between consecutive exposure conditions.
- Monitor the stone dissolution under different exposure conditions against the control interval obtained from the long-term exposure to stable conditions.

The following equation was applied to the mean dissolution rates of RP1, RP2 and RP3, and to the dissolution rates obtained from a single sampling point of RP4 and RP5.

$$DR^{(change)} = \frac{DR^{(RP)} - DR^{(CI)}}{DR^{(CI)}} \cdot 100$$

Where, $DR^{(change)}$ stands for the dissolution rate change; $DR^{(RP)}$ stands for the dissolution rate under a rainfall pattern; and $DR^{(CI)}$ stands for the dissolution rate under the control interval.

2.6 Statistical analysis

2.6.1 Principal component analysis

Principal component analysis (PCA) is a statistical technique used to identify patterns in complex data sets, verify the existence of correlation between objects or variables and identify any underlying structure. It is usually conducted on a matrix of the original data, which contains the results of the experimental analysis. A matrix consists of *n* rows, each row representing a sample (objects), and *n* columns, each column containing a variable.

The information is acquired through an algorithm (NIPALS), which performs a rotation of the space where the data is projected through an iterative procedure until the identification of the directions that provide the highest amount of information. These directions are linear combinations of the original variables, i.e., the principal components (PCs), also referred to as latent variables. The first principal component (PC1) is chosen to minimize the distance between the data and its projection onto the PC and convey the maximum variance. The second component (PC2) represents an orthogonal projection to PC1 and provides the maximum information that was not captured by the first component.

The exploratory process entails a graphic representation obtained from the projection of the data on the axes represented by the principal components. Information can be visualized from a score plot, a loading plot, or a combination of the two. A score plot shows the distribution of the samples on the 2-dimensional space described by two principal components, allowing to verify the existence of

relationships between observations and underlying patterns or structures in the dataset.

A loading plot represents the projection of the variables within the space of the principal components. The loading plot provides information on the relationship between variables and their relative importance for the system under investigation. The relative importance of each variable is quantified by the distance from its position and the centre of the plot (point 0). The more a variable is distant from this point the higher is its influence on the direction of the component over which it is projected.

Centring and scaling were applied as pre-treatments to the leachates dataset. To improve visualization, a descriptive variable referring to the stones typology was assigned to each sample. When plotted onto the PCs space, each object was coloured based on the assigned descriptive variable. The loadings plots were used in combination with the scores plots to gain information on the significance of each variable for each PC. Principal component analysis was also used to determine the presence of anomalies throughout the artificial weathering process and determine the effect of the scaling process of the leachates concentrations. In this case, a descriptive variable was assigned to gain information on the position of the sample in the exposure apparatus. Correlation matrices were used to measure the level of correlation between variables, such as the volumes of water delivered to the samples and the amount of cations released by the stone. All statistical analysis was conducted using the open-source R-based software CAT (Chemometric Agile Tool), developed by the Italian Group of Chemometrics of the Italian Society of Chemistry (SCI).

2.6.2 Analysis of Regression

2.6.2.1 Simple and multiple linear regression

Linear regression describes a statistical technique used to analyse the relationship between variables. Simple linear regression is a technique which examines the relationship between an independent variable (predictor) and one dependent variable (response). Multiple linear regression (MLR) is similar to simple linear regression, but the relationship with the response is investigated against multiple independent variables. The objective of both techniques is to predict the values of the response based on the values of the independent variables.

2.6.2.2 Principal component regression

Principal component regression (PCR) is a combination between PCA and MLR. As multiple linear regression, it has the objective of predicting a response based on the values of the independent variables. The main difference between the two techniques is that in PCR the independent variables are represented by the principal components, that are previously obtained from the PCA.

2.6.2.3 Measure of the model fit

The level of fitting of the data to the model is determined through different coefficients. For the present study, the coefficient of determination and the root mean squared error are used. The coefficient of determination, or R-squared (R^2), is a statistical index that captures how much of variance for a dependent variable is explained by an independent variable. The coefficient of determination represents the percentage of the variation between two variables and is expressed as a number between 0 and 1. An ideal fit of the predicted data to the model is represented by a R-squared value of 1, indicating that 100% of the dependent variable variation is explained by the variation of the predictor.

The root mean squared error (RMSE) is a metric that represents the standard deviation of the residuals. The RMSE value captures the average difference between observed values and the values predicted by the model. The error is expressed in the same units as the dependent variable. An ideal fit to the model is represented by a RMSE of zero.

3. Samples Characterization

The determination of the pore structure characteristics focused on the acquisition of a range of parameters, including the pore fraction total volume (P), the size of the pores (S), the effective porosity (EP), the level of tortuosity (T) and permeability (K). The application of X-ray µCT presented several constrains within the context of the present study. In some cases, the resolution of the scans was not sufficient to allow for a proper characterization of the sample pore system. The full characterization of the pore fraction was obtained only for five samples (BL-SS, BN-SS, CB-LM, DH-SS, DM-SS). For two of the remaining samples (CF-BC and PT-SS) only partial data was acquired. Relevant information about the pores characteristics could not be obtained for the rest of the test-set (PS-SS and PSX-SS). A summary of the data acquired for each stone type is presented in table 3-1.

Application of X-ray µCT also presented limitation with respect to the characterization of the mineral fraction. The main constraints referred to the discrimination between carbonate minerals, e.g., calcite and dolomite. Due to the limitations of X-ray µCT for the purposes of the present research, the samples characterization was combined with literature information and data acquired from the stone supplier.

The results of the data processing are presented in the Appendix.

Table 3-1: *Data acquired for each sample of the test-set; P: tot. porosity, S: pores average size, EP: effective porosity, K: permeability, T: tortuosity*

Sample	P (%)	S (µm)	EP (%)	K (µm$^{2)}$	T
BL-SS	11	70	65	1.72	1.45
BN-SS	11	90	90	1.74	1.9
CB-LM	8	69	2.72	1.72	1.27
CF-BC	3	20	NA	NA	NA
DH-SS	15	77	60	1.86	1.98
DM-SS	19	100	95%	1.68	1.60
GP-CA	1	51	NA	NA	NA
PS-SS	NA	NA	NA	NA	NA
PSX-SS	NA	NA	NA	NA	NA
PT-SS	1	34	NA	NA	NA

4. Results of trial-test and variability test

The chapter summarises the finding of two preliminary leaching tests. The trial test was performed to examine the exposure apparatus and sampling procedure, investigate the experimental approach and evaluate the performance of the samples at the end of the exposure based on their weight variation. The variability test was conducted to assess the variation in the response of replicate samples and compare the respective performance of the tested samples typologies.

4.1 Trial test

The test procedure and details of the exposure are summarised in chapter 2, section 2.2.1.1.

4.1.1 Evaluation of the apparatus performance

No experimental glitches were observed during the testing of the exposure apparatus. The experimental procedure was found be consistent throughout the full extent of the trial test. The nozzles delivered uniformly the surrogate rainwater solution to the samples surface. No spillage of surrogate rainwater was observed

from the nozzle to adjacent units and steady volumes were delivered to the samples during the 10 days of exposure. The gutters for the leachate collection did not degrade as a result of the extended contact with the leachate solution. The timing applied for the water spraying cycles produced a sufficient amount of leachate to allow the sampling of 30 mL of solution every two-days.

4.1.2 Weight change

At the end of the nine days exposure trial, mass loss for the two samples was different. The CB-LM specimen experienced a weight loss of 0.13 g, while for BN-SS the weight loss corresponded to 0.05 g (table 4-1). The change in weight of CB-LM was more than twice that experienced by BN-SS. The greater weight loss for CB-LM was consistent with the expected higher vulnerability of the stone on the basis of its composition, which consisted exclusively of carbonate minerals.

Table 4-1: pre- and post-accelerated exposure weight of BN-SS and CB-LM

SAMPLE	Pre-exposure weight (g)	Post exposure weight (g)	Mass loss (g)
BN-SS	60.20	60.15	0.05
CB-LM	44.91	44.78	0.13

4.2 Variability Test

This section summarises the findings of a preliminary leaching test conducted to verify the variability between the response of triplicate samples of three different stone typologies. The test procedure and details of the exposure are summarised in chapter 2, section 2.2.1.2.

4.2.1 Dissolution trends

4.2.1.1 Calcium and Magnesium

The dissolution profiles of Ca and Mg are shown in figures 4-1 and 4-2 respectively. The red dashed line that can be observed at the fourth sampling point (day 10 of the exposure) is aimed at indicating the sampling times that are affected by higher initial dissolution rates caused by the loss of debris from the sample, and that as such are no representative of actual dissolution rates. For this reason, sampling time 1 to 4 are not included in the calculation of the average dissolution rates. The replicates' individual behaviour was examined from the dissolution profile of the three samples typologies. As shown in figure 4-1, PT-SS samples exhibited the best correspondence between the Ca dissolution profiles of the triplicate samples at all sampling points. The same consistency between Ca release was not observed in BN-SS and CB-LM, whose replicate samples displayed occasional variations. This was particularly the case for BN-SS, where one replicate sample displayed an initial Ca release of 6 µg/mL, as opposed to the 2.6 µg/mL and 2.2 µg/mL obtained from the other two replicates. The overall

dissolution profile for the three sample typologies was found to be relatively stable. The initial sampling points displayed the largest difference between replicate samples for all stone types. In contrast, the highest correspondence between Ca concentrations was found for the last two sampling points, when dissolution rate appeared to reach stability. The temporal Ca dissolution trend of the three replicates was found to be comparable among the three samples topologies. All sample types displayed an initial peak in dissolution, which flattens out after the initial two/three sampling points.

Dissolution values at each sampling point were compared with the total volumes of water found in the leachate collection bottles. The sampling points that displayed significant difference between Ca concentrations of replicate samples were found to correspond to unusual amounts of water collected. The high volumes of water collected indicated an alteration of the volumes of surrogate rainwater delivered to the samples. Magnesium performed similarly to Ca, from the dissolution trend of the three replicate samples (figure 4-2). The PT-SS replicates showed the highest correspondence at all sampling points while CB-LM and BN-SS replicates displayed occasional discrepancies. The best agreement between the dissolution trends of replicate samples was found with the two last sampling points (sampling 4 and 5), while the highest divergence was recorded at the early stage of the experiment.

Replicates were found to display a dissolution profile similar to the one observed for Ca, with a close correspondence between variations in the release of the two analytes. It was observed that a variation of Ca dissolution usually corresponded with a variation in Mg. This behaviour is more evident for samples with a higher release of Mg, such as CB-LM.

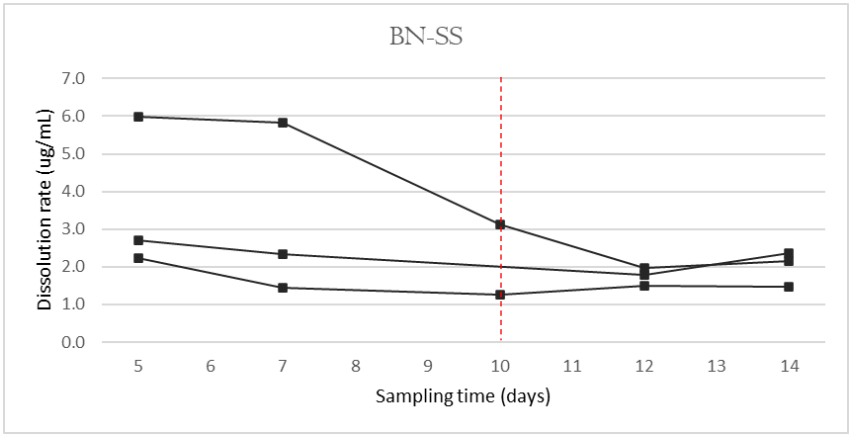

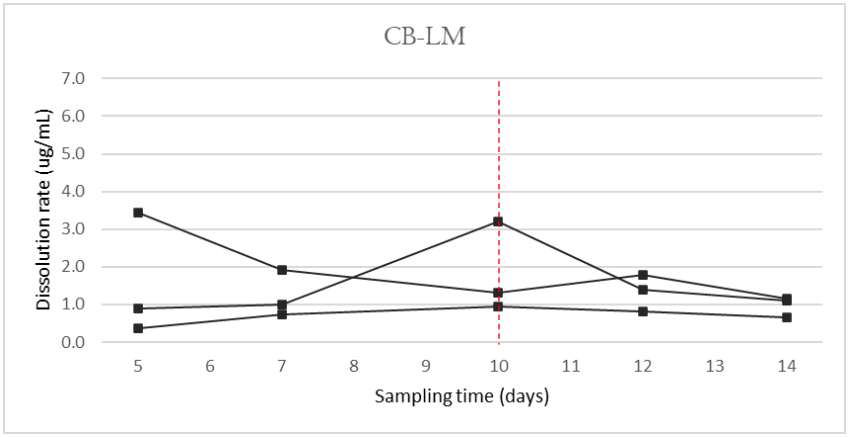

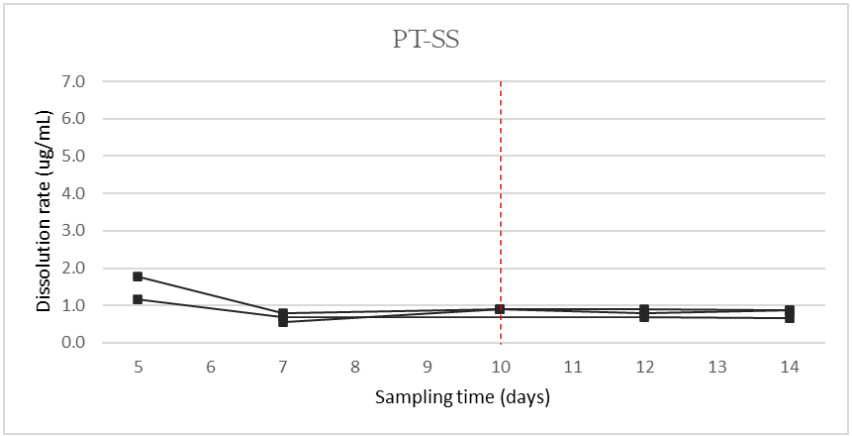

Figure 4-1: Ca dissolution profiles of the three replicate samples for each stone type.

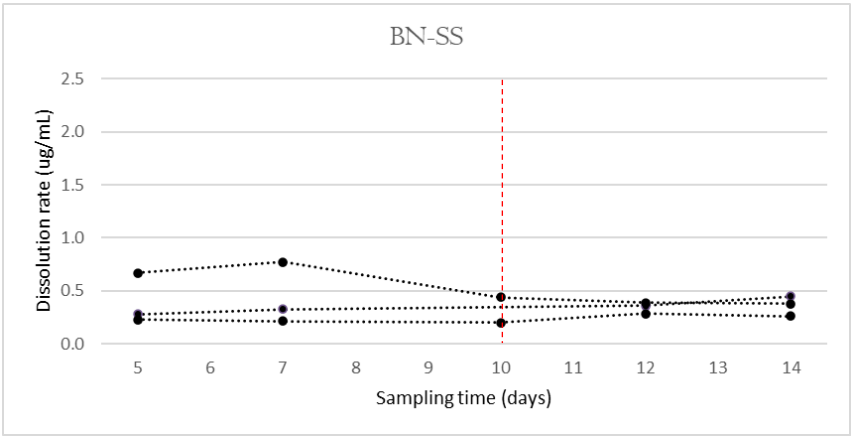

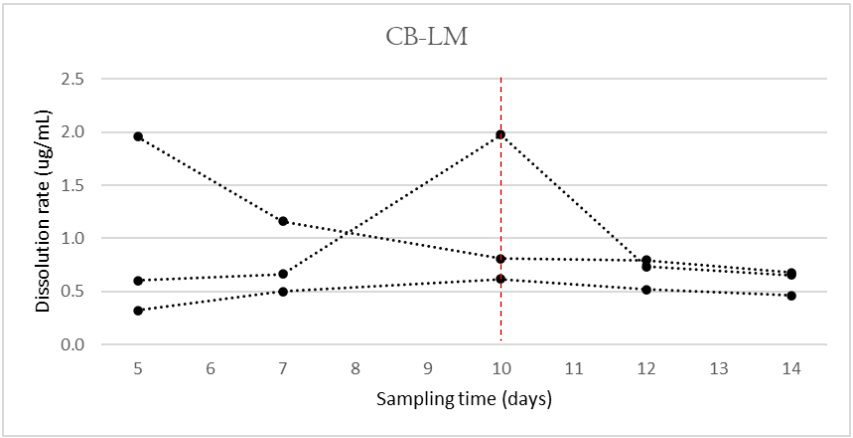

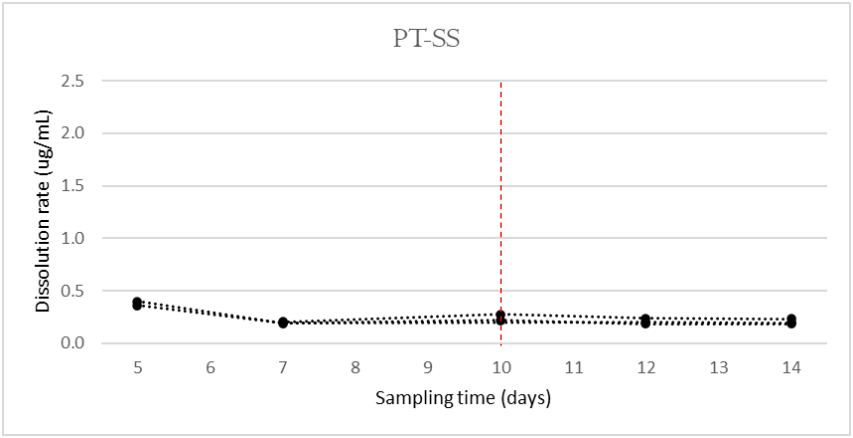

Figure 4-2: Mg dissolution profiles of the three replicate samples for each stone type.

4.2.1.2 Sodium, Potassium and Iron

Figures 4-3, 4-4 and 4-5 show the temporal dissolution trends obtained from Na, K and Fe concentrations at each sampling point for the three replicates of each stone type. As with Ca and Mg, the replicates performance displayed occasional divergence, although the dissolution trend was found to be comparable between replicates. With the exception of the first sampling points of CB-LM and PT-SS, which exhibited an exceptionally high release of K, all samples showed a stable dissolution profile.

Overall, Na displayed the highest fluctuation between the dissolution values at each sampling point (figure 4-3). This was especially relevant for the second sampling point of CB-LM, which displayed an exceptionally high dissolution rate. This sampling point was removed from the dissolution profile to allow for a proper resolution and improve visualization. In contrast, K showed a higher stability of the dissolution profiles, displaying a high level of correspondence between the dissolution rates of sampling point 3, 4 and 5 (figure 4-4).

Iron exhibited a relatively stable performance, characterised by low values at each sampling point, with a dissolution rate consistently below 0.05 ug/mL (figure 4-5). The performance trend of Fe was consistent with the dissolution displayed by other analytes, with PT-SS showing the best correspondence between replicate samples.

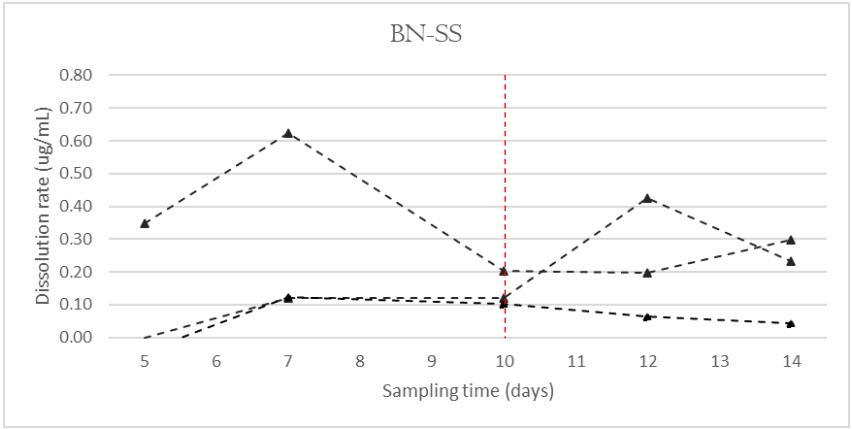

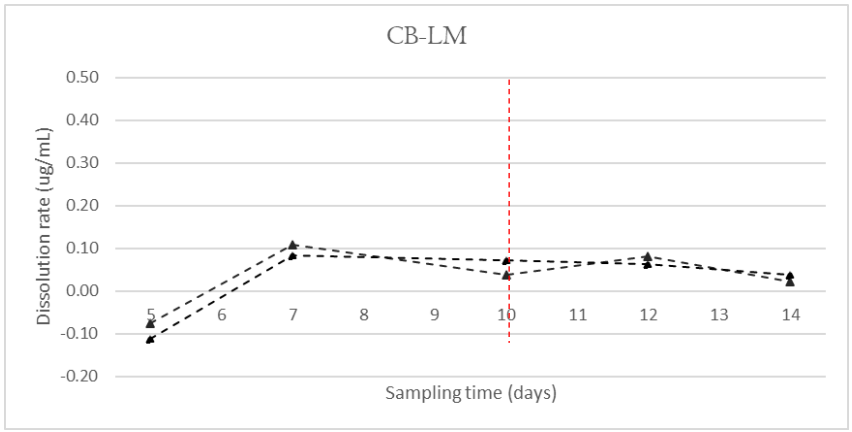

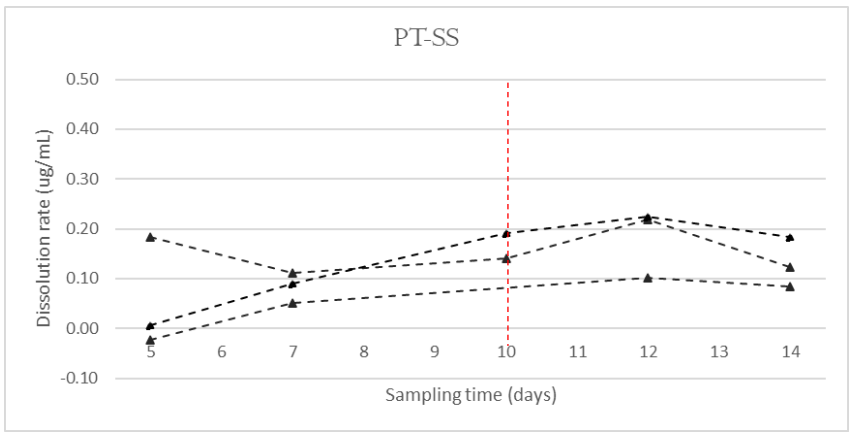

Figure 4-3: Na dissolution profiles of the three replicate samples for each stone type.

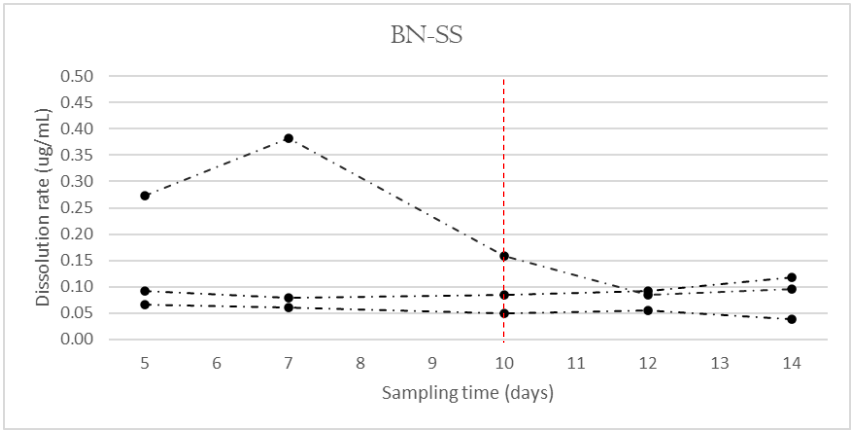

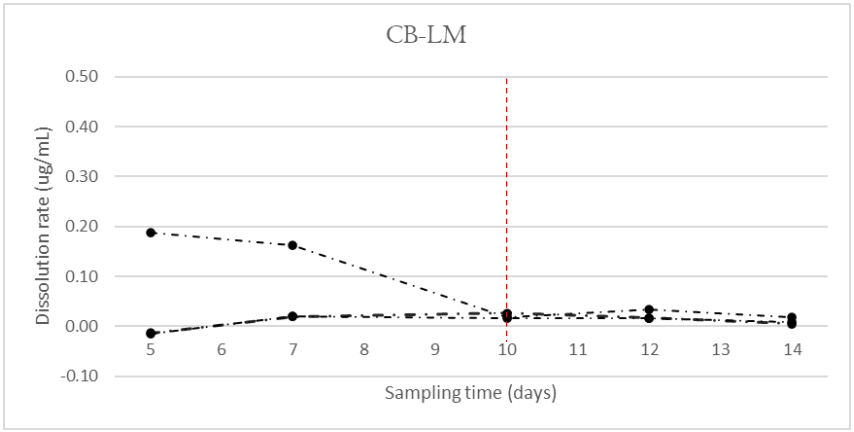

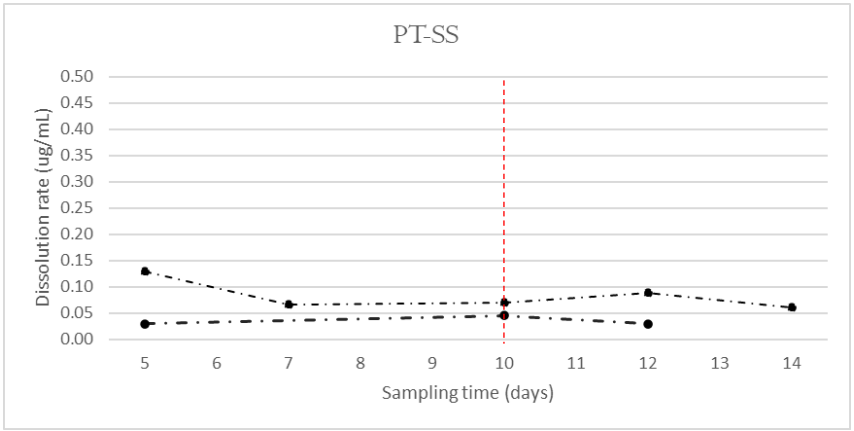

Figure 4-4: K dissolution profiles of the three replicate samples for each stone type.

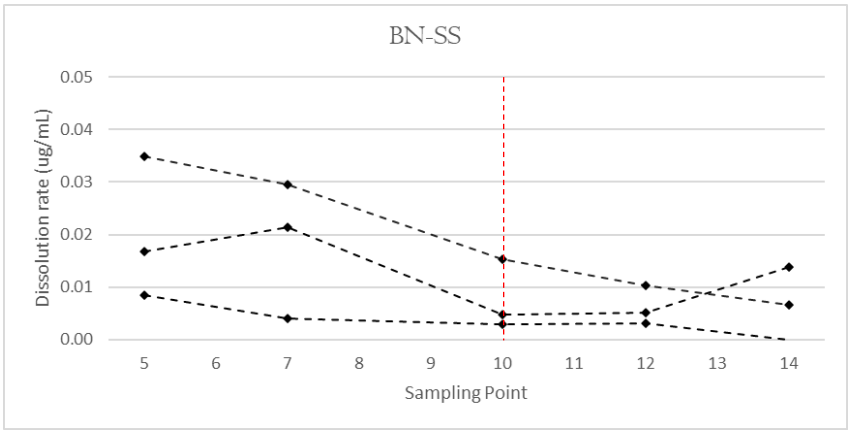

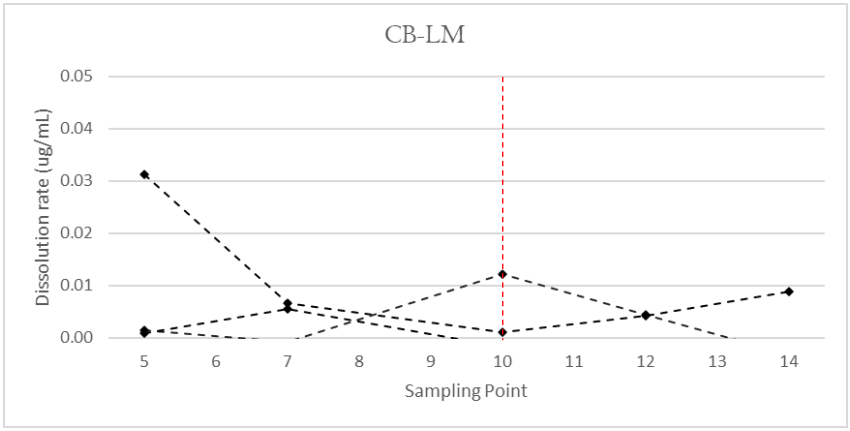

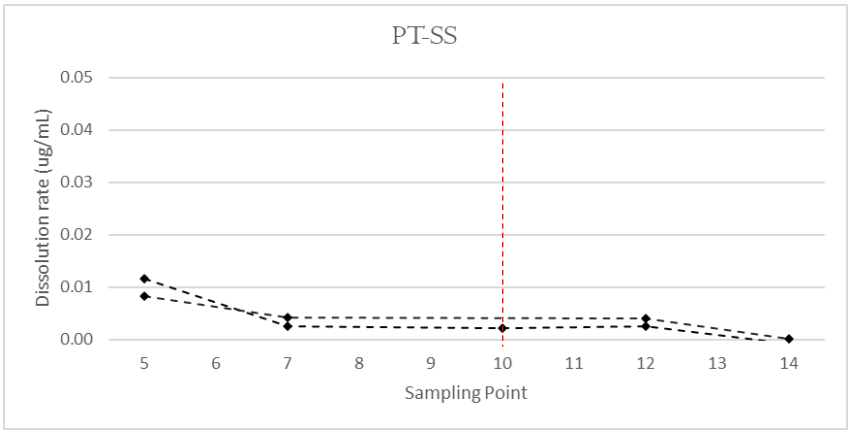

Figure 4-5: K dissolution profiles of the three replicate samples for each stone type.

4.2.2 Mean dissolution rates

The results of the ICP-MS analysis performed on the leachates collected were used to determine the mineral dissolution rate of each replicate. Average dissolution values were obtained from the last two sampling points (sampling point 4 and 5), which corresponded to the stable portion of the dissolution trend.

4.2.2.1 Calcium and Magnesium

Figure 4-6 shows the mean Ca dissolution rate between sampling point 5 and 4 obtained from the values of the three replicates for each stone type. The stone typology that displayed the highest overall release across the three replicate samples was BN-SS, followed by CB-LM and PT-SS. Calcium release obtained from the averaged values of the three replicates, was found to correspond to 1.87 µg/mL for BN-SS, 1.15 µg/mL for CB-LM and 0.81 µg/mL for PT-SS. Bernese sandstone displayed a significantly higher release of Ca despite the lower concentration of carbonate minerals in its composition compared to CB-LM. This suggests that the porosity is likely to be a controlling factor in the determination of the difference in dissolution rates between samples. Figure 4-7 shows the mean dissolution values for Mg. Magnesium was the element with the second highest concentration in the leachate for all sample types. The highest overall dissolution was found for CB-LM, where Mg release corresponded to 0.56 µg/mL, followed by BN-SS, 0.45 µg/mL, and PT-SS, 0.21 µg/mL.

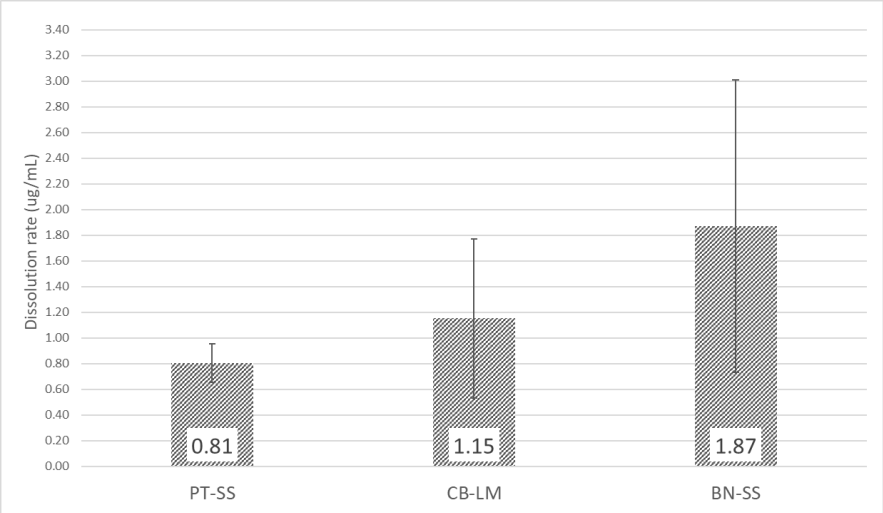

Figure 4-6: mean release of Ca obtained from the averaged valued of the three replicates for BN-SS, CB-LM and PT-SS

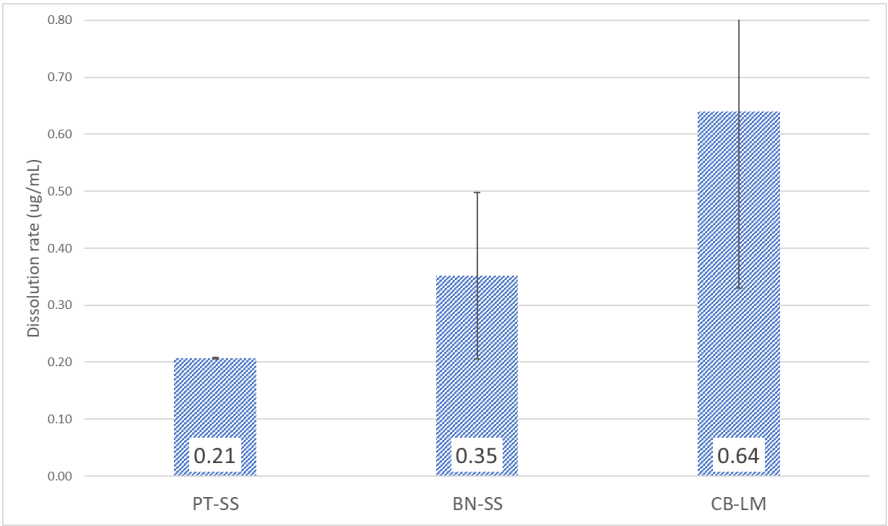

Figure 4-7: mean release of Mg obtained from the averaged valued of the three replicates for BN-SS, CB-LM and PT-SS

The correspondence between each replicate performance was investigated by comparing their individual average Ca dissolutions. As shown in figure 4-8, PT-SS and CB-LM displayed the highest similarity between the dissolution rates of the three replicate samples. A higher level of fluctuation was observed from the mean Ca dissolution of BN-SS replicates. However, the difference referred to only one of the three replicates, while the remaining two displayed comparable dissolution values.

The same correspondence was observed from the comparison of the mean dissolution values of Mg for each individual replicate (figure 4-9). Compared to Ca, Mg fluctuations between replicate samples was generally less pronounced. For instance, BN-SS displayed a higher level of consistency between replicate samples, with Mg dissolution values compared to the values obtained from Ca dissolution. The replicates of PT-SS showed comparable mean Mg dissolution, with a higher similarity between replicates compared to Ca. In contrast, CB-LM showed a greater difference between the mean dissolution of each replicate compared to Ca.

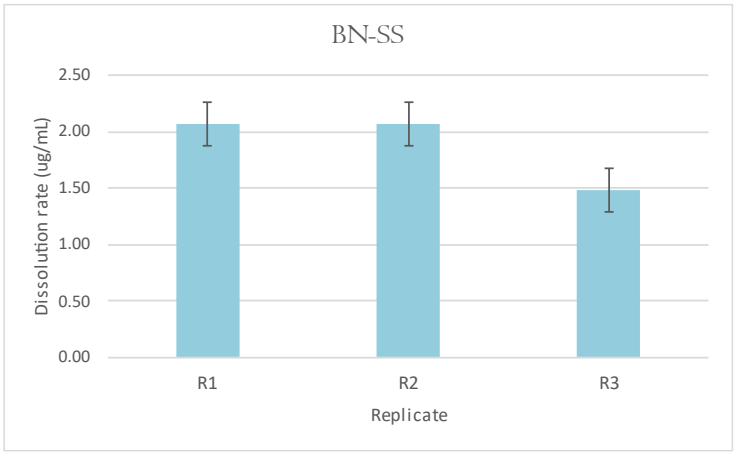

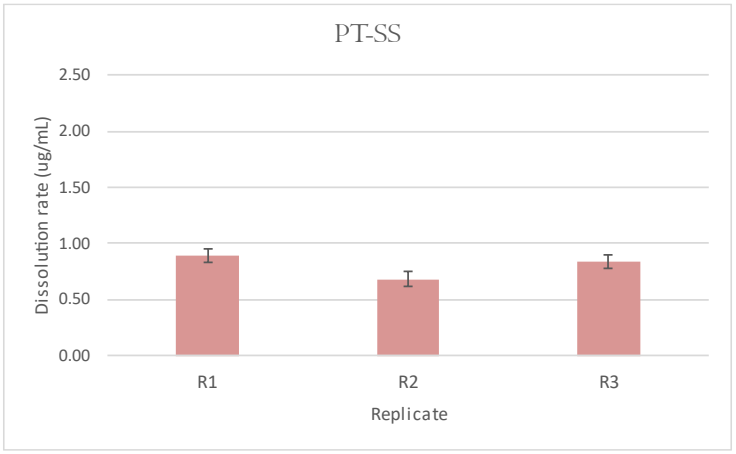

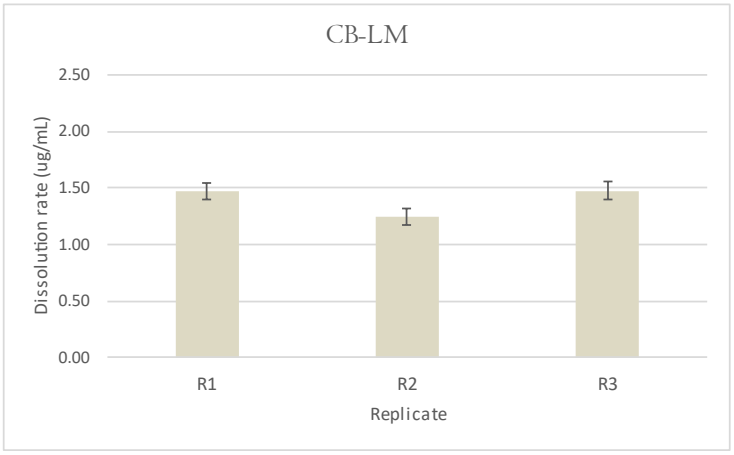

Figure 4-8: mean release of Ca by the three replicate samples for each stone type.

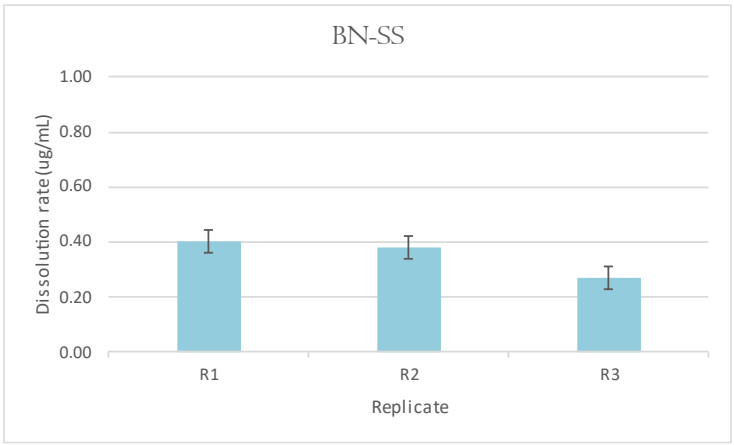

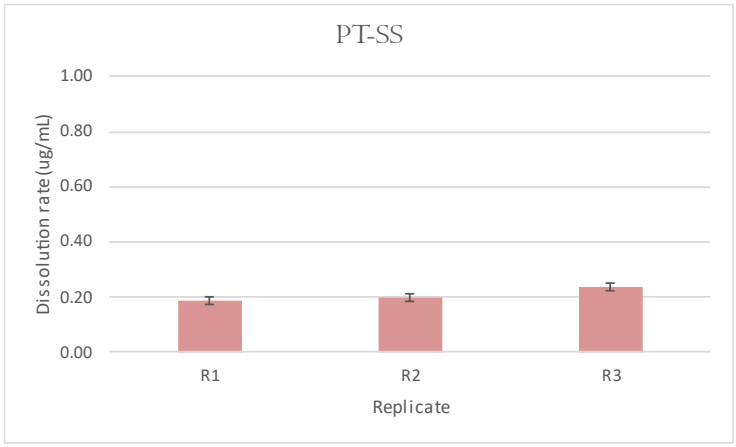

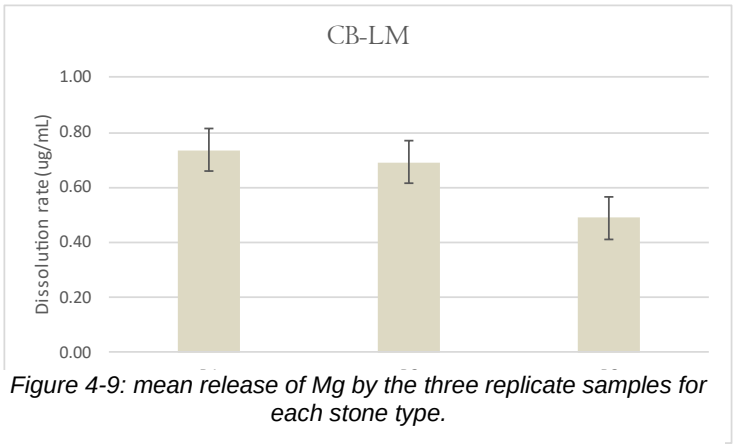

Figure 4-9: mean release of Mg by the three replicate samples for each stone type.

4.2.2.2 Sodium, Potassium and Iron

As shown in figure 4-10, considerably lower concentrations were found in the leachate solution for Na, K and Fe compared to Ca and Mg. Iron was the elements with the lowest overall release of those measured from the three sample typologies, with 0.0 µg/mL from PT-SS, 0.01 µg/mL from BN-SS and 0.00 µg/mL from CB-LM. Sodium and K dissolution was higher and presented different distribution across the different sample types. Sample BN-SS had the overall highest release of Na, corresponding to 0.21 µg/mL while the lowest values were obtained for CB-LM, with 0.06 µg/mL. Sample BN-SS also presented the highest release of K, with 0.08 µg/mL, followed by PT-SS (0.05 µg/mL) and CB-LM (0.02 µg/mL).

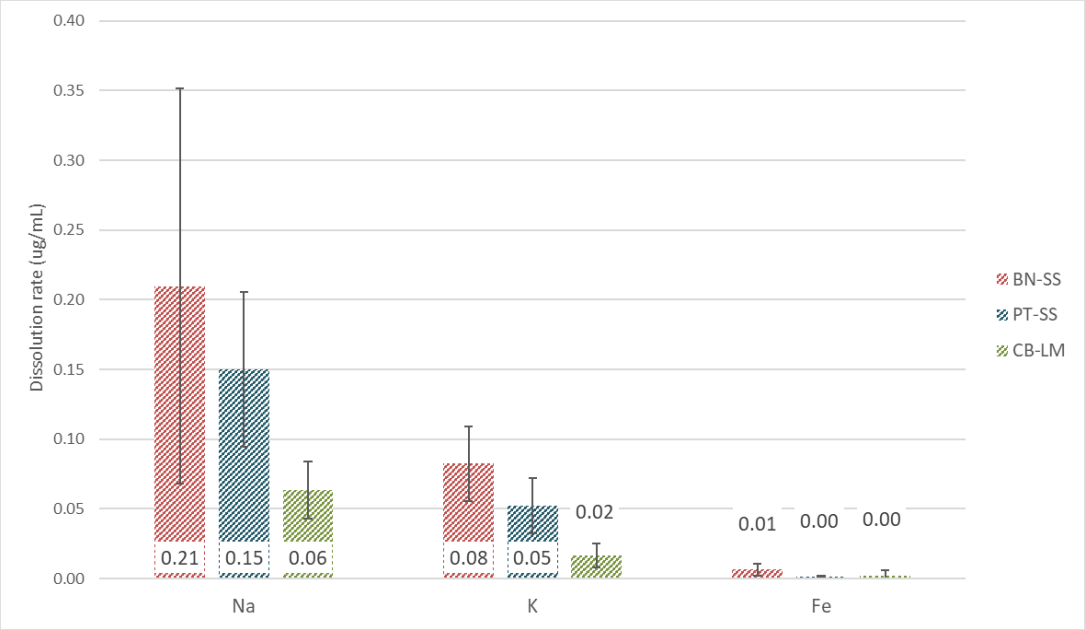

Figure 4-10: overall mean Na, K and Fe release for each stone type

As displayed in figure 4-11, the averaged values for the three stone typologies displayed occasional divergence between the dissolution values of the three replicates. Sample BN-SS showed the highest level of fluctuation between replicates for the three analytes. The discrepancy between replicates for Na, K and Fe, compared to Ca and Mg, appeared to be much more pronounced.

A relatively higher level of fluctuation in the dissolution rate of the replicate samples compared to Ca and Mg was observed for Na, K and Fe. The sample CB-LM presented similar values for replicate 2 and 3, but a significant difference with replicate 1. This difference between the dissolution values of each replicate samples was not observed for Ca and Mg.

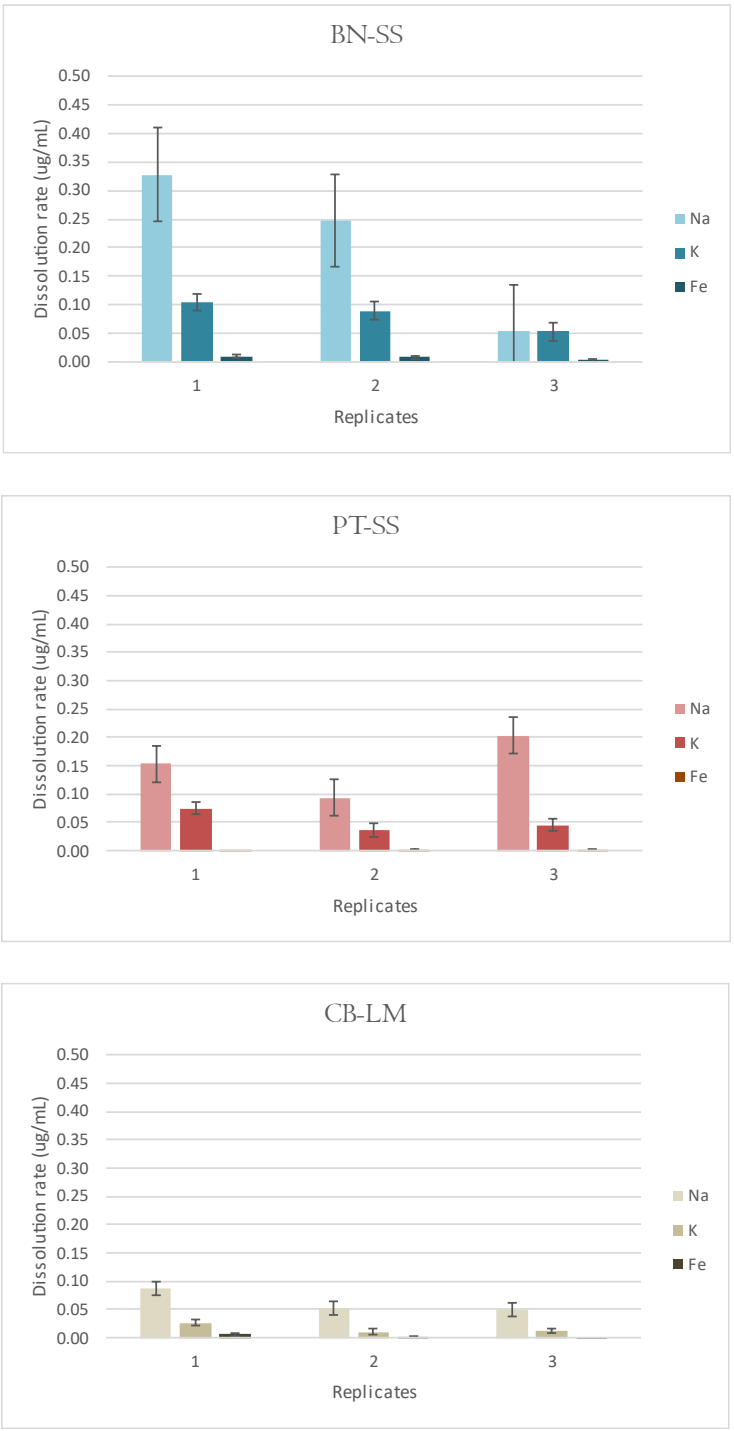

Figure 4-11: mean release of K, Na and Fe by the three replicate samples for each stone type.

4.2.3 Weight change

At the end of the test, the different stone types showed different mass-loss (table 3-2). The precision between replicates of the same typology that received comparable amounts of water was good enough for the mass loss of the three materials to be distinguished (figure 4-12). Average mass-loss values for each replicate were 0.010 ± 0.005 g for PT-SS, 0.017 ± 0.003 g for BN-SS, and 0.042 ± 0.001 g for CB-LM. Replicates displayed an average mass loss of 0.035% (CB-LM), 0.026% (BN-SS), and 0.011% (PT-SS).

The presence of salts within the stone pore system was also assessed. The difference between post-exposure weight (Δ^{1-2}) before and after washing was used to measure the amount of salts that formed after the stone interaction with the nitric acid solution. It was found that the BN-SS registered the highest weight loss after washing, with a decrease in weight of 0.007, 0.009 and 0.028 g for the three replicate samples. The magnitude of the weight changes compared to the other stone types indicated that the sample had likely accumulated the highest amount of salts in the pore system.

The sample PT-SS weight was almost unaffected by the washing procedure, with one replicate sample experiencing no weight change and two replicates varying their weight by 0.002%. Sample CB-LM experienced a weight change after washing of 0.006, 0.008 and 0.009 g.

Table 4-2: Weight change of BN-SS, CB-LM and PT-SS replicate samples. Weight 1: oven dried at 60°C for 24 h before exposure trial; Weight 2: oven dried at 60°C for 24 h after exposure trial; Weight 3: oven dried at 60°C for 24 h after exposure trial and after washing with de-ionized water.

SAMPLE	Δ (1-2) (g)	Δ (1-3) (g)	Salts content	Mass loss (%)
BN-SS (B5)	+0.001	- 0.008	0.009	0.014
BN-SS (W3)	+0.003	- 0.025	0.028	0.043
BN-SS (B3)	- 0.005	- 0.012	0.007	0.021
PT-SS (W1)	- 0.005	- 0.003	0.002	0.005
PT-SS (W4)	- 0.006	- 0.006	0	0.009
PT-SS (B2)	- 0.014	- 0.012	0.002	0.018
CB-LM (W2)	- 0.019	- 0.027	0.008	0.041
CB-LM (W5)	- 0.019	- 0.028	0.009	0.044
CB-LM (B4)	- 0.008	- 0.014	0.006	0.020

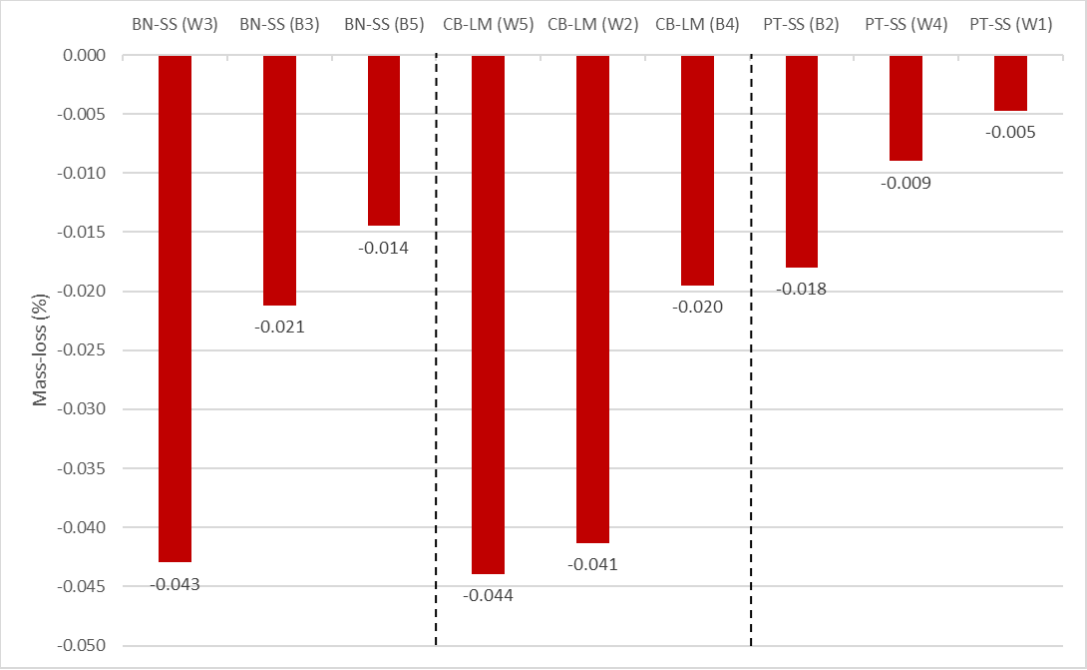

Figure 4-12: mass-loss experienced by each replicate of the three stone types

4.2.4 Principal component analysis

4.2.4.1 Identification of outliers

Principal component analysis was applied to the scaled dissolution rates of the samples replicates (figure 4-13). A first assessment involved the evaluation of the presence of outliers in the dataset containing the analytes concentrations at different sampling points for the three replicate samples and stone types. Three outliers were identified in the first two sampling points of CB-LM and in the first sampling point on BN-SS.

The outliers were found to be associated with the accidental delivery of unexpectedly high volumes of water, as suggested by the total volume found in the collection bottles, or with a malfunction of the nozzle. The outliers identified by the PCA corresponded to the collection points that showed the highest discrepancy in the dissolution profile of the two stone typologies.

The three sampling points were removed from the dataset before further treatment was undertaken. This step was necessary to allow the proper visualization of underlying patterns, which were obscured by the information associated with the outliers and allow the comparison between the performance of different stone types.

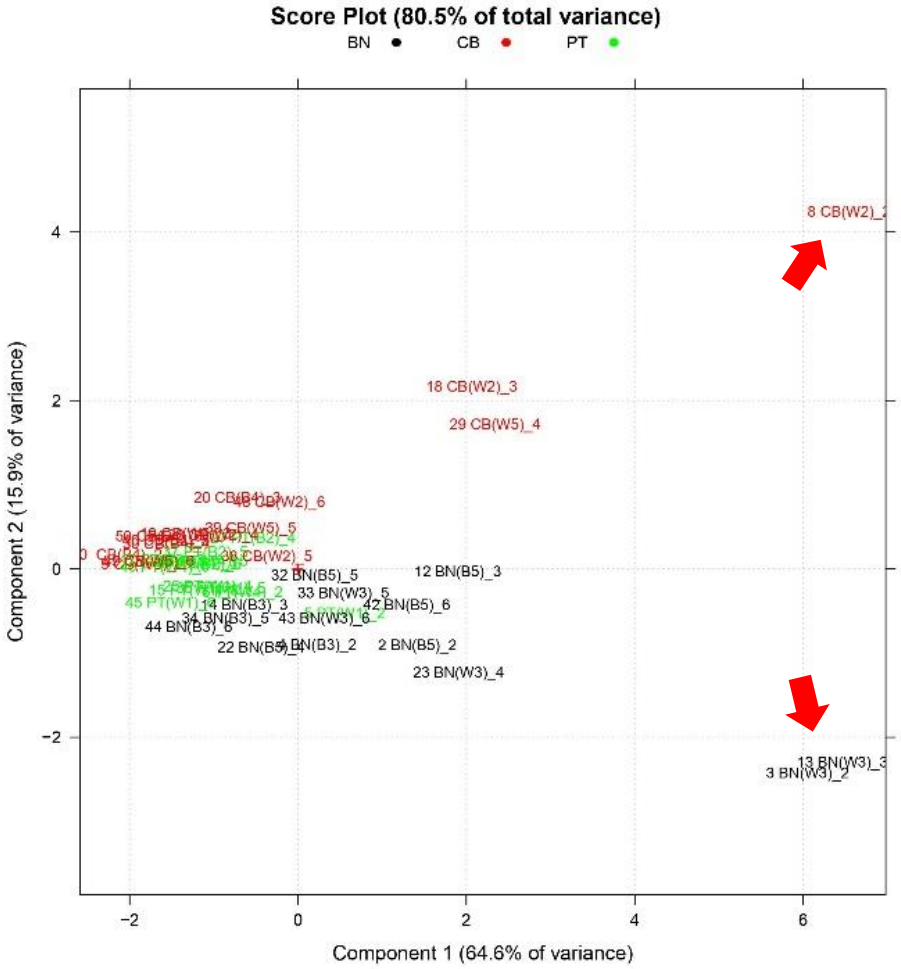

Figure 4-13: score plot showing the outliers BN (W3)_2 and BN (W3)_3 (upper-right) and CB (W2)_2 (bottom-right).

4.2.4.2 Evaluation of the effects of scaling

Principal components analysis was also used to verify the effects of the scaling process on the element concentrations based on the volumes of water delivered to each sample. Principal component analysis carried on PT-SS before scaling displayed a clear subdivision of the sampling points based on their position in the exposure apparatus, highlighted by the different colours assigned to each position (figure 4-14). The separation of the samples based on their position in the exposure apparatus suggested a strong influence of the differences between water volumes delivered to each sample.

Principal component analysis was repeated after the concentrations of each sampling point were scaled based on the total volume of surrogate rainwater delivered to each sample and on the total volume of leachate collected.

Figure 4-15 shows the score plot obtained from the scaled dataset. A reduced influence of the sample position was revealed by the less clear separation of samples based on their position in the exposure apparatus. Instead, a division of the scores into two clusters was observed. Cluster 1 includes the scores represented by the sampling points collected at the start of the exposure, while cluster 2 consist of the sampling points collected from a later stage.

After scaling the temporal feature became prominent. This was displayed by the colour variation associated the colour scale assigned to the sampling points (figure 4-16).

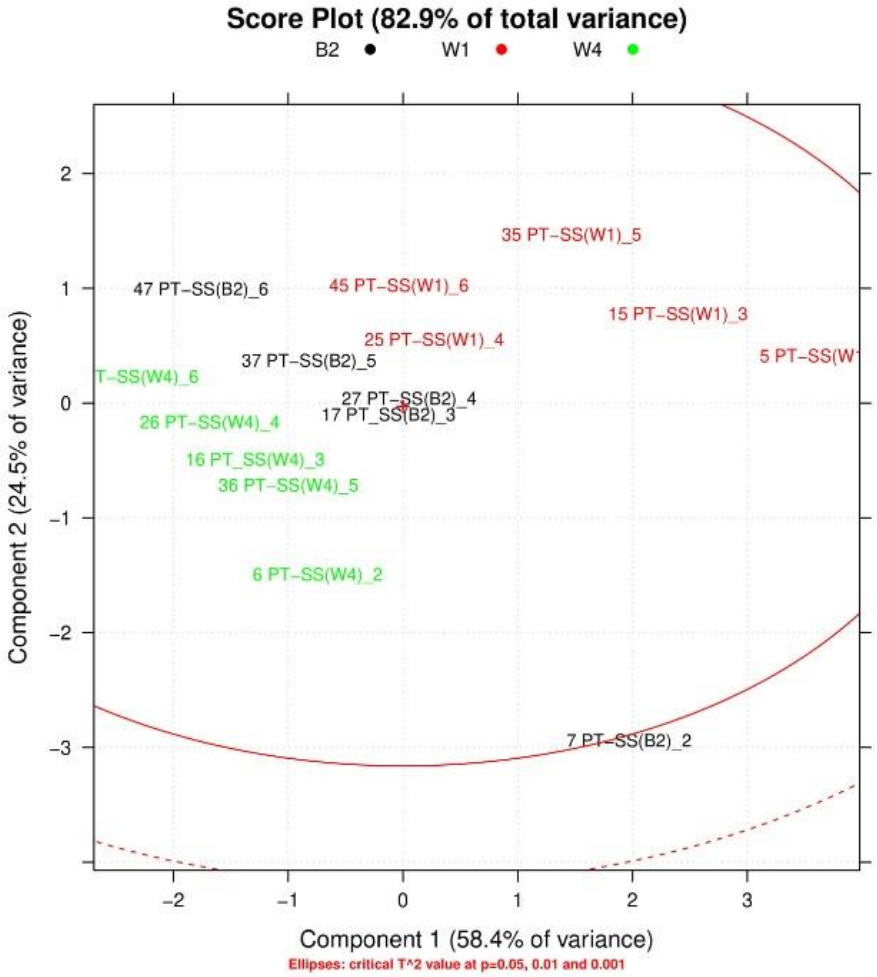

Figure 4-14: score plot of PT-SS samples before the scaling of the concentration values with the water supply volumes. The colours indicate the position of the sample within the exposure apparatus.

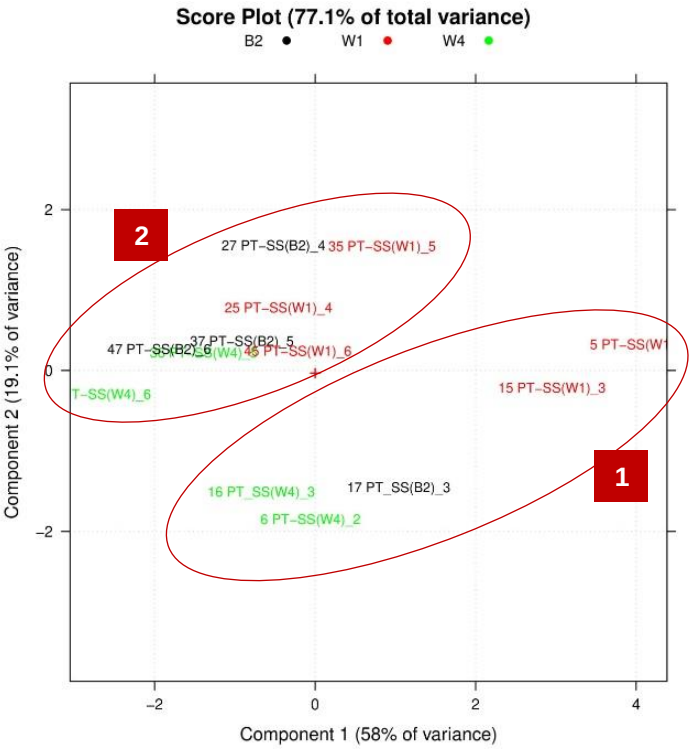

Figure 4-15: score plot of PT-SS samples after the scaling of the concentration values with the water supply volumes. The colours indicate the position of the sample within the exposure apparatus.

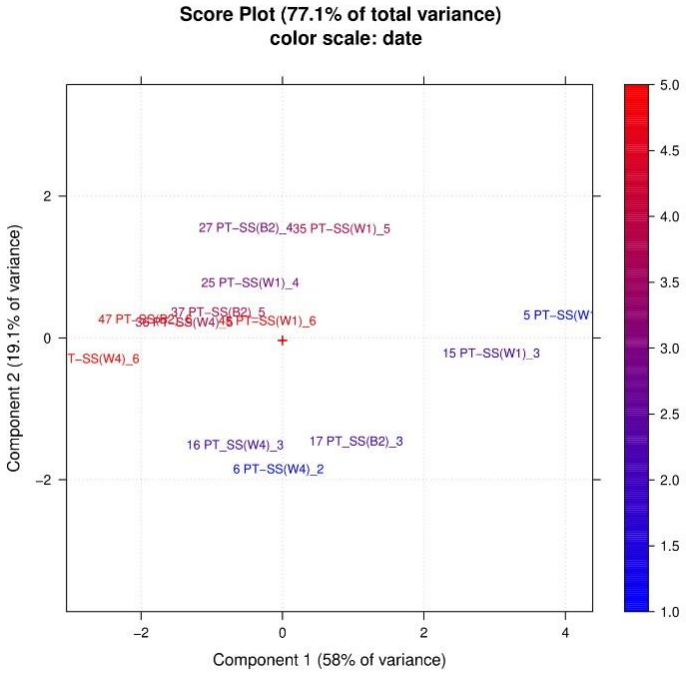

Figure 4-16: *score plot of PT-SS samples after the scaling of the concentrations with the supplied water volumes and total volume of leachate collected. The colour scale indicates the sampling number and is therefore representative of the time trend.*

4.2.4.3 Investigation of underlying patterns

The multivariate statistical treatment of the dissolution data by PCA after scaling and the removal of outliers showed that the three stone typologies were well differentiated based on their response to the leaching action of surrogate rainwater. The PCA score plot based on Ca, Mg, K and Na concentrations measured in all the leachates collected indicated three clusters, each relating to a type of stone (Figure 4-17). Iron was excluded from the treatment due to the to the low significance of this variable in the discrimination of the samples. The first two components (PC1 and PC2) captured a total variance of 81.2%. The first component contributed to the 54.3% of the total variance, while PC2 contributed to the 26.9%. The discrimination between samples typologies was mainly supported by PC1, while PC2 discriminated BN-SS and CB-LM from PT-SS.

Stone PT-SS was represented by the cluster with the lowest dispersion between scores, while a higher level of dispersion was observed with BN-SS and CB-LM. The cross examination with the loadings plot suggested that the dispersion of BN-SS scores was predominantly caused by the fluctuations in Ca concentration of the replicate leachates at each sampling point. Instead, both Ca and Mg contributed to the dispersion of CB-LM. Calcium, Mg and K were the variables with the highest discriminatory power for the three sample types, while K and Na represented the variables with the highest discriminatory power on PC1, which distinguished CB-LM from BN-SS and PT-SS. The release of Mg discriminated CB-LM and BN-SS from PT-SS, as the release of Mg was lower for PT-SS compared to the other two sample types. The rate of dissolution of Na and K displayed a respective positive correlation. Their significance was higher for the

BN-SS cluster, while a negative association was found for the CB-LM cluster. Occasional overlapping between scores was observed for PT-SS and CB-LM. Scores overlapping suggests comparable dissolution values between sampling points of the two sample types. Instead, CB-LM did not display overlaying with the other two clusters. The occurrence of overlapping between scores belonging to different stone typologies could have resulted from an uneven distribution of the surrogate rainwater solution.

4.2.4.4 Dissolution rate and volume of water delivered

The relationship between the amount of Ca released and the volume of surrogate rainwater supplied was investigated to improve the understanding of the effects of additional factors on the dissolution trend. Since the accidental variation in volume of water delivered was found to significantly affect the concentration of the analytes in solution, this aspect was subject to further evaluation. The scaled leachates concentration was plotted on a bivariate plot consisting of Ca release against water volume delivered. The plot showed that even small variations in volume of surrogate rainwater delivered to the sample corresponded to a relatively significant variation in Ca dissolved. The plots highlighted a positive association between Ca release and volume of surrogate rainwater supplied to PT-SS and CB-LM, where accidental delivery of a higher amount of water corresponded to a higher Ca concentration in the leachates. The opposite was observed in BN-SS, where the association between Ca release and water volume appeared to be negative (figure 4-18).

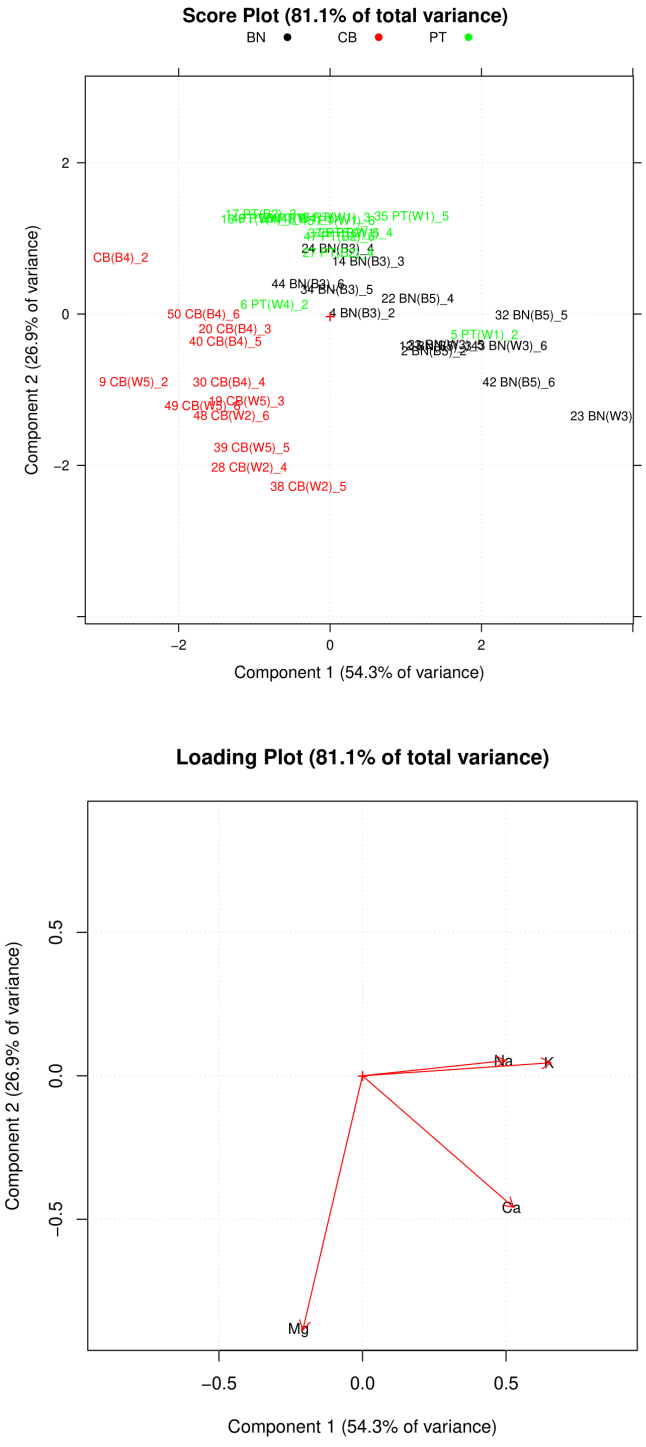

Figure 4-17: score plot (top) and loading plot (bottom) of the scaled dataset containing dissolution data for the three replicates of the three sample types.

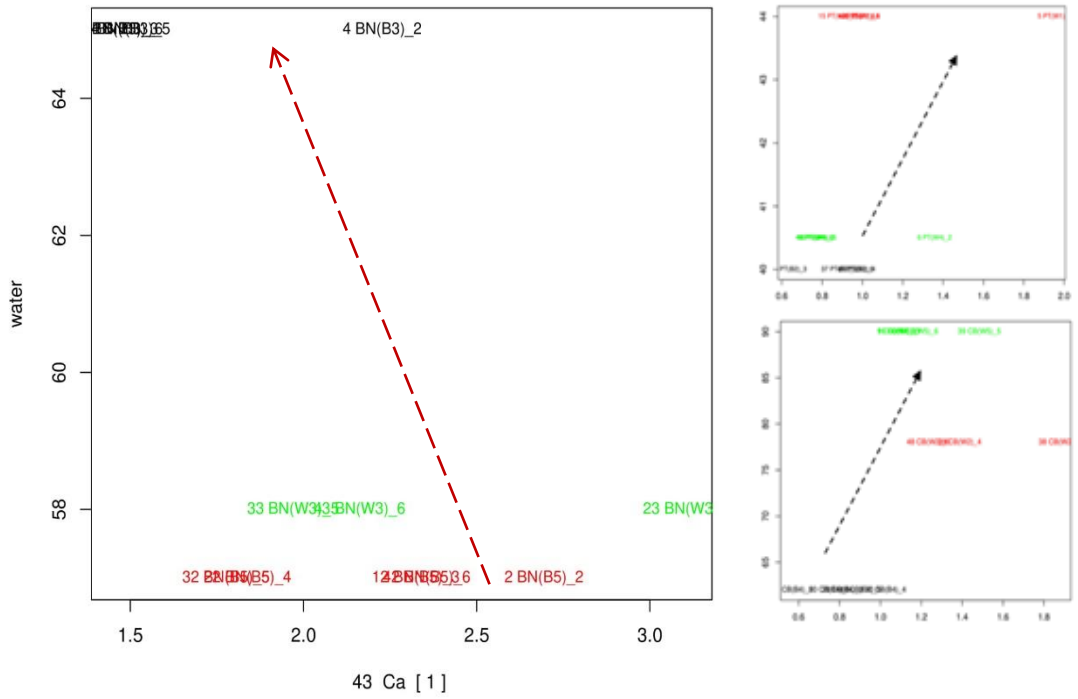

Figure 4-18: plot showing the relationship between volumes of surrogate rainwater delivered to the samples and amount of Ca released. The association appears to be negative for BN-SS (left) and positive for PT-SS (upper-right) and CB-LM (bottom-right).

5. Results of short-term exposure

The chapter summarises the findings of the short-term leaching test. The test was performed to investigate the dissolution profiles of a higher number of stone types over 1 month of accelerated exposure.

The test procedure and details of the exposure are summarised in chapter 2, section 2.2.2.1.

5.1 Dissolution Trends

5.1.1 Calcium and Magnesium

Figures 5-1 to 5-4 show the dissolution trend of each sample obtained by plotting the dissolution rate of Ca and Mg at each sampling point. The red dashed line that can be observed at the fourth sampling point (day 10 of the exposure) is aimed at indicating the sampling times that are affected by higher initial dissolution rates caused by the loss of debris from the sample, and that as such are no representative of actual dissolution rates. For this reason, sampling time 1 to 4 are not included in the calculation of the average dissolution rates. A common axis was adopted for all samples (maximum 6.00 µg/mL), except for PSX-SS (maximum 12 µg/mL), to ease data comparison. Performance trends displayed common features across the test set. Overall, two distinct phases were observed

in the release of Ca during accelerated exposure, i.e., an initial higher release of the analytes followed by a stabilization of the dissolution rate. For some stone types, the high dissolution of Ca during the early stage of exposure was particularly pronounced. For instance, PSX-SS exhibited an exceptionally high initial dissolution rate compared to the rest of the samples, with a peak of 10.50 µg/mL of Ca on the third sampling point. Similarly, BL-SS and DH-SS presented a high dissolution of Ca at the first sampling point, with a dissolution value of 5.97 µg/mL and 5.86 µg/mL, respectively. In other samples this feature was less prominent. For example, CB-LM and DM-SS displayed a relatively low release of Ca at the start of the exposure. The dissolution rate of Ca followed a decreasing trend before reaching stability between the third and fifth sampling point. The same trend was observed in all samples, with the only exception of PSX-SS, whose dissolution declined throughout the entire exposure without reaching stability. The dissolution trend for all stone types was found to be relatively stable, with only occasional alterations. Rather than the trend of dissolution, the dissolution rate represented the main difference in the samples performance. The difference between dissolution rates progressively decreased throughout the exposure as dissolution reached a stable trend. For the initial sampling points the difference between the highest (PSX-SS) and lowest (DM-SS) Ca dissolution value was of 7.68 µg/mL. In contrast, the last sampling point showed the lowest level of separation between Ca release values across the full test-set. Here the difference between the highest and lowest (PSX-SS and DM-SS respectively), was just 1.76 µg/mL. This feature is shown by the relative standard deviation (RSD) between dissolution values from sampling point 5 to 11, corresponding to the stable phase of dissolution (figure 5-5). The difference between Ca dissolution

rates in the samples was found to be higher at the fifth sampling, where it reached 162%. After this point, the variability progressively declined, until reaching a value of 50% at the last sampling point. The same observations applied to Mg dissolution, which displayed a similar performance to Ca (figures 5-1 to 5-4). The samples displayed an overall higher release of Mg at the first sampling points. However, the difference in dissolution rate between the initial phase and the stable trend was considerably less pronounced compared to Ca and the dissolution profile displayed an overall more stable trend throughout the exposure. Samples were found to show correspondence in their respective rates of dissolution of Ca and Mg. For instance, similarly to the behaviour displayed with Ca, DM-SS and CB-LM were found to present an overall higher stability compared to other samples, due to an almost unnoticeable difference between the dissolution rate at each sampling point. The same observation applied to PSX-SS, which exhibited a behaviour consistent with that observed with Ca and showed high dissolution rates of Mg at the first sampling points. However, dissolution reached stability sooner compared to Ca, and from sampling point 6 to sampling point 7 the dissolution values for PSX-SS were comparable to those of other samples. Similarly to that observed with Ca, samples DM-SS and PSX-SS provided the lowest and highest dissolution throughout the exposure. For each stone type, the initial high rate of dissolution of Mg was followed by a stable performance, with occasional variations in the rates of dissolution that matched the ones observed with Ca.

The main difference between the release of the two analytes in each stone type was represented by the different rate of dissolution, which was consistently higher for Ca, with the only exception of DM-SS.

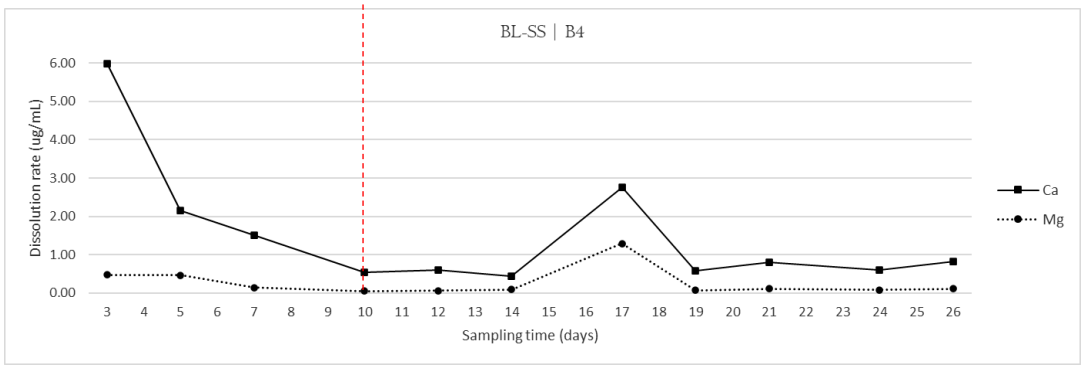

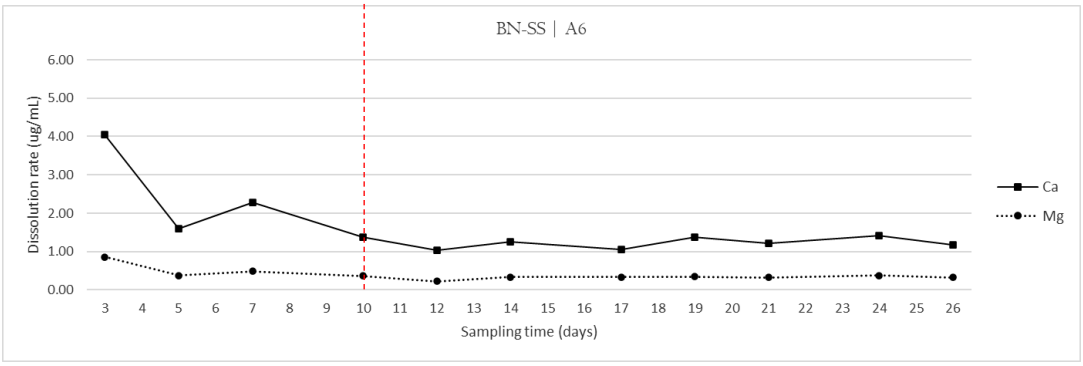

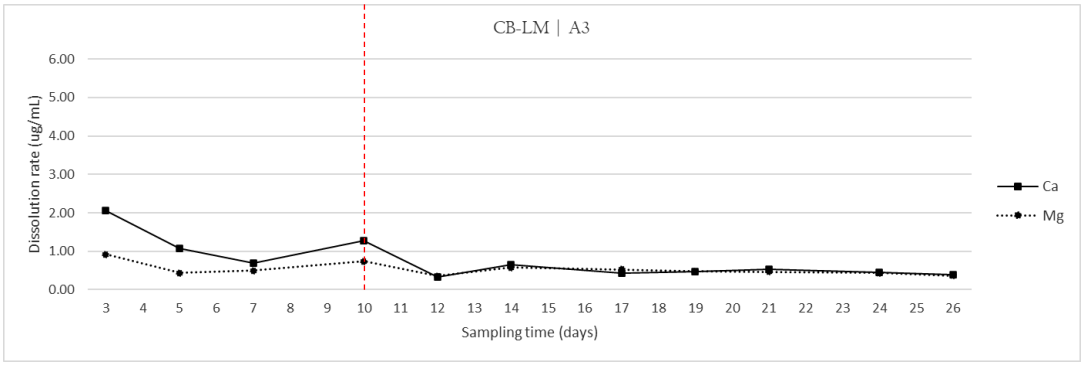

Figure 5-1: dissolution trend of BL-SS, BN-SS and CB-LM

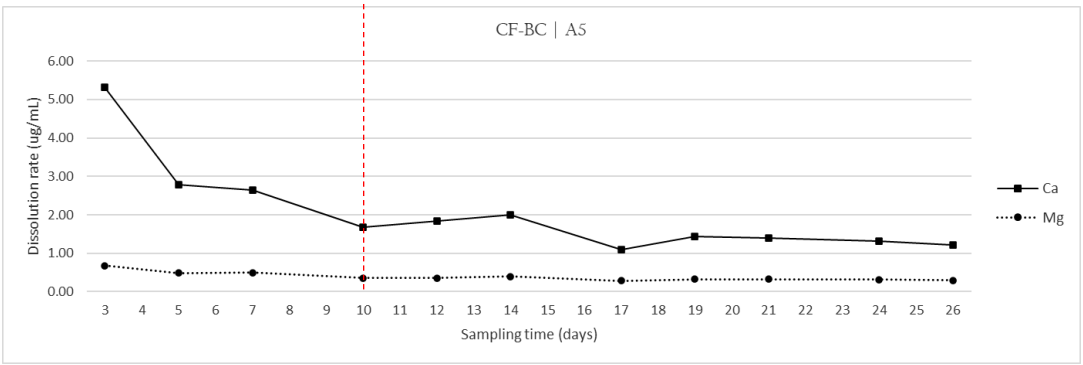

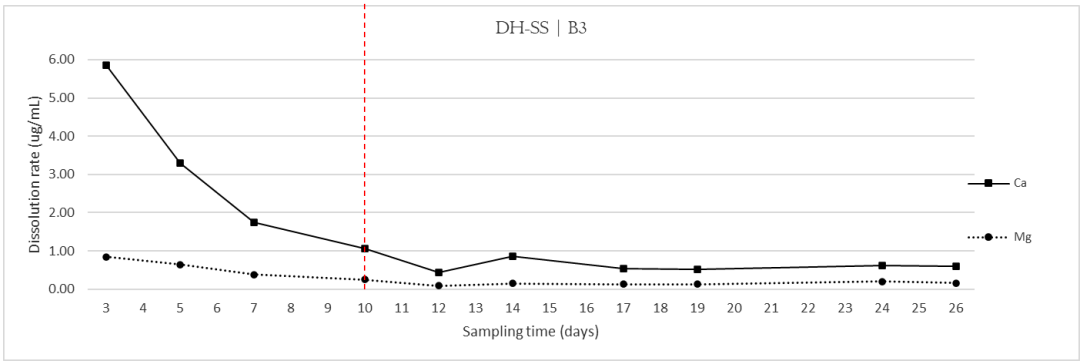

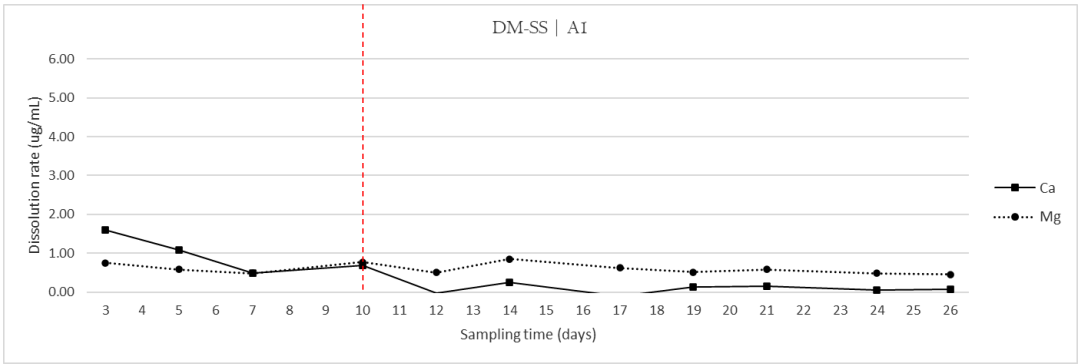

Figure 5-2: dissolution trend of CF-BC, DH-SS and DM-SS

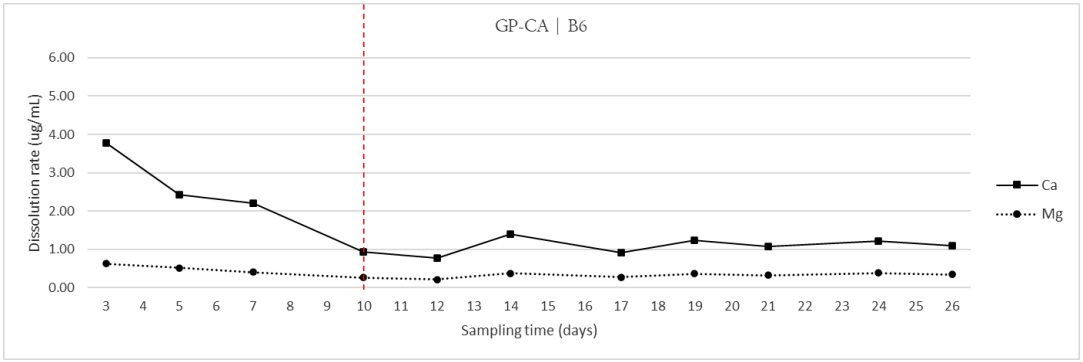

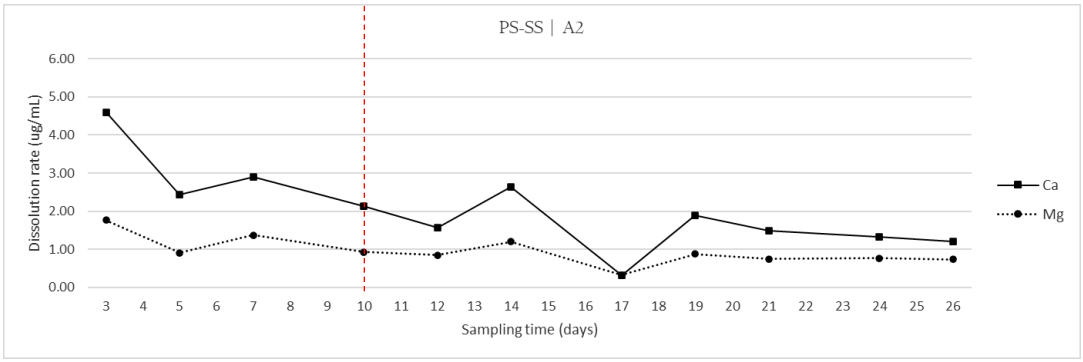

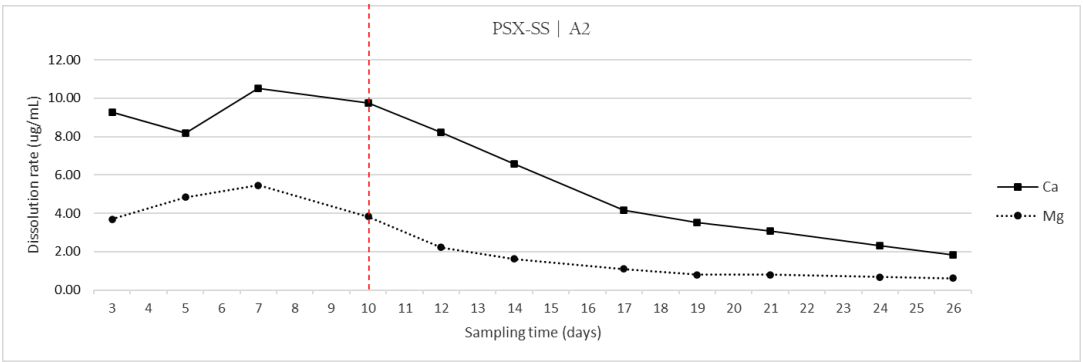

Figure 5-3: dissolution trend of GP-CA, PS-SS, PSX-SS

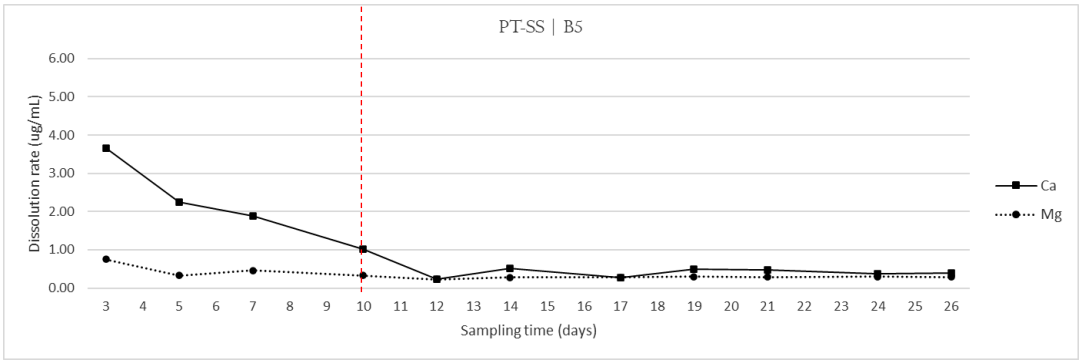

Figure 5-4: dissolution trend of PT-SS

The relative standard deviation (RSD) of the dissolution values for Mg is shown in figure 5-6. Differences in dissolution rates of Mg between the different stone types were lower than for Ca. However, similarly to Ca, the divergence between the samples rates of dissolution was higher at the third sampling point. After this point, the RSD between Mg dissolution values of the different stone types displayed a decreasing trend, which reached the lowest value on the final sampling. This corresponded to a standard deviation ranging between 127% at its highest value, and 51% at the last sampling point. This suggest that the extent of dissolution tends to become more similar between different stone types as dissolution proceeds.

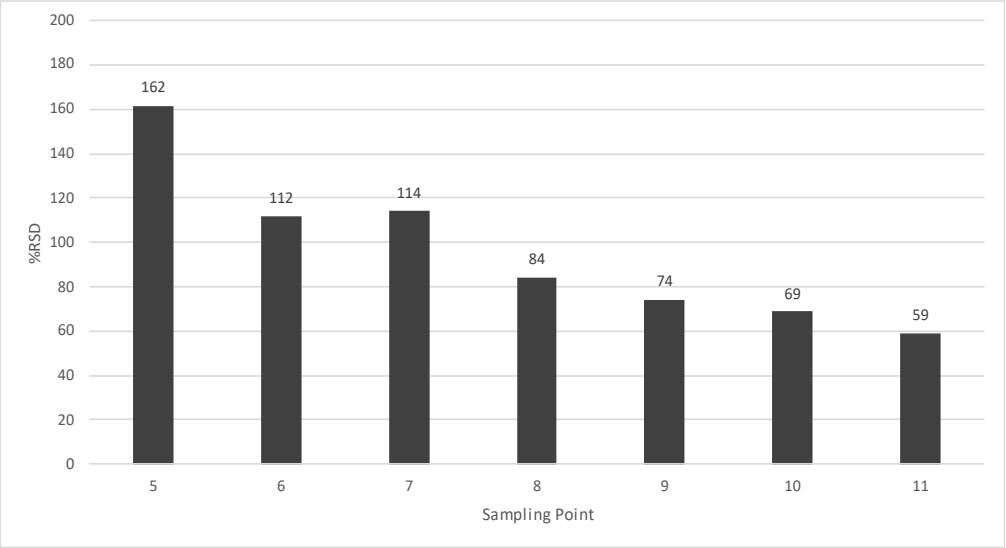

Figure 5-5: overall variability in Ca dissolution rates across the sample set, expressed as % RSD.

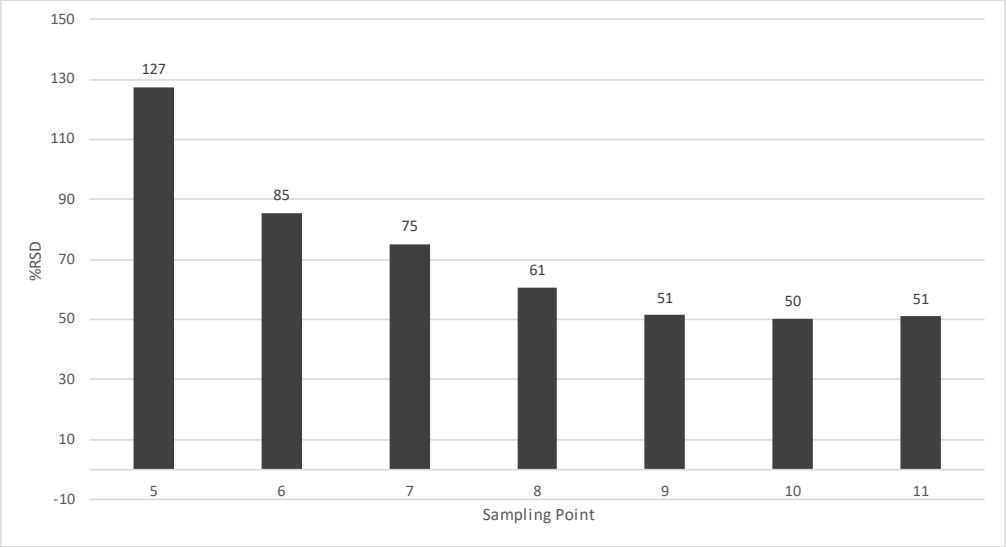

Figure 5-6: overall variability in Ca dissolution rates across the sample set, expressed as % RSD.

5.1.2 Potassium and Sodium

Potassium and Na were plotted separately to Ca and Mg, due to the different scale of the dissolution rates of both analytes. The second sampling point of Na was removed from the data treatment to allow a proper resolution by adopting a suitable scale for the axis plotting the dissolution rate (figure 5-7).

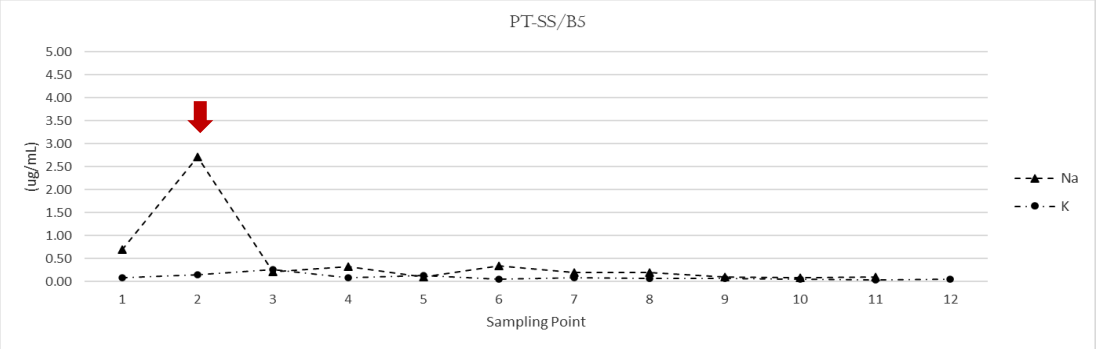

Figure 5-7: dissolution profiles of K and Na showing the high value of K dissolution at sampling point 2.

The analytes K and Na displayed similar trends, except for the dissolution rates reached by Na at the initial sampling points (figure 5-8 to 5-11). This feature of the dissolution profile was followed by the stabilization of the trend between the third and fifth sampling. Overall, the dissolution rates of K displayed a higher stability throughout the entire exposure, while Na exhibited occasional alterations of the dissolution rate, as shown by GP-CA, PS-SS, and PT-SS. As a consequence, the difference between the dissolution rates of the two analytes was higher during the first part of the exposure, while they were found to become progressively more comparable with the progression of time. After the third or fifth sampling, depending on the stone type, dissolution for the two analytes reached similar values. Most samples did not display a clear predominance of one analyte, but most dissolution trends displayed an alternation of the dissolution profile rates.

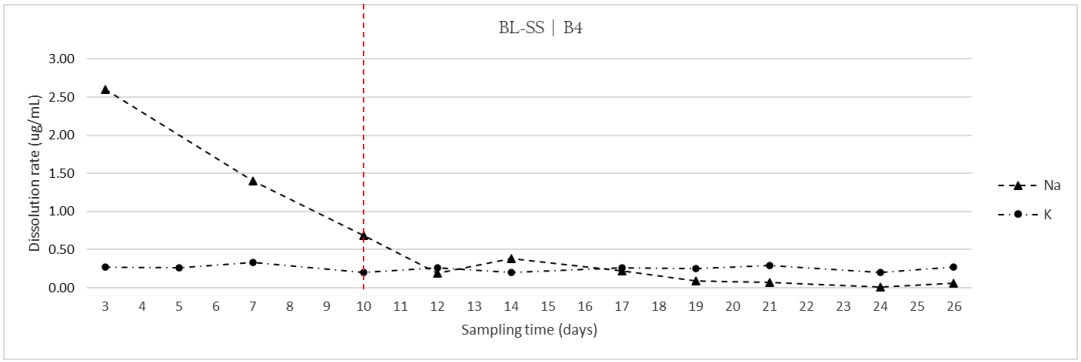

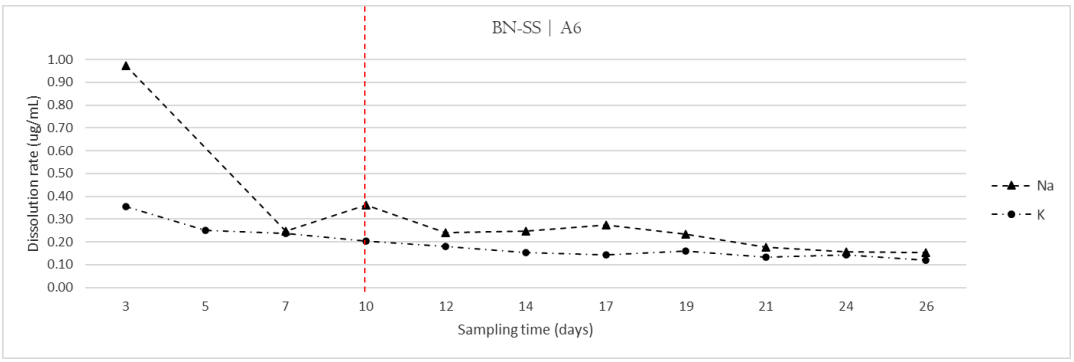

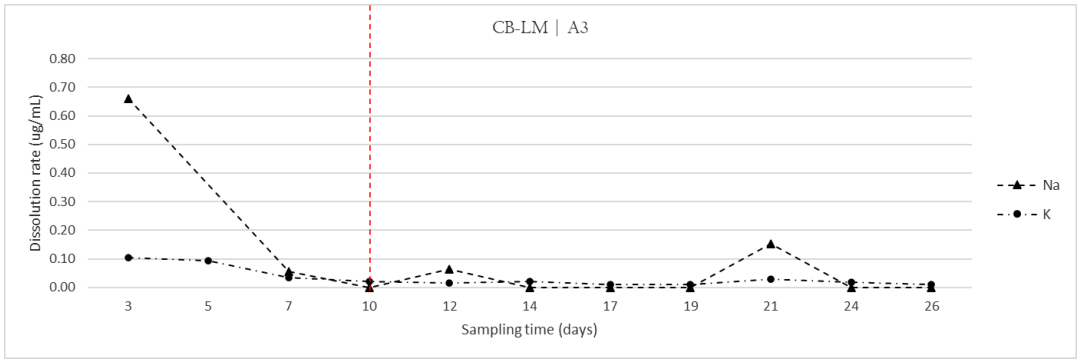

Figure 5-8: dissolution trend of BL-SS, BN-SS and CB-LM

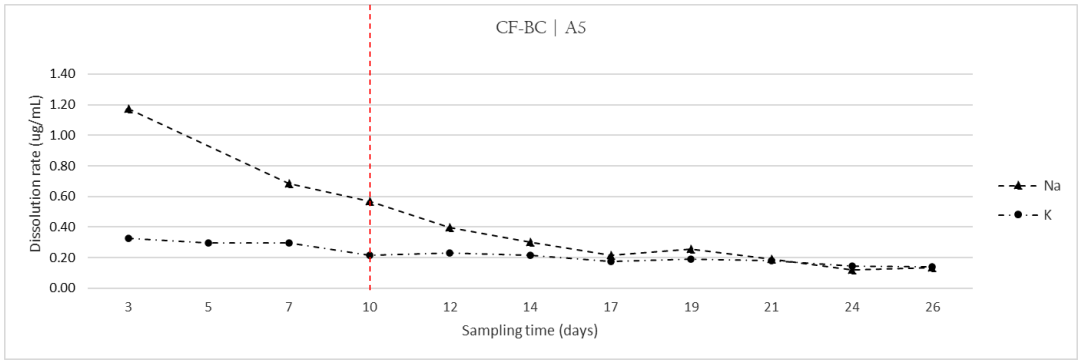

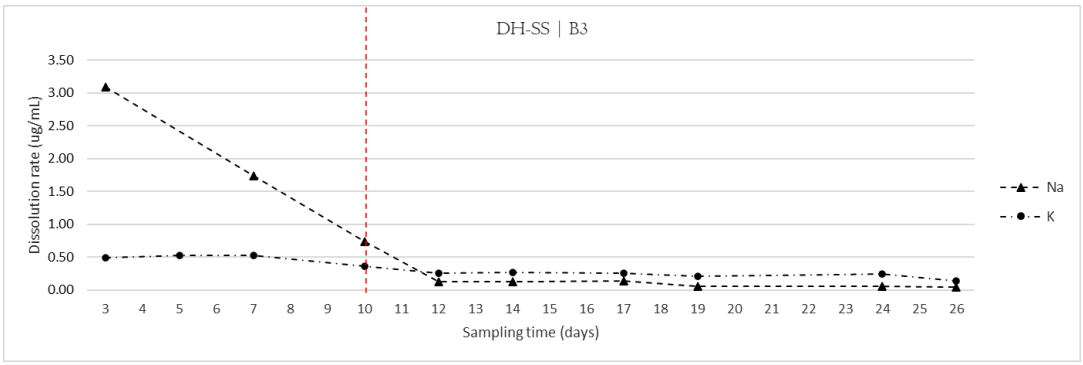

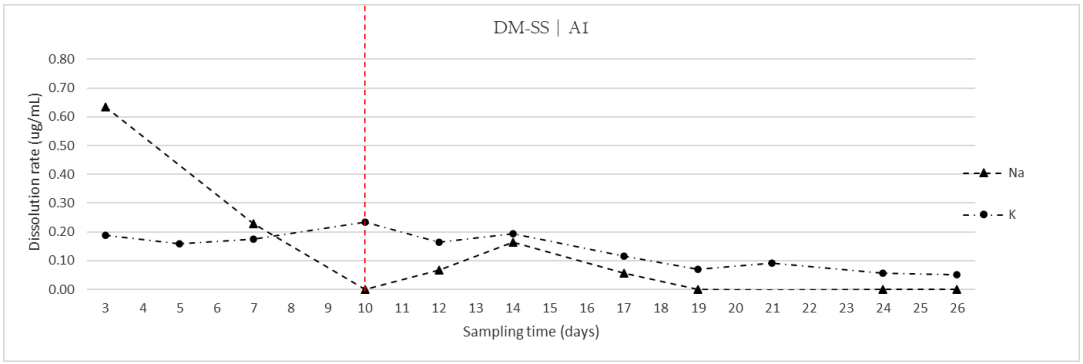

Figure 5-9: dissolution trend of CF-BC, DH-SS, DM-SS

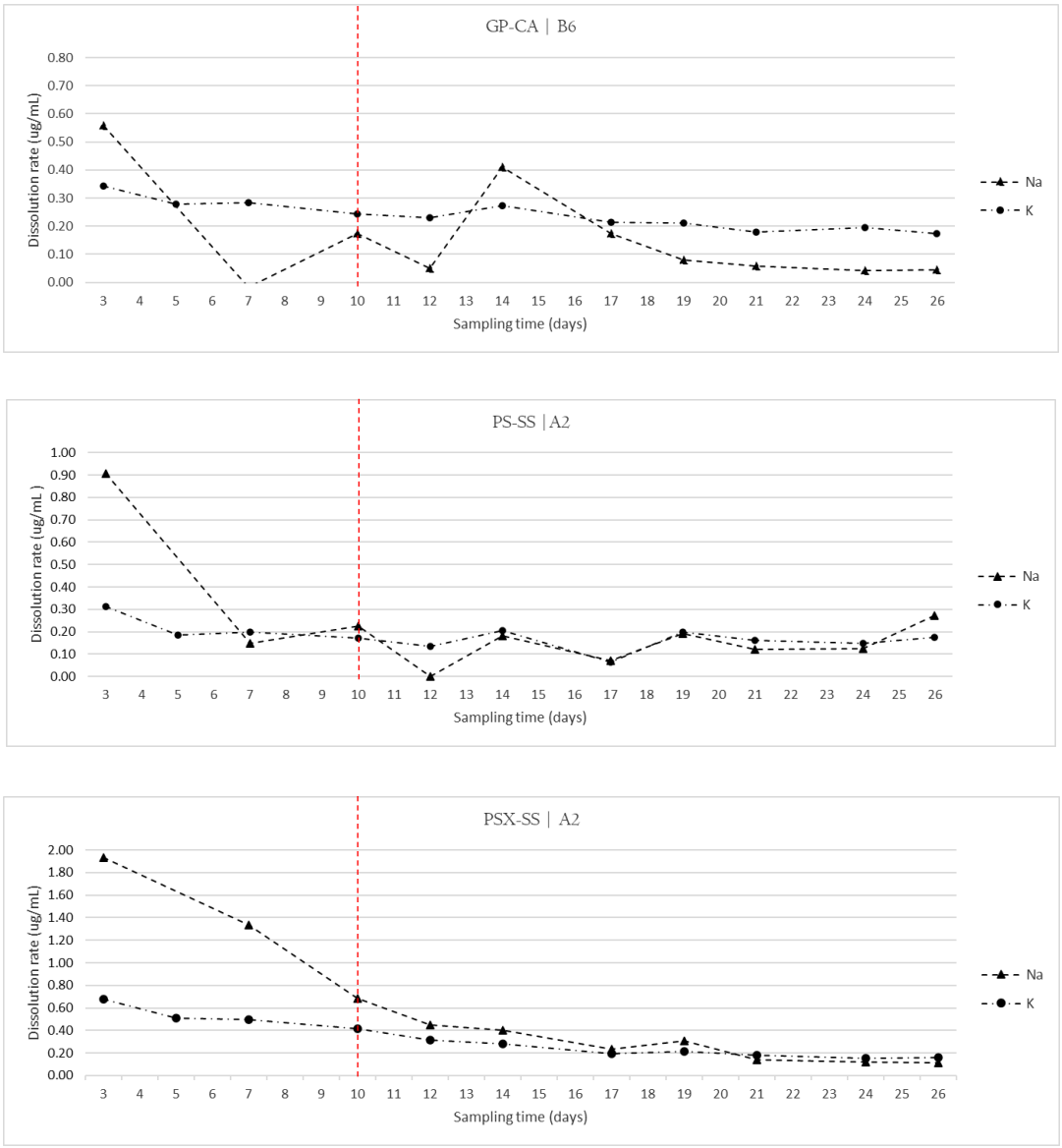

Figure 5-10: dissolution trend GP-CA, PS-SS and PSX-SS

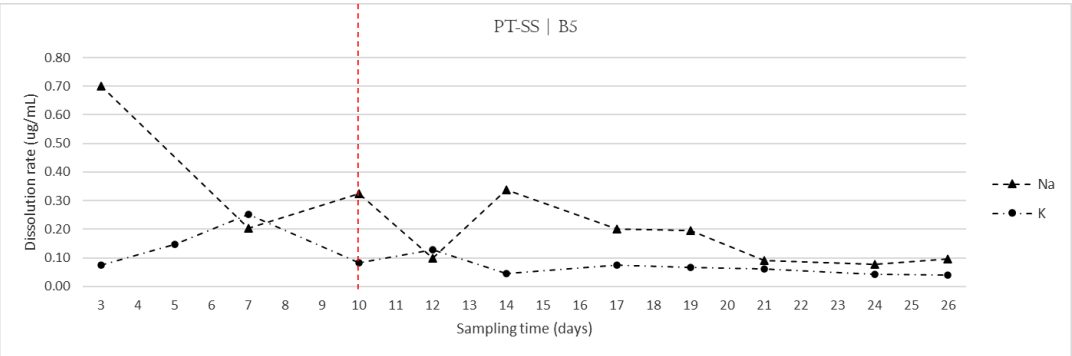

Figure 5-11: dissolution trend of PT-SS

5.1.3 Overall trend

Comparison between dissolution profiles of Ca-Mg and Na-K highlighted the similarity between the analytes' respective trends. All samples displayed a comparable profile, which showed distinctive decreasing dissolution rates at the early stage of the exposure, followed by a stable performance. This feature was observed for all analytes on a different scale. Calcium displayed the highest difference in dissolution rates between the initial and final stage of the accelerated exposure, while the lowest difference was shown by K. The occurrence of differences in the dissolution trends was mainly caused by the different dissolution rates of the analytes, rather than to a variation of the sample performance and profile of dissolution.

5.2 Mean dissolution rates

5.2.1 Calcium and Magnesium

Average dissolution rates were obtained by taking into account only the dissolution data obtained from the fifth sampling point onwards. The exclusion of the initial sampling points was aimed at capturing the average dissolution rate of the stable performance only. The samples of test-set 1 displayed mean dissolution rates for Ca within the range of 0.07 to 4.25 µg/mL (figure 5-12). The lowest Ca dissolution was found for DM-SS and PT-SS, corresponding to an average release of 0.07 µg/mL and 0.40 µg per mL of surrogate rainwater. The highest overall dissolution rate was exhibited by PSX-SS, with a mean value of 4.25 µg/mL.

Overall, the mean release of Ca from most samples varied within a range of 0.07 and 1.49 ug/mL. The specimen PSX-SS represented an exception, as its mean Ca release (4.25 µg/L) was nearly three times higher than the second highest value, which was obtained from CF-BC (1.49 µg/mL). In most cases, the extent of the dissolution did not correlate to the concentration of the carbonate mineral fraction. For instance, the higher concentration of carbonate minerals in BN-SS compared to PSX-SS did not convert into a higher Ca dissolution rate. Instead, the opposite was observed. Despite displaying relatively high dissolution rates, no carbonate minerals were observed in the composition of BL-SS. However, the occurrence of Ca in the leachate could also derive from the dissolution of calcium bearing feldspars, such as plagioclase. The mean Mg dissolution rate (figure 5-13) was less than the Ca dissolution rate for nearly all the sample.

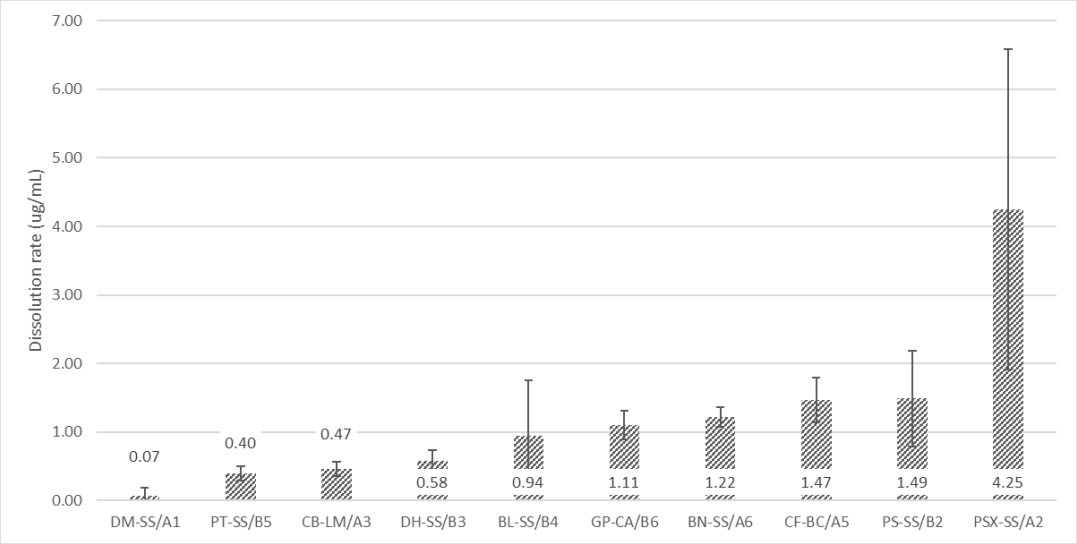

Figure 5-12: mean Ca dissolution of test-set 1 samples

The only exception was DM-SS, which displayed a higher overall release of Mg compared to Ca. The highest dissolution values for Mg were displayed by PSX-SS and PS-SS, with an average Mg release of 1.12 µg/mL and 0.79 µg/mL respectively. The lowest dissolution values were exhibited by DH-SS, which displayed a mean dissolution of 0.14 µg/mL. Mean dissolution rates between Ca and Mg only occasionally showed consistent rates across the test-set. For instance, PSX-SS and PS-SS represented the samples with the highest release of both analytes. However, the third highest release of Mg was provided by DM-SS (0.57 µg/mL), which was the sample with the lowest overall Ca release. In other cases, the relative dissolution rates for the two analytes were comparable. For instance, CB-LM provided a dissolution rate of 0.47 µg/mL and 0.46 µg/mL for Ca and Mg respectively. This last result is consistent with sample composition, which is characterised by equivalent concentrations of calcite and dolomite. The

presence of Mg in the leachate of samples that did not contain carbonate minerals could have arisen from the dissolution of Mg-bearing clay minerals, such as biotite and chlorite.

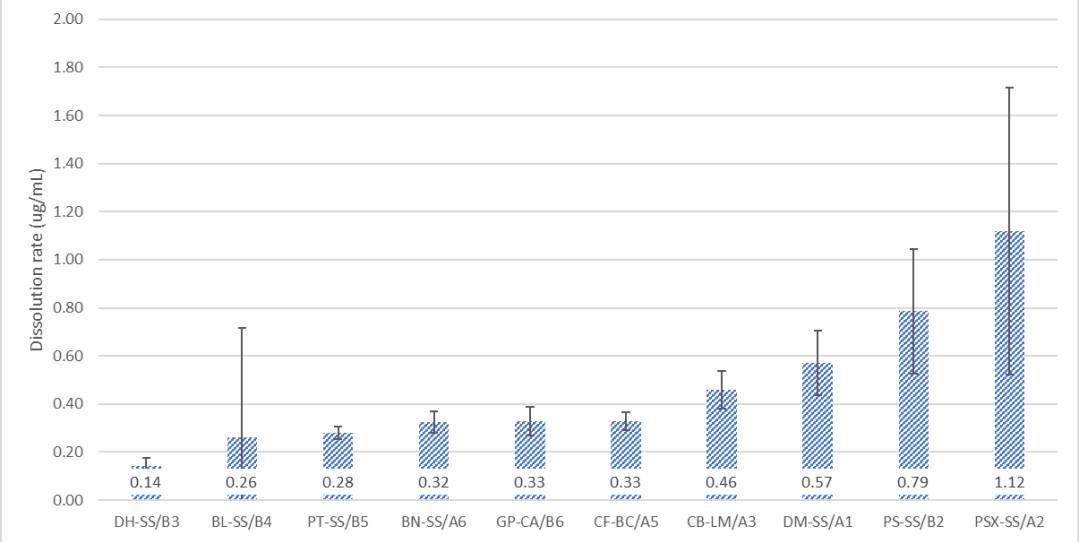

Figure 5-13: mean Mg dissolution of test-set 1 samples

A direct relationship between carbonate minerals content and rate of Ca dissolution was not unambiguously established. For example, as expected the high content of carbonate minerals of GP-CA and CF-BC corresponded to a consistently high dissolution rate of Ca. The same was not observed for CB-LM which, compared to other samples, displayed an overall higher resistance to dissolution. To this respect, the rate of dissolution of the individual analytes was not necessarily consistent with the concentration of the parent mineral in the sample. The most obvious example was provided by PSX-SS, which displayed the highest release of Ca and Mg, despite having an original lower concentration of carbonate minerals in its composition compared to other stone types. A similar

behaviour was observed for BN-SS, which was also subject to relatively high dissolution rates in all exposure tests.

5.2.2 Potassium and Sodium

Sodium and K displayed different dissolution rates across the test-set. The highest overall release was provided by Na, whose dissolution ranged between 0.02 µg/mL and 0.25 µg/mL (figure 5-14). The sample with the highest average release of Na was PSX-SS (0.25 µg/mL), followed by CF-BC (0.23 µg/mL) and BN-SS (0.21 µg/mL). The sample CB-LM displayed the lowest mean release of Na, with a dissolution rate of 0.02 µg/mL. The dissolution of Na is the product of the dissolution of feldspars. The low Na dissolution rate of CB-LM is consistent with the sample composition, which is exclusively composed of carbonate minerals.

The sample PSX-SS maintains the highest overall dissolution rate. The characterization of Pietra Serena Extradura by Franzoni and Sassoni (2011) identified high concentrations of albite, a Na-feldspar. The same was found for PS-SS, which was found to present high concentrations of Na-feldspars. However, PS-SS presented a lower dissolution rate of Na compared to samples that displayed lower amounts of feldspars in their composition, as CF-BC. Compared to Na, K exhibited lower dissolution rates, which covered a range between 0.02 µg/mL (CB-LM) and 0.33 µg/mL (CF-BC) (figure 5-15). The scale of K dissolution was comparable with the rates of Na dissolution and presented a degree of correlation across the test-set. For instance, in both cases CB-LM and DM-SS provided the lowest rates.

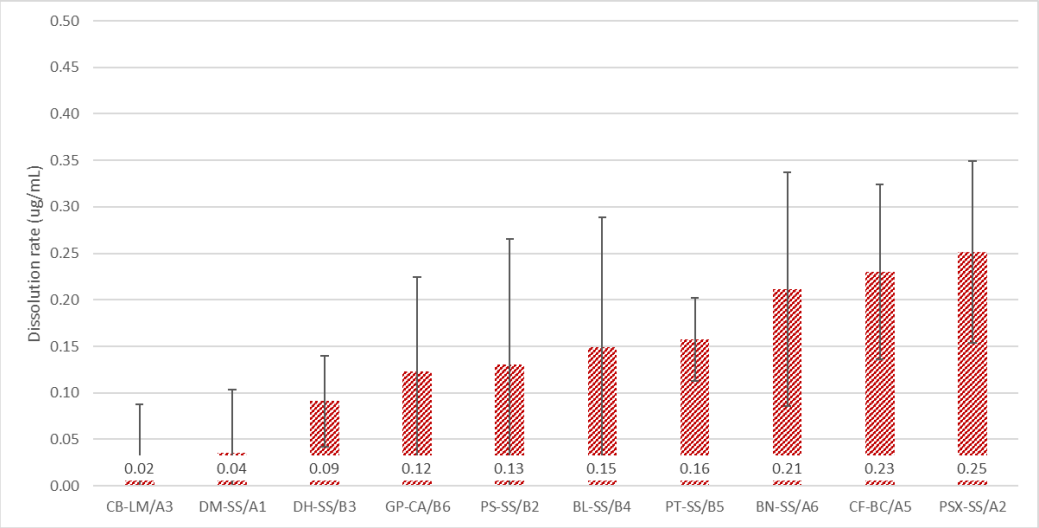

Figure 5-14*: mean Na dissolution of test-set 1 samples*

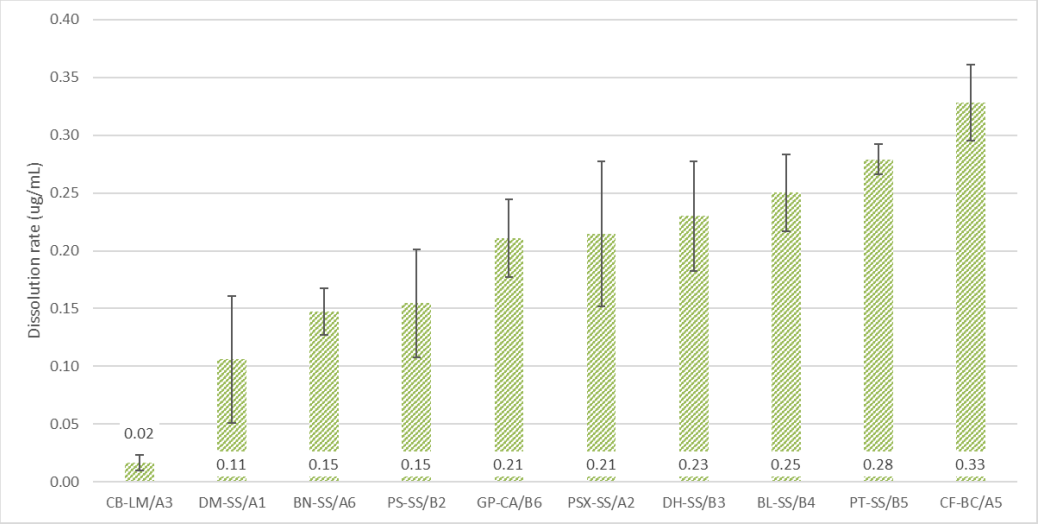

Figure 5-15*: mean K dissolution of test-set 1 samples*

1.1.1 Iron

The dissolution of Fe was next to negligible in most samples, preventing the possibility of extracting further information from the data. Due to this reason, Fe was excluded from the treatment of the average dissolution values.

1.1.2 Overall dissolution

The average dissolution rate of the analytes highlighted a predominance of Ca for all the samples, with the only exception of DM-SS. Average dissolution values showed a level of agreement between analytes. For instance, PSX-SS displayed high values in all four analytes, while in DM-SS the dissolution values were found to be consistently low. Other stone types, such as BN-SS, displayed intermediate values compared to the rest of the test-set for all five analytes. In some cases, no correlation was found between relative rates of dissolution of the analytes. For instance, DM-SS showed relatively low dissolution for Ca, K and Na, but high dissolution for Mg.

Overall, the scale of dissolution of each analyte was found to be comparable across different samples typologies. Only PSX-SS exhibited a distinct performance, due to the exceptionally high dissolution rates of Ca and Mg compared to the rest of the test-set. Overall, the presented data suggested that the stone composition alone is not sufficient to provide an indication of the stone vulnerability to dissolution. This aspect will be discussed in Chapter 9.

1.2 Weight Change

The change in weight of each stone type was acquired by subtracting the dry samples post-exposure weight from the dry samples pre-exposure weight (table 5-1). Results showed that all the samples experienced different levels of mass-loss. The samples with the highest weight change were PSX-SS and PS-SS, with an overall mass loss of 0.077 g and 0.065 g, corresponding to a change of 0.120% and 0.105% from the initial weight.

The specimens CB-LM and DM-SS were the samples with the lowest weight loss, corresponding to 0.010 g and 0.024 g, and a percentage change of 0.016 % and 0.038 %. Figure 5-16 showed the progressively increasing mass loss values across the test-set. Sample PSX-SS experienced a weight change more than seven times higher than that experience by CB-LM.

The extent of dissolution was consistent with the magnitude of the weight change. However, similarly to what was observed with the relative dissolution of each stone type, the stone nature and content of carbonate minerals did not provide a full representation of the stone vulnerability to the action of surrogate rainwater.

Table 5-1: pre- and post- exposure variation of test-set 1

SAMPLE	PRE-EXPOSURE WEIGHT (G)	POST-EXPOSURE WEIGHT (G)	MASS LOSS (G)	MASS LOSS (%)
BL-SS/B4	83.779	83.725	- 0.054	- 0.064
BN-SS/A6	71.640	71.596	- 0.044	- 0.061
CB-LM/A3	59.897	59.887	- 0.010	- 0.016
CF-BC/A5	53.053	53.014	- 0.039	- 0.073
DH-SS/B3	69.754	69.715	- 0.039	- 0.055
DM-SS/A1	62.105	62.081	- 0.024	- 0.038
GP-CA/B6	60.653	60.603	- 0.050	- 0.082
PS-SS/B2	61.674	61.609	- 0.065	- 0.105
PSX-SS/A2	64.178	64.101	- 0.077	- 0.120
PT-SS/B5	66.812	66.779	- 0.033	- 0.049

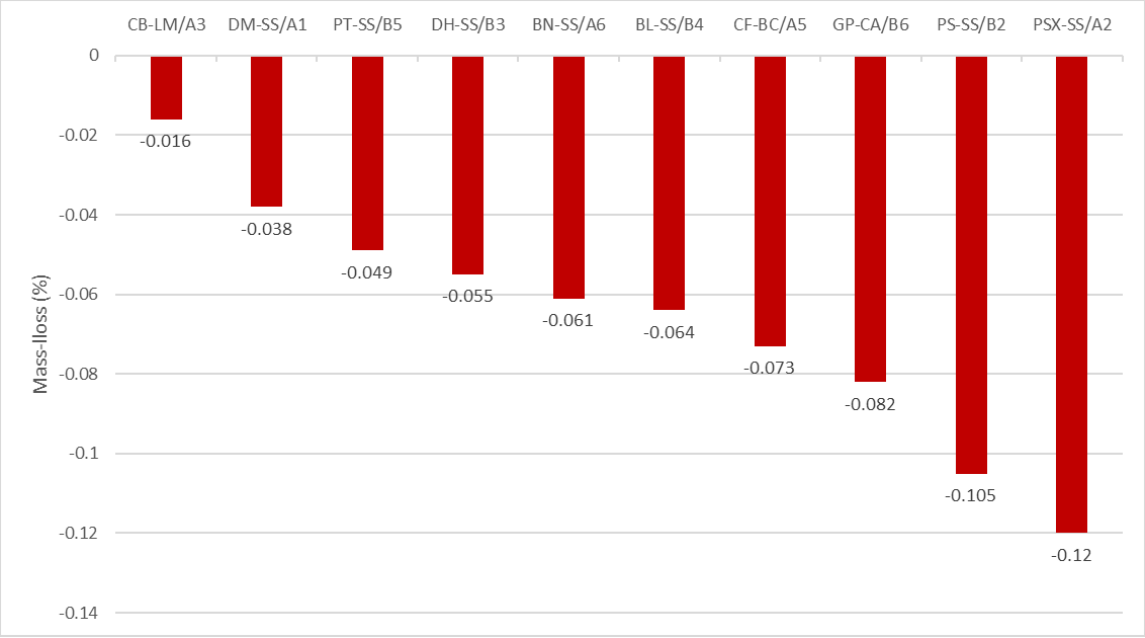

Figure 5-16: mass loss experienced by each sample of the test-set.

1.3 Principal components analysis

Principal component analysis was conducted to further explore the exposure dataset, which comprised the rates of dissolution of the analytes for each sample typology. Figure 5-17 shows the PCA score plot and loading plot obtained from the full dataset, i.e., the dissolution rates obtained from 11 sampling points. Each sample typology was identified by a colour on the first two components. Principal component 1 (PC1) and Principal Component 2 (PC2) displayed a variance of 67.2% and 15.8% respectively.

The PCA score plot showed a wide dispersion on PC1 for some dissolution rates. Outliers coincided with the initial sampling points of some of the samples, such as PSX-SS and DH-SS. Comparison between score plot and loading plot showed that the outliers were caused by exceptionally high rates of dissolution at these sampling points. The sample DH-SS/B3 displayed a remarkably high release of Na, while PSX-SS provided a considerably higher release of Ca and Mg.

The high dissolution rates of these sampling points compared to the rest of the test-set induced the clustering of the rest of the dataset. This happened because the difference in dissolution rate between the outliers and the rest of the dataset was bigger than the respective difference in dissolution rates between the rest of the observations.

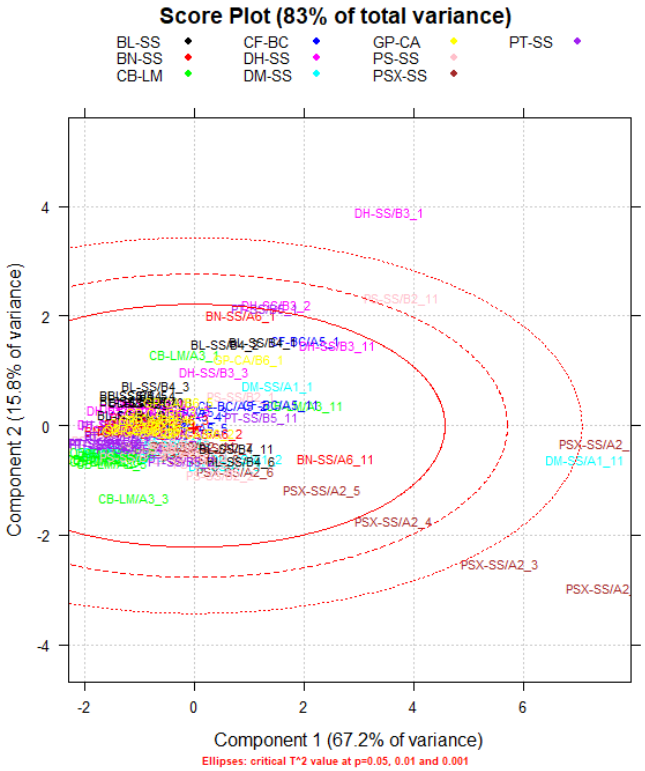

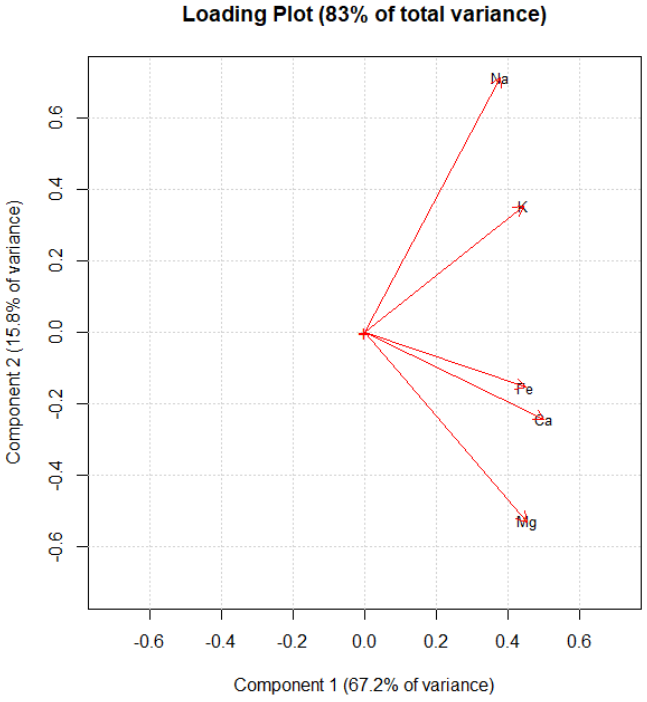

Figure 5-17: score plot (above) and loading plot (below) of the stone typologies leachates concentrations at all sampling points of Ca, Mg, Na, K and Fe at each sampling point.

Dissolution data was filtered to remove the initial sampling points (sampling point 1 to 4), to process dissolution data of sampling point 5 to 11. Further filtration was conducted on the dissolution rates of PSX-SS, to remove sampling point 5 and 6 from the principal component analysis. Iron was removed from the data treatment. Results show a considerable improvement in the visualization and discrimination of the individual scores (figure 5-18).

However, some level of overlapping between the different stone types is still present. The overlapping between scores indicates a comparable performance, given by similar dissolution rates of the four analytes. The level of dispersion for each individual stone type captured the fluctuation of the dissolution rates at each sampling point. For instance, PSX-SS and PS-SS displayed the highest fluctuation of the rate of dissolution, while CB-LM and PT-SS provided an overall high stability.

The first component discriminated the observations mainly based on their release of Ca, while the second component provided discrimination between observations based on Mg, Na and K. For instance, CB-LM and DM-SS displayed high dissolution rates of Mg compared to the rest of the test-set, while BL-SS, DH-SS and CF-BC were characterized by higher dissolution rates of Na and K. Samples PSX-SS and PS-SS were distinguished based on their high dissolution of Ca.

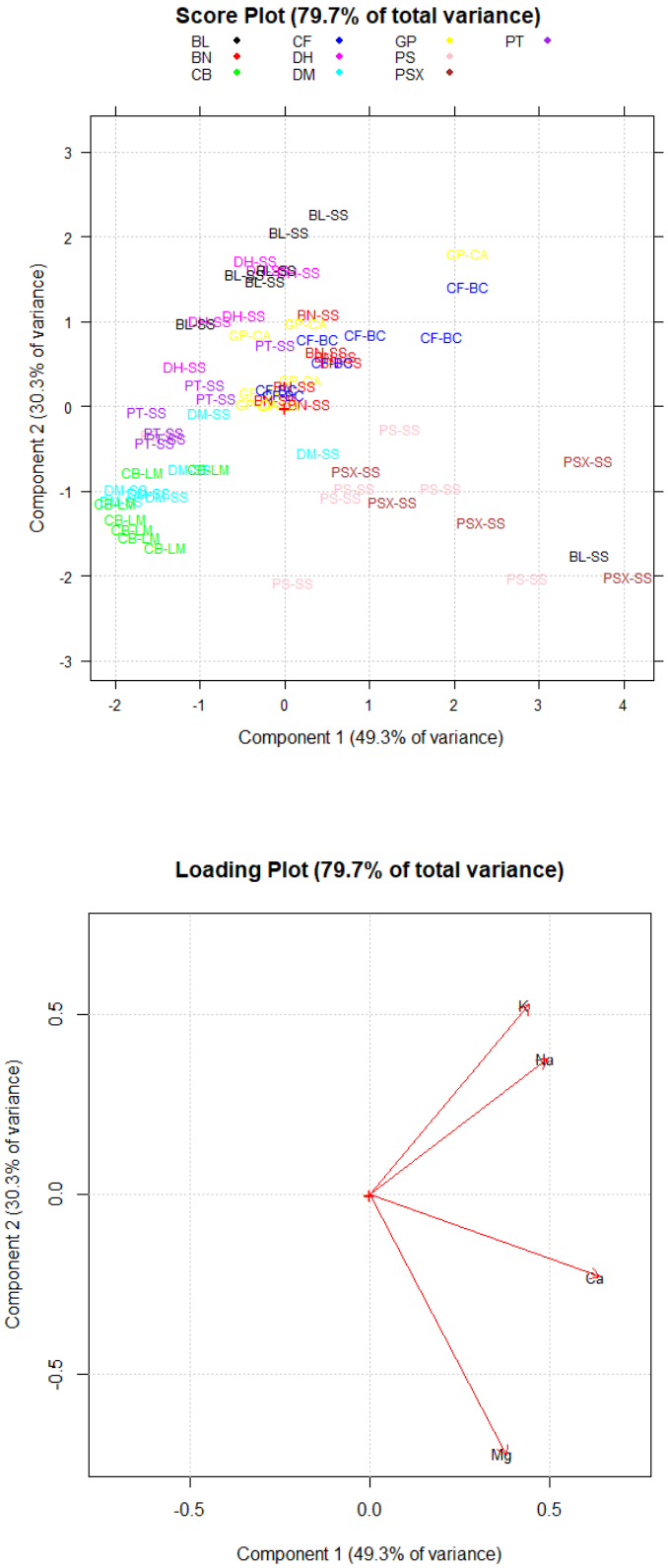

Figure 5-18: score plot (above) and loading plot (below) of the stone typologies leachates concentrations at sampling point 5 to 11 of Ca, Mg, Na, K and Fe at each sampling point.

1.4 Comparison of Ca dissolution trends from variability test and short-term exposure

Calcium dissolution trends of BN-SS, CB-LM and PT-SS from test-set 1 were compared with Ca dissolution trends obtained from the averaged values of the three replicates from the variability test (figure 5-19). The trends showed a high level of repeatability between the dissolution values of the three stone types at each sampling point. This was particularly the case for BN-SS and CB-LM. Bernese sandstone displayed a perfect correspondence between dissolution values at sampling points 4 and 6, while similar values were obtained for sampling point 3 and 4.

Cadeby limestone showed a nearly complete correspondence on sampling point 2, 4, 5 and 6, while a comparable performance was obtained at sampling point 3. Pitairlie sandstone represented the sample with the lowest level of similarity between dissolution trends. However, the distance between dissolution values appeared to decrease at each sampling point. Sampling point 6 displayed the closest proximity between the dissolution rates obtained from test-set 1 and the variability test.

Overall, the dissolution of the three stone types displayed very similar trends. For instance, BN-SS exhibited comparable variations in Ca in both exposures, particularly in the decline between sampling point 3 and 4. An analogous situation was observed in CB-LM, whose dissolution followed a decreasing trend between the sampling points 4 and 6 in both exposure rounds.

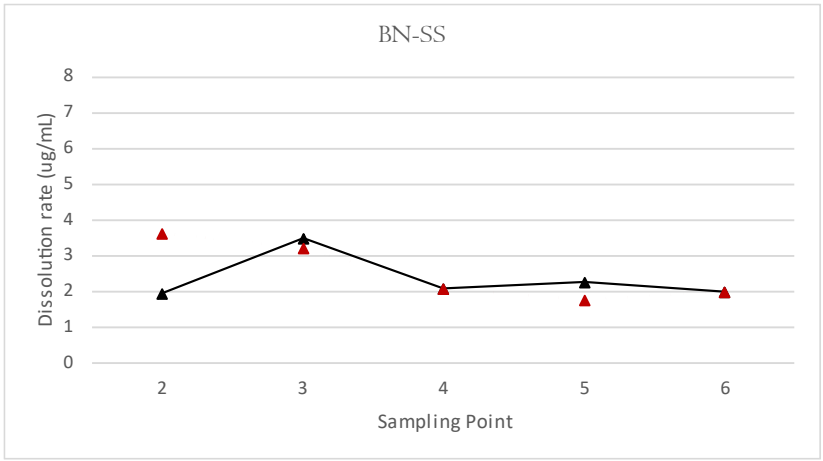

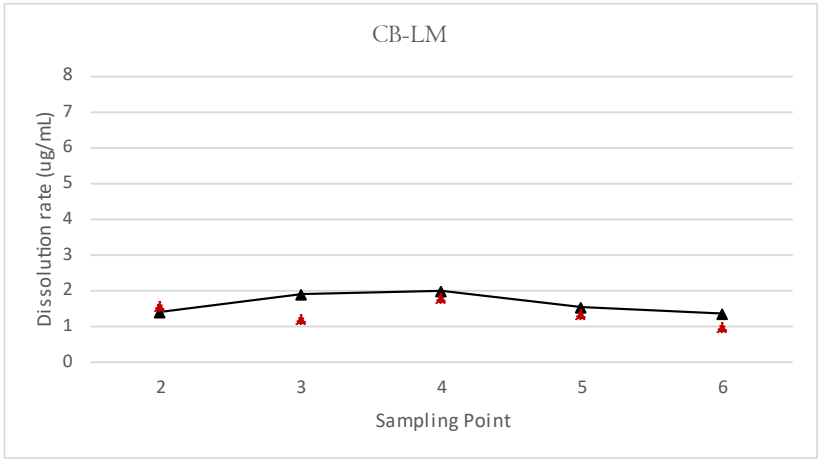

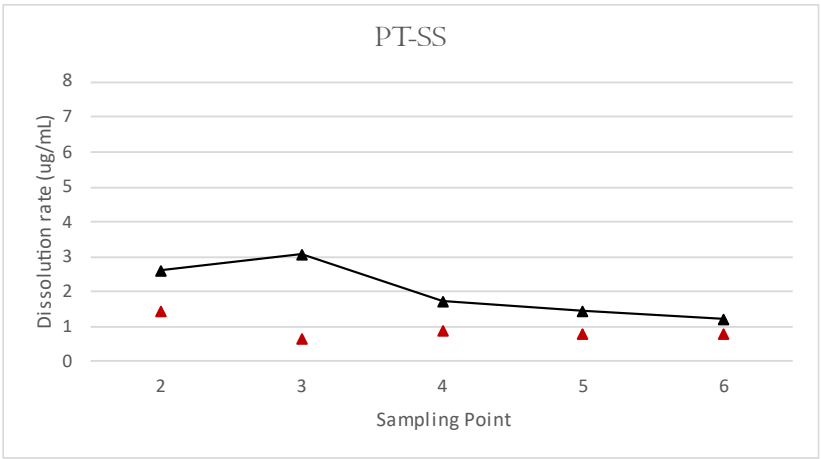

Figure 5-19: dissolution profiles from variability test obtained from the averaged values dissolution values of the three replicates (red), and dissolution profile for the corresponding sampling points of test-set 1 (black).

6. Result of long-term performance test with stable exposure patterns

The test was performed to investigate the dissolution profiles of different stone types over 4 months of accelerated exposure with stable rainfall patterns (RP). Samples were generally collected at weekly intervals, however on some occasions samples were collected after a 10 days exposure. The test procedure and details of the exposure are summarised in chapter 2, section 2.2.3.1.

6.1 Dissolution trends

6.1.1 Calcium and Magnesium

Figures 6-1 to 6-4 show the dissolution trend of each sample obtained by plotting the dissolution rate of Ca and Mg at each sampling point. A in previous chapters, the red dashed line that can be observed at the fourth sampling point (day 22 of the exposure) is aimed at indicating the sampling times that are affected by higher initial dissolution rates caused by the loss of debris from the sample, and that as such are no representative of actual dissolution rates. For this reason, sampling time 1 to 4 are not included in the calculation of the average dissolution rates. The trends of dissolution of the two analytes indicate the predominance of the

dissolution rate of Ca over Mg for most samples. The only exception was represented by DM-SS, which showed a higher dissolution of Mg compared to Ca for 14 sampling points out of 17. Occasionally, the dissolution rate of Ca and Mg displayed comparable values, indicated by the overlapping of markers at sampling points. However, the general trend denoted a consistently higher dissolution rate for Ca compared to Mg. The relatively higher release of Ca, compared to Mg, was likely controlled by the higher solubility of calcite compared to dolomite under comparable conditions. The difference between the performance of the two analytes was mainly expressed in terms of dissolution rates at individual sampling points. Trends for both analytes exhibited an overall good stability across the test set. Most dissolution trends provided an initial higher release of Ca which, comparably to what was observed in test-set 1, appeared to reach stability between the third and fifth sampling point. This general rule was not observed for PSX-SS, which instead showed a substantially higher initial release of Ca combined with an overall unsteady trend up to the 13th sampling point. A similar behaviour to PSX-SS was observed in GP-CA. Compared to Ca, Mg displayed an overall higher stability throughout the exposure. The dissolution rate obtained from the initial sampling points was more similar to the rest of the dissolution trend compared to Ca (figure 6-1 to 6-4). While Ca dissolution reached stability between the third and fifth sampling point, Mg trend became stable after the first sampling point for most samples. Similarly to Ca, an exceptionally high release of Mg was observed for GP-CA and PSX-SS, despite the magnitude of the alteration being significantly lower. The overall trend of both analytes was comparable in both samples, and the same variations in the dissolution rates were observed for the two analytes.

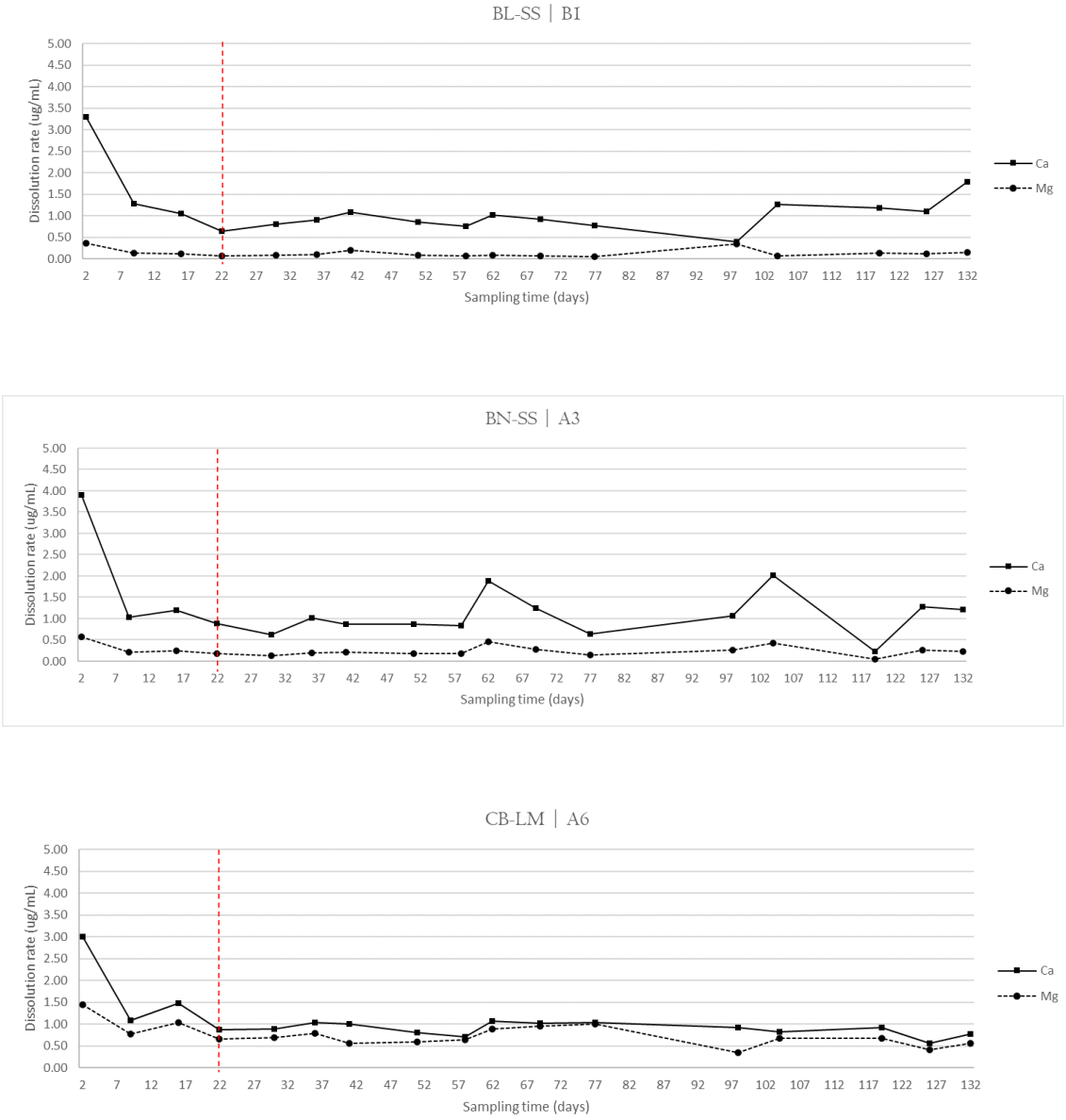

Figure 6-1: Ca and Mg *dissolution trends of BL-SS, BN-SS and CB-LM*

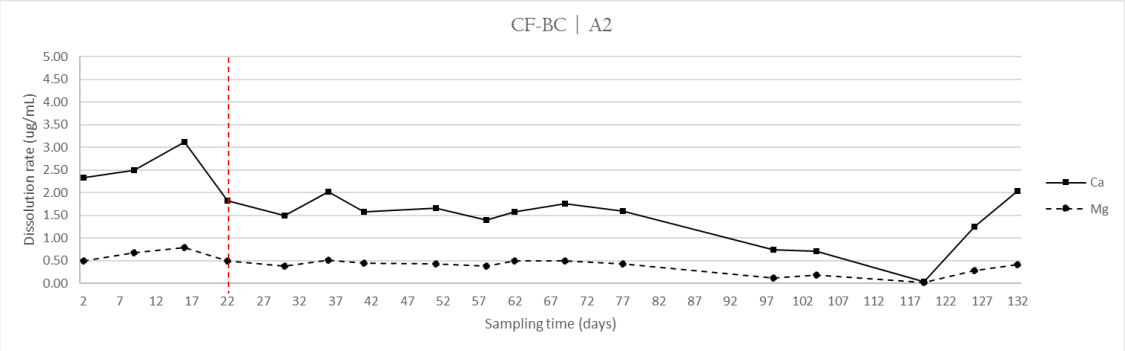

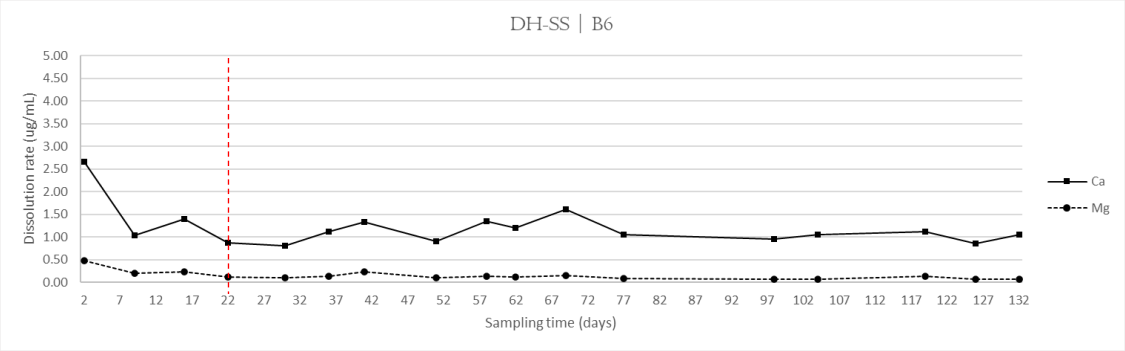

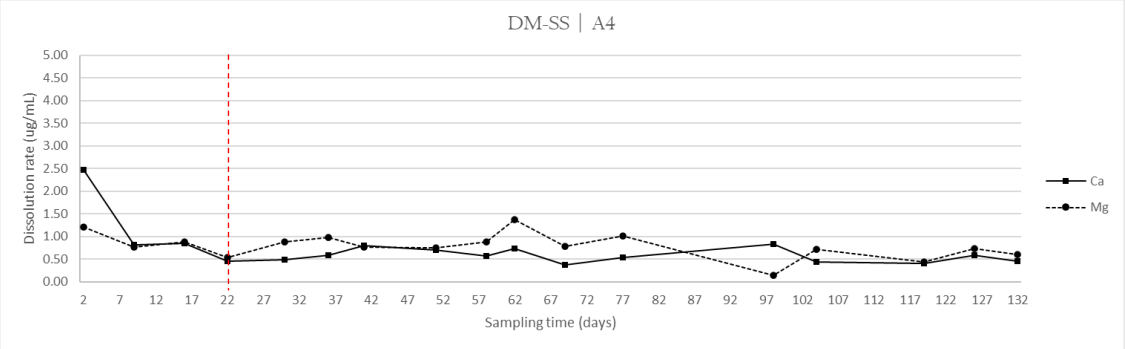

Figure 6-2: Ca and Mg dissolution trends of CF-BC, DH-SS and DM-SS

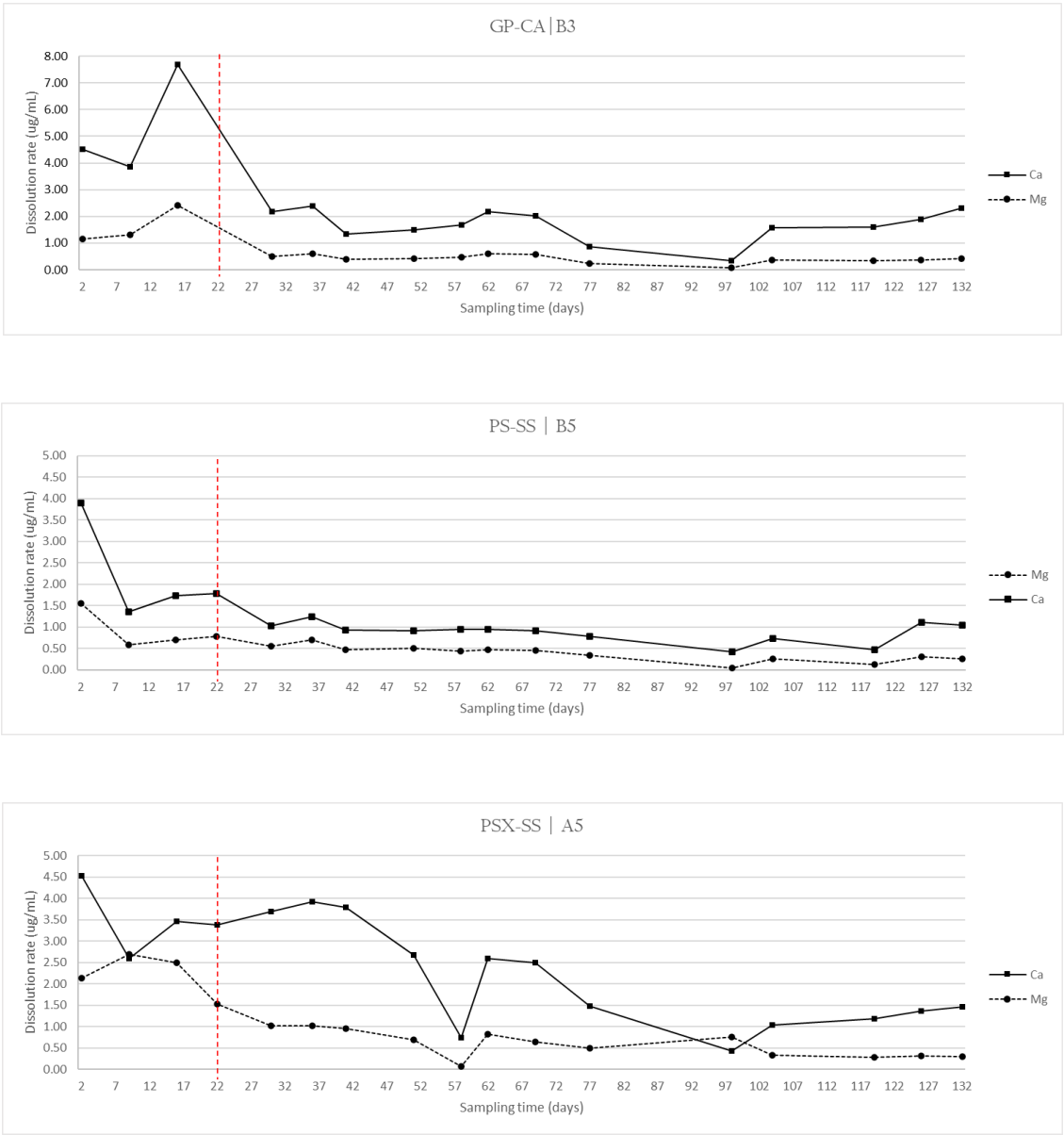

Figure 6-3: Ca and Mg dissolution trends of GP-CA, PS-SS and PSX-SS

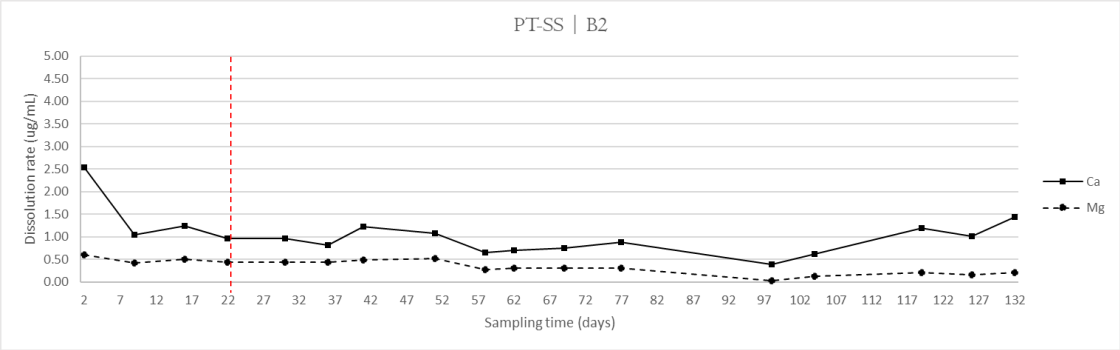

Figure 6-4: Ca and Mg dissolution trend of PT-SS

The variability in dissolution rates of Ca and Mg was investigated by extracting the relative standard deviation (RSD) of the dissolution values at each sampling point across all samples. The RSD was obtained from the fifth sampling point onwards, where most samples reached a stable trend. Results are shown in figures 6-5 and 6-6.

For Ca, the difference between dissolution values at each sampling point for the different samples showed a general decreasing trend, characterized by intervals of variations in the rates of dissolution throughout the exposure. In contrast, for Mg the RSD of dissolution rates at different sampling points across the test-set appeared to be generally constant, despite showing significant alterations throughout the exposure.

The highest difference between Ca dissolution rates was on the fifth sampling point, which provided a relative standard deviation of 75% (figure 6-5). The lowest values were obtained at sampling points 12 (33%) and 16 (34%). Overall, the

progressive decrease in difference between the dissolution rates of Ca was expressed by the average RSD value of the first three sampling points of the stable trend (67%) against the last three sampling points (41%).

A different performance was observed with Mg, which provided relatively higher RDS values compared to Ca, and did not display the same overall decreasing trend between the first sampling point of the stable trend and the last (figure 6-6).

The highest standard deviation between samples was observed in correspondence of the 13th sampling point (95%). The lowest standard deviation values instead were obtained from the third and last sampling points, with an RSD value of 48% and 51% respectively. As mentioned above, Mg did not appear to display a clear trend in the difference between dissolution rates during exposure, which appeared to display remarkable variation.

Comparison of the RSD values obtained from test-set 2 (long-term exposure) with test-set 1 (short-term exposure) highlighted a difference in the magnitude of the dissolution rate variation. This was relatively higher in test-set 1, where the fifth sampling point provided an RSD of 162%, compared to the 75% obtained from test-set 2. The decreasing trend exhibited by Ca was consistent between the two test-sets, with the exception of sampling point 10 and 11. These corresponded to the last two sampling points of test-set 1, and in test-set 2 did not maintain the decreasing tendency shown by the short-term exposure. The same applied to Mg, which presented lower RSD values with test-set 2. However, in contrast to Ca, the similarity in trend between the two exposure rounds was only exhibited for sampling points 5 to 7.

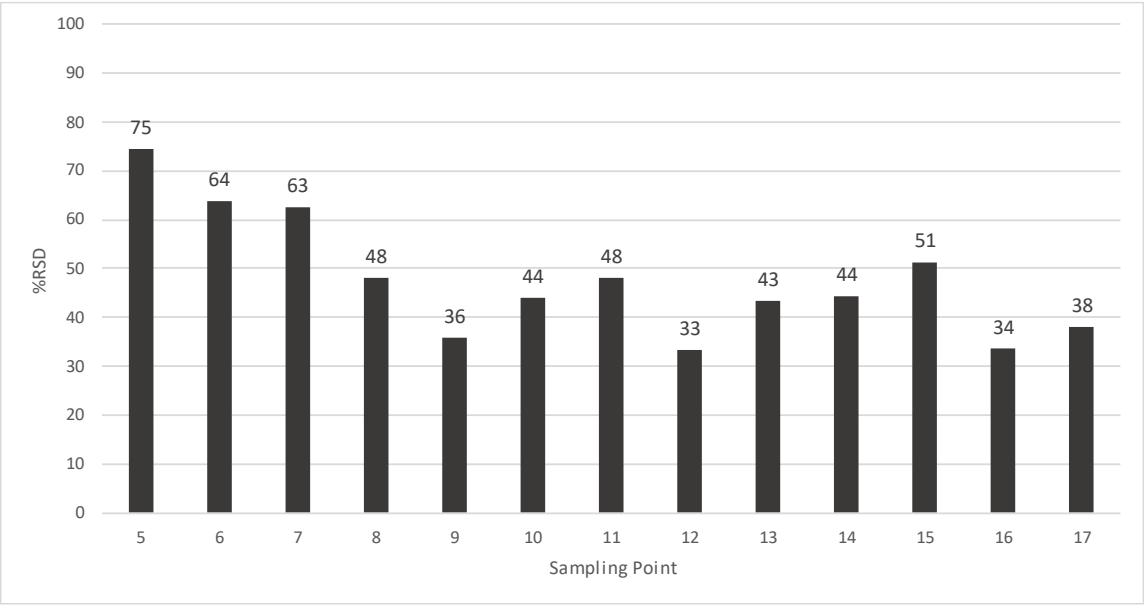

Figure 6-5: relative standard deviation of Ca dissolution values between samples at each sampling point

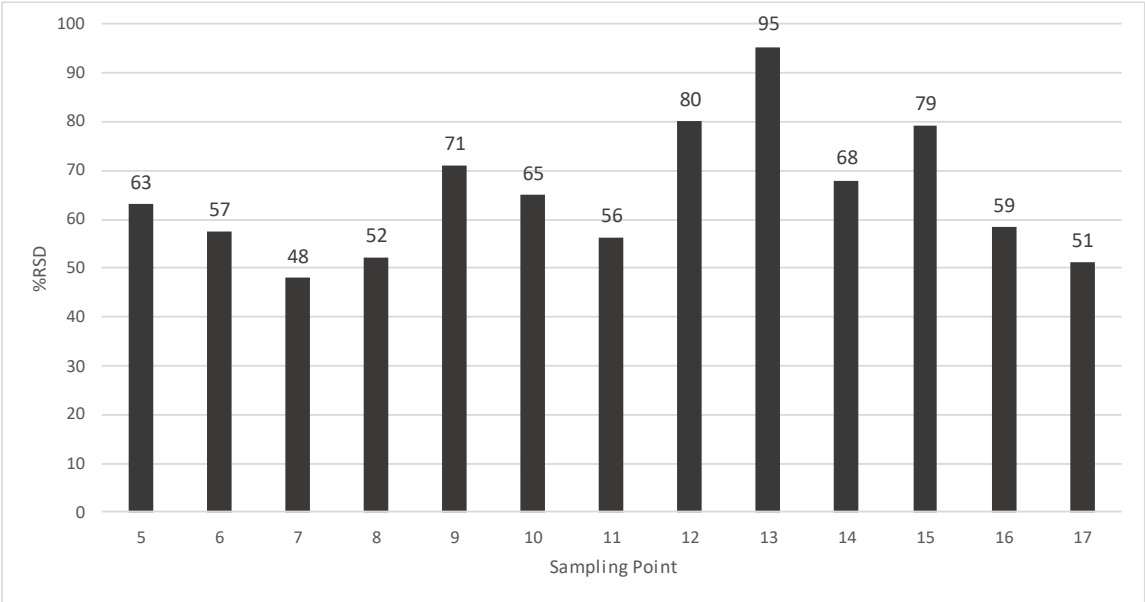

Figure 6-6: relative standard deviation of Mg dissolution values between samples at each sampling point

The RSD values obtained from the long-term exposure indicate that Ca and Mg were not entirely comparable in terms of their overall performance under long-term exposure conditions, which instead was the case for the short-term exposure.

Results suggest that the difference in magnitude of Ca dissolution between samples tends to decrease with time of exposure. The occasional increases in RSD values could have been caused by an external factor, such as the accidental uneven distribution of surrogate rainwater to the samples. The adjustment of the nozzles was required in some cases, where one of more samples were found to receive an excess or deficiency of surrogate rainwater. Such circumstances are likely to have impacted the dissolution rates, reflecting over the regular increase/decrease intervals of RSD values during the exposure period. In such a case, the adjustment of the nozzles to equalize the surrogate rainwater distribution would have happened where Ca RSD were lower, i.e., at sampling point 9, 12 and 16. This did not reflect on Mg, although from past exposure rounds Mg appeared to be less influenced by small variations in water release.

Another factor to consider is the influence of samples that displayed a performance not consistent with the one displayed by the rest of the test-set, as PSX-SS and GP-CA. When removing both samples from the computation of the RSD, the overall trend remains unaltered, but the RSD significantly decreases, from a minimum of 11% to a maximum of 54%.

6.1.2 Potassium and Sodium

Potassium and Na were plotted separately to Ca and Mg, due to the different scale of the dissolution rates of both analytes. Figure 6-7 shows the exceptionally high dissolution value of K at the second sampling point. The same behaviour was observed in all samples of the test-set. The sampling point was removed from the data treatment to allow a proper resolution by adopting a suitable scale for the axis plotting the dissolution rate.

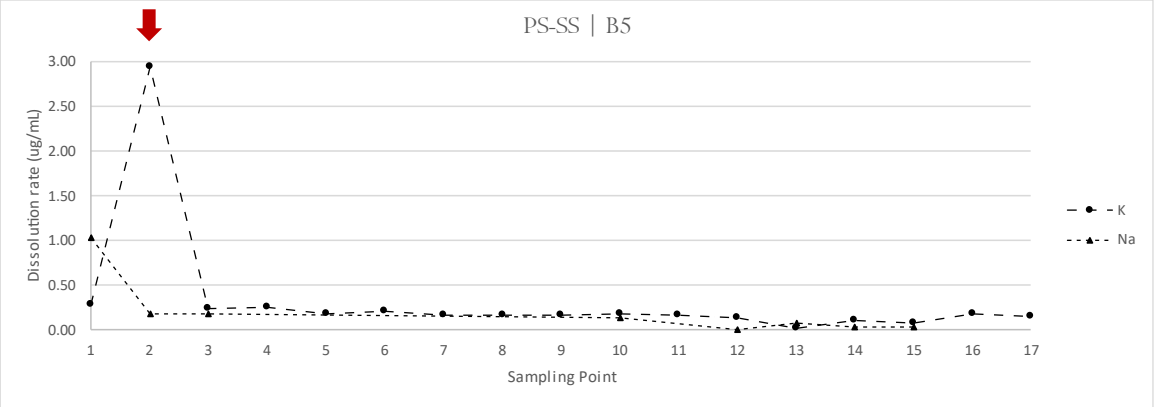

Figure 6-7: dissolution profiles of K and Na showing the high value of K dissolution at sampling point 2.

The same was done for the first sampling point of Na, which exhibited an exceptionally high dissolution rate in most samples of the test-set. The scale adopted for the dissolution rate axis was 0.50 µg/mL. Results are shown in figures 6-8 to 6-11.

Overall, K dissolution displayed a more stable pattern compared to Na. Similarly to Ca and Mg, the initial sampling points displayed a higher dissolution rate of K, reaching stability at different points of the exposure round. In contrast, Na showed a much more variable dissolution across the different sampling points. The divergence in dissolution values of K and Na was higher during the initial stage of the exposure and became progressively more comparable with time. The most significant difference between the two analytes was observed for BN-SS and CB-LM. Although on different scales, the performance of the two samples was similar. In both cases, Na showed a considerably high rate of dissolution, before approaching the dissolution value of K at the 11^{th} (CB-LM) and 13^{th} (BN-SS) sampling point.

In most samples, Na dissolution was predominant, although variations produced an occasional alternation between the respective dissolution rates of the two analytes. The only exception to the predominance of Na dissolution over K was represented by PS-SS, whose dissolution rate of Na was subordinate to the dissolution rate of Na for most of the exposure.

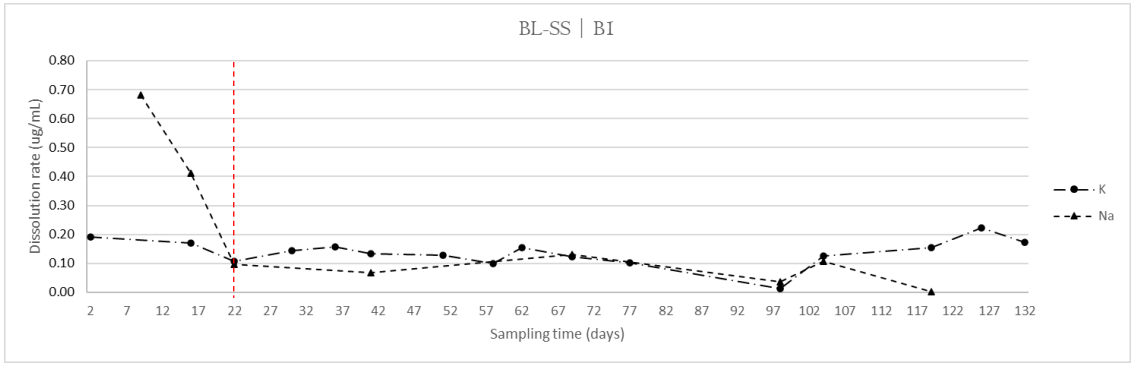

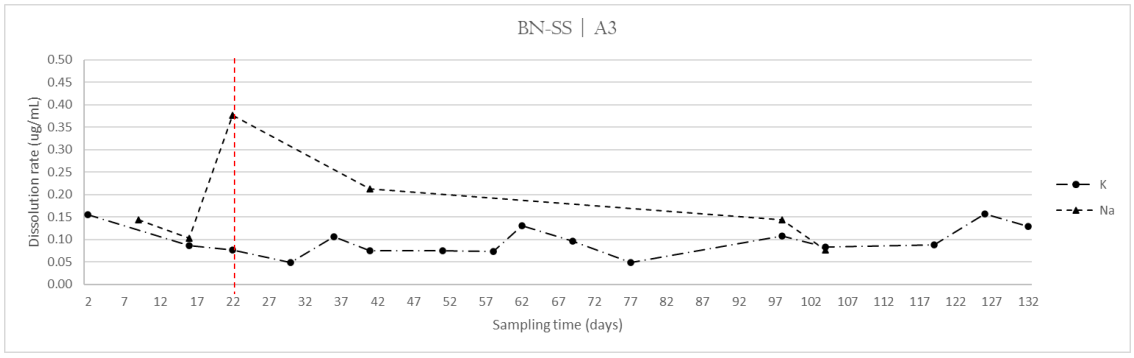

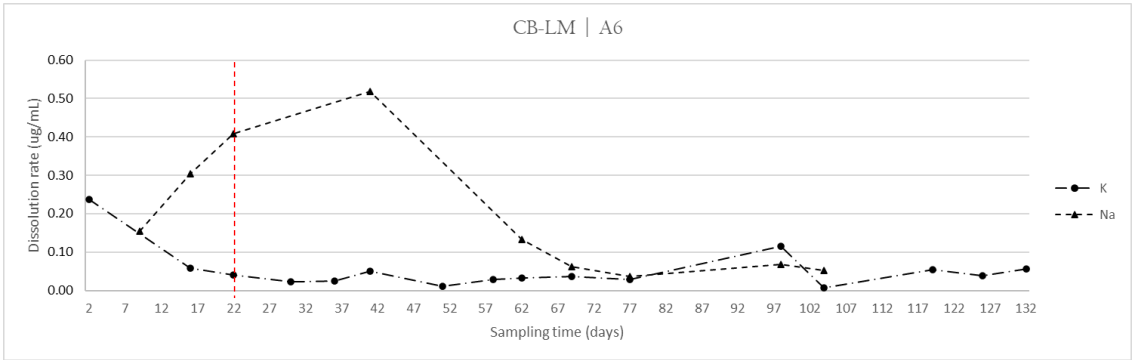

Figure 6-8: dissolution profiles of K and Na showing the high value of K dissolution at sampling point 2.

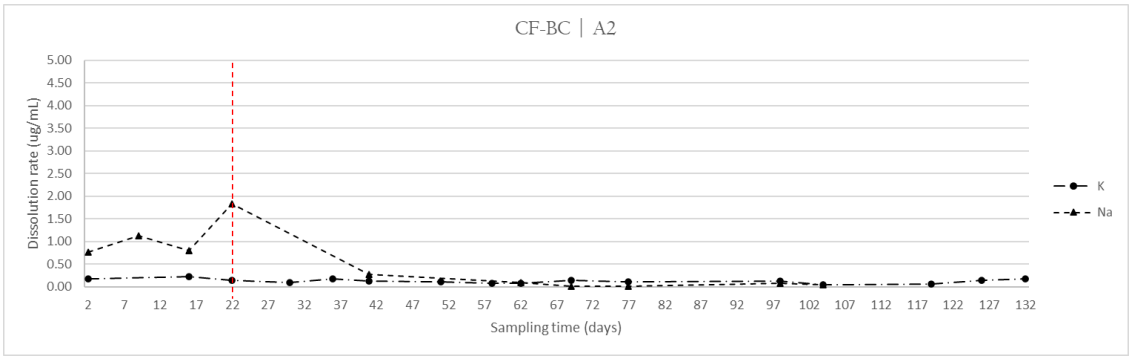

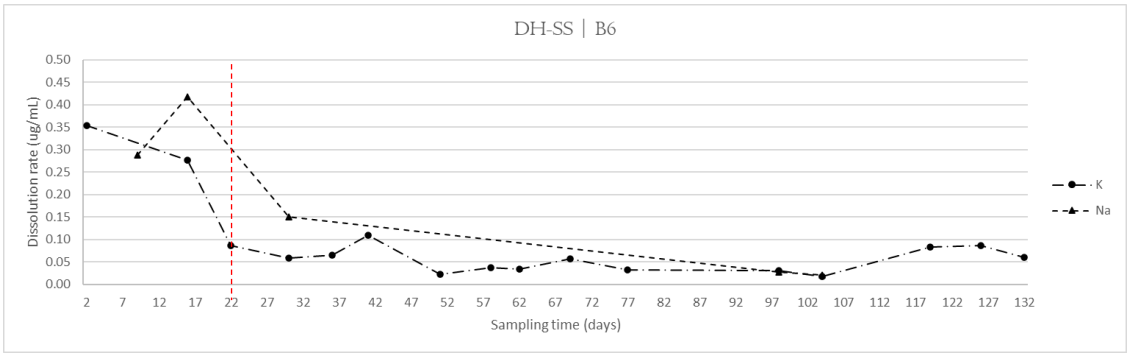

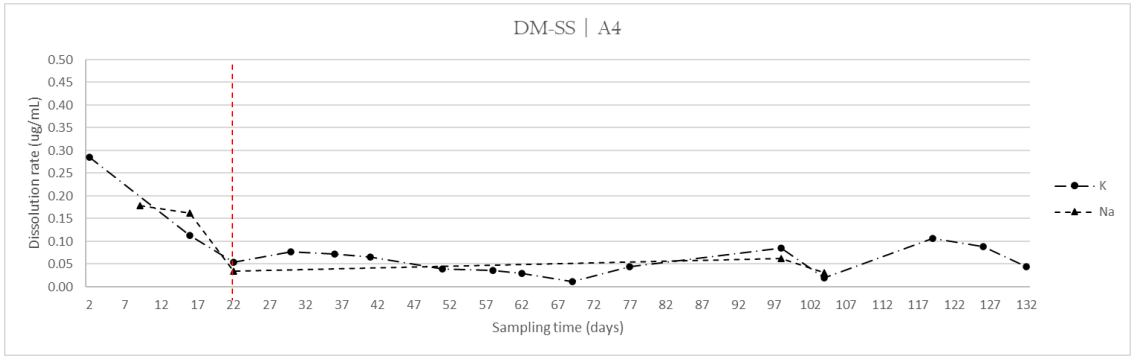

Figure 6-9: dissolution profiles of K and Na showing the high value of K dissolution at sampling point 2.

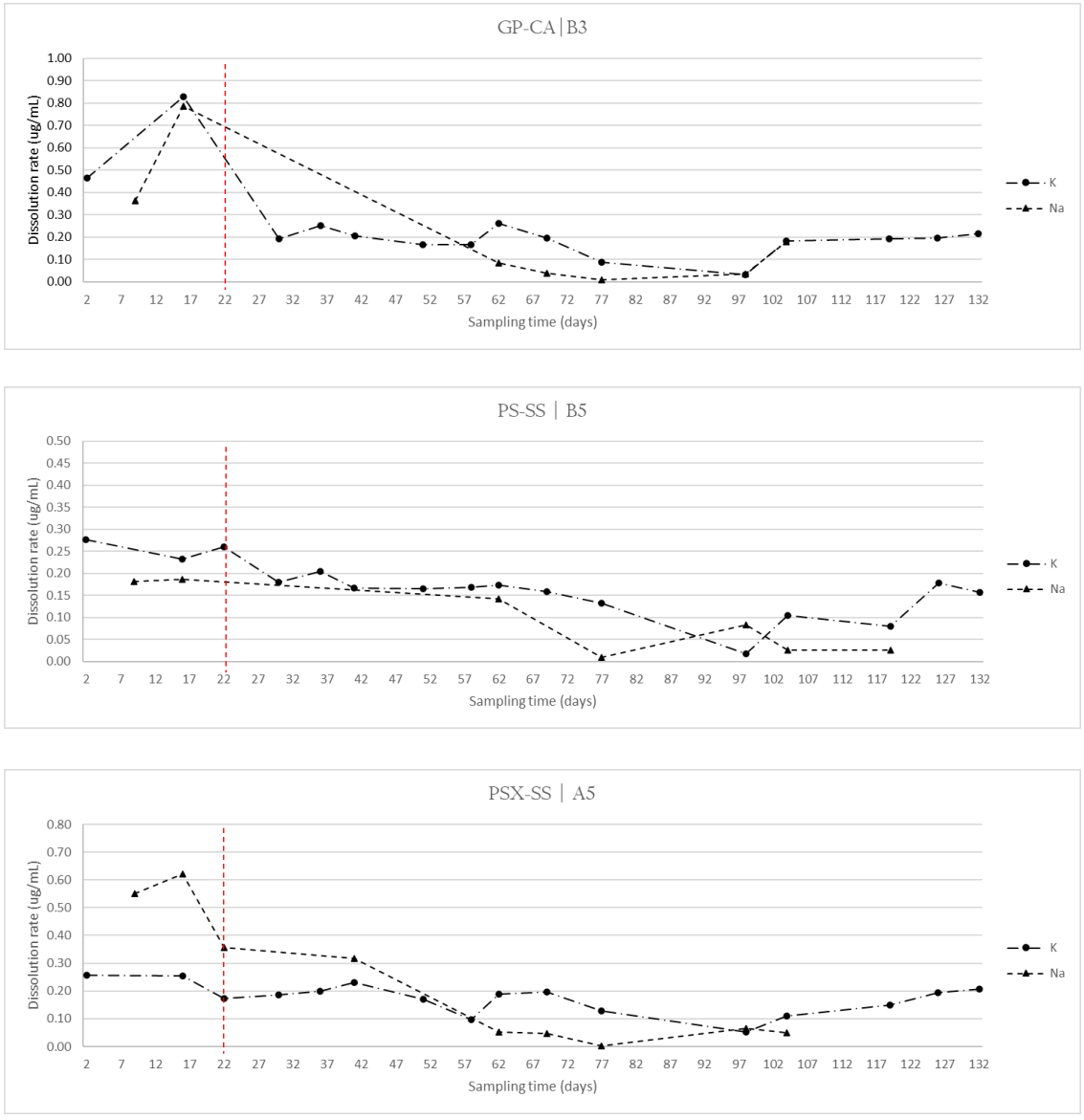

Figure 6-10: K and Na dissolution trend of GP-CA, PS-SS and PSX-SS.

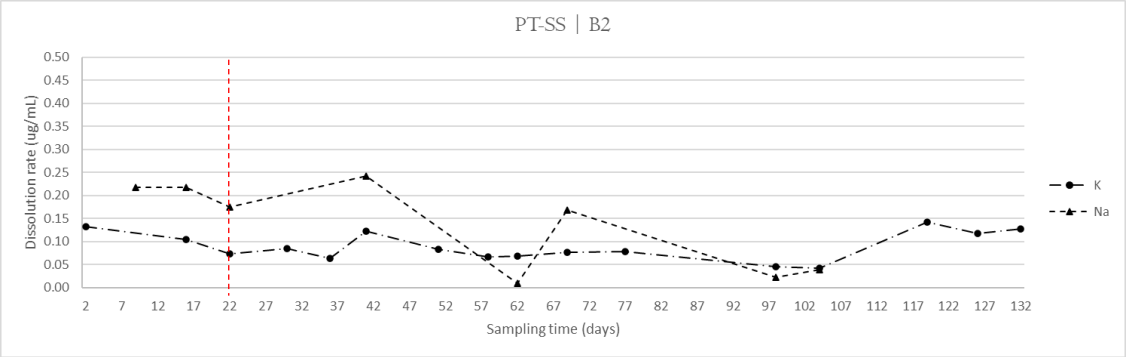

Figure 6-11: K and Na dissolution trend of PT-SS.

6.2 Mean dissolution rates

Mean dissolution rates were obtained for the stable dissolution trend of each stone type, i.e., from sampling point 5 onwards. This was done to avoid the bias caused by unstable and exceptionally high dissolution rates that most samples displayed at the initial sampling points.

6.2.1 Calcium and Magnesium

Mean dissolution values for Ca are shown in figure 6-12. Average dissolution rates were obtained by taking into account only the dissolution data obtained from the fifth sampling point onwards. Samples from test-set 2 displayed different mean dissolution values for Ca ranging from 0.58 µg/mL (DM-SS) to 2.07 µg/mL (PSX-SS), which were provided by DM-SS and PSX-SS respectively. The dissolution

rates displayed moderate differences between different samples, with most stone types fitting withing a range of 0.89 µg/mL to 1.11 µg/mL.

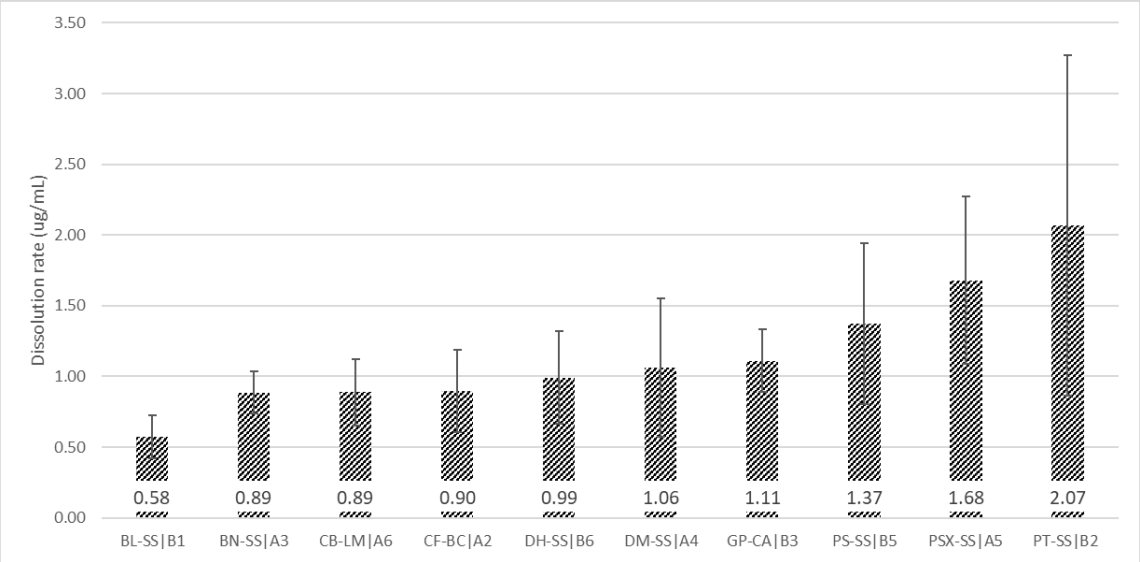

Figure 6-12: mean Ca dissolution of test-set 2 samples.

The performance of PSX-SS in terms of mean dissolution was found to be more compatible with that of other samples, compared to the performance of the same stone type from the short-term exposure. The sample with the second highest dissolution rate was GP-CA, with an overall dissolution value for Ca of 1.68 µg/mL. Some of the samples presented a similar performance. The specimens PS-SS and CB-LM displayed comparable dissolution velocities (0.89 µg/mL). Likewise, DH-SS and BN-SS also revealed similar dissolution rates, corresponding to 1.11 µg/mL and 1.06 µg/mL.

Mean values of Ca dissolution indicate that the samples performance was not necessarily correlated to their composition. For instance, PSX-SS and PS-SS presented equivalent concentration of carbonate minerals. However, both samples displayed a markedly different performance, with dissolution values of

0.89 µg/mL and 2.07 ug/mL. The high Ca dissolution displayed by GP-CA and CF-BC was expected on their basis of their nature as calcarenites, with dissolution values of 1.68 µg/mL and 1.37 µg/mL respectively. However, the same was not observed for the limestone CB-LM, whose dissolution was among the lowest in the test-set, despite the content in calcium carbonate of about 54%. In contrast, PSX-SS displayed the highest dissolution rate of the test-set, despite the lower concentration of carbonate minerals compared to other samples (about 15%). Mean dissolution values were obtained for Mg (figure 6-13). These were found to be consistently lower across the test-set compared to Ca, except for DM-SS, which presented a higher dissolution rate for Mg (0.77 µg/mL) compared to Ca (0.51 µg/mL). These results are likely related to the higher stability of dolomite compared to calcite. The mean dissolution rate of Mg was within the range of 0.11 µg/mL and 0.77 µg/mL. The lowest dissolution rate for Mg was displayed by DM-SS, while the highest value was provided by DM-SS.

In contrast to the performance obtained from Ca dissolution, CB-LM presented the second highest dissolution value for Mg (0.68 µg/mL). However, the concentration of dolomite in the sample (about 45%), was considerably higher than that of DM-SS, which presented the overall highest dissolution rate for Mg.

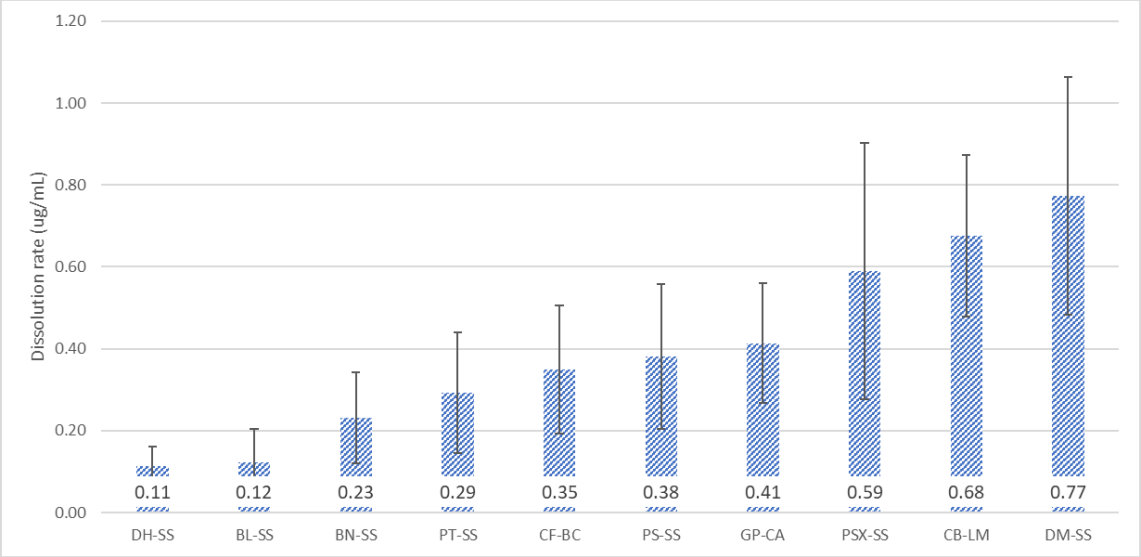

Figure 6-13: mean Mg dissolution of test-set 2 samples

6.2.2 Potassium and Sodium

The mean dissolution values of K and Na are presented in figures 6-14 and 6-15. Samples exhibited different values of Na and Ca dissolution. Overall, Na and K displayed comparable dissolution rates across the test-set. Sodium presented dissolution values within the range of 0.05 µg/mL (DM-SS) and 0.15 µg/mL (CB-LM) (figure 14). Potassium displayed a slightly larger range, with dissolution rates ranging between 0.04 µg/mL (CB-LM) and 0.18 µg/mL (GP-CA).

In general, the dissolution rates of K provided different values across the test-set, with the exception of PT-SS and BN-SS, both with average dissolution values of 0.09 µg/mL. Instead, more comparable rates among samples were obtained for Na, which provided the same rate of dissolution for DG-SS, BL-SS and GP-CA (0.07 µg/mL).

The dissolution of K and Na mainly stems from the presence of feldspars. However, the current samples characterization did not allow for a proper evaluation of the factors involved.

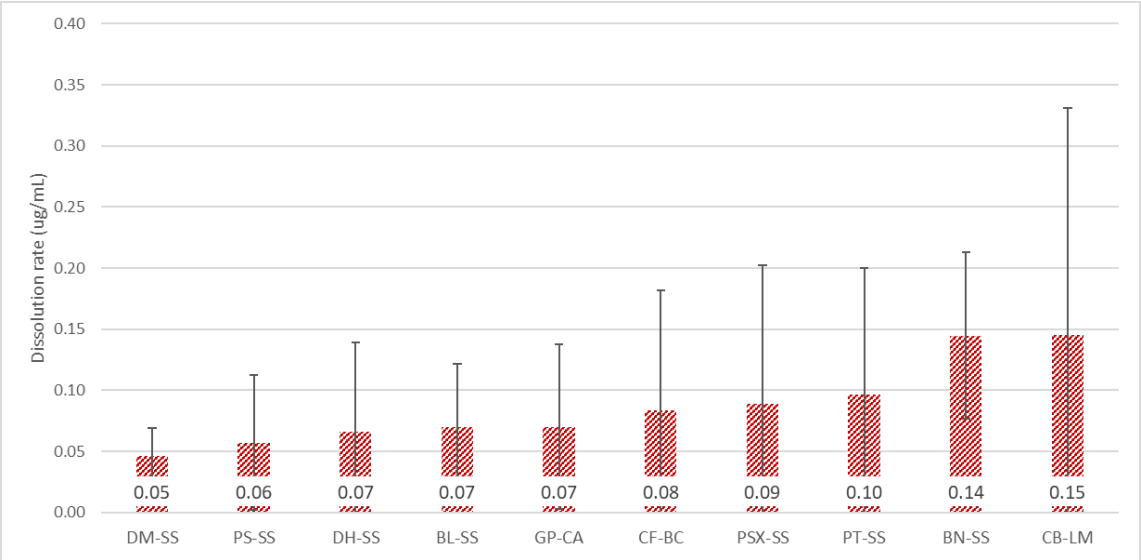

Figure 6-14: mean Na dissolution of test-set 2 samples

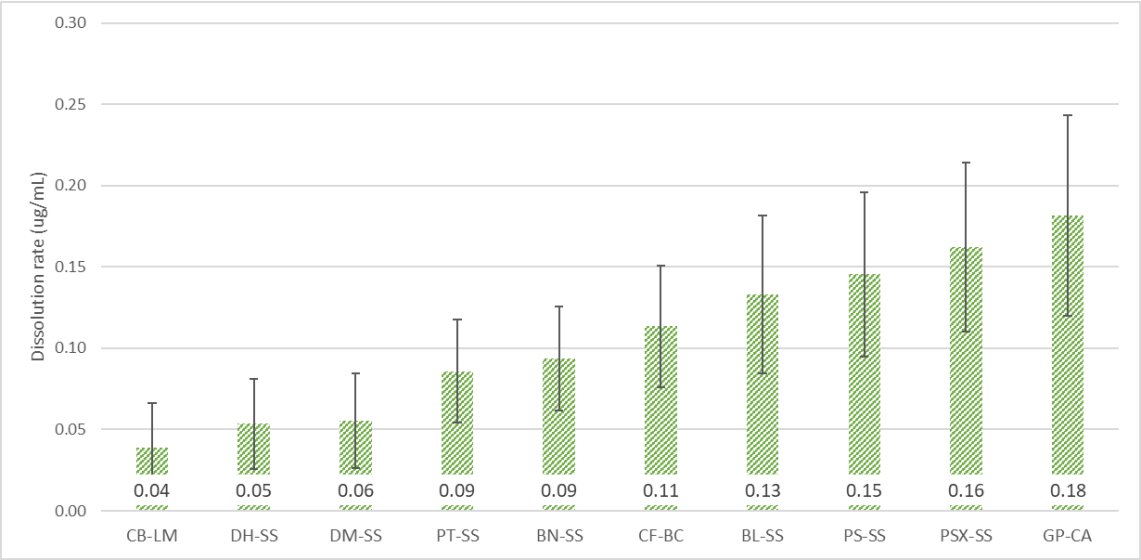

Figure 6-15: mean K dissolution of test-set 2 samples

6.2.3 Iron

The average dissolution values of Fe are displayed in figure 6-16. The dissolution of Fe was significantly low across the full test-set. The dissolution rate of the samples fitted within a narrow range of 0.04 and 0.06 µg/mL (CB-LM, CF-BC, GP-CA and PS-SS) and 0.06 µg/mL (PSX-SS). The difference in the dissolution values between different samples is small and prevents the possibility of conducting a proper evaluation of the samples behaviour based on the analyte performance.

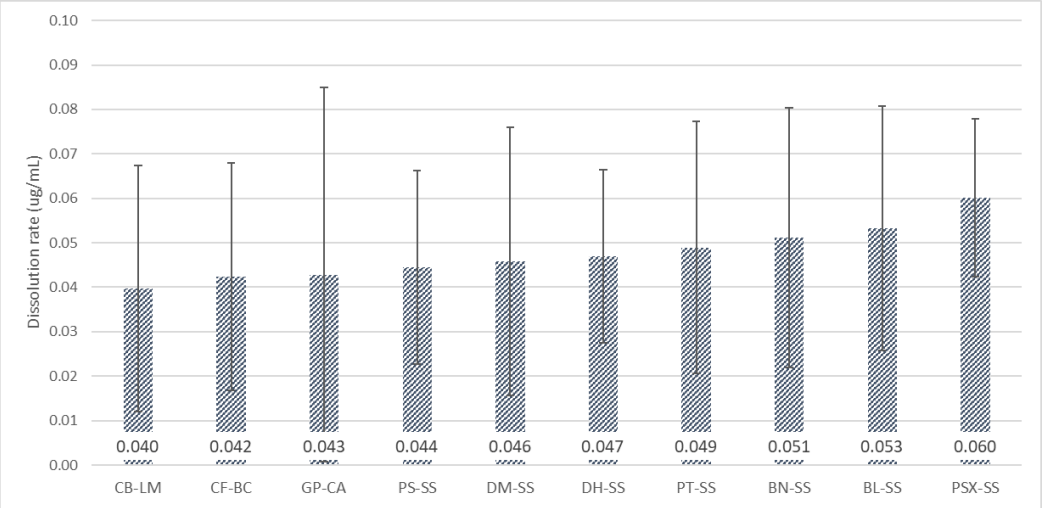

Figure 6-16: mean Fe dissolution of test-set 2 samples

6.2.4 Overall dissolution

It was not observed a consistency in the rate of dissolution between the different stone types in response to the action of surrogate rainwater. For instance, DM-SS

displayed the lowest values of Ca and Na, but presented relatively high dissolution rates for Mg. This is indicative of the role played by composition in the determination of the dissolution rates of individual analytes. At the same time, some samples appeared to be more vulnerable to exposure, regardless of the sample mineral composition. For instance, the sample PSX-SS presented some of the highest dissolution values for most analytes, despite presenting a lower concentration of carbonate minerals compared to the rest of the test-set. Instead, CB-LM displayed high dissolution rates for Mg and Na, but low dissolution rate for Ca and K. Results suggest that composition was not the only factor affecting samples rates of dissolution. This was particularly relevant for Ca, whose dissolution in some cases was higher for samples that presented a lower concentration of carbonate minerals. These observations were found to be consistent with the finding of previous exposure rounds.

6.3 Weight Change

Most samples of test-set 2 experienced different levels of mass-loss (table 6-1). Sample DH-SS provided the lowest mass-loss value, corresponding to a weight variation of 0.035%. The highest mass-loss value instead was reached by PSX-SS, which exhibited a weight variation of 0.223%. However, two samples increased in weight, i.e., BN-SS and PT-SS (figure 6-17).

The mass that was gained by these samples could be related to the formation of salts within the stone pore system, which might not have been completely dissolved during the washing stage. The longer timeframe of exposure could have

resulted in a higher amount of salts accumulating in the stone pore system. However, the post-exposure washing of the samples was kept consistent to the procedure applied for test-set 1, consisting in an equivalent duration of the procedure. The efficiency of the washing might have been affected by the longer duration of test-set 2 exposure, causing the retention of salts in the stone.

Consequently, it is possible that all the recoded weight measurements of test-set 2 were affected by the same bias, impacting the possibility of conducting a proper examination of the samples mass-loss.

Table 6-1: Mass loss values of test-set 2 after exposure

Sample	Pre-exposure weight (g)	Post-exposure weight (g)	Mass loss (g)	Mass Loss (%)
BL-SS/B4	90.284	90.240	- 0.044	- 0.048
BN-SS/A6	64.900	64.905	+ 0.005	+ 0.007
CB-LM/A3	62.474	62.448	- 0.026	- 0.041
CF-BC/A5	57.864	57.843	- 0.021	- 0.036
DH-SS/B3	70.553	70.528	- 0.025	- 0.035
DM-SS/A1	60.210	60.150	- 0.060	- 0.099
GP-CA/B6	52.632	52.586	- 0.046	- 0.087
PS-SS/B2	57.532	57.476	- 0.056	- 0.097
PSX-SS/A2	65.834	65.687	- 0.147	- 0.223
PT-SS/B5	69.929	69.932	+ 0.003	+ 0.004

Figure 6-17: mass loss experienced by the stone types of test-set 2.

6.4 Comparison of Calcium and Magnesium mean dissolution from long and short-term exposure

Test-set 2 (long-term exposure) and test-set 1 (short-term exposure) showed similar results. The average dissolution rates of test-set 2 were generally higher than the ones obtained from the short-term exposure.

A notable exception was represented by PSX-SS, which provided a mean dissolution value of 4.25 µg/mL in test-set 1 and 2.07 µg/mL in test-set 2. This was likely the result of the longer timeframe of exposure, which allowed the sample to reach stability.

In other cases the samples average dissolution presented a high level of similarity, such as for BL-SS, whose dissolution values corresponded to 0.99 µg/mL in test-

set 1 and 0.94 µg/mL in test-set 2. Correspondence between the dissolution rates obtained from the two test-sets was also displayed by CF-BC, whose dissolution rates were 1.47 µg/mL in test-set 1 and 1.37 µg/mL in test-set 2. In contrast, half of test-set 2 showed approximately double the dissolution rate exhibited by test-set 1. This could be caused by an overall higher dissolution rate throughout the exposure period, possibly influenced by factors such as the room temperature, or by a slight increase in dissolution rate during the long-term exposure.

In both test-sets DM-SS and PSX-SS represented the samples with the lowest and highest dissolution rate for Ca. However, DM-SS displayed a difference between Ca dissolution rate of test-set 1 and test-set 2 of 87% (table 6-2). In test-set 2, PSX-SS showed a 105% decrease in mean dissolution compared to test-set 1.

Table 6-2: percentage variation in dissolution rate of test-set 1 and test-set 2.

Sample	% Difference (Ca)	% Difference (Mg)
BL-SS	+ 5	-111
BN-SS	- 15	-39
CB-LM	+47	+32
CF-BC	-7	+5
DH-SS	+47	-23
DM-SS	+87	+26
GP-CA	+34	+20
PS-SS	-67	-106
PSX-SS	-105	-89
PT-SS	+56	+4

The comparison between Ca and Mg for the two test-sets indicate that the samples followed a comparable performance. Except for BL-SS, CF-BC, DH-SS, the negative or positive change in Ca from test-set 1 to test-set 2 was reflected in the performance of Mg.

7. Results of long-term performance test with variable exposure patterns

The test was performed to investigate the dissolution profiles of different stone types over 4 months of accelerated exposure with variable rainfall patterns (RP). The test procedure and details of the exposure are summarised in chapter 2, section 2.2.3.2.

7.1 Dissolution Trends

The dissolution profiles displayed the release of analytes at each sampling point. A colour was assigned to each RP pattern adopted during the exposure round. Colours indicate the exposure conditions for any section of the dissolution trend where certain conditions were tested. Each sampling point represents about one week of exposure, however in some cases they involved a longer interval of 10 days.

7.1.1 Calcium and Magnesium

The dissolution profiles of Ca and Mg are shown in figures 7-1 to 7-4.

7.1.1.1 Rainfall Pattern 1

Rainfall pattern 1 is represented by a total of 4 sampling points, highlighted in blue in the dissolution trend. Under RP1, both Ca and Mg dissolution followed a declining trend. The scale of the decrease in dissolution rate was found to vary depending on the analyte and stone type. For instance, the decrease in Ca dissolution rate was more pronounced in BN-SS and CF-BC, as opposed to the more stable performance displayed by PT-SS. Compatibly to previous exposure rounds, this tendency was significantly less prominent for Mg. The samples where a decline in dissolution rate was most noticeable were CB-LM and PSX-SS. For the remaining samples, the dissolution trend observed by the four initial sampling points was mostly horizontal.

The initial divergence between the dissolution rates of Ca and Mg is higher at the start of the exposure to RP1. The difference between the two analytes was found to progressively reduce throughout exposure. The decline in dissolution rate that occurred under the present rainfall regime was compatible with the performance observed in previous exposures. Therefore, the results obtained under RP1 are intrinsically affected by the initial higher dissolution rate of the analytes that occurs regardless of the exposure conditions.

7.1.1.2 Rainfall Pattern 2

Rainfall pattern 2 is represented by a total of 4 sampling points, highlighted in red in the dissolution trend. The dissolution trend under RP2 conditions showed the stabilization of the dissolution rate. This happens in proximity to the first sampling point of RP2 (sampling point 5). All stone types displayed lower Ca dissolution rates under RP2 compared to RP1. The only prominent exception is represented by sampling point 6 of DM-SS, which displayed a peak in the dissolution of Ca. In contrast, the dissolution of Mg exhibited an overall better continuity with RP1.

For most samples, the dissolution of Ca was relatively stable. Except for some occasional variations, visible at sampling point 6 and 7 of some stone types, the trend was predominantly flat. Only PSX-SS displayed an alteration of the dissolution, exhibited as an increase in rate after the sixth sampling point. The dissolution of Mg was also relatively stable throughout the exposure, and maintained a steady separation from the dissolution profile of Ca. The predominance of the dissolution rate of Ca over Mg was maintained. This was more pronounced for some stone types, such as BN-SS and CF-BC, while for other samples the difference in dissolution rate between the two analytes displayed a higher level of similarity, as in the case of DM-SS.

7.1.1.3 Rainfall Pattern 3

Rainfall pattern 3 is represented by 1 sampling point, highlighted in green in the dissolution trend. The third rainfall pattern showed an increase in the dissolution

rate of all samples. Under these exposure conditions, all samples displayed an increase in the dissolution rate of Ca. The steepness of the curve varied across the test-set. Some samples exhibited a lower level of susceptibility to the new exposure conditions, others instead showed a significant variation. For instance, PSX-SS revealed a considerable increase in dissolution at the variation of exposure conditions from RP2 to RP3.

In contrast, Mg dissolution maintained a continuity with RP2, and did not display any significant variations with the change in exposure regime. Consequently, the profiles of the two analytes, which displayed comparable performances under RP2, split under RP3 and the divergence between them increased.

7.1.1.4 Rainfall Pattern 4

Rainfall pattern 4 is represented by 1 sampling point, highlighted in yellow in the dissolution trend. Most samples displayed a further increase in the dissolution rate of Ca under rainfall pattern 4. Only BN-SS and PSX-SS displayed the opposite trend, with a decrease in Ca dissolution compared to the previous exposure regime. In most cases, the increase under RP4 showed a good continuity with the previous section of the trend. In a few cases, the increase presented a sharp change, as in the case of CF-BC and PS-SS.

The dissolution profile obtained for Mg either maintained a stable trend, without displaying any significant variation compared to the previous exposure regime or followed a similar trend to Ca on a significantly smaller scale. For some samples, such as DH-SS and PT-SS, the variation in dissolution rate compared to the

previous sampling point is unnoticeable. The samples with the more distinct change in rate of Mg dissolution were CB-LM, DM-SS, GP-CA and PS-SS.

7.1.1.5 Rainfall Pattern 5

Rainfall pattern 5 is represented by 1 sampling point, highlighted in light blue in the dissolution trend. Under RP5, most samples displayed a higher dissolution rate compared to RP4. For the majority of the stone types, RP5 represented the simulated rainfall regime that induced the highest Ca dissolution when compared to RP2 to RP4 conditions. A decrease in rate of Ca dissolution was only displayed by BL-SS, DM-SS and PT-SS. In BL-SS, the declining trend of Ca dissolution displayed under RP4 continued with RP5. For the two remaining samples, RP5 represented the first regime to induce a lowering of Ca dissolution rate. Comparably to RP5, the performance displayed by Mg was found to replicate that of Ca on a smaller scale. Changes in rate were less noticeable than the ones displayed by Ca under the same exposure conditions. The samples that displayed the most visible alterations were the same as in RP4, i.e., CB-LM, DM-SS, GP-CA and PS-SS.

7.1.1.6 Overall dissolution trend

The general trend was characterized by three specific moments of the dissolution process. All samples displayed an initial steep decrease in the dissolution rate of

both Ca and Mg. The decline in the rate of dissolution presented variable magnitude across the test-set. The same performance was observed from the exposure of previous test-sets. The first rainfall regime was followed by a stabilization of the dissolution rate of Ca when passing to the new exposure conditions. Under RP2, the trend is mostly horizontal and dissolution values are comparable for most sampling points. The last three exposure regimes showed a progressive increase in the rate of Ca dissolution for most samples. This trend occurred in response to shorter and more frequent cycles of surrogate rainwater. In general, the increase in the frequency of the rainwater cycles and reduction of surrogate rainwater volumes induced a higher rate of Ca dissolution. This was also clear from the comparison of the samples performance with the trends acquired from test-set 2, which displayed an overall more stable behaviour under the corresponding control interval. Results strongly suggested that the dissolution rate of Ca was inversely proportional to the duration of the rainfall event, while being directly correlated to the increase in frequency. The samples which displayed a different performance under the last two exposure regimes, i.e., BL-SS, DM-SS and PT-SS, shared a low content of carbonate minerals in their composition compared to other samples. This was likely connected to the decrease in Ca dissolution at RP4 (BL-SS, 0% carbonate minerals) and RP5 (DM-SS and PT-SS, 3 to 6 % of carbonate minerals).

A definite conclusion over the influence of RP1 with respect to other rainfall patterns was not possible, because the dissolution rate of the first sampling points was proven to not be related to the exposure conditions.

Overall, Mg showed a much better stability to the variations of the exposure conditions compared to Ca. In most cases, alterations of the dissolution rates were

significantly less pronounced compared to Ca. However, Mg appeared to follow a similar pattern to Ca, just on a smaller scale. This was also demonstrated by the relationship of the two analytes. The second rainfall pattern displayed the highest proximity between dissolution values of Ca and Mg for all samples. After RP2, the dissolution profiles of Ca and Mg started to diverge, reaching in most cases the maximum distance under RP5 (RP1 excluded).

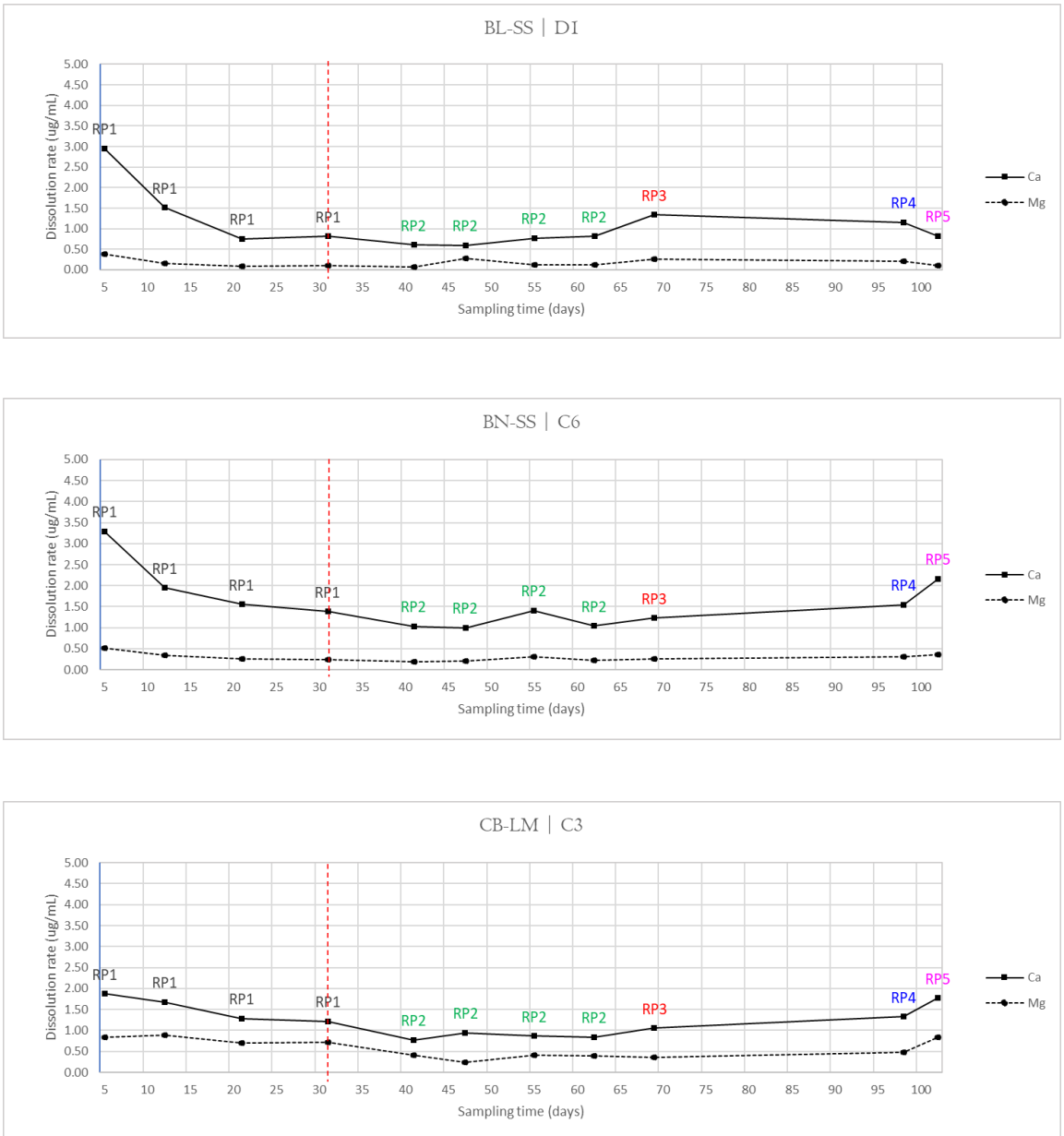

Figure 7-1: Ca and Mg dissolution trend of BL-SS, BN-SS and CB-LM.

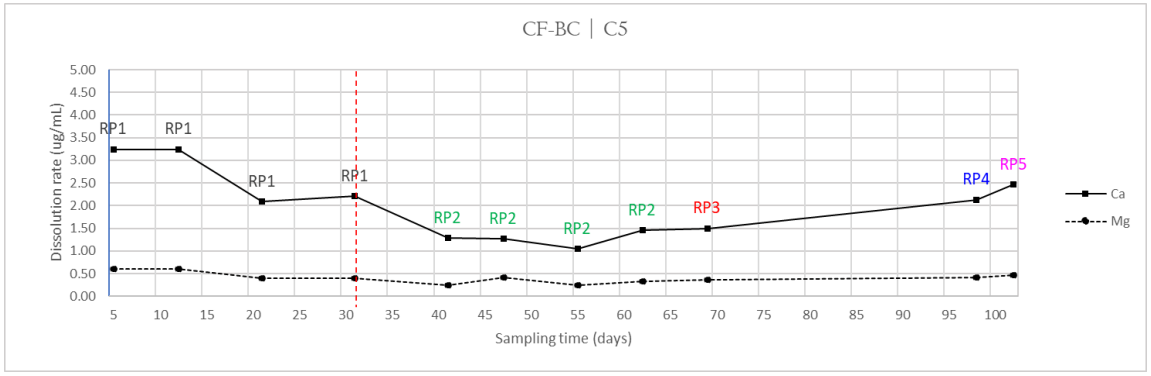

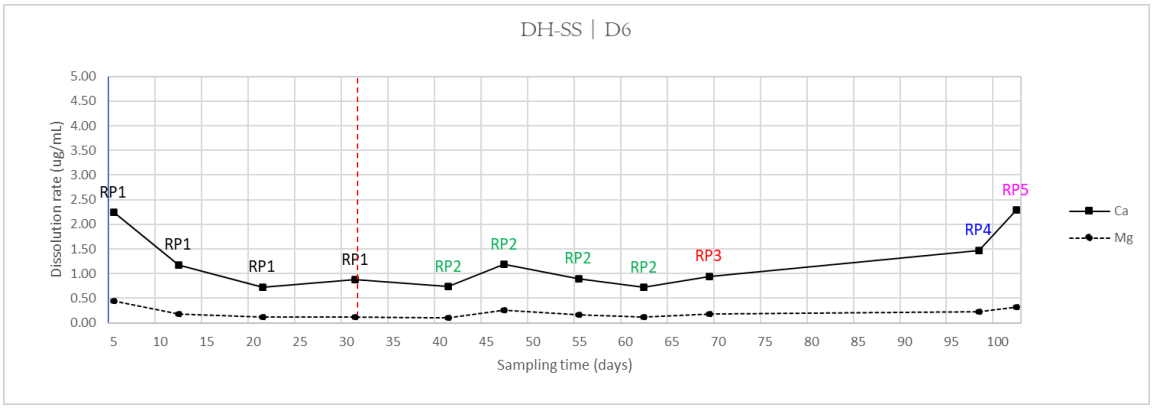

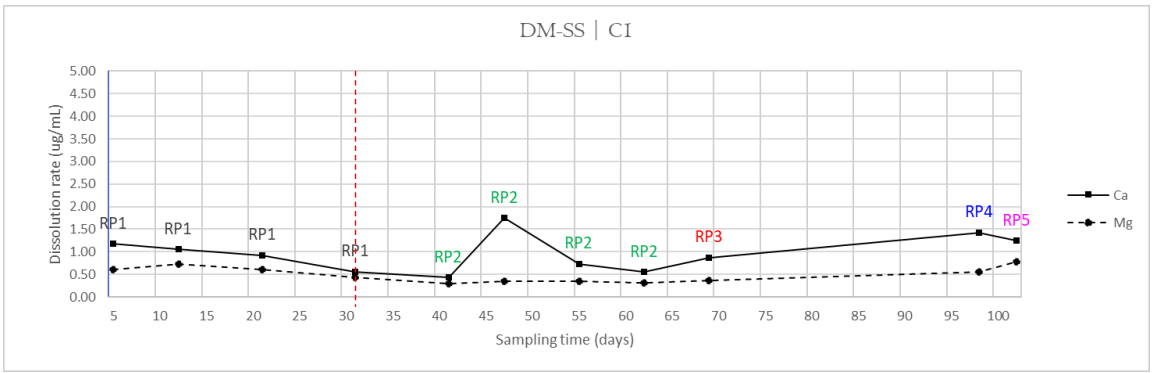

Figure 7-1: Ca and Mg dissolution trend of CF-BC, DH-SS and DM-SS.

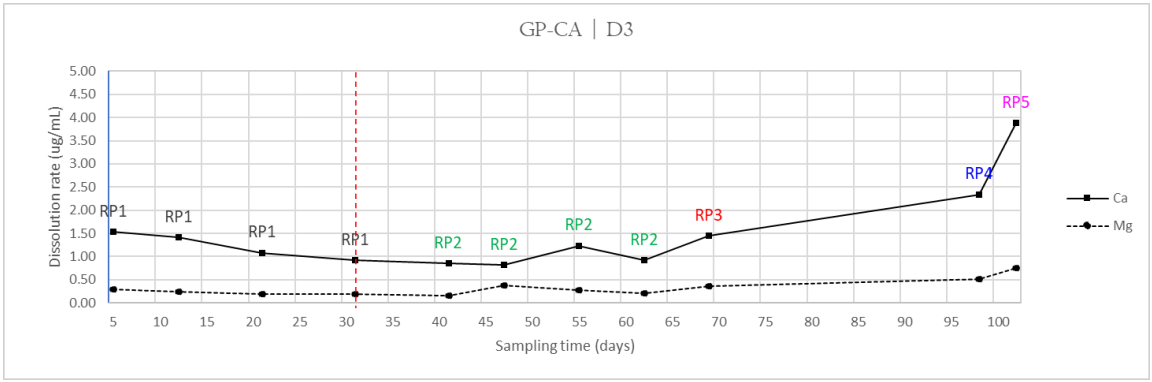

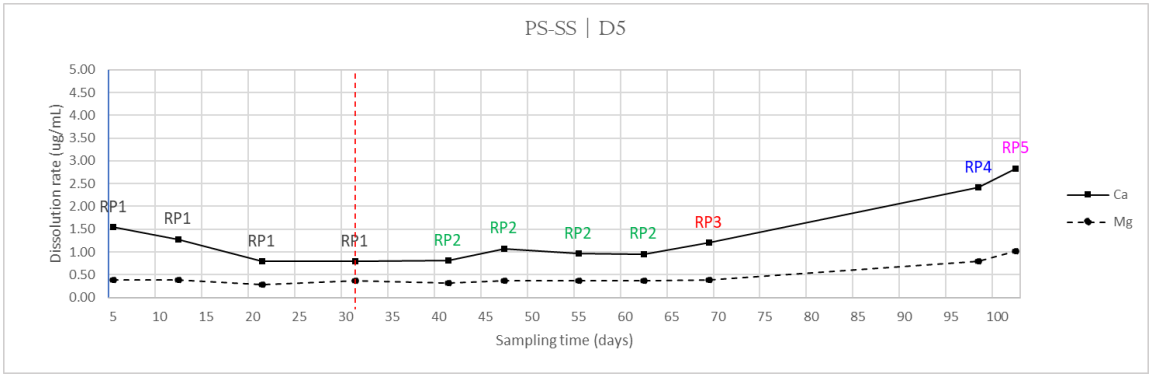

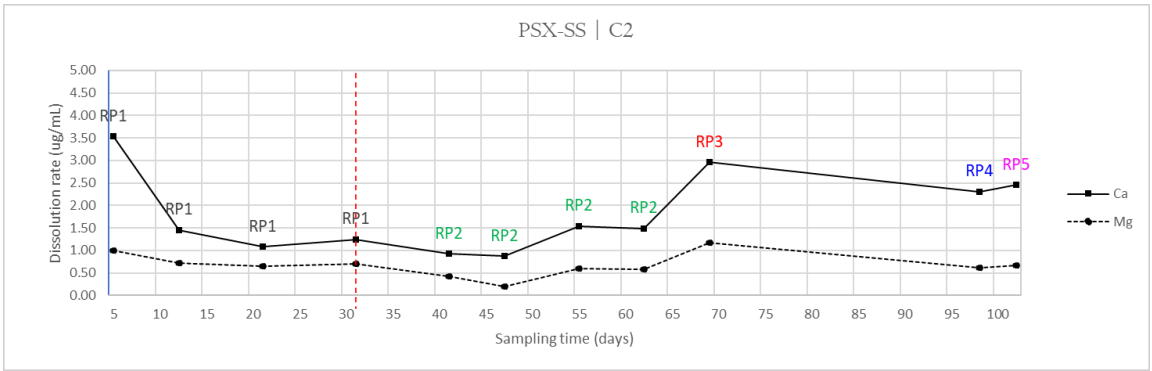

Figure 7-2: Ca and Mg dissolution trend of GP-CA, PS-SS and PSX-SS.

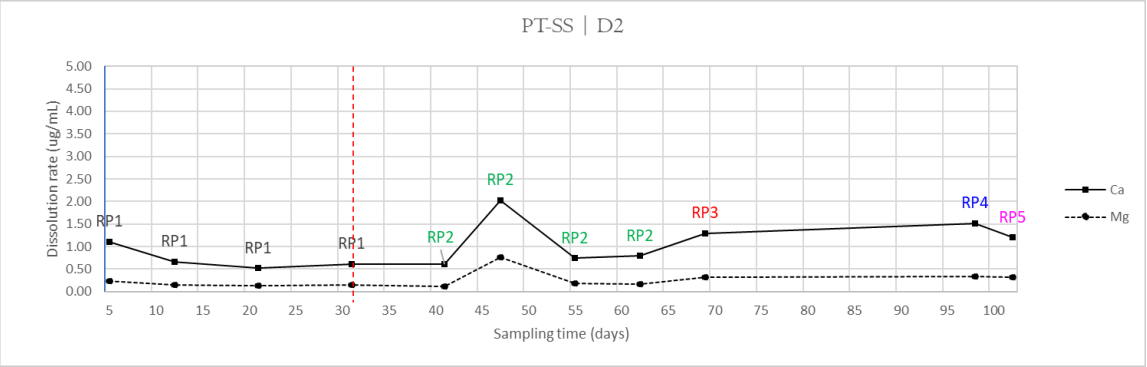

Figure 7-3: Ca and Mg dissolution trend of PT-SS.

7.1.2 Sodium and Potassium

The dissolution profiles of Ca and Mg are shown in figures 7-5 to 7-8.

7.1.2.1 Rainfall Pattern 1

At this initial sampling, the dissolution rate of Na was higher than the dissolution rate of K for all samples. However, the trend of Na dissolution formed by the first and fourth sampling points highlighted a steep decrease of the dissolution trend of the analyte. This trend was consistent with the performance displayed by Ca and Mg. By contrast, the dissolution of K appeared to be significantly more stable, and the dissolution values acquired from sampling points under the first exposure regime did not display a substantial alteration of the trend. As a consequence, the

difference in dissolution rate of the two analytes substantially decreased between the initial and last sampling point of the first exposure regime.

7.1.2.2 Rainfall Pattern 2

The divergence between Na and K dissolution was further reduced under RP2. The closest proximity between the two analytes was observed at the second and third sampling point. An increase in Na dissolution was observed for most samples under the third sampling point, with the exception of BL-SS, GP-CA and PT-SS. For these samples the trend maintained a stable pattern. A considerably higher stability was displayed by K throughout RP2. Potassium did not display any significant variation in dissolution rate and maintained a good continuity with RP1.

7.1.2.3 Rainfall Pattern 3

Under the third rainfall pattern, Na displayed an increase in dissolution rate for all samples. The trend variation from RP3 to RP4 was found to show variable magnitude across the test-set. The acceleration of the dissolution process was steeper for GP-CA and PT-SS compared to the rest of the samples. Such a level of alteration in the dissolution trend between RP2 and RP3 was not observed with K dissolution. Most samples exhibited a slight increase in dissolution rate; however, the magnitude of the change was considerably lower than that displayed by Na.

7.1.2.4 Rainfall Pattern 4

Most samples showed a decrease in Na dissolution rate under RP4. Only BL-SS and BN-SS did not display any change between the two rainfall patterns. The same response was not observed for K, whose dissolution rate showed a small constant increase.

7.1.2.5 Rainfall Pattern 5

Dissolution of Na under the last rainfall pattern was below the limit of detection and could not be determined for BL-SS, BN-SS, CB-LM and DM-SS. For the remaining samples, Na dissolution displayed either a rate decrease (CF-BC, PS-SS, PSX-SS, PT-SS) or increase (GP-CA). The same performance was observed for K on a smaller scale. Some samples showed a progressive decrease in the rate of K dissolution (BL-SS, BN-SS, DM-SS, GP-CA). The remaining stone types instead showed a small increase in dissolution rate.

7.1.2.6 Overall dissolution trend

Potassium and Na displayed a different response to the variation of the exposure conditions. Overall, Na showed a higher level of susceptibility to the changes in frequency and volume of surrogate rainwater. At the same time, a relationship between the frequency of cycles and dissolution rate of Na was not observed.

These results indicated a dependency in the type of response to variable exposure conditions on the mineral phase and its respective concentration in the sample. In contrast, K dissolution exhibited a much higher level of stability to the variation of the exposure conditions. In this connection, the performance of K was more similar to the performance of Ca and Mg, than to Na.

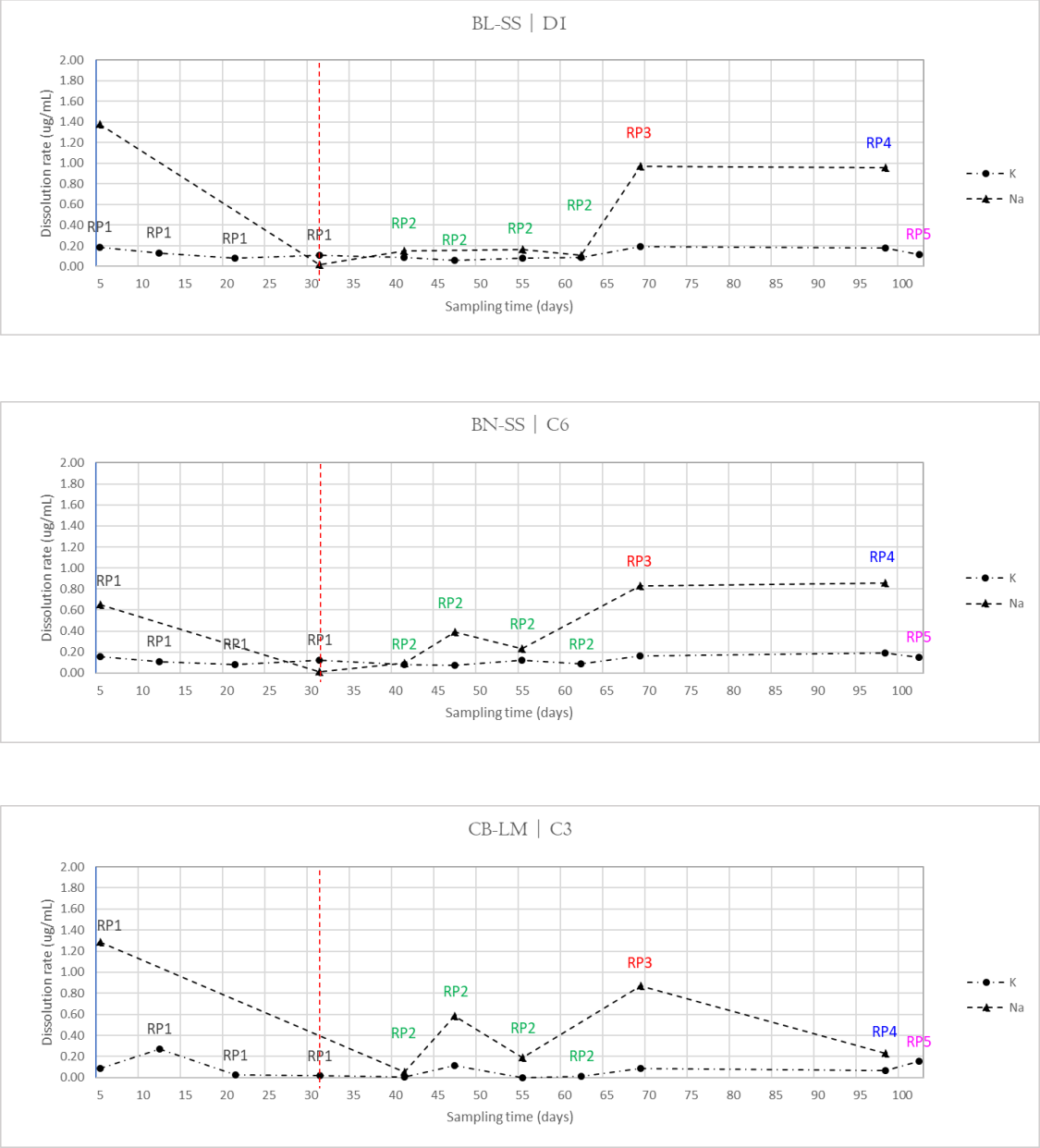

Figure 7-4: K and Na dissolution trend of BL-SS, BN-SS and CB-LM.

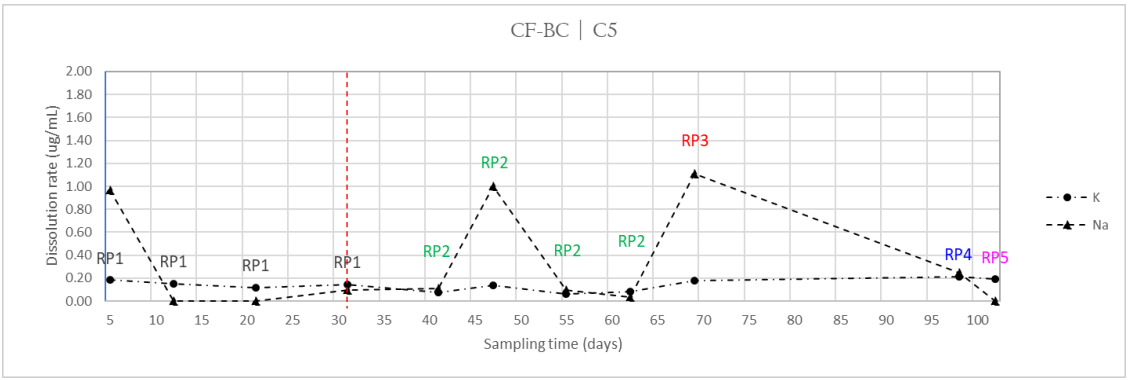

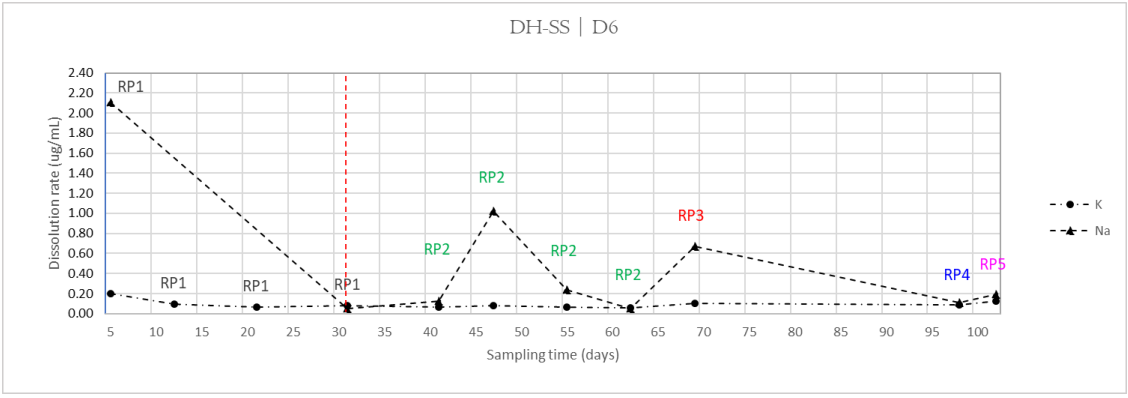

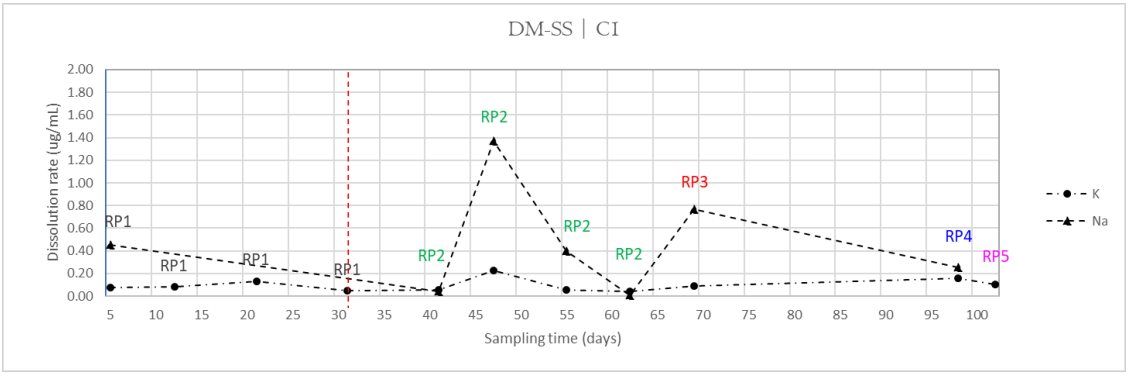

Figure 7-5: K and Na dissolution trend of CF-BC, DH-SS and DM-SS

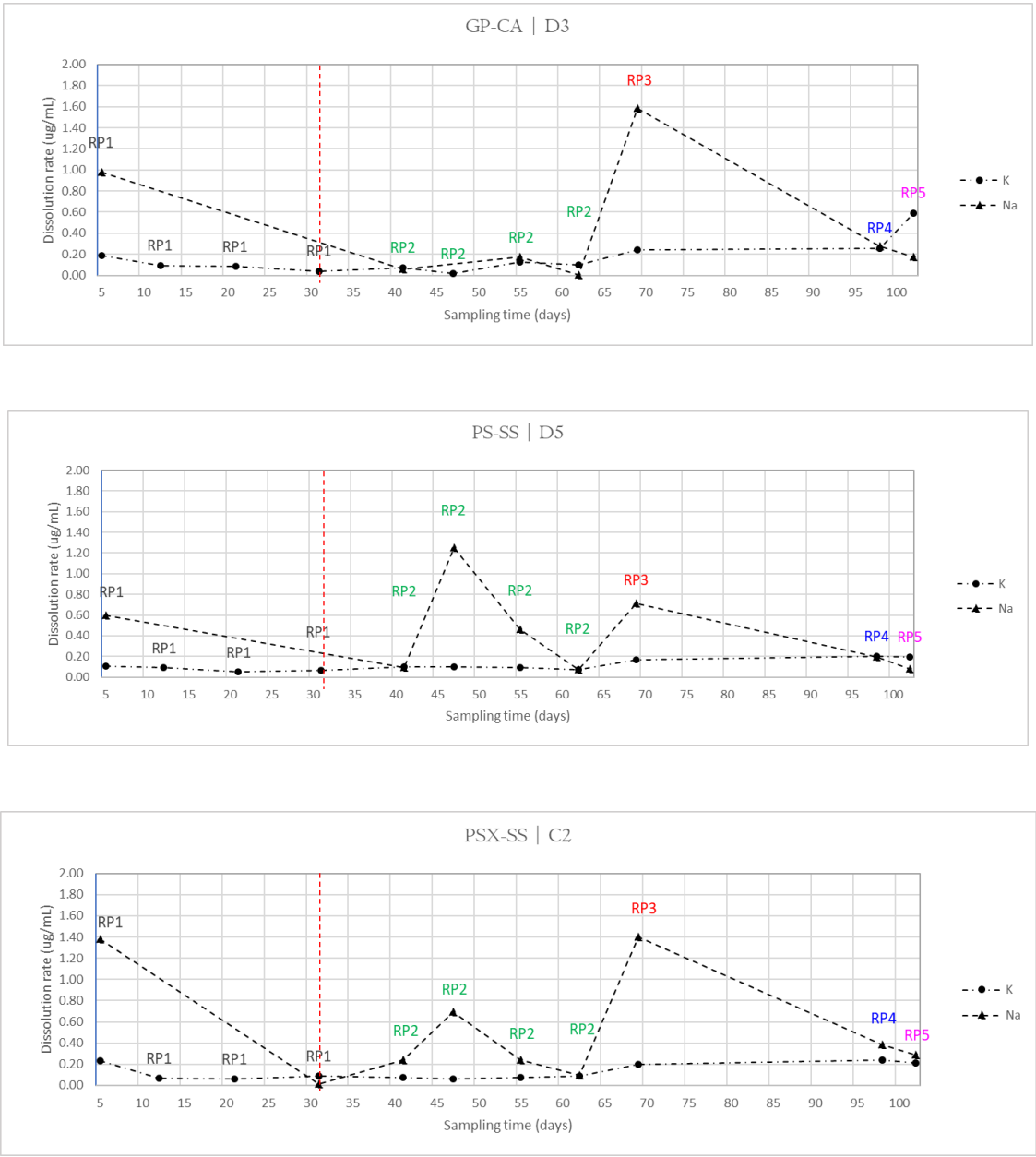

Figure 7-6: K and Na dissolution trend of GP-CA, PS-SS and PSX-SS.

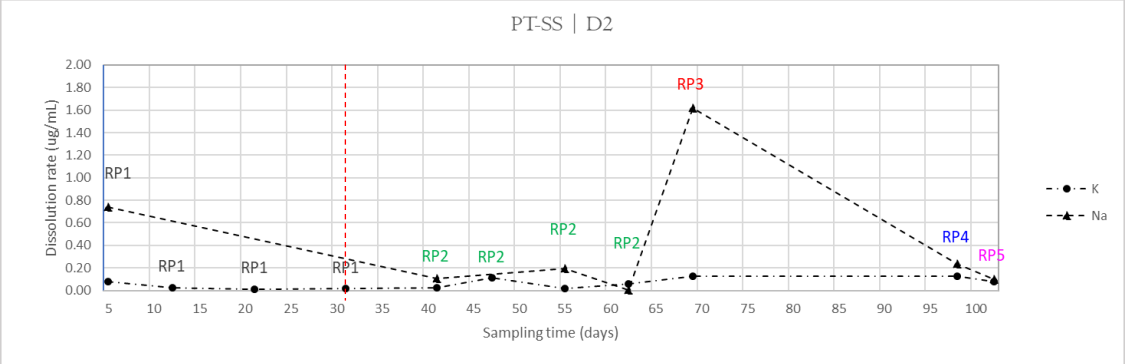

Figure 7-7: K and Na dissolution trend of GP-CA, PS-SS and PSX-SS.

7.2 Dissolution rates at rainfall intervals

7.2.1 Calcium and Magnesium

The dissolution rates of Ca and Mg for each RP are shown in figures 7-9 to 7-12 and 7-13 to 7-16, respectively. The percentage change in dissolution rate between rainfall patterns is displayed in tables 7-1 and 7-2.

7.2.1.1 Rainfall Pattern 1-2

The first rainfall pattern (RP1) displayed relatively high Ca dissolution rates, ranging between 0.73 µg/mL (PT-SS) and 2.69 µg/mL (CF-BC). Dissolution rates consistently decreased under rainfall patterns 2 (RP2). Calcium dissolution rates under RP2 ranged between 0.87 µg/mL (DM-SS) and 1.26 µg/mL (CF-BC). The difference in dissolution rate between between RP1 and RP2 extended to a 53%

decelereation of the process (CF-BC). The rate of dissolution of Mg during the initial rainfall interval ranged between 0.17 µg/mL (PT-SS) to 0.79 µg/mL (CB-LM). Comparably to Ca, most samples experienced a lower dissolution rate under RP2 compared to RP1. The only exception was represented by PT-SS, whose dissolution rate increased by 10% and 77%. The negative variation between the first and second rainfall pattern was found to vary between 18% (BL-SS) and 53% (CB-LM). The dissolution rate of the samples under RP1 is affected by the higher dissolution rates that the stones were found to experience during the initial phase of the exposure, and therefore is not representative of the samples response under RP1 exposure conditions.

7.2.1.2 Rainfall Pattern 3

Calcium dissolution values under RP3 ranged between 0.87 µg/mL (DM-SS) and 2.96 µg/mL (PSX-SS). With the shortening of the exposure cycles and decrease in volumes of surrogate rainwater under the third rainfall pattern, the samples experienced an increase in the rate of dissolution compared to RP2. Only DM-SS did not display any variation, as both dissolution values for RP2 and RP3 corresponded to 0.87 µg/mL. Aside from this exception, the rate of dissolution was found to increase at different levels. The most substantial change was displayed by PSX-SS, whose Ca dissolution of 2.96 µg/mL corresponded to a 144% increase in dissolution rate from RP2.

Under the third rainfall regime, all stone types displayed an increase in Mg dissolution rate, except for PT-SS. The difference in Mg dissolution between RP2

and RP3 ranged from 0.6% (CB-LM) and 162% (PSX-SS). However, for most samples the difference was not substantial. The sample PSX-SS represented an exception due to the very high Mg release compared to other stone types.

7.2.1.3 Rainfall Pattern 4

Dissolution values of Ca under the fourth rainfall pattern ranged from 1.16 µg/mL (BL-SS) to 2.41 µg/mL (PS-SS). Under RP4 all samples displayed a variation in the dissolution rate of Ca compared to RP3. For 8 of the 10 stone types, such variation consisted of an increase in the rate of dissolution, ranging from 17% (PT-SS) to 64% (DM-SS). On the other hand, the decline in dissolution rate between RP3 and RP4 corresponded to 13% for BL-SS and 21% for PSX-SS. Nonetheless, the dissolution rate at RP4 was higher in all samples compared to the dissolution rate displayed by RP2. Under the fourth rainfall pattern, most samples displayed an increase in Mg dissolution. The rate of Mg dissolution varied from 0.21 µg/mL (BL-SS and PT-SS) and 0.79 µg/mL (PS-SS). This corresponded to a variable increase in the dissolution process of RP4 compared to RP3 which stretched between 12% (CF-BC) and 106% (PS-SS).

7.2.1.4 Rainfall Pattern 5

The last rainfall pattern (RP5) involved the exposure of the samples to the shortest cycles of surrogate rainwater. Once again, the dissolution of the samples was

higher than the dissolution rate of RP4 for seven samples. Amont these samples, Ca dissolution ranged between 0.82 µg/mL (BL-SS) and 3.88 µg/mL (GP-CA). The value of Ca dissolution found for RP5 corresponded to an increase in the dissolution rate which stretched from 6% (PSX-SS) to 65% (GP-CA). Dissolution rates were found to decrease for BL-SS and PT-SS, by 29% and 20% respectively. Under RP5 conditions, Mg release from the samples ranged from 0.11 µg/mL (BL-SS) to 1.01 µg/mL (PS-SS). Most samples presented a rise in the rate of Mg dissolution compared to RP4. The increase in dissolution under the new exposure conditions varied between 9% (PSX-SS) and 76% (CB-LM).

7.2.1.5 Ca overall trend

As previously reported, samples displayed a high level of susceptibility to the variation of the exposure conditions and confirmed the relationship between the dissolution rate of Ca and Mg and the duration of the rainfall event. This observation did not apply to RP1, due to the bias caused by altered dissolution rates that were displayed by most samples between the first and fifth sampling point. This feature of the dissolution trend affected the comparability between the samples performance under RP1 and other RPs. Instead, the stone response to variable exposure conditions was better assessed from the second rainfall pattern regime. Most samples exhibited an increasing trend in the dissolution of Ca from RP2 to RP5. This was verified for BN-SS, CB-LM, CF-BC, DH-SS, GP-CA, PS-SS. For these samples, the magnitude of the difference in dissolution rates from RP2 to RP5 was substantial. It corresponded to a 92% variation for BN-SS, 105%

for CB-LM, 95% for CF-BC, 160% for DH-SS, 197% for PS-SS and 308% for GP-CA. For other stone types, the increasing trend stopped at RP4 (PT-SS and DM-SS). The same positive variation in dissolution rate between RP2 and RP5 was also shown by PSX-SS, discontinued by an exceptionally high Ca release under the RP3 conditions. Only one sample showed an opposite trend compared to the rest of the test-set. After an initial increase in Ca dissolution rate between RP2 and RP3, BL-SS displayed a constant decrease in the rate of dissolution between RP3 and RP5. It was observed that, in some cases, the dissolution variation between RPs regimes maintained a steady acceleration of the process. For instance, the increment between RP3, RP4 and RP5 for CB-LM corresponded to 23%, 25% and 33%. The same values for GP-CA followed an increase of 51%, 62% and 65%. The variation trend displayed by BN-SS corresponded to an increase in dissolution rate of 9%, 25% and 39%. In some other cases, despite the increment in dissolution rate, a steady decrease in the respective variation between rainfall patterns was observed. This was the case for PT-SS, whose performance displayed a positive variation from RP2 to RP5 corresponding to 43%, 24% and 17%, to ultimately produce a negative difference between RP4 and RP5 of 20%.

Overall, it was shown a clear increase in the values of dissolution with the progressive shortening of the rainwater cycles. The variation was not constant across the dataset, but different samples displayed different levels of susceptibility to the exposure conditions. The response to variable conditions and the nature of any variation are likely connected to the carbonate mineral content of the stone and its physical properties. These aspects will be discussed in greater detail in Chapter 9.

7.2.1.6 Mg overall Trend

In most samples, the dissolution rate displayed by Mg at the first rainfall interval was relatively higher than the one displayed by the following rainfall patterns. Comparably to Ca, this feature of the dissolution trend was caused by the higher dissolution rate observed in correspondence of the first sampling points. From the second rainfall regime, the dissolution rate displayed a steady increasing trend for most samples. The stone types whose dissolution under each rainfall pattern was higher than the previous, except for RP1, were BN-SS, CB-LM, CF-BC, DH-SS, DM-SS, GP-CA, and PS-SS. For PT-SS, the increasing trend stopped at RP4, to decrease again under RP5 conditions. The peak in dissolution rate was reached at RP3 for BL-SS. The sample PSX-SS showed an increasing trend from RP2 to RP4 and RP5 but displayed an exceptionally high release of Mg at RP3.

In most cases, the stone performance in terms of Mg dissolution replicated the behaviour observed with Ca dissolution. The susceptibility of the different stone types to the variation of the rainfall patterns was found to fluctuate. In some cases, the change in dissolution rate was stable, as in the case of GP-CA, where the variation between RP3, RP4 and RP5 was at 42%, 42% and 47%. For other samples, dissolution rate tended to increase with the progression of the rainwater regimes, as in the case of CB-LM. Overall, it was observed a substantial variation in the rate of dissolution between RP2 and RP5, which reached an increase of 180% with PS-SS.

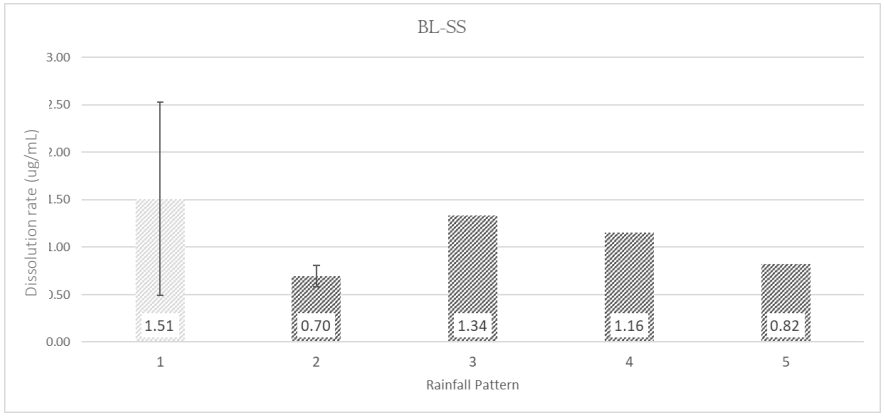

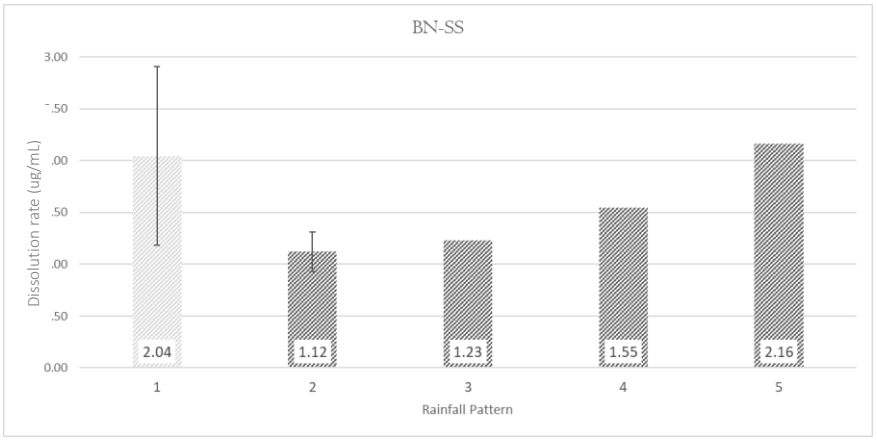

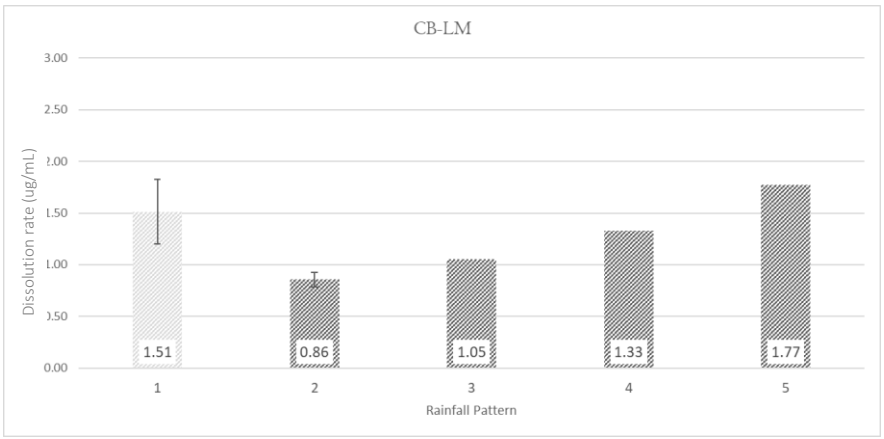

Figure 7-8: mean Ca dissolution at each rainfall patterns of BL-SS, BN-SS and CB-LM

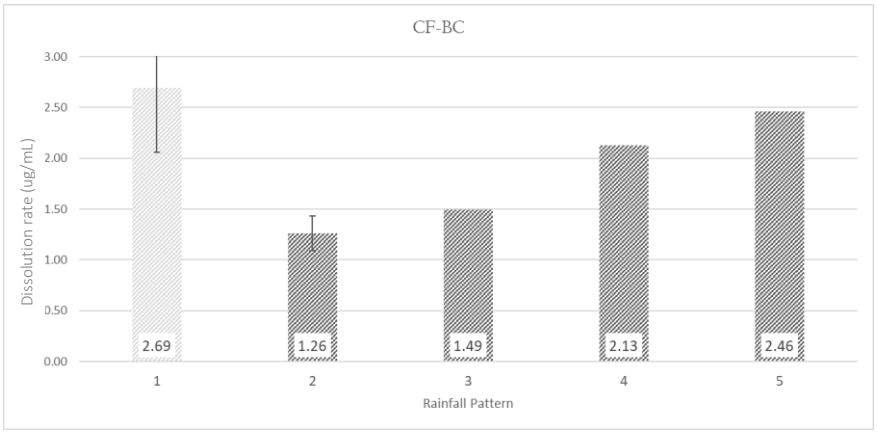

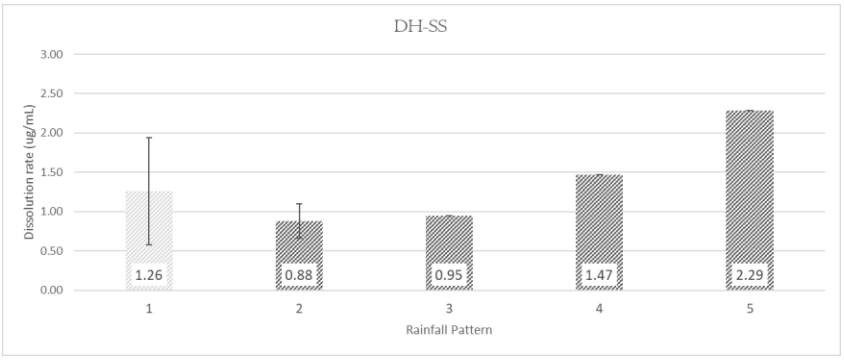

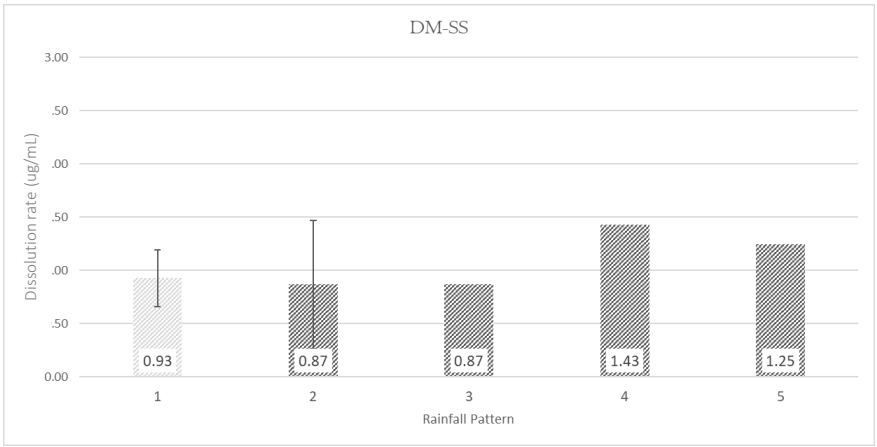

Figure 7-9: mean Ca dissolution at each rainfall patterns of CF-BC, DH--SS and DM-SS

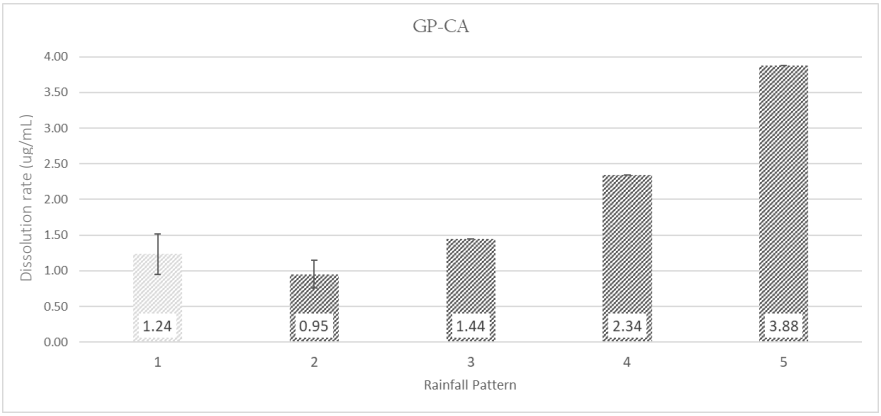

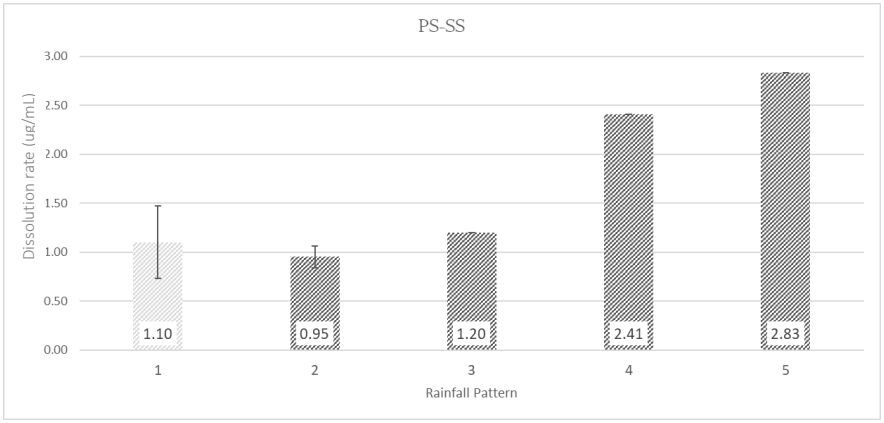

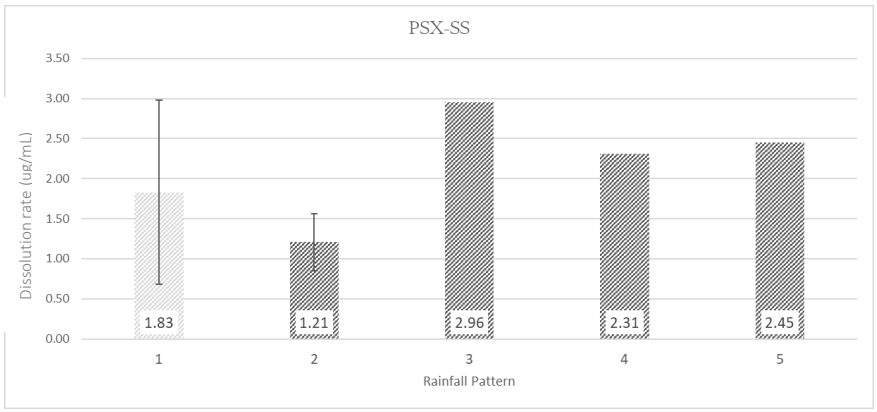

Figure 7-10: mean Ca dissolution at each rainfall patterns of GP-CA, PS-SS and PSX-SS.

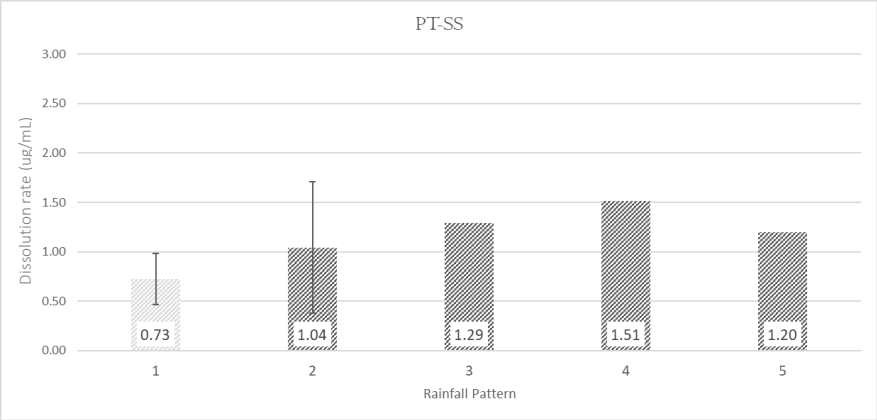

Figure 7-11: mean Ca dissolution at each rainfall patterns of PT-SS.

Table 7-1: *percentage variation in dissolution rate of Ca under different rainfall patterns*

Sample	RP2	RP3	RP4	RP5
BL-SS	- 53%	+ 91%	- 13%	- 29%
BN-SS	- 45%	+ 9%	+ 25%	+ 39%
CB-LM	- 43%	+ 23%	+ 25%	+ 33%
CF-BC	- 53%	+ 18%	+ 42%	+15%
DH-SS	- 29%	+ 7%	+ 55%	+ 55%
DM-SS	- 6%	0%	+ 64%	- 12%
GP-CA	- 23%	+ 51%	+ 62%	+ 65%
PS-SS	- 13%	+ 26%	+ 100%	+ 17%
PSX-SS	- 34%	+ 144%	- 21%	+ 6%
PT-SS	+ 43%	+ 24%	+ 17%	- 20%

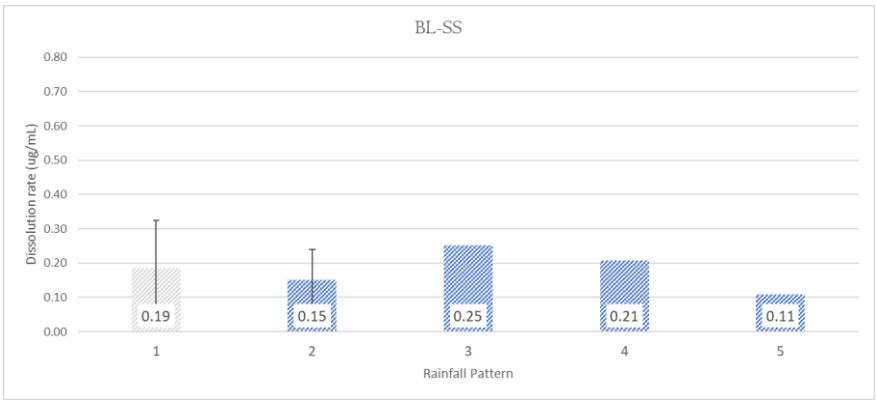

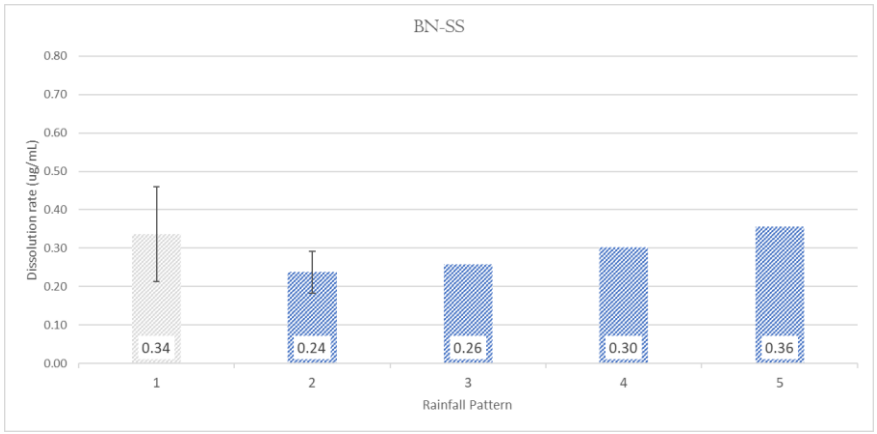

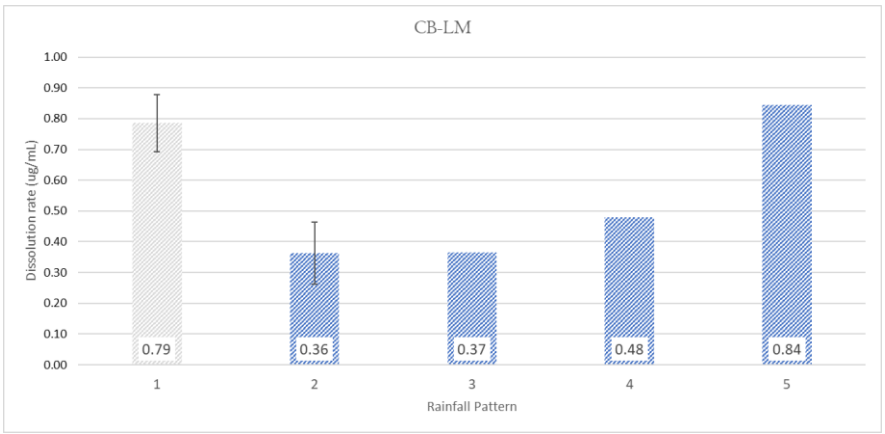

Figure 7-12: *mean Mg dissolution at each rainfall patterns of BL-SS, BN-SS and CB-LM*

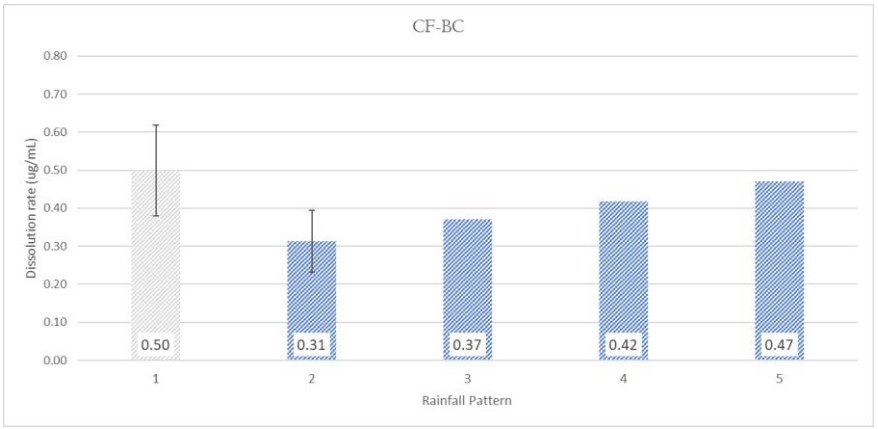

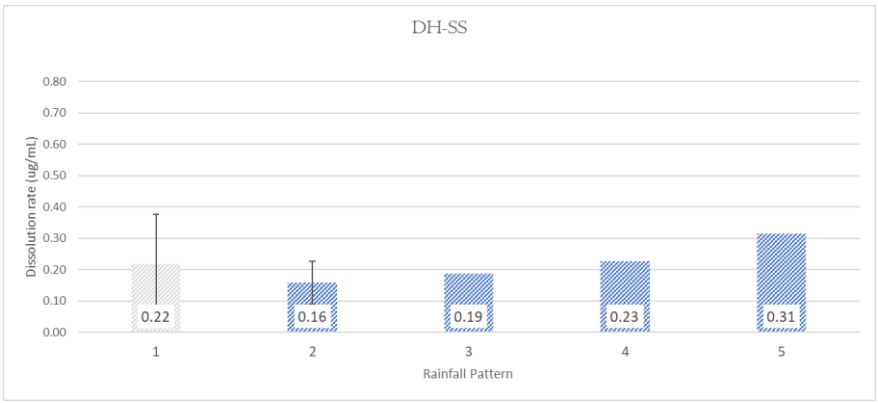

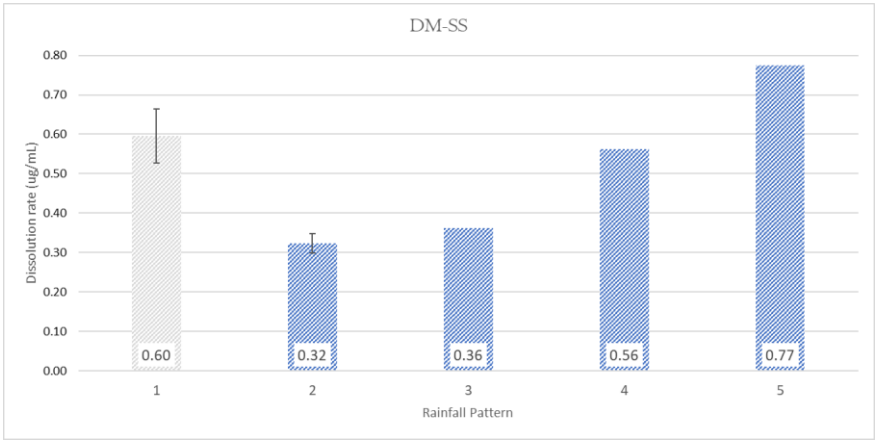

Figure 7-13: mean Mg dissolution at each rainfall patterns of CF-BC, DH-SS and DM-SS

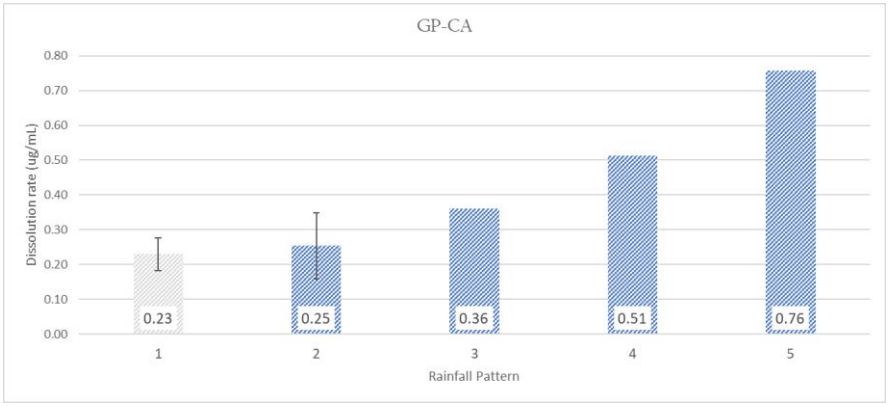

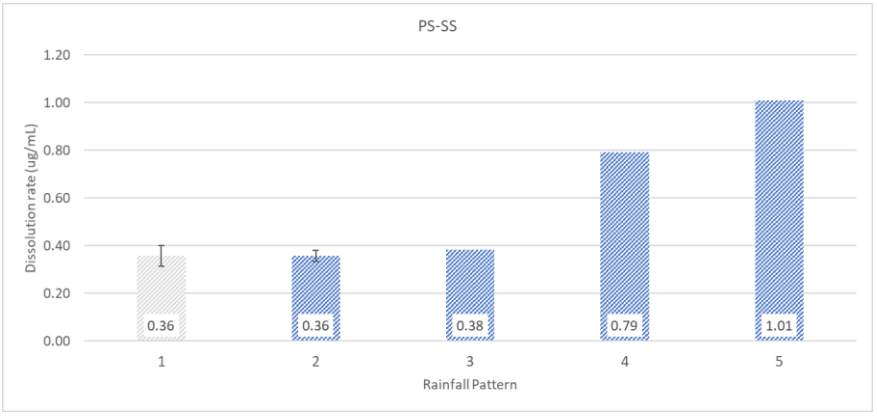

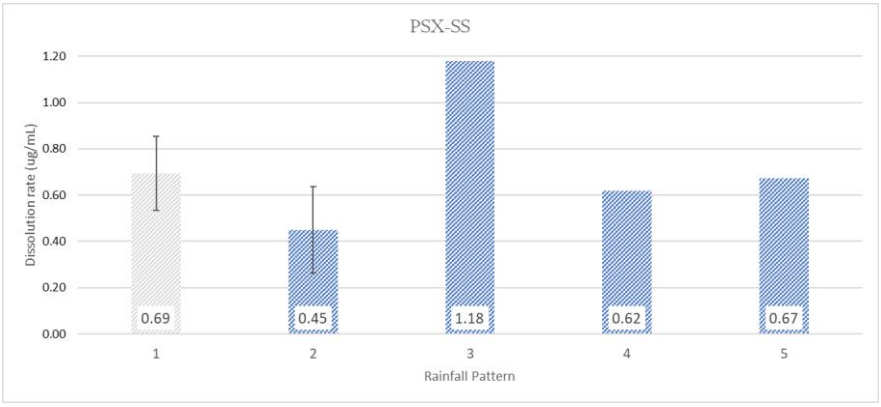

Figure 7-14: mean Mg dissolution at each rainfall patterns of GP-CA, PS-SS and PSX-SS

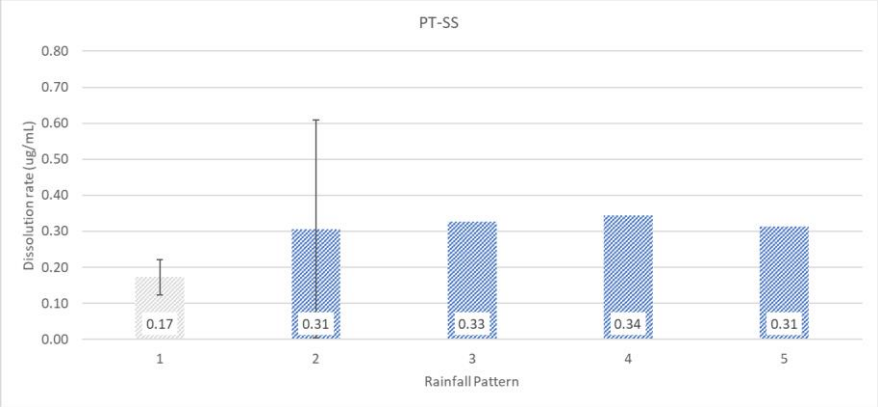

Figure 7-15: mean Mg dissolution at each rainfall patterns of PT-SS

Table 7-2: Table percentage variation in dissolution rate of Mg under different rainfall patterns

Sample	RP2	RP3	RP4	RP5
BL-SS	- 18%	+ 67%	- 17%	- 47%
BN-SS	- 29%	+ 8%	+ 17%	+ 17%
CB-LM	- 53%	+ 0%	+ 30%	+ 76%
CF-BC	- 37%	+ 18%	+ 12%	+12%
DH-SS	- 27%	+ 18%	+21%	+ 37%
DM-SS	- 45%	+11%	+ 55%	+37%
GP-CA	+ 10%	+ 42%	+ 42%	+ 47%
PS-SS	0 %	+ 7%	+ 106%	+ 27%
PSX-SS	- 35%	+ 162%	- 47%	+ 9%
PT-SS	+ 77%	+ 6%	+5%	- 8%

7.2.2 Potassium and Sodium

The dissolution rates of K and Na for each RP are shown in figures 7-17 to 7-20. The percentage change in dissolution rate between rainfall patterns is displayed in tables 7-3 and 7-4.

7.2.2.1 Rainfall Pattern 1-2

The change in dissolution displayed by K followed a similar pattern to Ca and Mg. The dissolution values under each rainfall pattern exhibited an initial decrease in dissolution rate from RP1 to RP2 for most samples. The range in K dissolution for from RP1 corresponded to 0.03 µg/mL (PT-SS) to 0.15 µg/mL (CF-BC) µg/mL, while the range of dissolution for RP2 corresponded to 0.03 µg/mL (CB-LM) to 0.09 µg/mL (BN-SS, CF-BC, DM-SS and PS-SS). As with previous analytes, the decrease was found to occur at different levels across the data set. The negative variation in K dissolution between RP1 and RP2 fitted within the range of 24% (BN-SS) to 66% (CB-LM). Some samples displayed an increase in dissolution rate, i.e., DM-SS, PS-SS and PT-SS. The positive variation in K dissolution between RP1 and RP2 ranged between 11% and 69%.

Overall, Na displayed higher dissolution rates compared to K. The range of dissolution corresponded to 0.33 µg/mL (BN-SS) to 1.29 µg/mL (CB-LM) µg/mL, and 0.08 µg/mL (GP-CA) and 0.47 µg/mL (PS-SS) under RP2. With the second rainfall regime, samples displayed a negative variation of the rate of Na

dissolution, ranging between 20% (PS-SS) and 91% (GP-CA). Only for DM-SS the dissolution rate remained unaltered between RP1 and RP2.

Comparably to Ca and Mg, the dissolution rate of the samples under RP1 is affected by the higher dissolution rates that the stones were found to experience during the initial phase of the exposure, and therefore is not representative of the samples response under RP1 exposure conditions.

7.2.2.2 Rainfall Pattern 3

The dissolution rate of K for RP3 corresponded to 0.09 µg/mL (CB-LM, DM-SS) to 0.24 µg/mL (GP-CA). Under the third exposure regime, most samples showed a substantial increase in the dissolution rate of K. Increased rates fitted within a wide range of variations, corresponding to 58% (DH-SS) and 213% (GP-CA). Only DM-SS exhibited a negative trend, with a small decrease in dissolution rate of 3%. The third rainfall pattern provided the highest divergence between the dissolution of Na and K. Sodium dissolution values ranged between 1.58 µg/mL (GP-CA) and 0.67 µg/mL (DH-SS). All samples displayed a substantial increase in dissolution rate of Na under RP3. This corresponded to an acceleration in the range of 68% (DM-SS) to 980% (PT-SS).

7.2.2.3 Rainfall Pattern 4

The dissolution range of K corresponded to 0.07 µg/mL (CB-LM) and 0.26 µg/mL (GP-CA). Potassium dissolution maintained an increasing rate under RP4 for most samples. The increase was less sharp compared to the previous rainfall pattern, ranging between 5% (GP-CA) and 72% (DM-SS). Compared to RP3, more samples displayed a decrease in dissolution rate, namely BL-SS, CB-LM, DH-SS. The deceleration of K dissolution for these samples was not substantial and fitted within the values of 8% (BL-SS) and 26 % (CB-LM). The fourth rainfall pattern provided the highest similarity between the dissolution rates of K and Na across the test-set. The dissolution of Na ranged from 0.11 µg/mL (DH-SS) to 0.96 µg/mL (BL-SS). The variation of the dissolution rate from RP3 to RP4 was negative for most samples and stretched from 1% (BL-SS) to 85% (PT-SS). The only exception was represented by BN-SS, which presented a 3% increase in Na dissolution between the two RPs.

7.2.2.4 Rainfall Pattern 5

The dissolution range of K during the last rainfall pattern was found to correspond to 0.08 µg/mL (PT-SS) and 0.59 µg/mL (GP-CA). The last rainfall pattern provided a negative association for most samples on the dissolution rate of K. Six of the ten samples displayed a deceleration of the dissolution process compared to RP4, which ranged from 3% (PS-SS) to 39% (PT-SS). An acceleration of the process occurred only for 4 samples, corresponding to a 12% (CF-BC) to 130% (CB-LM) increase. Most of Na dissolution values under RP5 were not determined. The samples whose concentrations could be measured were DH-SS, GP-CA, PS-SS,

PSX-SS and PT-SS. For these samples, the dissolution values ranged between 0.08 µg/mL (PT-SS) and 0.59 µg/mL (GP-CA). Most of these samples displayed a negative variation of the dissolution from 24% (PSX-SS) to 59% (PS-SS). The sample DH-SS was the only one that showed an acceleration of the process at RP5, corresponding to a variation of 67% compared to RP4.

7.2.2.5 Overall trend

Compared to Ca and Mg, the dissolution trend for K and Na displayed a less linear association with the increased frequency of exposure cycles and the progressive decrease in surrogate rainwater volumes. A linear correlation between rainfall patterns and K dissolution was exhibited by some stone types, as in the case of CF-BC and GP-CA. However, in other cases samples exhibited an alternation between higher and lower dissolution rates, as with CB-LM, DH-SS, DM-SS. On the other hand, no linear correlation was displayed by any of the samples for Na dissolution.

Overall, it was observed that RP3 provided the highest positive variation in dissolution values for both analytes, and that almost all samples displayed a level of susceptibility to such conditions. The number of samples that displayed susceptibility to dissolution across the dataset appeared to decrease with the two last exposure conditions. Ultimately, RP5 did not cause a uniform acceleration of K dissolution process across the dataset and induced an acceleration of the process for four samples only. With respect to Na, only one sample exhibited an acceleration of the dissolution process.

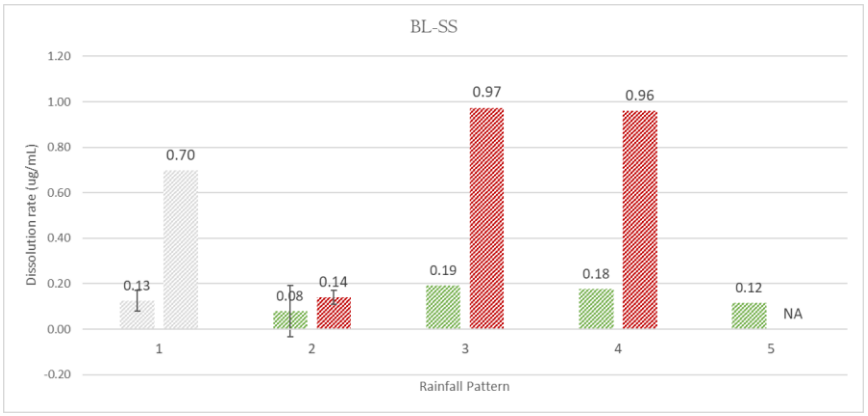

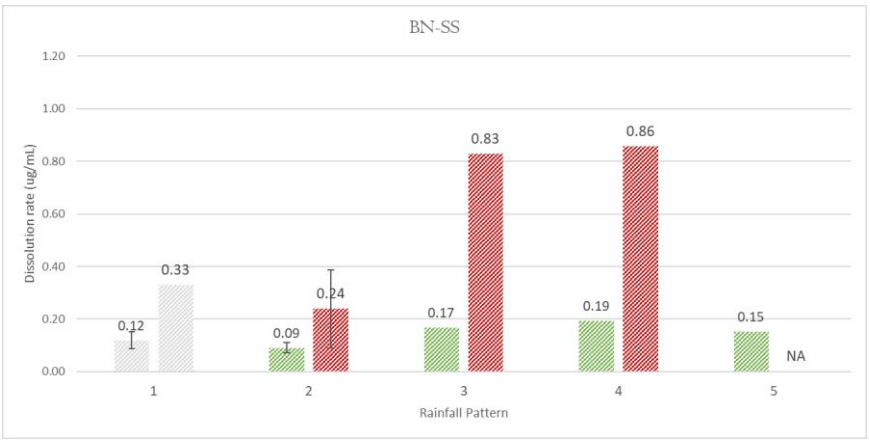

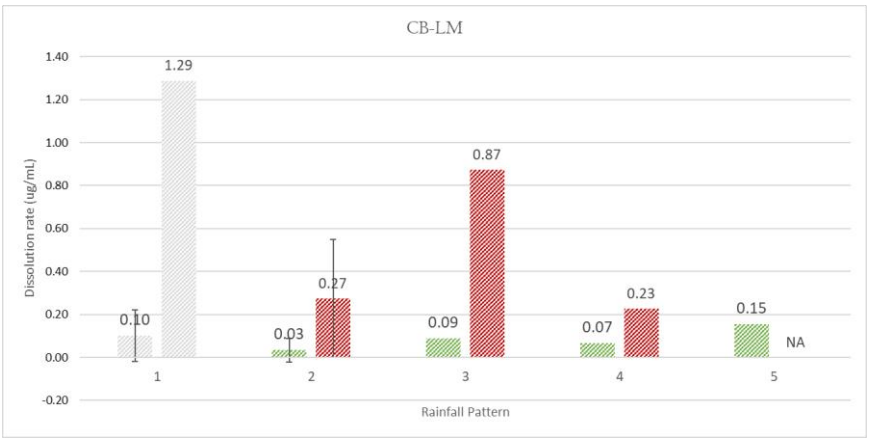

Figure 7-16: mean K and Na dissolution at each rainfall patterns of BL-SS, BN-SS and CB-LM.

Figure 7-17: mean K and Na dissolution at each rainfall patterns of CF-BC, DH-SS and DM-SS.

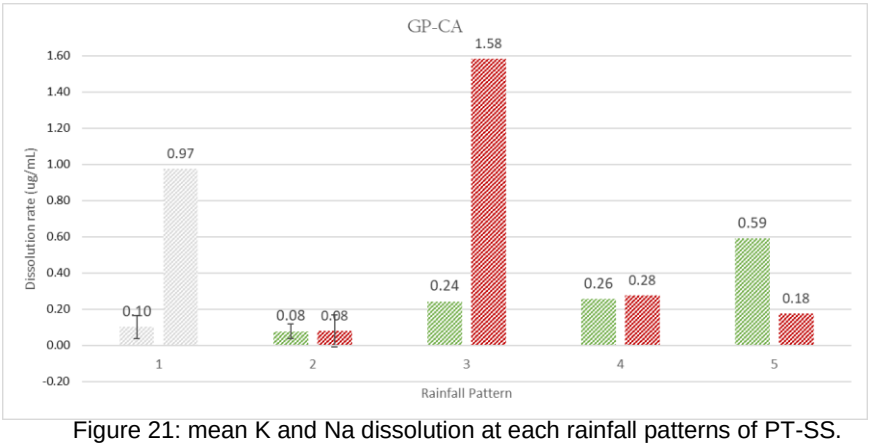

Figure 21: mean K and Na dissolution at each rainfall patterns of PT-SS.

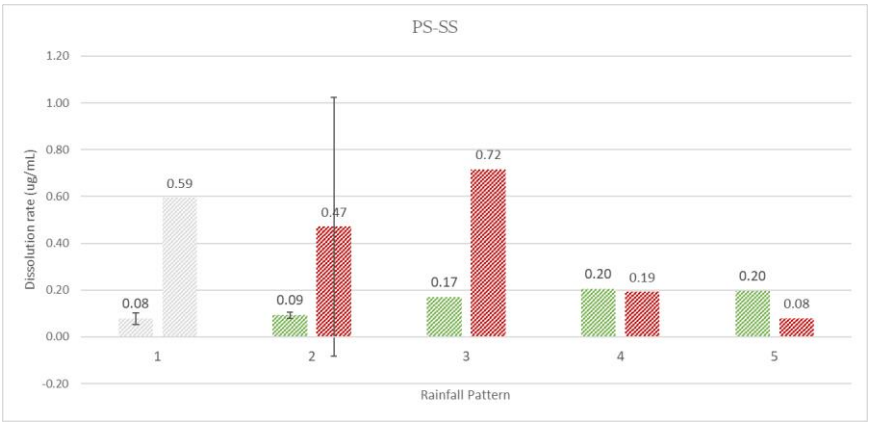

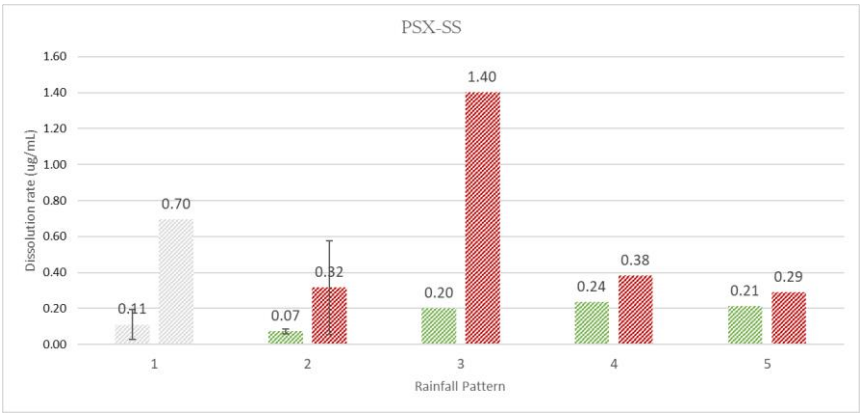

Figure 7-18: mean K and Na dissolution at each rainfall patterns of GP-CA, PS-SS and PSX

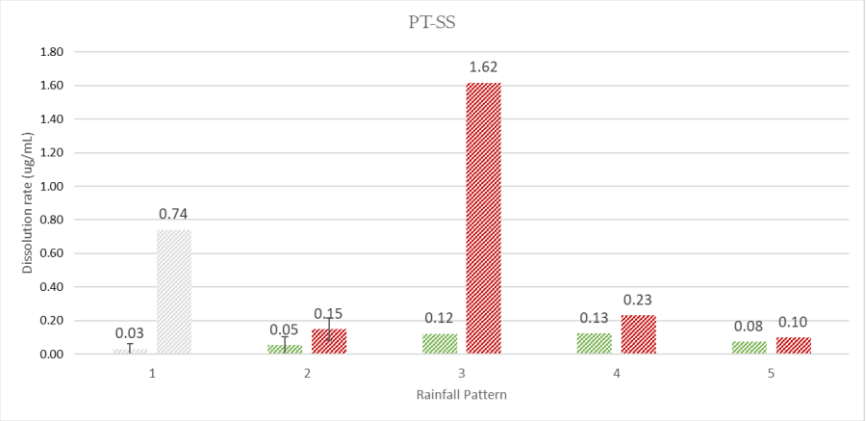

Figure 7-19: mean K and Na dissolution at each rainfall patterns of PT-SS

Table 7-3: percentage variation in dissolution rate of K under different rainfall patterns

Sample	RP2	RP3	RP4	RP5
BL-SS	- 37%	+ 146%	- 8%	- 34%
BN-SS	- 24%	+ 83%	+ 16%	- 20%
CB-LM	- 66%	+ 166%	- 26%	+ 130%
CF-BC	- 40%	+ 99%	+ 20%	- 12%
DH-SS	- 41%	+ 58%	- 17%	+ 47%
DM-SS	+ 11%	- 3%	+ 72%	- 34%
GP-CA	- 24%	+ 213%	+ 5%	+ 130%
PS-SS	+ 18%	+ 85%	+ 19%	- 3%
PSX-SS	- 33%	+ 172%	+ 18%	- 9%
PT-SS	+ 69%	+ 127%	+1%	- 39%

Table 7-4: percentage variation in dissolution rate of Na under different rainfall patterns

Sample	RP2	RP3	RP4	RP5
BL-SS	- 79%	+ 591%	-1%	NA
BN-SS	- 27%	+ 247%	+ 3%	NA
CB-LM	-78%	+ 217%	- 74%	NA
CF-BC	-41%	+ 256%	-77%	NA
DH-SS	- 66%	+ 87%	- 83%	67%
DM-SS	0%	+ 68%	-66%	NA
GP-CA	-91%	+ 190%	- 82%	- 36%
PS-SS	- 20%	+ 52%	- 73%	- 59%
PSX-SS	- 54%	+ 342%	-72%	-24%
PT-SS	- 79%	+ 980%	- 85%	-57%

7.2.3 Iron

The dissolution rates of K and Na for each RP are shown in figures 7-21 to 7-24. The percentage change in dissolution rate between rainfall patterns is displayed in tables 7-5.

7.2.3.1 Rainfall Pattern 1-2

The first rainfall pattern induced different levels of Fe dissolution, comprised between 0.02 µg/mL (GP-CA, PS-SS) and 0.13 µg/mL (DM-SS). Dissolution rate was higher under RP1 compared to RP2, whose dissolution values ranged between 0.01 µg/mL (CF-BC) and 0.05 µg/mL (PS-SS). This induced a negative variation of the dissolution rate for most samples. The deceleration in Fe dissolution under RP2 ranged between 29% and 76%. The opposite performance was observed for two samples of the test-set, i.e., GP-CA and PS-SS, which exhibited an increase in Fe dissolution rate of 61% and 160% respectively.

7.2.3.2 Rainfall Pattern 3

Under the third rainfall pattern all samples displayed a substantial increase in dissolution, ranging between 0.04 µg/mL (DH-SS) and 0.09 µg/mL (PS-SS). The positive variation in the rate of dissolution corresponded to a 24% (DM-SS) to a 277% (DM-SS) rise.

7.2.3.3 Rainfall Pattern 4

The range of dissolution of RP4 fitted within the values of 0.03 µg/mL (GP-CA) and 0.07 µg/mL (DM-SS). The fourth rainfall pattern was characterized by a moderate decrease in the rate of dissolution for all samples. In only one case the dissolution rate of Fe under RP4 was higher compared to RP3, i.e., DM-SS. In

two cases, the rates under the two rainfall regimes were found to be equivalent. For the remaining samples, the rate variation fitted within a range of -5% to -53%.

7.2.3.4 Rainfall Pattern 5

Under the last regime, all samples displayed a decrease in dissolution rate, corresponding to a dissolution between 0.02 µg/mL (BL-SS, DH-SS, PS-SS) and 0.06 µg/mL (DM-SS). The deceleration of Fe dissolution was found to range between 19% (PT-SS) and 69% (PS-SS).

7.2.3.5 Overall trend

Most samples displayed a similar trend of Fe dissolution. Comparably to other analytes, the first exposure period was characterized by a higher release of Fe for most stone types. This was followed by a decrease in the rate of dissolution under RP2. The third rainfall patterns induced the overall higher dissolution rate across the test-set, after which most samples displayed a progressive decline in the dissolution rate. In this sense, Fe performance was distinctive when compared to the one displayed by other analytes. From RP3 the dissolution rate appeared to be inversely proportional to the increase in frequency of the exposure cycles and decrease in volumes of surrogate rainwater for most samples.

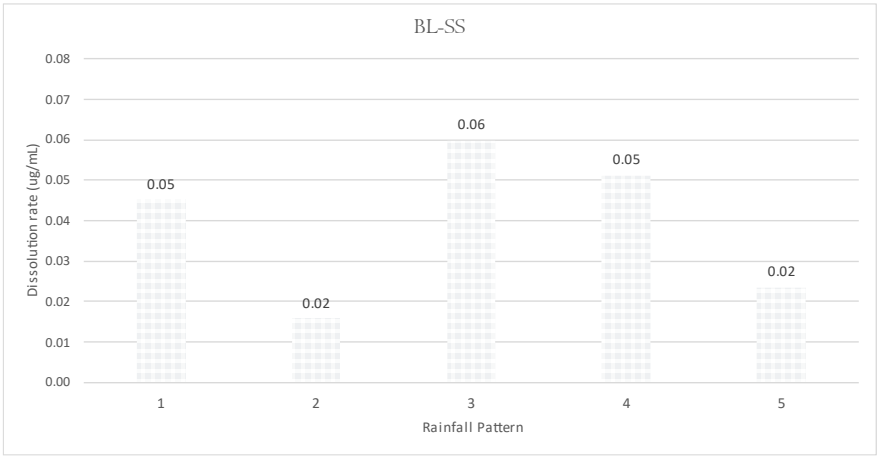

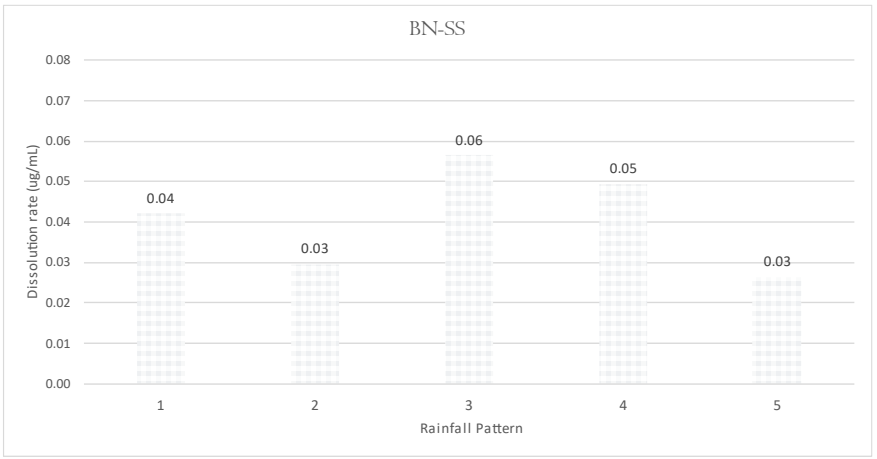

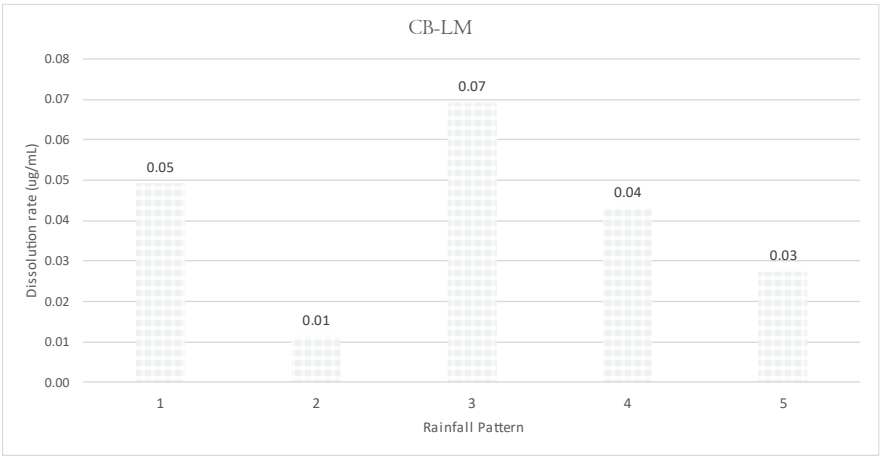

Figure 7-20: mean Fe dissolution at each rainfall patterns of BL-SS, BN-SS and CB-LM

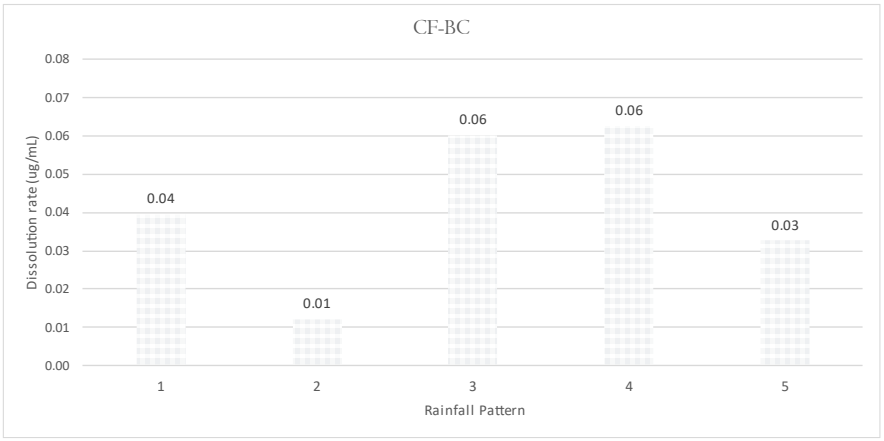

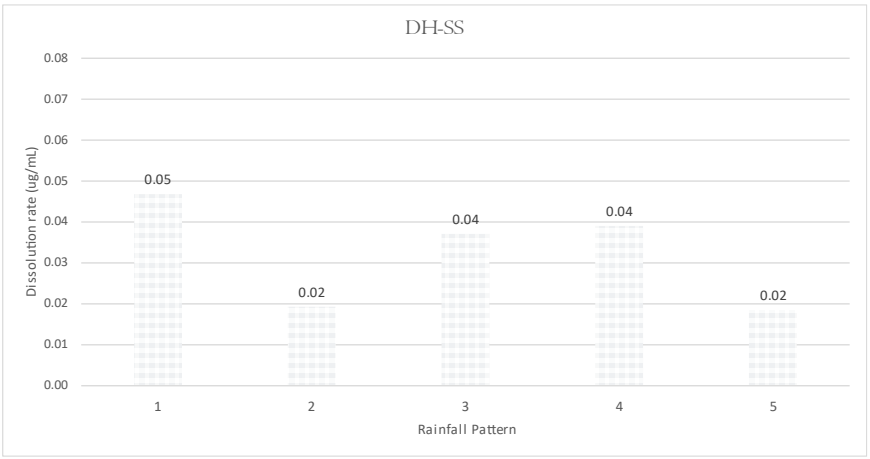

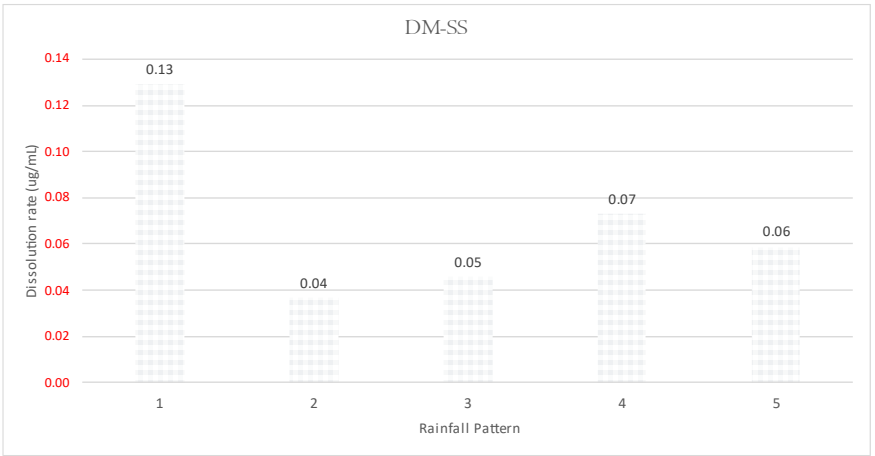

Figure 7-21: mean K and Na dissolution at each rainfall patterns of CF-BC, DH-SS and DM-SS.

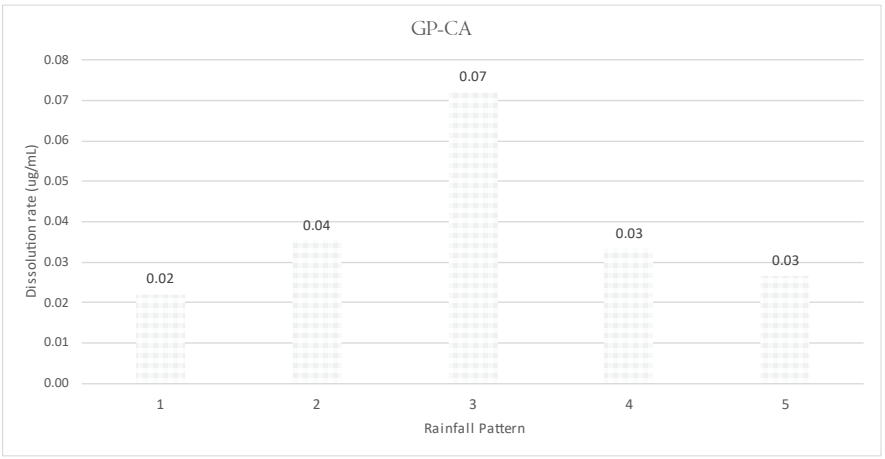

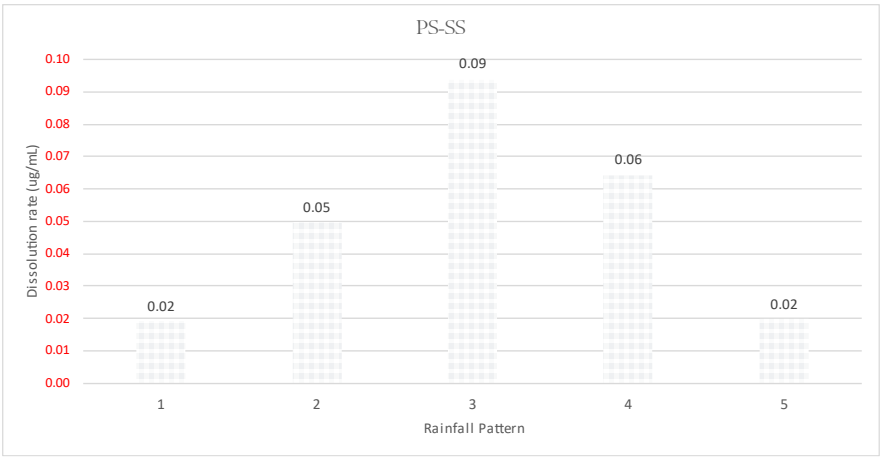

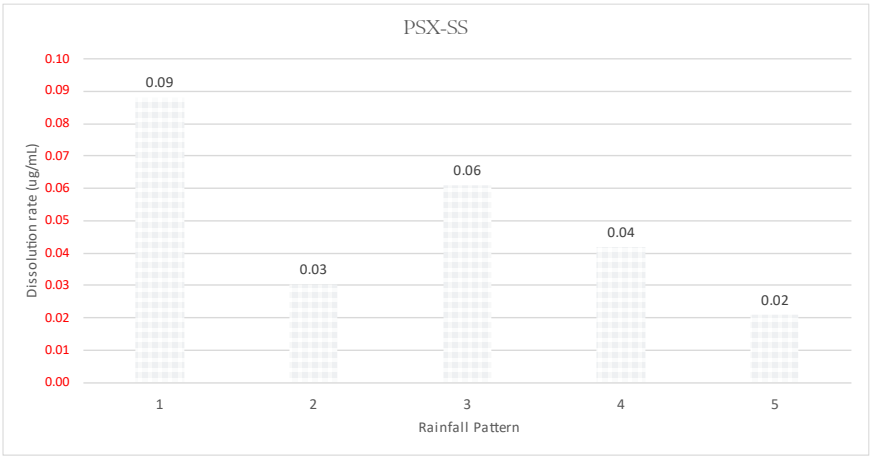

Figure 7-22: mean Fe dissolution at each rainfall patterns of GP-CA, PS-SS and PSX-SS

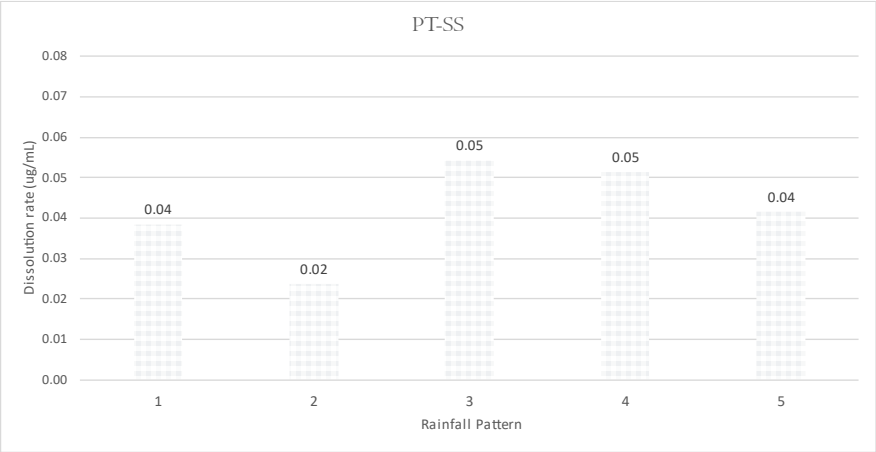

Figure 7-23: mean Ca dissolution at each rainfall patterns of PT-SS

Table 7-5: percentage variation in dissolution rate of Fe under different rainfall patterns

Sample	RP2	RP3	RP4	RP5
BL-SS	-65%	+ 277%	-14%	-53%
BN-SS	- 29%	+ 91%	- 12%	- 46%
CB-LM	- 76%	+ 495%	- 37%	- 36%
CF-BC	- 69%	+ 395%	+ 4%	-47%
DH-SS	- 58%	+ 93%	+ 5%	- 52%
DM-SS	- 71%	+ 24%	+ 59%	- 19%
GP-CA	61%	+ 102%	- 53%	- 20%
PS-SS	160%	+ 89%	- 31%	-69%
PSX-SS	- 65%	+ 100%	- 31%	-50%
PT-SS	- 38%	+ 128%	- 5%	- 19%

7.3 Control Intervals for test-set 3

Control Intervals (CI) captured the mean dissolution of Ca and Mg at specific intervals of time (figure 7-25 to 7-28). Each exposure interval of test-set 2 corresponded to an exposure interval of test-set 3, during which comparable volumes of water were delivered to the samples.

7.3.1 Control interval 1

Except for BN-SS and DH-SS, the average dissolution rate of the first control interval (CI1) of test-set 2 was higher compared to the following exposure periods. The highest value from CI1 was obtained for PSX-SS, with a mean Ca dissolution rate of 3.20 ug/mL. The lowest value was obtained for DM-SS, with a mean Ca dissolution rate of 0.86 ug/mL. Magnesium displayed consistently lower mean dissolution values at CI1 compared to Ca. The lowest dissolution rate was displayed by BL-SS, corresponding to 0.14 µg/mL. The higher dissolution rate of Mg was obtained from PSX-SS, with a mean dissolution for CI1 of 1.40 µg/mL.

7.3.2 Control interval 2

The second control interval (CP2) of test-set 2 displayed a consistently lower Ca dissolution rate compared to the first one. The only exception was represented by BN-SS and DH-SS. The values of dissolution for these two stone types were

comparable in both CI1 and CI2, corresponding to 1.25 µg/mL and 1.26 µg/mL in BN-SS and 1.28 µg/mL and 1.29 µg/mL in DH-SS. The difference between CI1 and CI2 reflected the high Ca dissolution rate displayed by the first sampling points. Also Mg showed lower mean dissolution under CI2 compared to CI1, except for CB-LM and DM-SS, whose mean dissolution was higher under the second CI.

7.3.3 Control Interval 3

Calcium dissolution rates further decrease in the third control interval (CP3). The only two exceptions were represented by BL-SS and DM-SS, whose mean dissolution values at CI3 were comparable to CI2. The lowest and highest rate for CI3 were displayed by CF-BC and GP-CA, corresponding to 0.49 µg/mL and 1.16 µg/mL. A comparable performance was observed for Mg, whose mean dissolution under CI3 was consistently lower across the test-set than CI2. Only BL-SS showed a higher dissolution rate for Mg during CI3, with a mean dissolution of 0.19 µg/mL against the 0.07 µg/mL provided by CI2.

7.3.4 Control Interval 4

After the third control interval, Ca dissolution appeared to accelerate. The rate of dissolution increased for most samples under the fourth control interval (CI4) at different levels. For instance, CF-BC mean dissolution moved from 0.49 µg/mL to

1.25 µg/mL, while GP-CA reached 1.89 µg/mL. For other stone types, the change in rate was less relevant, as in the case of BN-SS (1.11 to 1.28 µg/mL), DM-SS (0.56 to 0.58 µg/mL), or PT-SS (0.73 µg/mL to 1.01 µg/mL). Only in two cases, the rate of dissolution kept decreasing after CI3, i.e., CB-LM (0.89 µg/mL to 0.56 µg/mL), and DH-SS (1.05 µg/mL to 0.86 µg/mL). This behaviour was less evident with Mg dissolution. The apparent acceleration in dissolution rate occurred for a lower number of samples (BN-SS, CF-BC, DM-SS, GP-CA, PS-SS and PT-SS) and on a different scale compared to Ca.

7.3.5 Control interval 5

The rate of Ca dissolution appeared to further increase at the last control interval (CI5). For instance, Ca dissolution rate of BL-SS increased from 1.11 µg/mL to 1.79 µg/mL. The same applied to CB-LM, which experienced an increase from 0.56 µg/mL to 0.77 µg/mL, CF-BC (1.25 µg/mL to 2.04 µg/mL), DH-SS (0.56 µg/mL to 1.05 µg/mL), GP-CA (1.89 µg/mL to 2.30 µg/mL), PSX-SS (1.36 µg/mL to 1.47 ug/mL) and PT-SS (1.01 µg/mL to 1.44 µg/mL). The only exceptions that exhibited a slight decline in the mean dissolution during the last control interval of test-set 2 were BN-SS (1.28 µg/mL to 1.22 µg/mL), DM-SS (0.58 µg/mL to 0.45 µg/mL) and PS-SS (1.11 µg/mL to 1.06 µg/mL). Similarly, Mg displayed an increase in dissolution during CI5 compared to CI4, however the scale of the variation between the two control intervals was smaller. For instance, the mean dissolution of Mg for BL-SS increased from 0.12 µg/mL (CI4) to 0.16 µg/mL (CI5). For CB-LM, the mean dissolution value moved from 0.41 µg/mL (CI4) to 0.56

µg/mL (CI5). With GP-CA, the dissolution rate of CI5 was of 0.43 µg/mL, as opposed to the 0.36 µg/mL experienced during CI4.

7.3.6 Overall trend of control intervals

Most samples displayed a comparable trend. The initial control intervals presented an initial decline of the rate of dissolution which reached the lowest value at control interval 3. From CI3 it was observed an overall increase in the rate of dissolution within a rather short timeframe. Control intervals refer to different timeframe of exposure. Each of the last two control intervals represents one week of exposure, as opposed to the rates experienced during CI1, which referred to an exposure of 2 months.

Among the samples that experienced an increase in the rate of Ca dissolution from control period 3 to control period 5, the acceleration coefficient varied across the dataset. For instance, BL-SS experienced an 81% increase in the rate of dissolution, while in BN-SS the positive variation in dissolution rate corresponded to only 9%. The most significant alteration was presented by CF-BC, whose rate of Ca dissolution increased by 122% at the last control period.

A similar performance was observed with Mg on a lower scale and for a fewer number of samples. A positive continuous increase in dissolution rate from CI3 to CI5 was only observed for CF-BC, GP-CA and PT-SS.

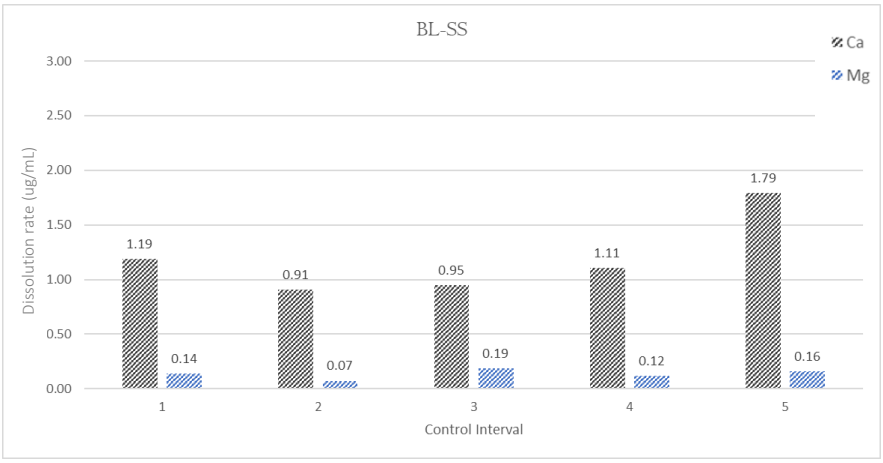

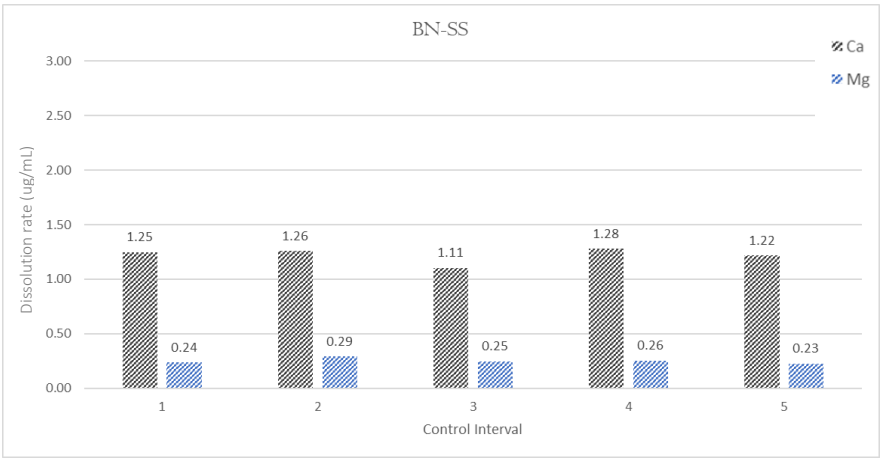

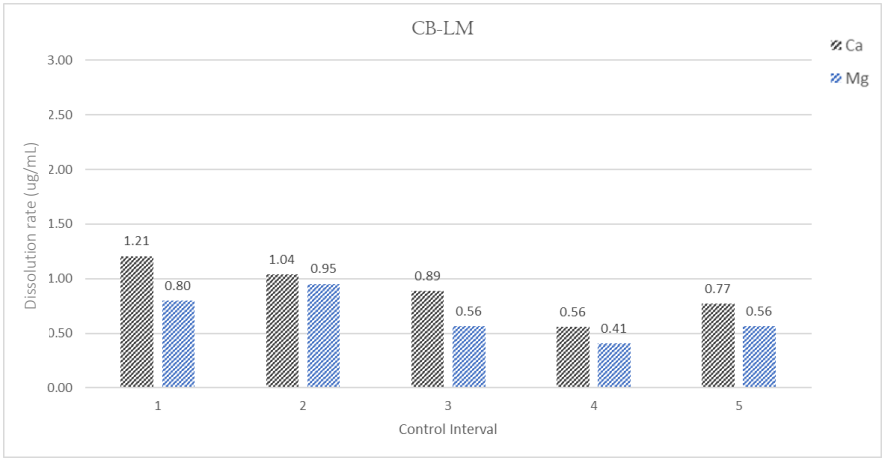

Figure 7-24: control intervals of test-set 2 exposure of BL-SS, BN-SS and CB-LM.

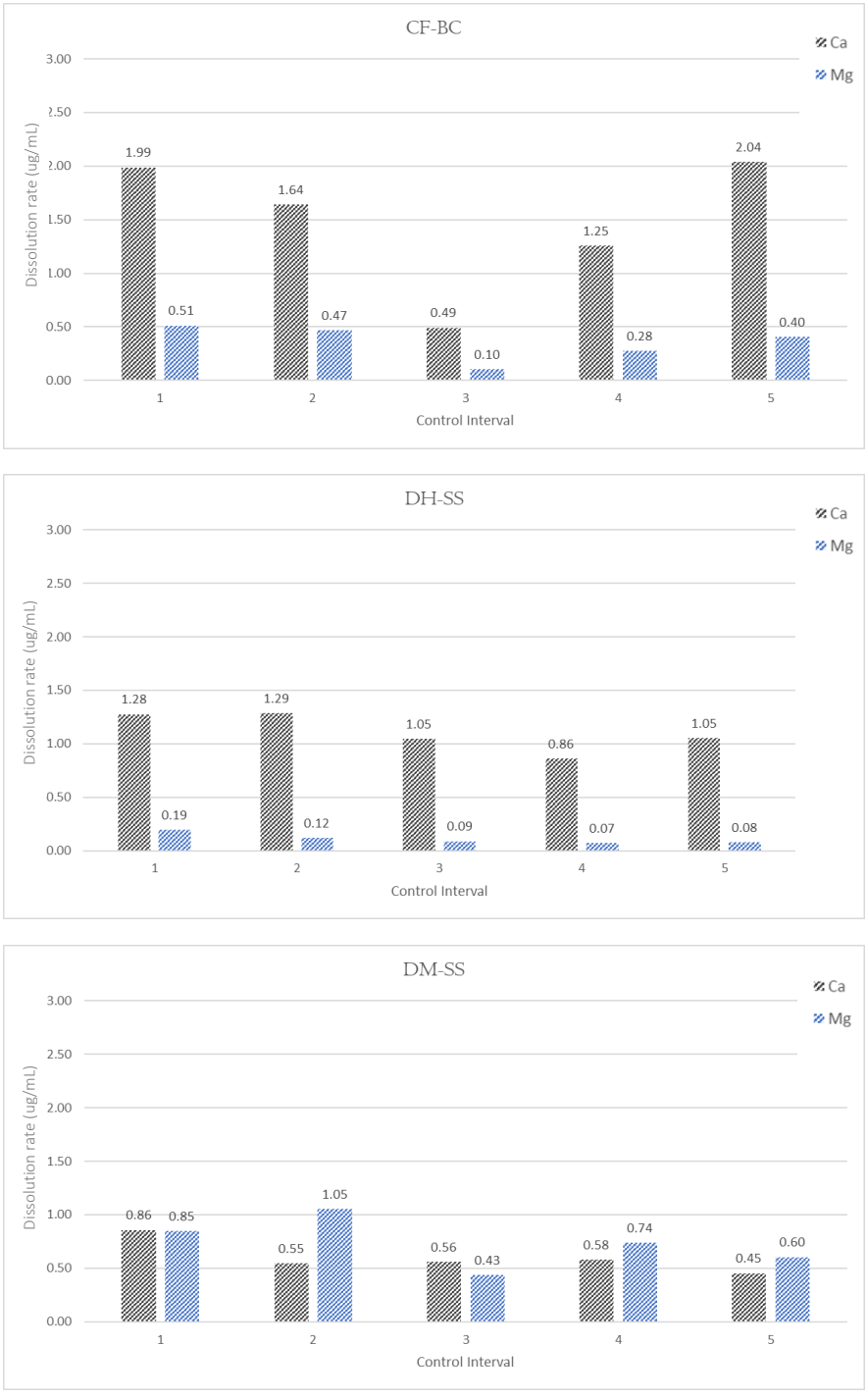

Figure 7-25: control intervals of test-set 2 exposure of CF-BC, DH-SS and DM-SS.

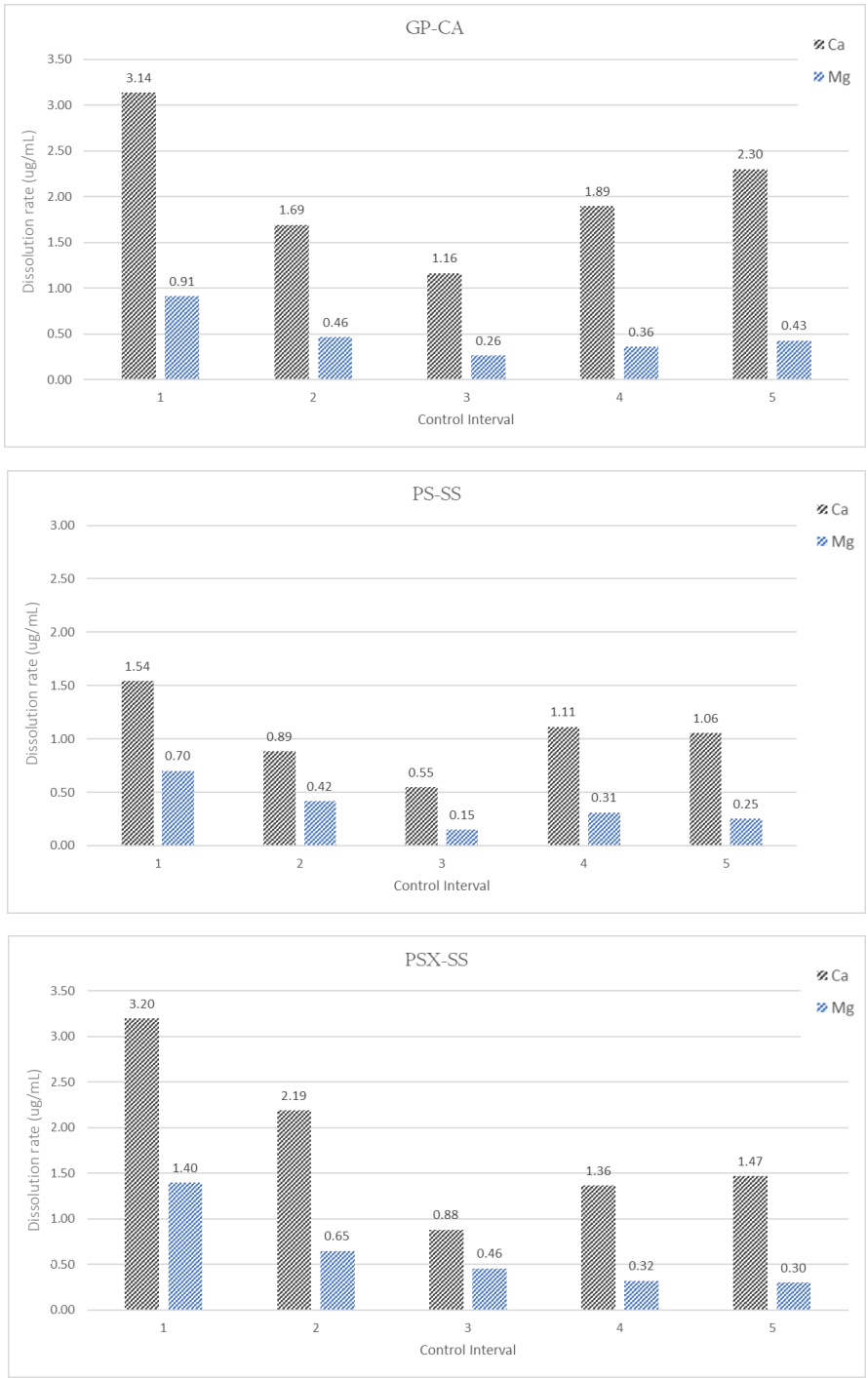

Figure 7-26: control intervals of test-set 2 exposure of GP-CA, PS-SS and PSX-SS.

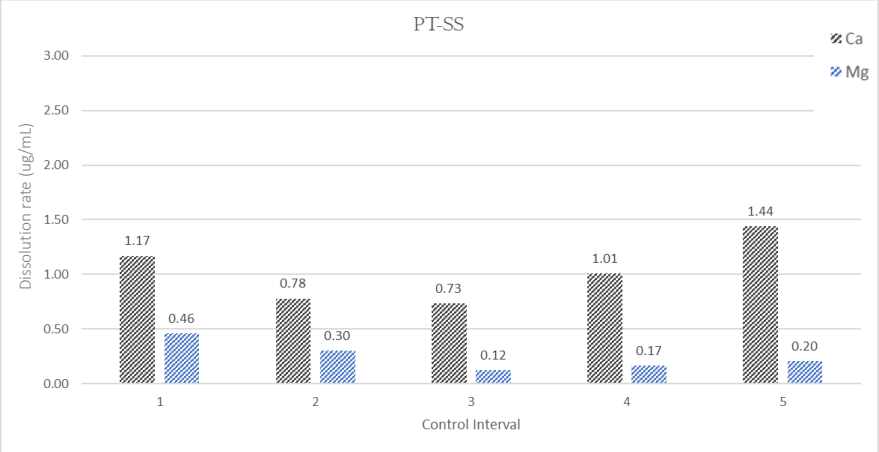

Figure 7-27: control intervals of test-set 2 exposure of PT-SS.

7.4 Comparison between Calcium mean dissolution rates under rainfall patterns and control intervals

The dissolution rates at each rainfall interval were compared to the dissolution rates obtained from analogous timeframes of exposure of test-set 2 under stable conditions. Results are displayed in figures 7-29 to 7-32.

7.4.1 Rainfall Pattern 1

Comparison of Ca dissolution under RP1 with the first control interval (CI) of test-set 2 provided variable levels of fluctuations. Some stone types displayed a higher level of dissolution under RP1 compared to CI1. Among the stone types that experienced a positive variation in dissolution rate, BN-SS provided the highest divergence from CI1, corresponding to a 64% variation. Where the variation was found to be negative, GP-CA underwent a 61% decrease in mean dissolution when subject to RP1 conditions.

7.4.2 Rainfall Pattern 2

Under the second rainfall regime, most samples displayed a negative variation of the dissolution rate compared to CI2. For these samples, the divergence between dissolution rates under RP2 and CI2 was found to range between 44% (GP-CA) and 11% (BN-SS). Only DM-SS, PS-SS and PT-SS exhibited an increase in dissolution under RP2, corresponding to a 59%, 7% and 34% variation respectively.

7.4.3 Rainfall Pattern 3

Most samples displayed higher dissolution values under RP3 compared to the third control interval. The fluctuation between RP3 and CI3 was substantial, ranging between a 12% (BN-SS) and 235% (PSX-SS). The only exception was

represented by DH-SS, whose dissolution rate exhibited a divergence from CI3 of only 9%.

7.4.4 Rainfall Pattern 4

Comparison with the fourth control interval showed a higher dissolution rate with RP4 for all samples, ranging between 5% (BL-SS) and 147% (DM-SS). A clear trend in the level of divergence between CI4 and RP4 and CI3 and RP3 was not observed. For some samples, the difference was greater under RP4 (BN-SS, CB-LM, DH-SS, DM-SS). For others, the opposite situation was observed (BL-SS, CF-BC, PS-SS, PSX-SS, PT-SS). In one case, no difference was exhibited between the two RPs (GP-CA).

7.4.5 Rainfall Pattern 5

Except for BL-SS and PT-SS, all samples displayed a higher dissolution rate under RP5 compared to the control interval CI5. The divergence in dissolution rate between RP5 and CI5 fitted within the range of 21% (CF-BC) and 175% (DM-SS). For many stone types, the difference was substantial. For instance, PS-SS, experienced a 91% variation in Ca dissolution. Other samples fitted within the 70-50% increase, i.e., 78% for CB-LM, 74% for BL-SS, 74% for DH-SS, 55% for BN-SS, 51% for GP-CA and 50% for PSX-SS.

7.4.6 Overall trend

The lowest overall difference between RPs and CIs was displayed with the first and second regimes. For most samples, the variation between dissolution rates of rainfall patterns and control intervals was found in correspondence of RP3, RP4 and RP5. The last rainfall pattern in particular provided the overall higher difference between the mean dissolution values of RP5 and CI5. Test-set 2 and test-set 3 were exposed to equivalent conditions under CI4 and RP4. For some samples, a good level of correspondence was determined between the dissolution rates of both test-sets. For instance, BL-SS displayed the lower variation in correspondence of this exposure interval, with only a 5% change in dissolution rate between RP4 and CI4. In other cases, the difference was substantial, as in the case of CB-LM (137%).

A possible reason for the divergence of dissolution values acquired from comparable exposure conditions refers to the influence of previous exposure condition. Although the overall volumes of surrogate rainwater distributed at RPs and CIs were equivalent, the duration of the exposure was not the same for the two test-sets. The volumes distributed by RP1 over one month corresponded to the volumes of surrogate rainwater received by the samples during two months of exposure (CI1). This implies a potential effect of the duration of the rainfall event over the future rates of dissolution, as well as of the overall timeframe of exposure.

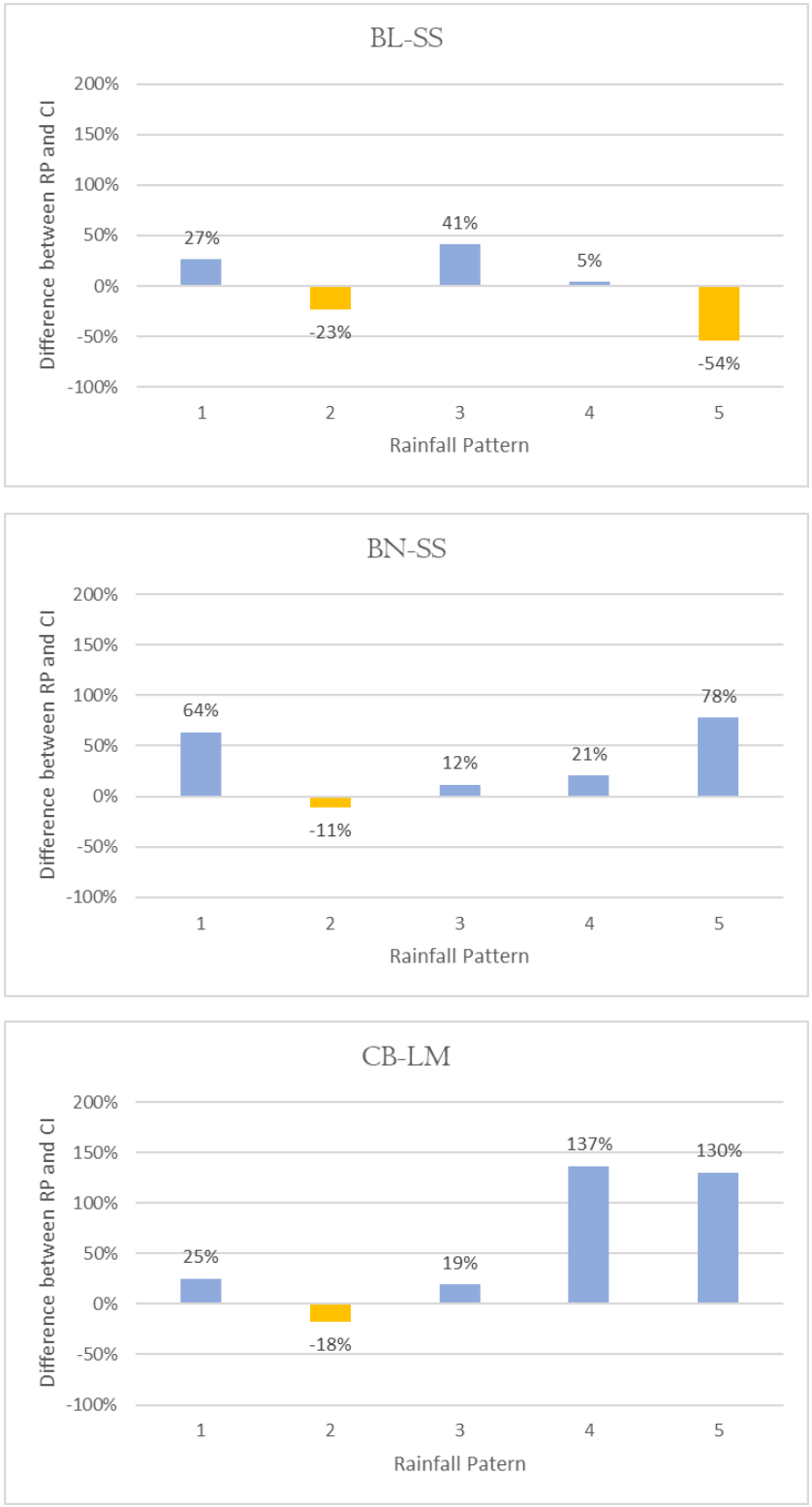

Figure 7-28: percentage difference between Ca dissolution values of rainfall patterns and control intervals for BL-SS, BN-SS and CB-LM.

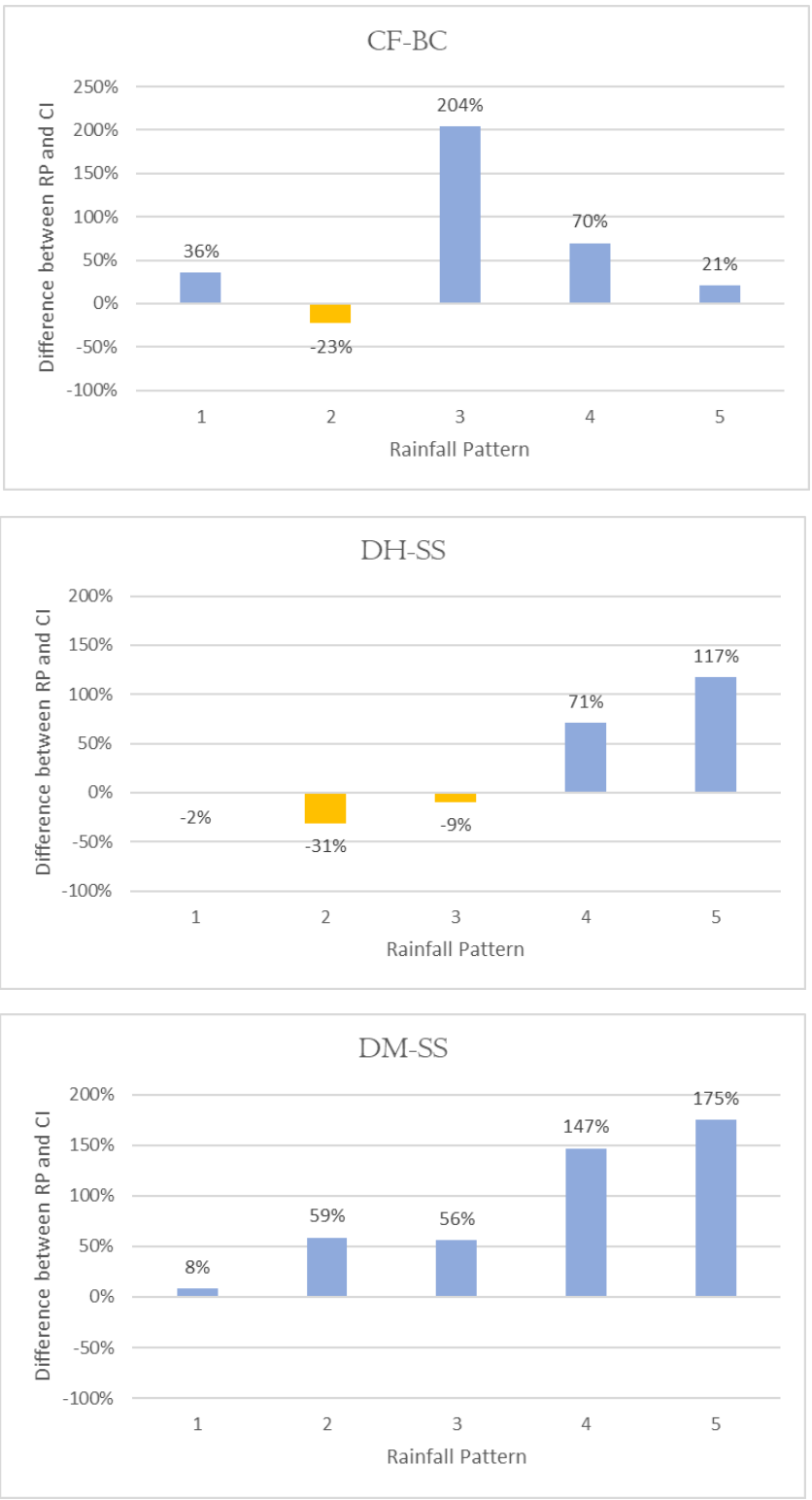

Figure 7-29: percentage difference between Ca dissolution values of rainfall patterns and control intervals for CF-BC, DH-SS and DM-SS.

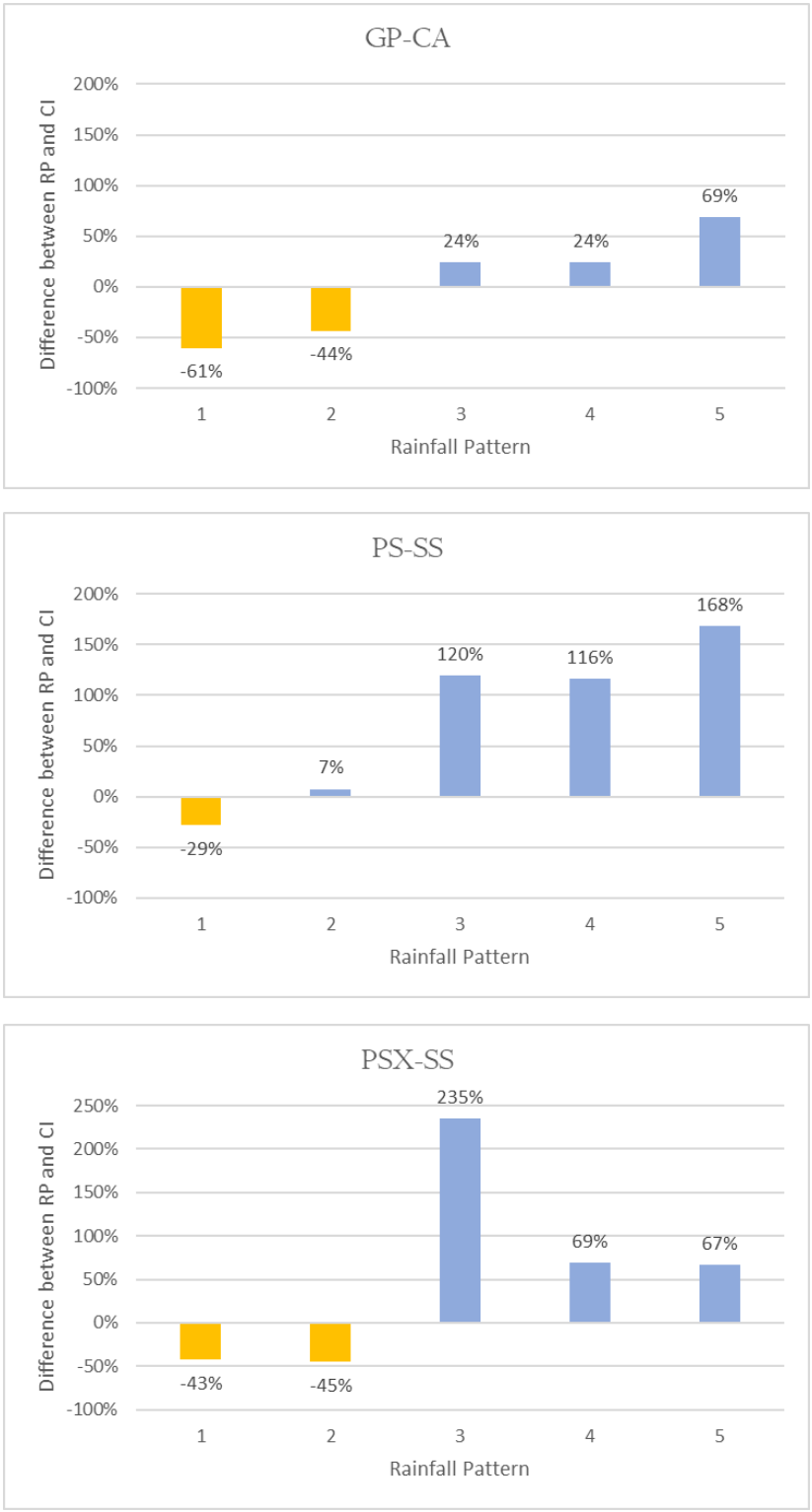

Figure 7-30: percentage difference between Ca dissolution values of rainfall patterns and control intervals for GP-CA, PS-SS and PSX-SS.

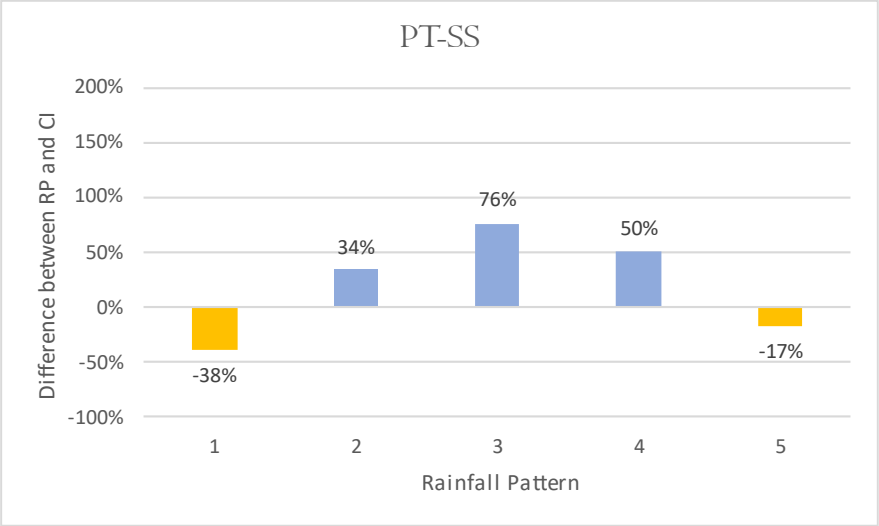

Figure 7-31: percentage difference between Ca dissolution values of rainfall patterns and control intervals for PT-SS

7.5 Weight Change

All samples from test-set 3 experienced a negative weight change (Figure 7-33). Different levels of mass-loss were exhibited by the samples. The highest value was achieved for BN-SS, which displayed a 5.11% loss of its original mass. Bernese sandstone was followed by BL-SS, whose mass-loss was equivalent to 1.18% change from its original value. These two samples displayed a significantly higher change in weight compared to the rest of the test-set. The third sample by mass-loss value was found to be PSX-SS, whose weight variation corresponded to 0.13%. The relationship between mass-loss and mineral dissolution rate will be discussed in Chapter 9.

Table 7-6: mass loss values of test-set 3 after exposure

Sample	Pre-exposure weight (g)	Post-exposure weight (g)	Mass loss (g)	Mass Loss (%)
BL-SS/B4	90.172	89.100	1.072	-1.189
BN-SS/A6	68.742	65.223	3.519	-5.119
CB-LM/A3	69.223	69.174	0.049	-0.071
CF-BC/A5	54.134	54.088	0.046	-0.085
DH-SS/B3	73.120	73.052	0.068	-0.093
DM-SS/A1	59.584	59.519	0.065	-0.109
GP-CA/B6	58.355	58.347	0.008	-0.014
PS-SS/B2	64.145	64.112	0.033	-0.051
PSX-SS/A2	63.960	63.874	0.086	-0.134
PT-SS/B5	65.560	65.544	0.016	-0.024

Figure 7-32: mass loss experienced by the stone types of test-set 3.

8. Discussion of results and implications in the modelling of the stone performance

8.1 Advancements in the design of accelerated weathering methodology

The simulation of natural stone weathering under artificial conditions is notoriously complex to achieve, due to the impossibility of accurately reproducing all the possible factors that contribute to the process of decay (Lisci et al., 2023). Nonetheless, artificial laboratory weathering should still try to maximize the replicability of the natural environment to which the tested stones are exposed (Gomez-Heras and Fort, 2006). The proposed design for an exposure apparatus aims at offering a solution to fit the requirement of a realistic simulation of the interaction between the stone and rainwater, while allowing for the investigation of the process of dissolution during exposure. The developed methodology offered an innovative solution to the most common approaches to the simulation of building stone exposure to rainwater under laboratory conditions. At present, the samples immersion represents one of the most common laboratory tests of chemical decay processes (Eyssautier-Chuine et al., 2016; Franzoni and Sassoni 2011; Gybeaux et al., 2018; Holynska et al., 2003; Kryza et al., 2009; Thornbush and Viles, 2007). Despite providing informative data over the interaction between

samples and solution, exposure by immersion fails to fully characterize the weathering process and does not provide a sufficient level of representativity of the decay progression. With immersion, the contact time between the stone and the water solution is continuous and allows for the saturation of the stone. In contrast, the spraying of the solution is more representative of the real conditions that govern the interaction. These limitations have been previously acknowledged within the context of laboratory ageing of cementitious materials (Jabbour et al., 2022). Exposure to acidic solutions by immersion of the sample is subject to continuous alterations of the solution pH as the leaching process progresses (Tecer, 1999).

Compared to the sample immersion, the spraying of the solution provides a better representativity of real exposure conditions and does not require the regular adjustment of the solution pH to maintain it at a constant value. Labus and Bochen (2012), Fereidooni and Khajevand (2017) and Tacer et al., (2009) adopted a spraying system to replicate the samples weathering under artificial laboratory conditions, which was examined in terms of weight variation. As a result, none of these included a collection system for the samples leachates to assess the progression of the weathering throughout exposure. The same consideration applies to the use of environmental chambers, which usually do not involve the collection of the run-off solution. The exposure apparatus here presented was designed to address these constrains, while allowing for a consistent and replicable experimental process.

At present, one of the most relevant requirements for field and laboratory exposure refers to the comparability of results obtained from different studies. This condition can be significantly affected by dissimilarities in the methodological

approach applied for their acquisition. This is why accelerated exposure methods for the study of the effects of rainwater on stone samples require a standardization. The proposed exposure apparatus allowed for the acquisition of dissolution data across the different exposure trials in a consistent and replicable way. Additionally, the use of single exposure units for each individual sample allows to easily variate their number based on necessity, as well as to modify their arrangement. Furthermore, the dimension of the stone samples provides the advantage of conducting the exposure within a limited space. Thanks to the straightforward design, easy installation, and use of common materials, the exposure apparatus here presented may provide a solution to standardize laboratory testing of stone samples exposed to precipitation, in both academic and industrial contexts.

8.2 Factors affecting the stone vulnerability to rainwater exposure

The trace element analysis was consistent with the hypothesis that carbonate minerals represent the main phase involved in the dissolution process. Calcium and Mg were the elements with the highest release for all samples and the most important discriminatory variables as established by the principal component analysis. This finding is consistent with the overall higher susceptibility of carbonate minerals to dissolution upon contact with acidic solutions (Bauer and Velde, 2014). Calcium and Mg represented the dominant analytes in all samples, followed by Na and K. Iron was the analyte whose concentration was the lowest

for all stone types. This finding was in agreement with the results obtained from the analysis of the leachates obtained from field exposure studies (Sweevers et al., 1998).

These results suggest the contribution of additional factors to the overall stone performance. The application of X-ray μCT only allowed for an incomplete characterization of the samples employed in the controlled exposure. This limitation impacted on the possibility of acquiring accurate data on the samples composition and pore structure. However, the influence of porosity on the decay progression is well documented.

In this respect, the respective responses of PSX-SS and PS-SS to comparable conditions is meaningful. Pietra Serena Extradura (PSX-SS) and Pietra Serena (PS-SS) present similar mineral composition but different density and levels of porosity. However, the rate of Ca dissolution of PSX-SS was higher than that experienced by PS-SS. This consideration is consistent with the reported findings of Buj et al., (2010), who suggest that stones with low porosity and a high amount of micropores are more susceptible to degradation compared to stones with high porosity and high average pore radius when these are characterised by a lower connectivity and high tortuosity.

To some extent this was also verified during the variability test. The residual moisture contents recorded after the drying of the samples, but before exposure to the surrogate rainwater, were an average of 1.1 ± 0.12 % in BN, 0.56 ± 0.06 % PT-SS, and 0.09 ± 0.02 % in CB-LM. Moisture content is a function of several intrinsic parameters, such as the pore volume, their size and distribution, geometry and level of interconnection (Franzen and Mirwald, 2004), all associated

to the stone durability. Indeed, stone decay can be correlated to moisture transport and retention, as most mechanisms, including chemical weathering, require the presence of water (Torraca et al., 2009). Similarly, the type of porosity might also be associated to the different variations in dissolution rate of the different stone types in response to an alteration of the exposure cycles. At present, the data produced by this study is insufficient to fully verify this hypothesis, although the connection between the rate of water absorption and the pore system of the stone is well known (Gibeaux et al., 2018) and the influence of porosity on the decay progression is well documented in literature.

The pores' dimension has been indicated as one of the most important structural parameters for the stone deterioration (Torraca, 2009); in this respect, the relative impact of very large pores depends on how these are interconnected (Benavente, 2011). The observation of the larger pores from the X-ray μCT scans of CB-LM showed a poor level of interconnection. This might explain the better performance displayed by CB-LM compared to other samples despite its nature as a carbonate stone. However, additional factor might also be linked to the presence of dolomite in the sample's composition, which was reported to increase the stone resistance to dissolution (Heidari et al., 2017) and salt crystallization (Alves et al., 2020).

Despite the reported importance of the pore system characteristics in controlling the stone vulnerability to chemical degradation (Benavente et al., 2004; Benavente, 2011; Germinario et al., 2019; Gibeaux et al., 2018; Uğur et al., 2020), these factors are usually not incorporated in prediction models for the chemical weathering of the stone. In most cases, DRFs were developed from a limited number of lithotypes, which were selected mostly on account of their carbonate nature. As a consequence, the suitability of prediction models to stone typologies

different from the ones that were tested is questionable. This concern was acknowledged by different authors. Lipfert (1989) stated that differences between the response of stone types exposed to the same conditions were likely to be significant. His function was postulated for generic calcite, rather than a specific stone typology, assuming a density constant of 2.7 g cm^{-3}. However, as observed by Bonazza et al. (2009), some stones with 20% porosity have an approximate density of 2.0 g cm^{-3}. Therefore, a wide variation between responses of carbonate stones is to be expected as a function of their different physical properties (Lipfert, 1989). Under the UNECE/ICP program, a sudden change in corrosion rate was reported corresponding with a change in the quality of the tested stone, with the adoption of specimens with a higher level of porosity and lower saturation coefficient (UNECE/ICP Environmental Report). Similarly, the employment of more than one stone type under natural conditions reported different levels of susceptibility between samples and the estimated surface recession caused by clean rain for different carbonate building stones was found to vary significantly with porosity values above 25% (Mikhailov, 2001).

The impossibility of adopting one stone typology to represent the performance of a class of samples is also contradicted by literature information in the context of physical decay. Accelerated exposure data suggests that the stone type does not provide sufficient information with respect to its resistance to decay (Mutluturk et al., 2003; Altindag et al., 2004; Jamshidi et al., 2015). Mutlutürk et al. (2003) noted that the response of a stone to physical ageing was sometimes more compatible with the performance displayed by a different stone type than with the response of a stone of the same nature. This finding was validated by other studies, which confirmed that different stone types often exhibited a more similar behaviour than

samples of the same type (Altindag et al., 2004; Jamshidi et al., 2013; Jamshidi at al., 2015). The same was found to apply to stones sourced from the same stratigraphic layer, and therefore presenting the same provenance (Ghobadi et al., 2014).

This was also shown by the contradictory outcomes obtained from the comparison of Decay Constants obtained from different accelerated exposure tests involving the same stone types (Hale and Shakoor, 2003; Mutlutürk et al., 2003; Yao, Zhang and Zhu, 2011; Akin et al., 2011; Wang et al., 2016; Abdelhamid et al., 2020). For this reason, most models can only be applied to stone typologies sourced from the same geographical area as the ones that were tested (Bayram, 2012), (Ince et al., 2016). This is due to the significant differences in internal characteristics that the same stone types can display, and which are found to be key control factors in the decay progression.

In this respect, it was observed that the integration of information on the stone physical properties significantly increased the statistical significance of the model (Jamshidi et al., 2015). For this reason, most damage functions integrate the stone porosity, or other related variables, as predictors of the stone performance (Amirkiyaei et al., 2021; Yavuz et al., 2006; Jamshidi et al., 2015; Ince et al., 2016; Bayram et al., 2012). Benavente et al. (2004) developed a petrophysical durability estimator based on the ratio between the pore structure and the strength of the material. Recently, also the stone compositional properties were included as predictors of the stone response in damage models of physical decay (Jamshidi et al., 2021).

Mineralogical information applied in the context of decay modelling against physical stress was integrated for the first time only recently (Jamshidi et al., 2021), although its contribution to the overall degradation process had been previously addressed. For instance, dissolved calcite was reported to be the fundamental mechanism affecting the material mechanical behaviour in the long-term (Ciantia et al., 2015). The incremental weakening process was reported to be caused by the gradual dissolution of the bonds and grains (Castellanza and Nova, 2004). A decrease in calcite content as a consequence of mineral dissolution was reported to be a leading factor in the exponential decrease of the deformation modulus (Momeni et al., 2017).

8.3 Dissolution trend under stable rainfall patterns

8.3.1 Variability in the dissolution rates of replicate samples

The determination of the variability in the responses of the same stone types under comparable exposure conditions was examined as a prerequisite for any following investigations of the samples' performances. The dissolution profiles obtained from each individual replicate suggested that their responses were comparable. Occasional differences in the rates of dissolution appeared to be connected to the minor alterations of the rainwater distribution. The level of susceptibility to such alterations was observed to be related to the stone type, and especially to the amount of carbonate minerals of each stone.

Stone is a heterogeneous material, therefore a level of dissimilarity in the performance of replicates is expected. This was also verified by a field exposure

study by Sweevers et al., (1998), who reported differences in the analytes concentrations in the leachate of replicate samples, with an RSD of to 14% for Ca and 15% for Mg. However, and despite the occasional discrepancies observed in correspondence of alterations of the surrogate rainwater distribution, replicate samples showed characteristic dissolution rates. This vas verified by the principal component analysis of the dissolution rate of the replicate samples, which discriminated each stone type could be discriminated based on its dissolution rates.

The same level of correspondence was also observed when the dissolution rates from different rounds of exposure were compared. The dissolution profiles obtained from the averaged dissolution rates of replicate samples were found to agree with the dissolution profiles obtained from the short-term exposure of test-set 1, which was subject to the same conditions as the variability test. These results indicate a consistency in the performance of the stone under equivalent conditions, which apply to both the trend of dissolution and the dissolution rate values at different sampling points.

8.3.2 Stages of the dissolution process

As demonstrated by the correspondence between dissolution profiles, Ca and Mg performed similarly. The main difference between the two analytes was the degree of variation in the rate of dissolution of Mg, which was less prominent and displayed an overall higher stability. The dissolution trends of Ca and Mg obtained from the initial stable exposure trials highlighted the presence of two distinct

stages in the profile of dissolution of every stone type (figure 8-1). The first stage was characterized by a progressive decline of the dissolution rate after the first sampling point. Only on rare occasions did the highest rate of dissolution does not correspond to the initial sampling point but to the second or third (PSX-SS and GP-CA). The magnitude of the change in rate was different between samples as shown by the steepness of the dissolution curve.

The initial higher dissolution rate was likely partially influenced by residues of the washing procedure, which were leached away during the initial phase of the exposure. Other factors might relate to the immediate solubilization of the mineral that are present on the surface of the stone and have been partially ground during the stone cutting process.

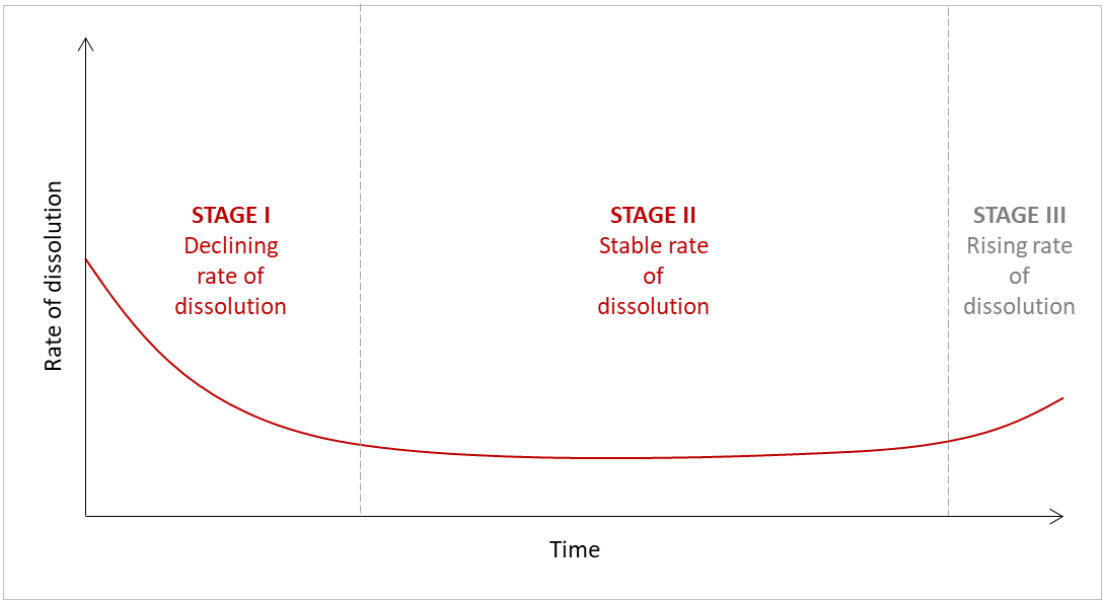

Figure 8-1: stages of the dissolution trend identified from the stable exposure rounds of test-set 1 and 2.

After the initial period, samples experienced a stabilization of the rate of dissolution, characterized by comparable dissolution values between sampling

points. A stable trend represented the dominant feature of the dissolution profile of Ca and Mg for most stone samples.

A constant dissolution is in partial disagreement with the outcome of previous studies, where the release of Ca and Mg was observed to increase with time (Holynska et al., 2004; Gibeaux et al., 2018). However, in these cases the artificial exposure process involved the immersion of the samples rather than the spraying of the solution on the surface. This suggests that the stone performance might have been influenced by the artificial weathering methodology, in which case the representativity of the stone performance would be affected. In contrast, a stabilization of Ca dissolution was reported from field-exposure data (Sweevers et al., 1998), which suggests that the natural process of mineral dissolution is better represented by the methodology adopted as part of the present study compared to immersion.

The limitations associated with laboratory exposure are well recognised (Jelle, 2012) and so are the issues connected to the correlation between laboratory and natural exposure data (Crewdson, 2011). Laboratory accelerated exposure allows control of the factors involved to evaluate the direct influence of independent variations of individual parameters, however the actual representativity of the natural process is an essential requisite. The progressive variations of the rates of degradation achieved under laboratory conditions have fundamental implications for the generation of data needed to formulate a model. When degradation is achieved as an artificial process, the metric to measure its progression is represented by the number of cycles rather than time. It is therefore important to determine whether an increase in the number of cycles corresponds to an evolution of the trend that is compatible to a natural progression.

The point to which a constant dissolution rate was achieved was found to vary across different stone types. Overall, it was observed that samples that presented higher early dissolution tended to reach stability later, compared to samples whose initial dissolution was relatively low. The duration of the first stage of dissolution was found to vary also depending on the analyte. Calcium reached a stable trend between the third and fourth sampling point, as opposed to Mg which usually achieved a stable performance after the second sampling point. For the short-term exposure of test-set 1, samples did not display any significant variation of the trend after having reached a steady dissolution rate. A small alteration was instead observed at the end of the long-term exposure of test-set 3, where some displayed a slight increase in the rate of Ca dissolution. However, the trend variation was not substantial enough to fully demonstrate the presence of a third stage in the process of dissolution. Dissolution trends of most samples exhibited occasional variations of the dissolution profiles, which can be connected to several external factors, including a temporary change in the surrogate rainwater distribution or fluctuations of the room temperature. The two major stages of the dissolution process, i.e., the initial decrease and the following stabilization of the dissolution rate, applied to different extent to each analyte. Iron was the only exception, as no substantial variation was observed throughout the exposure.

The occurrence of alterations in the rate of the stone degradation were also reported by studies involving accelerated artificial exposure to physical stressors. The occurrence of an acceleration of the decay process for carbonate rocks exposed to physical decay was verified by Martínez-Martínez et al., (2013). The study found that the evolution of decay in response to the freeze-thaw action is not linear but displays a sudden acceleration following a stable phase. The point

where the stone degradation experienced an acceleration, identified as critical weathering threshold, was reportedly reached at different moments for different stone types, mainly based on the characteristics of their pore structure.

Similarly, building stone exposed to salt weathering experienced three stages of degradation (Angeli et al., 2007). The last stage of the process was found to be connected to a weight decrease in connection to the propagation of the damage caused by the salts' cyclic crystallization. Within the context of the same study it was concluded that a significant variation of the stone performance could be observed within the deterioration progression. Angeli et al, (2007) suggested that a higher initial resistance of the stone not necessarily is preserved through time but might be subject to changes in the rate of the decay progression.

Prediction models developed from field exposure data normally assume a constant trend of the stone degradation (Saba et al., 2018). The representativity of such models would be limited if a variation of the stone performance was established. In this respect, the acquisition of long-term data by field exposure is subject to a time constrain. For instance, the study conducted by Delalieux et al., (2002) involved an exposure period of three years. Other models were developed from a 4-years exposure (Kucera and Fitz, 1995). The timeframe adopted by these exposure programs under natural conditions might not be sufficient to acquire a representative trend of the stone response to outdoor exposure. As a consequence, the models derived from data acquired by field-exposure might have limited accuracy in predicting the performance of the stone beyond a certain point in time.

The results here presented of the short- and long-term exposure trials provided an insight into the evolution of the relationship between the dissolution rates of different samples. The comparison between the dissolution trends of Ca and Mg displayed a progressively higher correspondence between the dissolution rates of different stone types as leaching progressed. This feature was more evident in the short-term exposure test, while the long-term performance was affected by occasional divergence between the dissolution rates at different sampling points. This indicates a progressive stabilization of the trend, as well as a gradually increasing compatibility between the response of different stones types to the same conditions.

8.3.3 Relationship between weight change and mineral dissolution

A direct relationship between weight change and rate of dissolution was verified only in some cases during the short-term exposure of the samples. For instance, PSX-SS reported the highest overall dissolution rate and weight loss. The sample PS-SS displayed a similar behaviour, where high dissolution rates of Ca and Mg were found to correspond to high values of mass-loss. Correspondence between dissolution rate and weight change was also verified for CB-LM. Despite its carbonate nature, the sample showed an overall better resistance to dissolution, which was substantiated by the low mass-loss values compared to the rest of the test-set. The same results were obtained from the variability test, where mass-

loss was found to follow the concentration of the carbonate minerals content, with the highest and lowest values reported for CB-LM and PT-SS respectively.

In contrast, the relationship between weight change and dissolution rates could not be evaluated for the long-term exposure of test-set 2. A weight increase was recorded for some stone types, possibly caused by the crystallization of salts forming after the interaction with the surrogate rainwater solution. The formation of nitrocalcite was reported following the dry and wet deposition of nitrogen oxides (Yerrapragada et al., 1996). This suggests that the time adopted for the post-exposure washing procedure was insufficient in eliminating the salts that formed during the accelerated weathering of the samples.

The relevance of weight change relates to its implications on the progressive erosion of the building stone. Mineral dissolution represents the mechanisms underlying the process. However, it can be used only to some extent as an indicator of the stone degradation due to its underestimation of the actual damage to the stone. The reason is that mineral dissolution only partially regulates the weight loss, as part of it is controlled by the disaggregation and mechanical detachment of the grains (Labus & Bochen, 2012). This was shown when field exposure studies integrated different approaches for the quantification of the stone degradation. Divergent results were obtained from the confrontation of dissolution results with gravimetric and interferometric data, as mass-loss and surface recession (Baedecker et al., 1992) or mass loss and surface roughness (Jaynes and Cooke, 1986). Recession rates based on interferometric and gravimetric methods proved to be double (marble) and triple (limestone) the recession rate obtained from run-off calcium concentrations in the run-off water (Baedecker et al., 1992). This observation is compatible with the divergence

observed between measured and predicted values obtained from different models. For instance, Lipfert's model provided the best fit to the experimental data acquired by Delalieux et al., (2002), while the predicted losses from Baedecker's model always underestimated the actual values of surface recession (Delalieux et al., 2002). On some occasions, measured erosion values were more than three times higher compared to responses obtained from other models (Inkpen, 2012).

In general, suspended particulate matter in the leachate coming from the physical detachment of stone particles was found to contribute up to 50% on average to the total material loss of limestone (Roekens and Van Grieken, 1989). As a result, the dissolution data here presented should inform about the trend of dissolution and the related controlling factors, and not provide a full representation of the actual damage.

8.4 Dissolution trend under variable exposure conditions

The influence of the rainwater cycle duration on the rate of dissolution was tested during a long-term exposure, where samples were subject to cycles of progressively shorter duration and increased frequency. Results verified the dependency of the dissolution rate of Ca and Mg on the duration of the rainfall event. All samples exhibited a variation of the dissolution rate in correspondence to decreased rainwater volumes, and for most samples it corresponded to an increase in the rate of dissolution. The acceleration of the dissolution rate was not the same across the test-set but varied depending on the stone type. Some

samples appeared to be more affected by changes in exposure conditions while, for others the alteration of the dissolution rate was less significant. Among all analytes, Ca displayed the highest susceptibility to variations in exposure conditions. This observation was consistent with the results of field exposure studies where, as opposed to other analytes, Ca and to a lesser extent Mg showed seasonal variability (Sweevers et al., 1998).

A correlation between higher dissolution rates and shorter rainwater cycles was not evident for a small number of samples. Among these, one showed the highest susceptibility under RP3 (BL-SS), whilst others exhibited the highest dissolution rates under RP4 (DM-SS and PT-SS). The same performance was reported from previous exposure rounds. For instance, PT-SS replicate samples displayed a better stability to occasional alterations of the surrogate rainfall volumes compared to BN-SS and CB-LM. In contrast, BN-SS and CB-LM showed divergent results in the response of individual replicates due accidental minor variations in the volume of surrogate rainwater. Thus, the dependency between dissolution rates and rainwater cycles duration appeared to be related to the concentrations of carbonate minerals in the sample. It was observed that the stone types that exhibited a negative variation in the rate of dissolution presented little (PT-SS and DM-SS) or no concentration of carbonate minerals (BL-SS). These results suggest that the type of response to variations in the rainfall distribution pattern likely depends on the carbonate mineral content of the stone. In this respect, the contact time of the surrogate rainwater with the sample is expected to be a controlling factor of the dissolution rate.

Most DRFs account for the effect of rainwater in terms of volume, with the most frequent precipitation predictors being rainwater acidity and yearly precipitation

(Lipfert, 1989; Webb et al., 1992; Yerrapragada et al., 1996; Delalieux et al., 2002). To some extent, this affects the accuracy of the stone response, which can fluctuate significantly depending on the duration of the rainfall event and on the stone characteristics. The present results show that the overall volume of rainwater received within a certain period of time is secondary to the distribution pattern. For instance, from RP2 to RP5, samples received equivalent volumes of surrogate rainwater within 24 hours. The variation was in terms of the frequency of the distribution of such volume, i.e., the number of simulated rainwater cycles and the volume of surrogate rainwater delivered by each of them. The importance of the rainfall event duration on the stone rate of mineral dissolution was also indirectly verified during previous exposure rounds, even for smaller variations in the volumes of surrogate rainwater. Such variations occurred due to the accidental uneven distribution of surrogate rainwater to a replicate sample during the variability test, which induced alterations of the dissolution rate.

For instance, the outliers captured by the principal component analysis of the dissolution dataset obtained from the variability were found to be associated to altered deliveries of surrogate rainwater solution to the sample. The subsequent analysis of the relationship between the volumes of surrogate rainwater and amount of Ca released found a negative correlation between these two factors for BN-SS and CB-LM. Similarly, it was observed that the relative standard deviation for dissolution values at individual sampling points across the long-term exposure of test-set 2 presented occasional irregularities throughout exposure. Although not directly verifiable, such occasional alterations are likely the result of the occasional adjustment and stabilization of the water flow that was carried out as part of the exposure monitoring. These observations strongly suggest that the volume of

solution that interacts with the stone within a single cycle largely controls the rate of the leaching process.

Currently, the association between the rate of dissolution and the duration of the rainfall event has been rarely addressed by literature. A field exposure study where rate of Ca dissolution was monitored reported results that are compatible with the findings of the present study. Schuster et al., (1994) reported that the dissolution of carbonate stone generally increased up to twofold during coincident episodes of low rainfall rate and decreased rainfall pH. Contact time has been used in the past to refer to the interaction between the stone and the water solution. Siegesmund and Snethlage (2011) stated that the rate of mineral dissolution is dependent on the contact time with liquid water, as well as to the solubility of the mineral phase and acidity of the solution.

In the context of performance modelling, a similar parameter was implemented by the UNECE/ICP Materials program. Time of Wetness was used as a predictor for the development of a dose-response function after 4-years of field exposure (Kucera and Fitz, 1995). However, rather than being connected to active rainfall, this variable describes a condition related to atmospheric relative humidity.

A hazard map of areas at risk of recession for calcareous stone in Europe was developed by Bonazza et al., (2009). The study was conducted adopting Lipfert model and identified areas with high-annual rainfall, such as Scotland, as at higher risk of recession. However, based on the data here presented, regions with a comparable risk of recession might be found where lower annual rainfall rates are characterised by shorter events and frequent occurrence. On this basis, the average rainfall event duration should be integrated into future models to improve

the accuracy of the predicted data. Given equal volumes of rainfall, short and closer events will be considerably more harmful to carbonate stones than longer and continuous precipitation. These findings highlight the importance of accounting for the characteristics of the precipitation when evaluating the performance of carbonate building stone exposed to the environment.

It should also be considered that the percentage increase in frequency of the cycles presented in Chapter 8 refers to the variation between two sequential exposure conditions. This implied a gradual modification of the cycle duration, indicating that the acceleration in dissolution rate between two consecutive rainfall patterns is lower that the acceleration that the same stone would experience following sharper variations. For instance, an increment in dissolution rate of 33% resulting from a reduction of the exposure time to surrogate rainwater by half, reaches 68% when the time of exposure is four times shorter.

An increase in dissolution rate corresponding with of the shortening of the cycles was not observed for every analyte, and the level of dependency with the simulated rainfall pattern was variable. While the increasing dissolution rate was proved for Ca and Mg for most samples, and for K to a lesser extent, Na dissolution did not display a clear association with the rainfall patterns. In contrast, the performance of Fe was opposite to the one shown by Ca and Mg, and the increased frequency of the rainfall cycles corresponded to a decrease in the rates of dissolution for most samples.

This evidence suggest that carbonate stones might be subject to a different type of influence from the rainfall event duration compared to stone types that do not contain carbonate minerals. This observation is consistent with the data collected

from samples containing a low amount of carbonate minerals or none. For instance, the performance of BL-SS might be connected to the different type of response of its constituent minerals to variable exposure conditions.

8.5 Modelling of the rate of Calcium dissolution based on the rainfall event duration

As discussed in Chapter 1, the future impact of changes in precipitation patterns have been recently addressed as a concern in relation to Climate Change. An increase in the rates of building stone degradation is connected to the projected climatic alterations as a result of global warming. The attention was raised over the effects that increased precipitations and extreme rainfall events might have on the built environment in the future (Basu et al, 2020). The same reflection was made by Smith et al. (2010), who suggested that addressing the changes in environmental conditions is fundamental for the understanding of present and future rates of degradation. Available prediction models for the chemical degradation of the stone are unsuitable to fully capture this change.

A modelling test was conducted to investigate the possibility of predicting the rate of Ca dissolution based on the duration of the rainfall event. The relationship between the dissolution rate of Ca and time of exposure to surrogate rainwater was explored by univariate regression. Calcium dissolution rates, as the dependent variable, were regressed against the surrogate rainwater cycle, as the dependent variable (figure 8-2). The relationship between the two variables is described by a trendline crossing the datapoints that represent the dissolution

rates under each rainfall regime. Due to the notably higher dissolution rates of the initial sampling points, RP1 was excluded from the data treatment.

The trendline describes the increment in Ca dissolution as a function of the time of exposure. The plotted datapoints at each time point display a significant vertical distribution. This was likely caused by the differences in the samples which partially control the rate of dissolution. The absence of these factors from the model induces dispersion of the dissolution data around the model, which translates into a poor coefficient of correlation (R^2 0.31). As previously observed, one of the controlling factors in the rate of Ca dissolution was represented by their concentration of carbonate minerals.

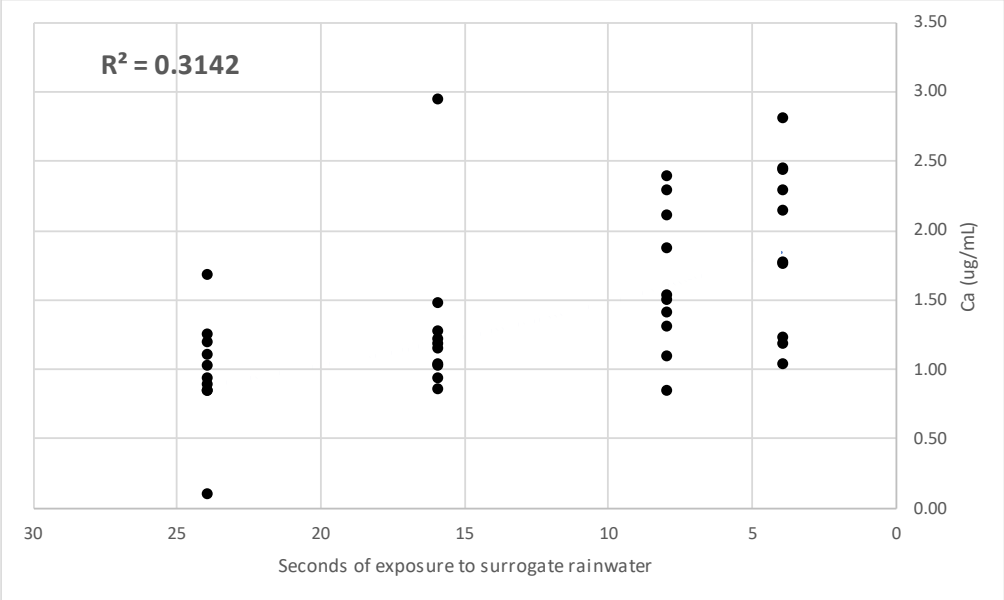

Figure 8-2: scatter plot displaying the relationship between seconds of exposure and mean Ca dissolution values at each rainfall pattern for the full dataset.

The influence of the carbonate mineral content of the stones was excluded by only incorporating stone types with similar carbonate mineral content in the regression analysis. With regression conducted only for limestone (CB-LM) and calcarenites

(CF-BC and GP-CA), the model provided a better fit to the datapoints (R^2 0.60) (figure 8-3). The outcome of the regression analysis indicates the possibility of predicting the rate of dissolution for stone types with comparable characteristics with a good level of accuracy, based exclusively on the duration of the rainfall event. However, minor differences in the stone composition, such as the respective concentration of carbonate minerals, are still likely to affect the fit to the model. The three stone types used for the modelling still present differences in composition, including in the respective concentration of calcite and dolomite, which likely also affects the overall rate of dissolution.

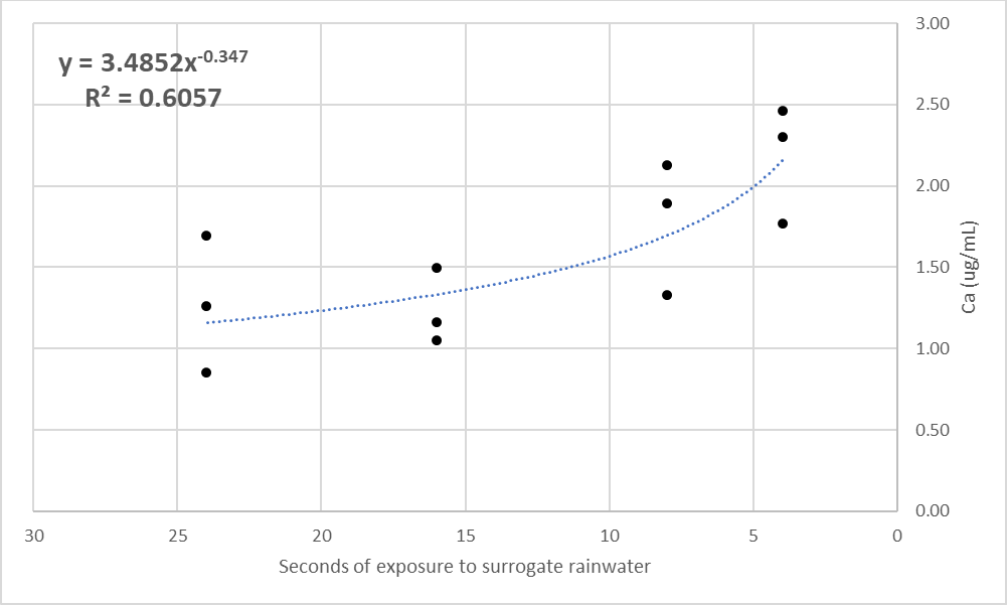

Figure 8-3: scatter plot displaying the relationship between Seconds of Exposure and mean Ca dissolution values at each rainfall pattern for limestone samples.

The contribution of the compositional factor was further investigated by PCA. Principal component analysis was conducted on a dataset that included the samples dissolution rates under the four rainfall patterns (RP1 to RP2) and the carbonate mineral content of each stone type. The score plot identified two

clusters, one comprising all the sandstones, identified by the -SS suffix, the other incorporating the limestones (figure 8-4). The significance of the carbonate mineral content in the discrimination of the data was captured by the colour scheme assigned to the variable.

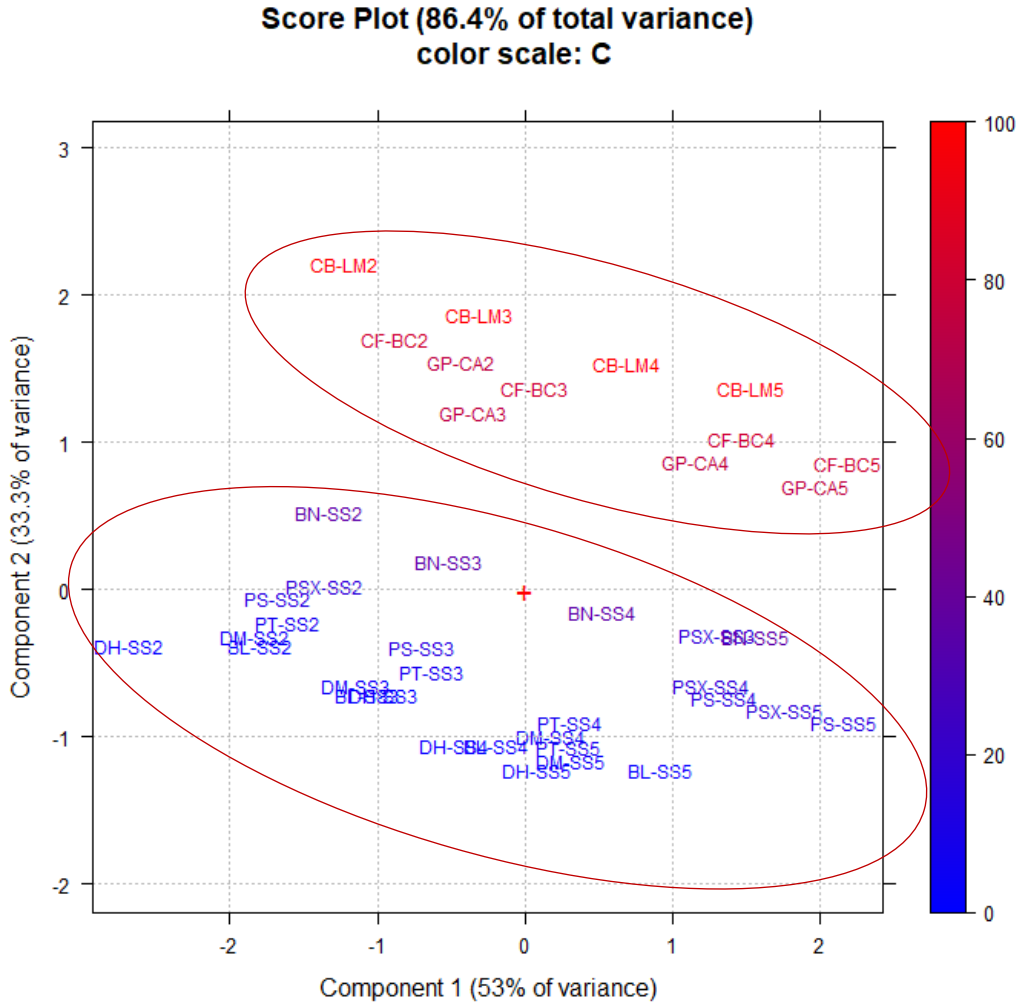

Figure 8-4: score plot from the principal component analysis of the mean Ca dissolution values at each rainfall pattern, the carbonate mineral content of each stone type and the duration of the rainfall cycle. A colour scale is assigned to the carbonate mineral content of the stone.

The higher concentration of carbonate minerals was represented by the blue end of the colour scheme, which identified the limestone and calcarenite samples, while the sandstones, due to the lower carbonate minerals content, were highlighted in red. The relationship between variables is displayed by the loading plot (figure 8-5). The respective position of Ca and the duration of the surrogate water cycles (Secs) with respect to the chart origin suggests a strong anti-correlation between the two variables. Figures 8-6 and 8-7 show the same score plot but with the colour scheme assigned to Ca dissolution (figure 8-6) and seconds of exposure (figure 8-7).

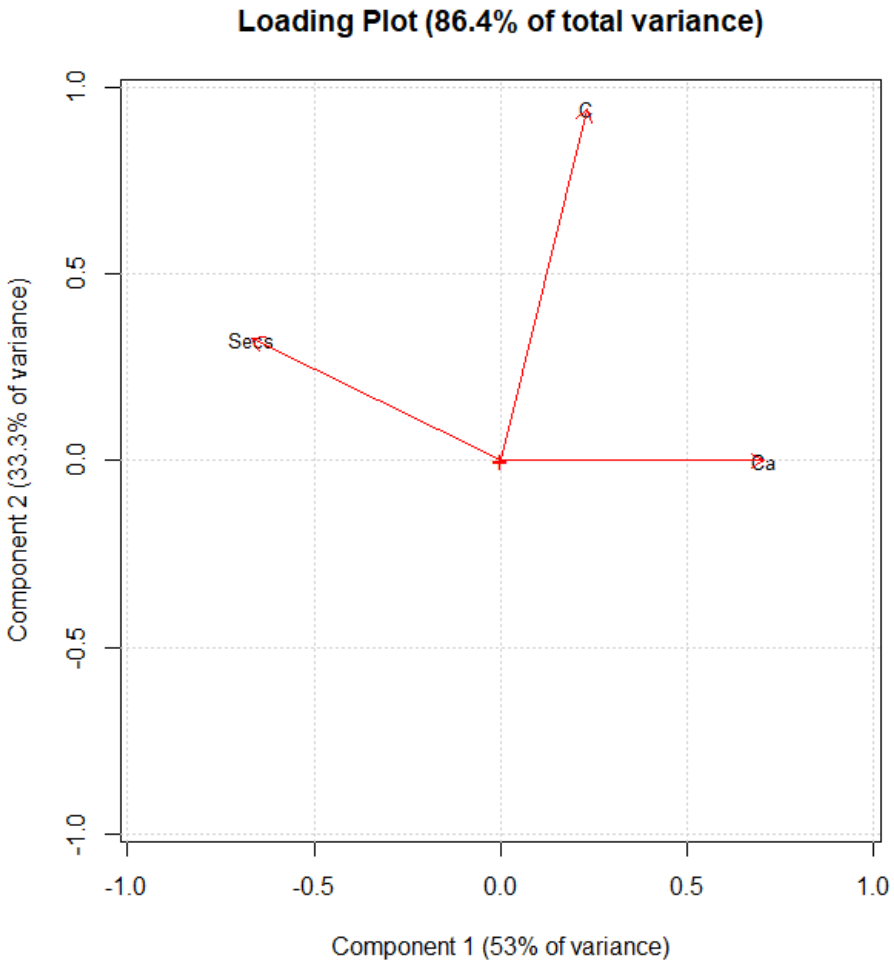

Figure 8-5: loading plot showing the variables within the space of the principal components. Ca and Secs have a high influence on component 1, while C has a high influence on component 2.

The combined examination of the two score plots shows that the samples with the higher dissolution rate of Ca (highlighted in red in figure 8-6) were the ones that were subject to a lower duration of the rainwater cycle (highlighted in blue in figure 8-7).

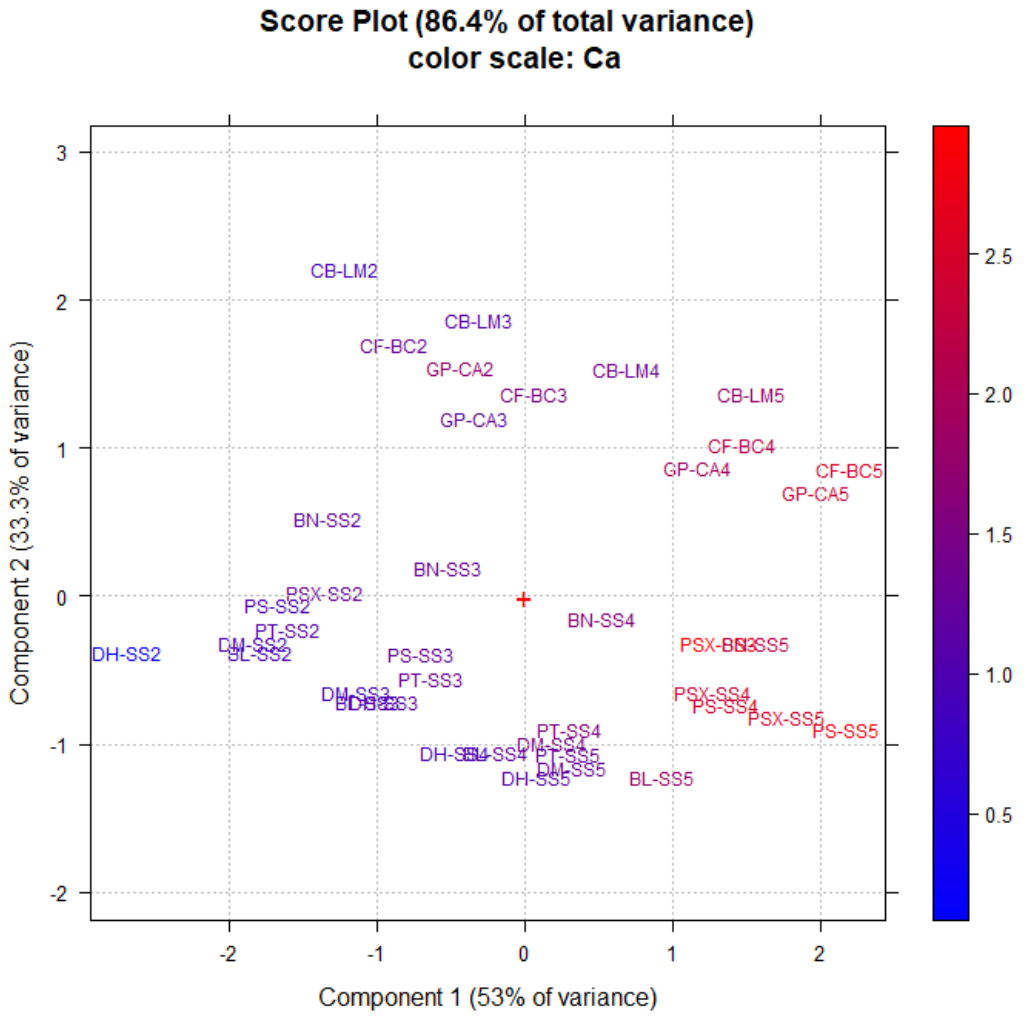

Figure 8-6: score plot from the principal component analysis of the mean Ca dissolution values at each rainfall pattern, the carbonate mineral content of each stone type and the duration of the rainfall cycle. A colour scale is assigned to Ca dissolution values.

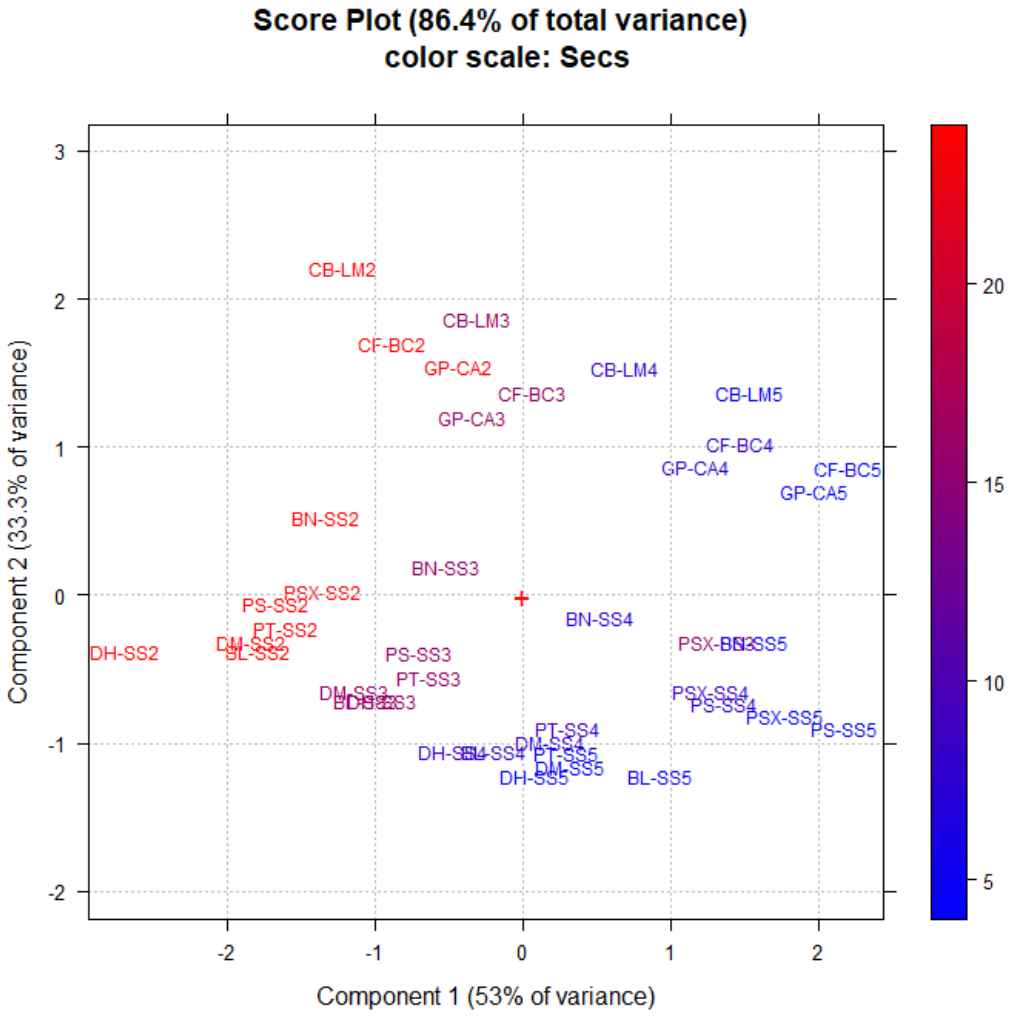

Figure 8-7: score plot from the principal component analysis of the samples based on their mean Ca dissolution values at each rainfall pattern, the carbonate mineral content of each stone type and the duration of the rainfall cycle. A colour scale is assigned to the duration of the rainfall cycle.

Based on these observations, the prediction ability of the model could potentially be extended to all stone types if the characteristics that contribute to the dissolution rate were integrated in the model as predictors. The regression of a response against more than an independent variable is usually conducted in a multivariate context. Principal components regression was performed on the dataset comprising the samples carbonate mineral content and the duration of the rainwater as predictors, and the dissolution rate of the samples as response (figure 8-8). Results of the regression on the first two principal components suggested a decent level of agreement between fitted and predicted data (RMSEP 0.49).

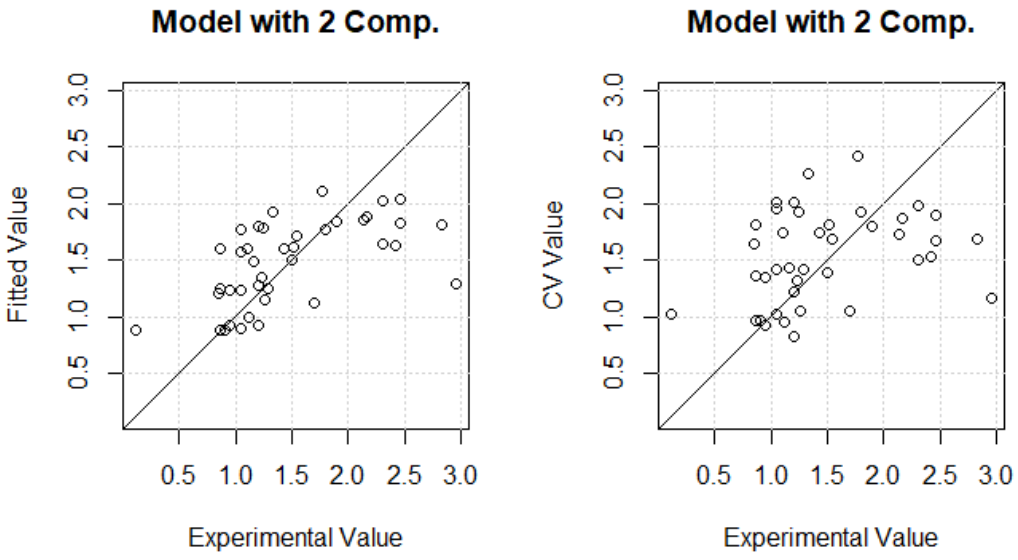

Figure 8-8: fitted and experimental values obtained from the principal component regression (PCR) of the first two components. The model identified the correlation between the carbonate mineral content of the samples and the duration of the exposure to surrogate rainwater (predictors) and the rate of Ca dissolution (response).

The residual dispersion that occurs from the cross validation is likely the result of carbonate mineral content of the stone only partially explaining the performance of the samples with respect to Ca dissolution. Additional intrinsic factors, such as porosity, are also likely to influence the stone vulnerability to the interaction with rainwater and, as such, control part of the response.

Multiple linear regression (MLR) conducted on the same dataset displayed similar results. The fitting of the experimental data showed a linear association between predictors and response (figure 8-9). Results of the cross validation provided an estimation of the MLR model performance and are displayed in figure 8-10. Similarly to the PCR model, a level of dispersion of the predicted data indicated a moderate accuracy of the prediction of Ca dissolution based on the selected independent variables (RMSECV 0.6521). This suggested that the rate of Ca dissolution can be predicted based on the duration of the rainfall with a discrete level of confidence if the carbonate mineral content is integrated into the model.

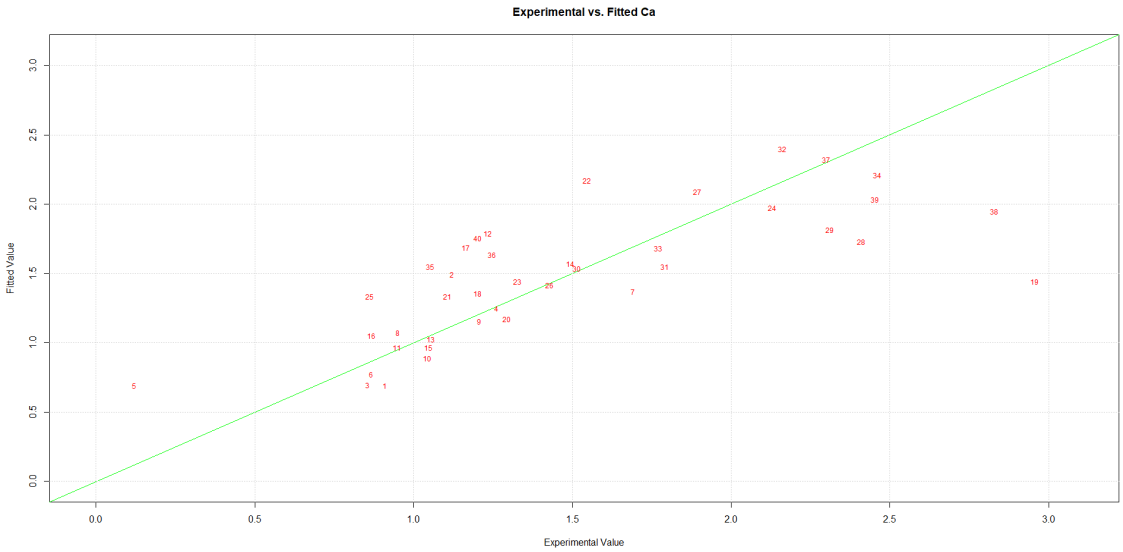

Figure 8-9: fitted values from the multiple linear regression (MLR) model.

However, additional factors control the stone response to the variation of exposure conditions and need to be accounted for in order to increase the accuracy of the model. These likely refer to the necessity of discriminating the carbonate minerals into individual mineral phases, e.g., calcite and dolomite, and including factors that are known to regulate the stone permeability, such as porosity and the level of pores interconnections.

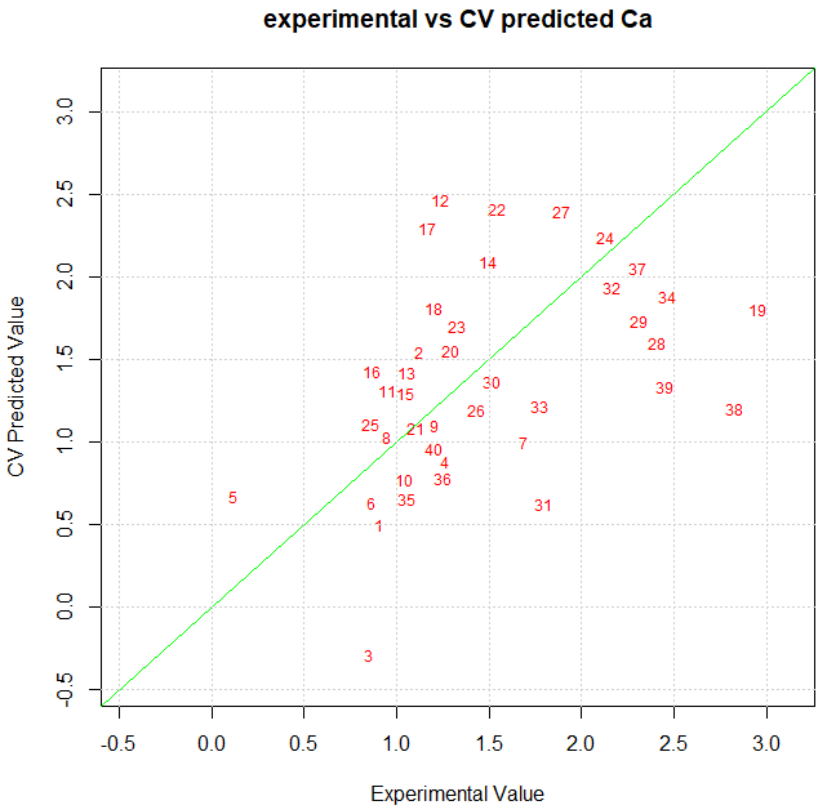

Figure 8-10: predicted values from the cross-validation process of the MLR model.

Such improvements were not carried out in the context of the present research due to the impossibility of acquiring comprehensive information on the required factors during the characterization of the samples.

9. Conclusions

Building stone is a fundamental component of the historic built environment and research about its conservation is vital. Despite being known for its resilience, the response of building stone to atmospheric exposure is subject to a wide variability. The stone properties, as well as multiple environmental agents, control the type and rates of the interactions underlying the stone progressive deterioration. This is of fundamental importance for the conservation of the built environment, especially in areas which are subject to high annual precipitation.

Climate Change is expected to cause an acceleration of the decay processes induced by the interaction of the stone with rainwater. Scotland has been identified as one of the regions at higher risk of future surface recession of carbonate building stone. To allow for the enforcement of appropriate conservation strategies and interventions, it is crucial to measure the durability of the stone based on the factors that control the rate of the decay progression. Being able to determine the contribution of each variable and its relative influence on the rate of degradation is fundamental for the assessment of stone vulnerability to future climatic conditions.

Although the processes underlying the stone response to rainwater are well understood, the influence of the factors contributing to their rate of progression is less clear. In this respect, the ability of a model to provide accurate information

about the stone performance relies on its capacity to reflect the interactions that occur between the variables that regulate the decay process. This condition is crucially dependent on the experimental data used for their derivation and can be affected from an incorrect representation of the factors involved.

This research has explored some of the aspects controlling the rates of sedimentary stone degradation caused by rainwater. The study tested the influence of precipitation on different types of sedimentary building stones containing variable amounts of carbonate minerals. The early stage of the project involved the design of an artificial exposure apparatus aimed at achieving a high degree of reproducibility of the natural degradation process under laboratory conditions. The designed apparatus offered a number of benefits compared to the most common methods for the artificial exposure of stone samples to water solutions, such as immersion. These included:

A more accurate simulation of the natural interaction between the stone and rainwater.

- The option to regulate the parameters of interest throughout the course of the exposure.
- The possibility to monitor the samples dissolution through the collection of the stones leachates.

For these reasons, the apparatus here presented could improve the reliability and efficiency of methodologies applied to the study of the impact of rainwater by means of accelerated ageing.

Leachates were analysed to determine the concentration of dissolved Ca, Mg, K, Na, and Fe at each sampling point and produced a dissolution profile for every

sample. The following conclusions were drawn from the combined findings of the artificial exposure rounds:

- Replicate stone samples exhibit comparable performance when exposed to the same conditions, in terms of both dissolution trend and rates.
- Different stone types provide similar dissolution profiles under stable exposure conditions, characterized by an initial sharp decline in dissolution rates followed by a stabilization of the trend.
- The difference between Ca dissolution rates of different samples appeared to gradually decrease with time.
- The rate of Ca dissolution is highly receptive to small changes in the volumes of surrogate rainwater delivered to the stone.
- The duration of the rainfall cycle has significant influence over the rate of dissolution of carbonate minerals. The scale of the variation is not constant but depends on the stone type.
- The dissolution rate of Ca was inversely correlated with the duration of the rainwater cycle in samples containing higher concentrations of carbonate minerals. In contrast, lower concentrations of carbonates appeared to be connected to a progressive deceleration of the process.
- The concentration of carbonate minerals in the stone is not the only factor controlling the rate of Ca and Mg dissolution. However, it represents the primary factor affecting the variation of Ca dissolution rates in response to changes in rainfall distribution.
- Sodium and K did not display the same performance of Ca and Mg and their dissolution appeared to be unrelated to the duration of the rainfall event.

An estimation of the Ca dissolution rates can be obtained from the duration of the rainfall cycle and the amount of carbonate minerals present in the stone. The lack of accurate information on the microstructure of the stones is likely the source of residual error.

The development of damage models obtained from laboratory accelerated exposure informed about the impossibility to conduct prediction only based on the stone type, due to the elevated number of intrinsic variables that control the decay progression. Different internal properties are likely to induce a high level of fluctuations in the response to both physical and chemical degradation mechanisms. Results from the present work suggest that possible differences in the properties of the stone will likely have an effect on the rate of degradation equivalent to that caused by variations of the environmental conditions. The approach used to model decay in response to physical processes supports this claim, confirming the impossibility of extrapolating the stone performance based on its nature. The integration of structural and physical information to prediction models was found to significantly improve the prediction ability in response to specific stressors, with porosity being the principal structural parameter investigated.

According to the presented data, current and future precipitation patterns are expected to be as significant as the yearly precipitation volume which, up until this point, was the dominant descriptor of the rainfall term. Based on the findings, if the precipitation pattern is characterized by shorter and more frequent episodes, geographical areas with lower average rainfall may be just as vulnerable to higher rates of deterioration as regions with higher annual precipitation. The scale of the

potential damage associated with shorter and more frequent precipitation patterns is highly dependent on the stone. This is the reason why any evaluation of the future impact of precipitation should be considered in connection to the relevant stone properties. Although it was previously acknowledged that variations in the characteristics of the stone could cause dissimilarities in their respective responses, the data used to model performance against precipitation was usually gathered from the field exposure of a limited number of stone types.

Additionally, the following remarks address the constrain of some stages of the experimental process:

- The spraying of de-ionized water proved to be insufficient in eliminating the totality of the salts from the stone, which is necessary for the acquisition of mass-loss information.
- A precise description of the stone pore system could not be obtained using X-ray μCT tomography. Water transport properties could not be adequately characterized due to the insufficient spatial resolution of the technique for extrapolating information about the stones' micropores.

These findings improve the understanding of the factors that control the rate of degradation of carbonate sedimentary building stone exposed to rainfall and point to potential improvements of the methodological approach for the data acquisition process to support the future development of prediction models. In Scotland, because of its climate and important and extensive stone-built heritage, this is a particularly urgent necessity. At present, there is not a clear line of research studying the effects of exposure of stone to rainwater, despite rainwater representing the main agent of stone degradation. Current impact assessment of climate change on Scotland's built environment only briefly touches on the effect

of rainwater on stone decay and with a very narrow description of its possible impact. In the current study, generalizations based upon the stone nature or on a limited range of factors were proved to be unreliable in providing information about the performance of the stone. Instead, future damage should be assessed thought the exact quantification of the synchronized effects of all the factors underlying the interaction with rainwater.

9.1 Recommendations for future work

The outcome of the artificial accelerated exposure suggested a direct relationship between the rainfall event duration and the rate of mineral dissolution. However, some points still remain open for further study. Although the compositional aspect was proved not to be the only factor controlling the rate of dissolution, the respective contribution of the individual stone properties remains unclear.

Future short-term objectives should focus on the integration of the following points to the outcomes of the present research:

- Acquisition of X-ray diffraction data for the exact characterization of the samples' composition.
- Acquisition of information about the physical properties that control the interaction of the stone with rainwater.
- Evaluation of the correlation of both factors to the rate of dissolution of each analyte.

Similarly, some questions remain unanswered with respect to the mechanism underlying the change in rate of dissolution that was found in correspondence to shorter rainwater cycles. It appeared that the increase in dissolution rate under shorter and more frequent cycles was related to the carbonate mineral content of the stone. However, this alteration was also likely controlled by the stone water retention properties, and hence by the stone pores characteristics. Therefore, further short-term objectives should involve the following aspects:

- Establishment of the correlation between relevant compositional and physical data with the rate of dissolution under each rainfall regime.
- Evaluation of the model residual error after integration of the sample physical properties as predictors of the dissolution rate under different rainfall durations.

To the present day, the modelling of field exposure data has mainly focused on the influence of environmental parameters, while the respective contribution of the stone properties on the rate of degradation has not been investigated. These recommendations indicate the benefit of an interdisciplinary approach that integrates the procedures adopted for the modelling of physical degradation processes. In most cases, the incorporation of the stone physical properties as predictors of the stone performance has provided good results. The possibility to develop a model capable of adapting to a wider range of stones requires the acquisition of extensive data from samples presenting a wide range of characteristics. In this respect, the medium-term objectives should focus on the following aspects:

- Acquisition of a test-set that comprises sedimentary stones with a wide combination of compositional and physical properties.
- Long-term artificial exposure of the test-set to stable and variable rainwater regimes.
- Monitoring of the stone performance by analysis of the leachates and quantification of the damage by mass-loss data.
- Extrapolation of a model to quantify the rate of dissolution and mass-loss values of sedimentary stone based on the relevant stone properties and duration of the rainfall regime.

Sedimentary stones, and sandstone in particular, represent the prevailing construction material of historic buildings in Scotland. However, built heritage encompasses a wide range of stone types, which were not tested as part of this project. Longer term-objectives should aim at:

- Expanding the knowledge of the factors that control the rates of dissolution for other stone types.
- Evaluating the contribution of other environmental parameter in the dissolution process, such as temperature and humidity.

The accuracy of the output will rely upon the capacity of the laboratory exposure to capture the natural progression of the decay. In this respect, further research is needed to evaluate the existing approaches to accelerated weathering and assess the reproducibility of field exposure data. Such research will enable the acquisition of information that will support the long-term assessment of building stone performance under future changing climatic conditions.

References

Bawden R. J. (1989) Weathering rates of fresh Portland limestone. European Cultural Heritage Newsletter on Research (in press).

Luckat S. (1981). A quantitative investigation of the effect of air pollutants on the destruction of natural stone. In Particular, Environmental Chemicals and the Effects of Deleterious Substances. Environmental Research Project of the German Home Office (as cited by Jaynes and Cooke, 1987).

Akin, M., & Özsan, A. (2011). Evaluation of the long-term durability of yellow travertine using accelerated weathering tests. Bulletin of Engineering Geology and the Environment, 70(1), 101-114.

Altindag, R., Alyildiz, I., & Onargan, T. (2004). Mechanical property degradation of ignimbrite subjected to recurrent freeze–thaw cycles. International Journal of Rock Mechanics and Mining Sciences (Oxford, England: 1997), 41(6), 1023-1028.

Alves, C. et al. (2021). Effects of water on natural stone in the built environment - a review. Geosciences (Basel), 11(11), p. 459.

Alves, C., Figueiredo, C. and Sanjurjo-Sánchez, J. (2020) Rock features and alteration of stone materials used for the built environment: A review of recent publications on ageing tests, Geosciences (Basel), 10(3), p. 91.

Amirkiyaei, V., Ghasemi, E., & Faramarzi, L. (2021). Estimating uniaxial compressive strength of carbonate building stones based on some intact stone

properties after deterioration by freeze–thaw. Environmental Earth Sciences, 80(9), Environmental earth sciences, 2021, Vol.80 (9).

Amoroso, G.G. (2002) Trattato di scienza della conservazione dei monumenti: Etica della Conservazione, Degrado dei Monumenti, Interventi Conservativi, Consolidanti e protettivi. Firenze: Alinea.

Andriani, G., & Germinario, L. (2014). Thermal decay of carbonate dimension stones: Fabric, physical and mechanical changes. Environmental Earth Sciences., 72(7), 2523-2539.

Angeli, M. et al. (2007) Salt crystallization in pores: quantification and estimation of damage. Environmental geology (Berlin), 52(2), pp. 205–213.

Aral, &., Boy, R., & Dinçer, A. (2021). Effects of freeze-thawing cycles on the physical and mechanical properties of basaltic and dolomitic rocks evaluated with a decay function model. Bulletin of Engineering Geology and the Environment, 80(4), 2955-2962.

Ausset, P. et al. (1996). Experimental study of limestone and sandstone sulphation in polluted realistic conditions: The Lausanne Atmospheric Simulation Chamber (LASC). Atmospheric environment (1994), 30(18), pp. 3197–3207.

Baedecker, P., Reddy, M., Reimann, K., & Sciammarella, C. (1992). Effects of acidic deposition on the erosion of carbonate stone — experimental results from the U.S. National Acid Precipitation Assessment Program (NAPAP). Atmospheric Environment, Part B, 26(2), 147-158.

Baedecker, P.A. and Reddy, M.M. (1993). The Erosion of Carbonate Stone by Acid Rain: Laboratory and Field Investigations. Journal of chemical education, 70(2), pp. 104–108.

Basu, S., Orr, S., & Aktas, Y. (2020). A geological perspective on climate change and building stone deterioration in London: Implications for urban stone-built heritage research and management. Atmosphere, 11(8), 788.

Bauer, A. and Velde, B. (2014) Geochemistry at the Earth's surface: movement of chemical elements. 1st edition 2014.

Bayram, F. (2012). Predicting mechanical strength loss of natural stones after freeze–thaw in cold regions. Cold Regions Science and Technology, 83-84, 98-102.

Beck, K., Al-Mukhtar, M., Beck, K, & Al-Mukhtar, M. (2014). Cyclic wetting–drying ageing test and patina formation on tuffeau limestone. Environmental Earth Sciences., 71(5), 2361-2372.

Benavente, D. (2011). Why pore size is important in the deterioration of porous stones used in the built heritage. Macla, 15,41- 42.

Benavente, D. et al. (2018) Impact of salt and frost weathering on the physical and durability properties of travertines and carbonate tufas used as building material. Environmental earth sciences, 77(4), p. 1.

Benavente, Durability estimation of porous building stones from pore structure and strength, Eng. Geol., № 74, c. 113

Bläuer, C. (1985). Weathering of Bernese sandstones. 5th International Congress on Deterioration and Conservation of Stone, Lausanne, 1985, 381-390

Bonazza, A., Messina, P., Sabbioni, C., Grossi, C., & Brimblecombe, P. (2009). Mapping the impact of climate change on surface recession of carbonate buildings in Europe. The Science of the Total Environment, 407(6), 2039-2050.

Bonazza, A., Sabbioni, C., Messina, P., Guaraldi, C., De Nuntiis, P., Bonazza, A., De Nuntiis, P. (2009b). Climate change impact: Mapping thermal stress on Carrara marble in Europe. Science of the Total Environment, 407(15), 4506-4512.

Brimblecombe, P. (2014). Refining climate change threats to heritage. Journal of the Institute of Conservation, 37(2), pp. 85–93.

Brimblecombe, P. and Grossi, C.M. (2007). Damage to Buildings from Future Climate and Pollution. APT bulletin (1986), 38(2/3), pp. 13–18.

Brotons, V. et al. (2013). Temperature influence on the physical and mechanical properties of a porous rock: San Julian's calcarenite. Engineering geology, 167, pp. 117–127.

Buj, Oscar, Gisbert, Josep, Buj, Oscar, & Gisbert, Josep (2010). Influence of pore morphology on the durability of sedimentary building stones from Aragon (Spain) subjected to standard salt decay tests. Environmental Earth Sciences., 61(7), 1327-1336.

Butlin, R., Yates, T., Murray, M., & Ashall, G. (1995). The United Kingdom national materials exposure programme. Water, Air and Soil Pollution, 85(4), 2655-2660.

Cardell, C., Benavente, D., & Rodríguez-Gordillo, J. (2008). Weathering of limestone building material by mixed sulfate solutions. Characterization of stone microstructure, reaction products and decay forms. Materials Characterization, 59(10), 1371-1385.

Cardell, C., Delalieux, F., Roumpopoulos, K., Moropoulou, A., Auger, F., & Van Grieken, R. (2003). Salt-induced decay in calcareous stone monuments and buildings in a marine environment in SW France. Construction & Building Materials, 17(3), 165-179.

Cardell-Fernández, C., Vleugels, G., Torfs, K., & Van Grieken, R. (2002). The processes dominating Ca dissolution of limestone when exposed to ambient atmospheric conditions as determined by comparing dissolution models. Environmental Geology (Berlin), 43(1-2), 160-171.

Carvalho, C., Silva, Z. and Simão, J. (2018). Evaluation of Portuguese limestones' susceptibility to salt mist through laboratory testing. Environmental earth sciences, 77(13), pp. 1–15.

Castellanza, R., & Nova, R. (2004). Oedometric Tests on Artificially Weathered Carbonatic Soft Rocks. Journal of Geotechnical and Geoenvironmental Engineering, 130(7), 728-739.

Cerfontaine, B. and Collin, F. (2018). Cyclic and Fatigue Behaviour of Rock Materials: Review, Interpretation and Research Perspectives. Rock mechanics and rock engineering, 51(2), pp. 391–414.

Charola, A., & Ware, R. (2002). Acid deposition and the deterioration of stone: A brief review of a broad topic. Geological Society Special Publication, 205(1), 393-406.

Chen, T.C., Yeung, M.R. and Mori, N. (2004). Effect of water saturation on deterioration of welded tuff due to freeze-thaw action. Cold regions science and technology, 38(2), pp. 127–136.

Ciantia, M., Castellanza, R., Crosta, G., & Hueckel, T. (2015). Effects of mineral suspension and dissolution on strength and compressibility of soft carbonate rocks. Engineering Geology, 184, 1-18.

Crundwell, F.K. (2015). The mechanism of dissolution of the feldspars: Part I. Dissolution at conditions far from equilibrium, Hydrometallurgy, 151, pp. 151–162.

Dawson, G.K.W. et al. (2015). Experimental mineral dissolution in Berea Sandstone reacted with CO2 or SO2–CO2 in NaCl brine under CO2 sequestration conditions. Chemical geology, 399, pp. 87–97.

De Kock, T. et al. (2017). Laminar gypsum crust on lede stone: Microspatial characterization and laboratory acid weathering. Talanta (Oxford), 162, pp. 193–202.

De la Fuente, D. et al. (2013) Mapping air pollution effects on atmospheric degradation of cultural heritage. Journal of cultural heritage, 14(2), pp. 138–145.

Delalieux, F., Cardell-Fernandez, C., Torfs, K. et al. Damage Functions and Mechanism Equations Derived from Limestone Weathering in Field Exposure. Water, Air, & Soil Pollution 139, 75–94 (2002). https://doi.org/10.1023/A:1015827031669

Deng H, Li J, Zhu M, Wang K, Wang L, Deng C (2012). Experimental research on strength deterioration rules of sandstone under ‘‘saturation-air dry’’ circulation function. Rock Soil Mech33:3306–3312 (In Chinese).

Doehne, Eric & Price, C. (2011). Stone Conservation: An Overview of Current Research. 10.2307/3179804.

Du, B., Bai, H., & Wu, G. (2019). Dynamic Compression Properties and Deterioration of Red-Sandstone Subject to Cyclic Wet-Dry Treatment. Advances in Civil Engineering, 2019, 1-10.

Eslami, J., Walbert, C., Beaucour, A., Bourges, A., & Noumowe, A. (2018). Influence of physical and mechanical properties on the durability of limestone subjected to freeze-thaw cycles. Construction & Building Materials, 162, 420-429.

Eyssautier-Chuine, S., Marin, B., Thomachot-Schneider, C., Fronteau, G., Schneider, A., Gibeaux, S., & Vazquez, P. (2016). Simulation of acid rain weathering effect on natural and artificial carbonate stones. Environmental Earth Sciences, 75(9), 1-19.

Fereidooni, D. and Khajevand, R. (2019). Utilization of the accelerated weathering test method for evaluating the durability of sedimentary rocks. Bulletin of engineering geology and the environment, 78(4), pp. 2697–2716.

Franzoni, E. and Sassoni, E. (2011). Correlation between microstructural characteristics and weight loss of natural stones exposed to simulated acid rain. The Science of the total environment, 412, pp. 278–285.

Freire-Lista, D., Fort, R., & Varas-Muriel, M. (2016). Thermal stress-induced microcracking in building granite. Engineering Geology, 206, 83-93.

Gaddi, R., Cacace, C. and Di Menno di Bucchianico, A. (2022). The risk assessment of surface recession damage for architectural buildings in Italy. Journal of cultural heritage, 57, pp. 118–130.

Germinario, L. and Török, Ákos (2019). Variability of technical properties and durability in volcanic tuffs from the same quarry region – examples from Northern Hungary. Engineering geology, 262, p. 105319.

Ghobadi, M., & Babazadeh, R. (2015). Experimental Studies on the Effects of Cyclic Freezing–Thawing, Salt Crystallization, and Thermal Shock on the Physical and Mechanical Characteristics of Selected Sandstones. Rock Mechanics and Rock Engineering, 48(3), 1001-1016.

Gibeaux, S., Thomachot-Schneider, C., Eyssautier-Chuine, S., Marin, B., & Vazquez, P. (2018). Simulation of acid weathering on natural and artificial building stones according to the current atmospheric SO2/NOx rate. Environmental Earth Sciences, 77(9), Environmental earth sciences, 2018, Vol.77 (9).

Gomez-Heras, M.; Fort, R. (2007) Patterns of halite (NaCl) crystallisation in building stone conditioned by laboratory heating regimes. Environ. Geo. 52, 239–247. http://dx.doi.org/10.1007/s00254-006-0538-0.

González, I., & Scherer, G. (2006). Evaluating the potential damage to stones from wetting and drying cycles. In measuring, monitoring and modelling concrete properties (pp. 685-693). Dordrecht: Springer Netherlands.

Groentoft, T. (2011). Climate change impact on building surfaces and façades. International Journal of Climate Change Strategies and Management, 3(4), 374-385.

Hale, P.A. and Shakoor, A. (2003). A laboratory investigation of the effects of cyclic heating and cooling, wetting and drying, and freezing and thawing on the

compressive strength of selected sandstones, Environmental & engineering geoscience, 9(2), pp. 117–130.

Hall, K. (1997) 'Rock temperatures and implications for cold region weathering. I: New data from Viking Valley, Alexander Island, Antarctica', *Permafrost and Periglacial Processes*, 8(1), pp. 69–90. doi:10.1002/(sici)1099-1530(199701)8:1<69::aid-ppp236>3.3.co;2-h.

Hall, K. (1999). The role of thermal stress fatigue in the breakdown of rock in cold regions. Geomorphology (Amsterdam), 31(1), 47-63.

Haynie F. H. (1982/3). Deterioration of marble. Durability of Building Materials 1, 241-254

Heidari, M., Torabi-Kaveh, M., & Mohseni, H. (2017). Assessment of the Effects of Freeze–Thaw and Salt Crystallization Ageing Tests on Anahita Temple Stone, Kangavar, West of Iran. Geotechnical and Geological Engineering, 35(1), 121-136.

Holynska, B. et al. (2004). Study of the deterioration of sandstone due to acid rain and humid SO_2 gas. X-Ray Spectrometry, 33(5), pp. 342–348. doi:10.1002/xrs.723.

Hua, W. et al. (2015). The influence of cyclic wetting and drying on the fracture toughness of sandstone. International journal of rock mechanics and mining sciences (Oxford, England: 1997), 78, pp. 331–335.

İnce, & Fener, M. (2016). A prediction model for uniaxial compressive strength of deteriorated pyroclastic rocks due to freeze–thaw cycle. Journal of African Earth Sciences (1994), 120, 134-140.

J. Martínez-Martínez, A. Abellán, E. Berrezueta, Erosion directionality and seasonality study using the anisotropy matrix. Application in a semiarid Mediterranean climate (SE Spain), Science of The Total Environment, Volume 804, 2022, 150165, https://doi.org/10.1016/j.scitotenv.2021.150165

Jabbour, M. et al. (2022) 'A critical review of existing test-methods for external sulfate attack', Materials, 15(21), p. 7554. doi:10.3390/ma15217554.

Jamison, C. et al. (2010). Mapping the spatial distribution of precipitation, biological soiling, and decay on monuments in Northern Ireland: towards understanding long-term stone response to moisture. Proceedings XIX Congress of the Carpathian-Balkan Geological Association.

Jamison, C. et al. (2010). Mapping the spatial distribution of precipitation, biological soiling, and decay on monuments in Northern Ireland: towards understanding long-term stone response to moisture. Proceedings XIX Congress of the Carpathian-Balkan Geological Association.

Jamshidi, A. (2021). Predicting the Strength of Granitic Stones after Freeze–Thaw Cycles: Considering the Petrographic Characteristics and a New Approach Using Petro-Mechanical Parameter. Rock Mechanics and Rock Engineering, 54(6), 2829-2841.

Jamshidi, A. (2024) 'Study of building stones durability against the freeze-thaw process: Current methods and recommendations for the future', Journal of Building Engineering, 86, p. 108772. doi:10.1016/j.jobe.2024.108772.

Jamshidi, A., Nikudel, M., & Khamehchiyan, M. (2013). Predicting the long-term durability of building stones against freeze–thaw using a decay function model. Cold Regions Science and Technology, 92, 29-36.

Jamshidi, A., Nikudel, M., & Khamehchiyan, M. (2015). Estimating the engineering properties of building stones after freeze-thaw using multiple regression analysis. Iranian Journal of Science and Technology. Transaction A, Science, 39(2), 147-163.

Jaynes, S., & Cooke, R. (1987). Stone weathering in Southeast England. Atmospheric Environment, 21(7), 1601-1622.

Jelle, B.P. (2012). Accelerated climate ageing of building materials, components and structures in the laboratory. Journal of materials science, 47(18), pp. 6475–6496.

Jiménez-González, I., Rodríguez-Navarro, C., and Scherer, G.W. (2008). Role of clay minerals in the physicomechanical deterioration of sandstone. Journal of geophysical research. Earth surface, 113(2), pp. Journal of geophysical research. Earth surface, 2008, Vol.113 (2).

Johnson, J.B. et al. (1990). Laboratory exposure systems to simulate atmospheric degradation of building stone under dry and wet deposition conditions. Atmospheric environment. Part A, General topics, 24(10), pp. 2585–2592.

Ke, B. et al. (2020). Dynamic characteristics of sandstone under coupled static-dynamic loads after freeze-thaw cycles. Applied sciences, 10(10), p. 3351.

Keppert, M., Žumár, J., Čáchová, M., Koňáková, D., Svora, P., Pavlík, Z., . . . Černý, R. (2016). Water Vapor Diffusion and Adsorption of Sandstones: Influence

of Rock Texture and Composition. Advances in Materials Science and Engineering, 2016, 1-7.

Khanlari, G. and Abdilor, Y. (2015). Influence of wet–dry, freeze–thaw, and heat–cool cycles on the physical and mechanical properties of Upper Red sandstones in central Iran. Bulletin of engineering geology and the environment, 74(4), pp. 1287–1300.

Kryza, Ryszard et al. (2009). Acidic weathering of carbonate building stones: experimental assessment. Studia Universitatis Babes-Bolyai, Geologia. 54. 33-36. 10.5038/1937-8602.54.1.7.

Kucera, V., & Fitz, S. (1995). Direct and indirect air pollution effects on materials including cultural monuments. Water, Air and Soil Pollution, 85(1), 153-165.

Kucera, V., Mikhailov, A., Henriksen, J., Kreislova, K., Yates, T., Stöckle, B., & Schreiner, M. (2001). Un ece ICP materials: Dose-response functions on dry and wet acid deposition effects after 8 years of exposure. Water, Air, and Soil Pollution, 130(1-4), 1457-1462.

Kucera, V., Tidblad, J., Kreislova, K., Knotkova, D., Faller, M., Reiss, D., Kobus, J. (2007). UN/ECE ICP Materials Dose-response Functions for the Multi-pollutant Situation. In Acid Rain - Deposition to Recovery (pp. 249-258). Dordrecht: Springer Netherlands.

Labus, M. and Bochen, J. (2012). Sandstone degradation: An experimental study of accelerated weathering. Environmental Earth Sciences, 67(7), pp. 2027–2042. doi:10.1007/s12665-012-1642-y.

Lin, M.L. et al. (2005). Wetting weakening of tertiary sandstones - Microscopic mechanism. Environmental geology (Berlin), 48(2), pp. 265–275.

Lipfert, F. (1989). Atmospheric damage to calcareous stones: Comparison and reconciliation of recent experimental findings. Atmospheric Environment, 23(2), 415-429.

Lisci, C. et al. (2022) 'Building stones durability by UVA radiation, moisture and spray accelerated weathering', Journal of Building Pathology and Rehabilitation, 7(1). doi:10.1007/s41024-022-00196-9.

Lisci, C. et al. (2023) 'Stone endurance: A comparative analysis of natural and artificial weathering on Stone Longevity', Heritage, 6(6), pp. 4593–4617. doi:10.3390/heritage6060244.

Livingston RA. Graphical methods for examining the effects of acid rain and sulfur dioxide on carbonate stones. In: Delgado Rodrigues J, Henriques F, Telmo Jeremias F, editors. Proceedings of the 7th International Congress on Deterioration and Conservation of Stone; 1992. p. 375–86

López-Arce, P. et al. (2010). Artificial weathering of Spanish granites subjected to salt crystallization tests: Surface roughness quantification. Catena (Giessen), 83(2), pp. 170–185.

López-González, L., Miguel Gomez-Heras, Raquel Otero-Ortiz de Cosca, Soledad Garcia- Morales, Rafael Fort, 2022. Coupling electrical resistivity methods and GIS to evaluate the effect of historic building features on wetting dynamics during wind-driven rain spells. Journal of Cultural Heritage, p. 209-218 https://doi.org/10.1016/j.culher.2022.10.009

Lott, G.K. & Cooper, A.H. 2005. The building limestones of the Upper Permian, Cadeby Formation (Magnesian Limestone) of Yorkshire. British Geological Survey Internal Report, IR/05/048.

Ludovico-Marques, M. and Chastre, C. (2016). Chapter 10 - Effect of artificial accelerated salt weathering on physical and mechanical behavior of sandstone samples from surface reservoirs, in Handbook of Materials Failure Analysis with Case Studies from the Oil and Gas Industry. Elsevier Ltd, pp. 215–233.

Mansfeld, F. Regional air pollution study: effects of airborne sulfur pollutants on materials. Final report. United States: N. p., 1980. Web.

Martínez-Martínez, J. *et al.* (2013). Non-linear decay of building stones during freeze–thaw weathering processes. Construction and Building Materials, 38, pp. 443–454. doi:10.1016/j.conbuildmat.2012.07.059.

Martínez-Martínez, J. et al. (2019). Changes on the surface properties of foliated marbles at different cutting orientations. Construction & building materials, 222, pp. 493–499.

McAllister, D., Warke, P. and McCabe, S. (2017) 'Stone temperature and moisture variability under temperate environmental conditions: Implications for sandstone weathering', *Geomorphology*, 280, pp. 137–152. doi:10.1016/j.geomorph.2016.12.010.

McCabe, S., Brimblecombe, P., Smith, B., McAllister, D., Srinivasan, S., & Basheer, P. (2013). The use and meanings of time of wetness in understanding building stone decay. Quarterly Journal of Engineering Geology and Hydrogeology, 46(4), 469-476.

Mikhailov, A. (2001). Dose-Response Functions as Estimates of the Effect of Acid Precipitates on Materials. Protection of Metals, 37(4), 357-366.

Mohamed Aly Abdelhamid, M., Li, D., Ren, G., & Zhang, C. (2020). Estimating Deterioration Rate of Some Carbonate Rocks Used as Building Materials under Repeated Frost Damage Process, China. Advances in Materials Science and Engineering, 2020, 1-12.

Molina, E., Cultrone, G., Sebastian, E., Alonso, F. J., Carrizo, L., Gisbert, J., Buj, O. (2011). The pore system of sedimentary rocks as a key factor in the durability of building materials. Engineering Geology, 118(3-4), 110-121.

Momeni, A., Hashemi, S., Khanlari, G., & Heidari, M. (2017). The effect of weathering on durability and deformability properties of granitoid rocks. Bulletin of Engineering Geology and the Environment, 76(3), 1037-1049.

Morbidelli, L. (2014). Le Rocce e i Loro Costituenti. Roma: Scienze e Lettere.

Moses, C., Robinson, D., & Barlow, J. (2014). Methods for measuring rock surface weathering and erosion: A critical review. Earth-science Reviews, 135, 141-161.

Mutlutürk, M., Altindag, R., & Türk, G. (2004). A decay function model for the integrity loss of rock when subjected to recurrent cycles of freezing–thawing and heating–cooling. International Journal of Rock Mechanics and Mining Sciences (Oxford, England: 1997), 41(2), 237-244.

Nicholson, D.T. and Nicholson, F.H. (2000). Physical deterioration of sedimentary rocks subjected to experimental freeze-thaw weathering. Earth surface processes and landforms, 25(12), pp. 1295–1307.

Okrusch, M., Frimmel, H.E. (2020). Mineralogy - An Introduction to Minerals, Rocks, and Mineral Deposits / [internet resource]. 1st ed. 2020. (Springer textbooks in earth sciences, geography and environment).

Ozcelik, Y., & Ozguven, A. (2014). Water absorption and drying features of different natural building stones. Construction & Building Materials, 63, 257-270.

Phillipson, M.C., Emmanuel, R. and Baker, P.H. (2016). The durability of building materials under a changing climate, Wiley interdisciplinary reviews. Climate change, 7(4), pp. 590–599.

Pichler, C., Lackner, R., Bader, T., & Perfler, L. (2022). Water vapor diffusion properties of Obernkirchener sandstone: Analysis of DVS data. Construction & Building Materials, 347, 128554.

Potysz, Anna et al. (2022). Bioweathering of minerals and dissolution assessment by experimental simulations - Implications for sandstone rocks: A review. Construction & building materials, 316, p. 125862.

Reddy, M. M., Sherwood, S. I., & Doe, B. R. (1986). Limestone and marble dissolution by acid rain: An onsite weathering experiment. ACS Symposium Series, 226-238. doi:10.1021/bk-1986-0318.ch015

Rodriguez-Navarro, C. and Doehne, E. (1999). Salt weathering: influence of evaporation rate, supersaturation and crystallization pattern. Earth surface processes and landforms, 24(3), pp. 191–209.

Roekens, E., Bleyen, C., & Van Grieken, R. (1989). Sulphite and sulphate concentrations in weathering products of sandy limestone and in deposition samples. Environmental Pollution (1987), 57(4), 289-298.

Ruedrich, J, & Siegesmund, S. (2006). Fabric dependence of length change behaviour induced by ice crystallisation in the pore space of natural building stones. Fabric Dependence of Length Change Behaviour Induced by Ice Crystallisation in the Pore Space of Natural Building Stones, 497-505.

Ruedrich, J. and Siegesmund, S. (2007). Salt and ice crystallisation in porous sandstones. Environmental geology (Berlin), 52(2), pp. 225–249.

Ruedrich, J., Kirchner, D. and Siegesmund, S. (2011). Physical weathering of building stones induced by freeze–thaw action: a laboratory long-term study. Environmental earth sciences, 63(7-8), pp. 1573–1586.

Ruiz-Agudo, E. et al. (2007). The role of saline solution properties on porous limestone salt weathering by magnesium and sodium sulfates. Environmental geology (Berlin), 52(2), pp. 269–281.

Saba, M., Quiñones-Bolaños, E., & Barbosa López, A. (2018). A review of the mathematical models used for simulation of calcareous stone deterioration in historical buildings. Atmospheric Environment (1994), 180, 156-166.

Sabbioni, Cristina & Brimblecombe, Peter & Lefèvre, Roger-Alexandre. (2009). Vulnerability of cultural heritage to climate change. Pollution Atmospherique. 157-169.

Salvini, S. et al. (2023) ‘Petrographic characterization and durability of carbonate stones used in UNESCO World Heritage Sites in Northeastern Italy’, Environmental Earth Sciences, 82(1). doi:10.1007/s12665-022-10732-y.

Sawdy, A., & Price, C. (2005). Salt damage at Cleeve Abbey, England. Part I: A comparison of theoretical predictions and practical observations. Journal of Cultural Heritage, 6(2), 125-135.

Schnabel, L. (2014). Lectures on Materials Science for Architectural Conservation. Studies in Conservation, 59(2), 123-124.

Schuster P.F. and Reddy M.M. (1994). Effects of acid deposition on dissolution of carbonate stone during summer storms in the Adirondack Mountains, New York, 1987-89 [Preprint]. doi:10.3133/wri934189.

Sesana, E. *et al.* (2019). Mitigating climate change in the Cultural Built Heritage Sector. Climate, 7(7), p. 90. doi:10.3390/cli7070090.

Sesana, E., Gagnon, A., Bonazza, A., & Hughes, J. (2020). An integrated approach for assessing the vulnerability of World Heritage Sites to climate change impacts. Journal of Cultural Heritage, 41, 211-224.

Sesana, E., Gagnon, A., Ciantelli, C., Cassar, J., & Hughes, J. (2021). Climate change impacts on cultural heritage: A literature review. Wiley Interdisciplinary Reviews. Climate Change, 12(4), N/a.

Shahidzadeh-Bonn, N., Bertrand, F., Bonn, D., & Chateau, X. (2009). Salt Deterioration of Porous Materials Subject to Repeated Cycles of Wetting and Drying. Salt Deterioration of Porous Materials Subject to Repeated Cycles of Wetting and Drying, 246.

Siegesmund, S., & Snethlage, R. (2011). Stone in Architecture (4. Aufl. ed.). Berlin, Heidelberg: Springer-Verlag.

Siegesmund, S., Snethlage, R. and Ruedrich, J. (2008). Monument futures: Climate change, air pollution, decay and conservation—the wolf-dieter grimm-volume. Environmental Geology, 56(3–4), pp. 451–453. doi:10.1007/s00254-008-1447-1.

Silva, A., De Brito, J., & Gaspar, P. (n.d.). Methodologies for Service Life Prediction of Buildings (Green Energy and Technology). Cham: Springer International Publishing.

Sitzia, F., Lisci, C. and Mirão, J. (2021) 'Building Pathology and Environment: Weathering and decay of stone construction materials subjected to a CSA mediterranean climate laboratory simulation', Construction and Building Materials, 300, p. 124311. doi:10.1016/j.conbuildmat.2021.124311.

Sitzia, F., Lisci, C. and Mirão, J. (2021) 'Building Pathology and Environment: Weathering and decay of stone construction materials subjected to a CSA mediterranean climate laboratory simulation', *Construction and Building Materials*, 300, p. 124311. doi:10.1016/j.conbuildmat.2021.124311.

Smith, B.J. *et al.* (2010). A commentary on climate change, Stone Decay Dynamics and the "greening" of natural stone buildings: New perspectives on "deep wetting". Environmental Earth Sciences, 63(7–8), pp. 1691–1700. doi:10.1007/s12665-010-0766-1.

Smith, B.J., Gomez-Heras, M. and McCabe, S. (2008). Understanding the decay of stone-built cultural heritage. Progress in Physical Geography 32(4) (2008) pp. 439–461

Smith, B.J., Warke, P.A., McGreevy, J.P. and Kane, H.L. 2005: Salt-weathering simulations under hot desert conditions: agents of enlightenment or perpetuators of preconceptions? Earth Surface Processes and Landforms 67, 211–27.

Spedding, D. (1969). Sulphur dioxide uptake by limestone. Atmospheric Environment, 3(6), 683,IN5-683,IN6.

Spiker, E., Hosker, R., Comer, V., White, J., Werre, R., Harmon, F., . . . Sherwood, S. (1992). Environmental chamber for study of the deposition flux of gaseous pollutants to material surfaces. Atmospheric Environment, 26(16), 2885-2892.

Stück, H.L. et al. (2018). Natural stones of the Saale–Unstrut Region (Germany): petrography and weathering phenomena. Environmental earth sciences, 77(8), pp. 1–29.

Sumner, P.D. and Loubser, M.J. (2008). Experimental sandstone weathering using different wetting and drying moisture amplitudes. Earth surface processes and landforms, 33(6), pp. 985–990.

Sweevers, H., Delalieux, F. and Van Grieken, R. (1998). Weathering of dolomitic sandstone under ambient conditions. Atmospheric Environment, 32(4), pp. 733–748. doi:10.1016/s1352-2310(97)00341-5.

Tecer, L. (1999). Laboratory experiments on the investigation of the effects of sulphuric acid on the deterioration of carbonate stones and surface corrosion. Water, air, and soil pollution, 114(1-2), pp. 1–12.

Thornbush, M.J. and Viles, H.A. (2007). Simulation of the dissolution of weathered versus unweathered limestone in carbonic acid solutions of varying strength. Earth surface processes and landforms, 32(6), pp. 841–852.

Tidblad J, Kucera V, Mikhailov A A, Henriksen J, Kreislova K, Yates T, Stöckle B and Schreiner M (2001) UN ECE ICP Materials. Dose-response functions on dry and wet acid deposition effects after 8 years of exposure. Water, air and soil pollution, 130(1-4 III), 1457-1462

Tomasic, I. et al. (2011). Dynamics of capillary water absorption in natural stone. Bulletin of engineering geology and the environment, 70(4), pp. 673–680.

Torabi-Kaveh, M. et al. (2019). Role of petrography in durability of limestone used in construction of Persepolis complex subjected to artificial accelerated ageing tests. Environmental earth sciences, 78(10), pp. 1–18.

Torraca, G. (2009). Lectures on materials science for architectural conservation. Los Angeles: Getty Conservation Institute.

Uğur, İbrahim and Toklu, H.Özer (2020). Effect of multi-cycle freeze-thaw tests on the physico-mechanical and thermal properties of some highly porous natural stones. Bulletin of engineering geology and the environment, 79(1), pp. 255–267.

Unterwurzacher, M. and Mirwald, P.W. (2008). Initial stages of carbonate weathering: climate chamber studies under realistic pollution conditions. Environmental geology (Berlin), 56(3-4), pp. 507–519.

Viles, H. (2013). Durability and conservation of stone; coping with complexity. Quarterly Journal of Engineering Geology and Hydrogeology, 46(4), 367-375.

Wang, P., Xu, J., Liu, S., & Wang, H. (2016a). Dynamic mechanical properties and deterioration of red sandstone subjected to repeated thermal shocks. Engineering Geology, 212, 44-52.

Wang, P., Xu, J., Liu, S., Liu, S., & Wang, H. (2016b). A prediction model for the dynamic mechanical degradation of sedimentary rock after a long-term freeze-thaw weathering: Considering the strain-rate effect. Cold Regions Science and Technology, 131, 16-23.

Warke, P.A. and Smith, B.J. (1998). Effects of direct and indirect heating on the validity of rock weathering simulation studies and durability tests. Geomorphology (Amsterdam, Netherlands), 22(3-4), pp. 347–357.

Watt, J. (2009). The effects of air pollution on cultural heritage / [internet resource] (1st ed. 2009. ed.). New York; London: Springer.

Webb, A., Bawden, R., Busby, A., & Hopkins, J. (1992). Studies on the effects of air pollution on limestone degradation in Great Britain. Atmospheric Environment, Part B, 26(2), 165-181.

Xu, Z., Feng, G., Sun, Q., Zhang, G., & He, Y. (2020). A modified model for predicting the strength of drying-wetting cycled sandstone based on the P-Wave Velocity. Sustainability (Basel, Switzerland), 12(14), 5655.

Yavuz, H. (2011). Effect of freeze–thaw and thermal shock weathering on the physical and mechanical properties of an andesite stone. Bulletin of engineering geology and the environment, 70(2), pp. 187–192.

Yavuz, H., Altindag, R., Sarac, S., Ugur, I., & Sengun, N. (2006). Estimating the index properties of deteriorated carbonate rocks due to freeze–thaw and thermal shock weathering. International Journal of Rock Mechanics and Mining Sciences (Oxford, England: 1997), 43(5), 767-775.

Yerrapragada, S., Chirra, S., Jaynes, J., Li, S., Bandyopadhyay, J., & Gauri, K. (1996). Weathering Rates of Marble in Laboratory and Outdoor Conditions. Journal of Environmental Engineering (New York, N.Y.), 122(9), 856-863.

Yuan, G. et al. (2019). A review of feldspar alteration and its geological significance in sedimentary basins: From shallow aquifers to deep hydrocarbon reservoirs. Earth-science reviews, 191, pp. 114–140.

Zhao, Z. et al. (2017). Effects of Wetting and Cyclic Wetting–Drying on Tensile Strength of Sandstone with a Low Clay Mineral Content. Rock mechanics and rock engineering, 50(2), pp. 485–491.

Zhou, Z., Cai, X., Chen, L., Cao, W., Zhao, Y., & Xiong, C. (2017). Influence of cyclic wetting and drying on physical and dynamic compressive properties of sandstone. Engineering Geology, 220, 1-12.

10. Appendix

10.1 Results and data processing of X-ray µCT analysis

10.1.1 Bearl sandstone

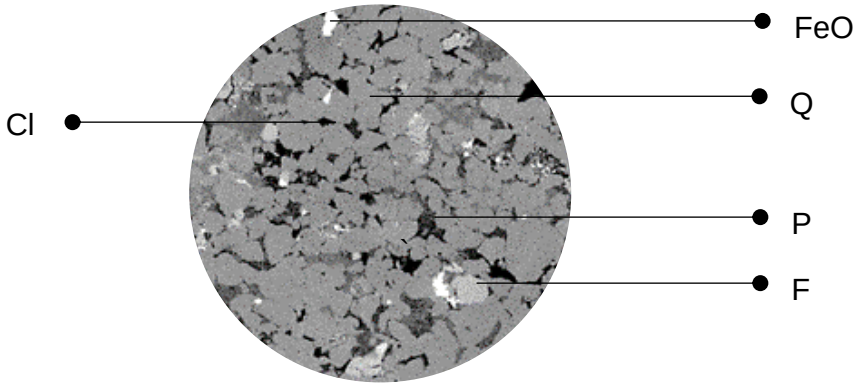

Figure 10-1: slice of the stack of images acquired from XCT scan data of BL-SS

Feldspars (F) and iron oxides (FeO) are visible from the sample cross-section (figure 10-1). The clastic fraction was found to be mainly composed of sub-rounded to sub-angular quartz (Q) grains, with a concentration of approximately 80% (figure 10-2). An extensive part of the intergranular fraction was found to be occupied by pore filling clays (Cl).

The pores segmentation showed a pore structure occupying about 11% of the total volume. Pores displayed a wide range of dimensions. The average size was 0.070 mm in diameter, with larger pores measuring about 0.7 mm. The effective

porosity acquired from the 3D modelling of the pore fraction found a moderate level of interconnection between pores. Effective porosity, representing the fraction of connected pores, accounts for 65% of the stone total porosity, with a tortuosity factor of 1.45. The sample overall permeability was found to correspond to 1.72 μm^2.

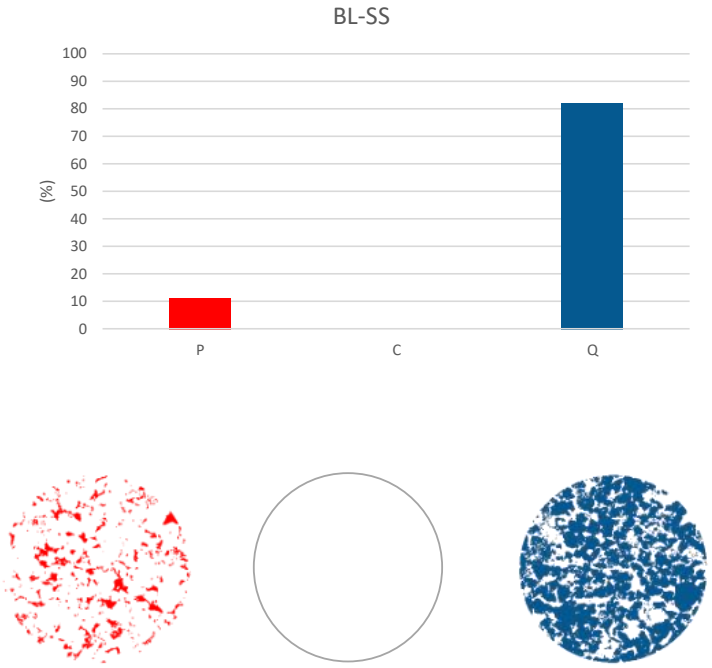

Figure 10-2: Information acquired from image processing techniques on total porosity (P), carbonate minerals (C) and quartz (Q) for BL-SS.

10.1.2 Bernese sandstone

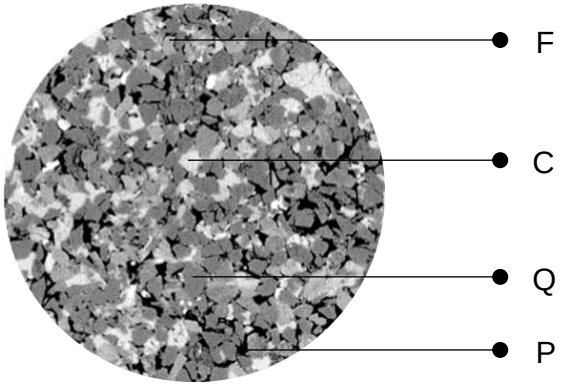

Figure 10-3: slice of the stack of images acquired from XCT scan data of BN-SS

X-ray µCT data shows a sub-angular and moderately well sorted clastic fraction with medium sand grade (figure 10-3). The main component is quartz (Q), combined to feldspars (F) which are homogeneously distributed across the section. The cement is mainly composed of carbonate minerals (C), which represent a substantial component of the stone intergranular fraction (figure 10-4).

The stone appears to be highly porous. The average pore diameter is 0.09 mm, with larger pores measuring up to 0.6 mm. Modelling of the pore structure found that isolated pores are rare. Total and effective porosity present similar values, with over 90% of the pores being connected. The tortuosity factor is 1.9, and the sample presents an overall permeability of 1.74 μm^2.

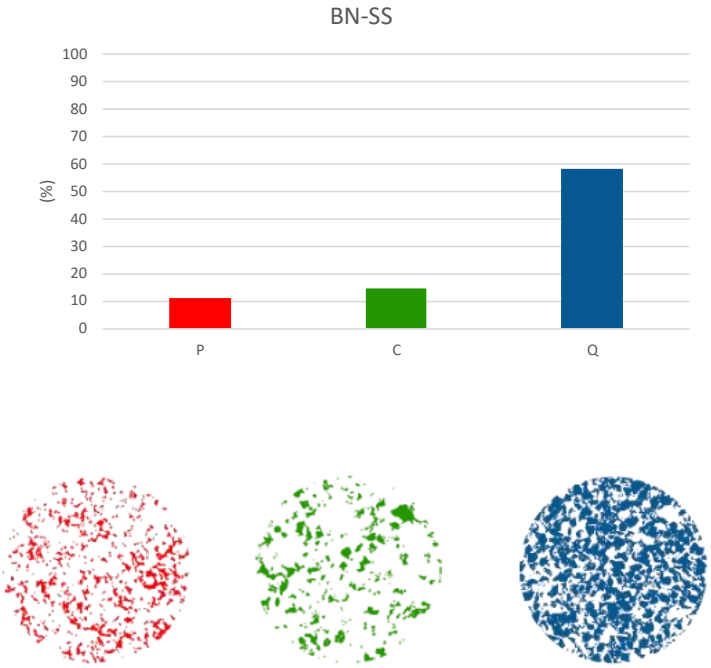

Figure 10-4: information acquired from image processing techniques on total porosity (P), carbonate minerals (C) and quartz (Q) for BN-SS.

10.1.3 Cadeby Limestone

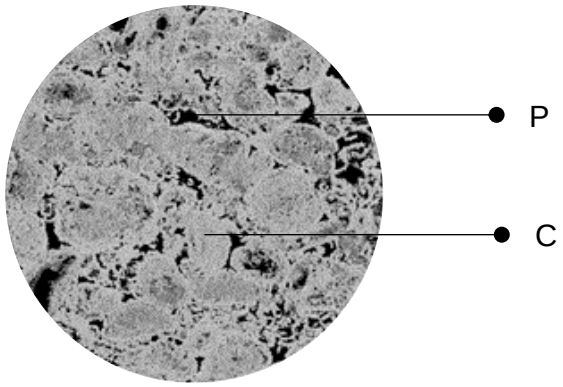

Figure 10-5: slice of the stack of images acquired from XCT scan data of CB-LM

Carbonates are present in the form of ooiliths, which are cemented by a lime mud (figure 10-5). The carbonate minerals fraction represents the main component of the stone, contributing to over 90% of the stone composition (figure 10-6). The pore average size corresponds to 0.069 mm, with bigger pores measuring c. 0.76 mm. The level of interconnection between pores is low (2.72%) with a tortuosity factor of 1.72. The overall permeability of the samples is 1.27 μm^2.

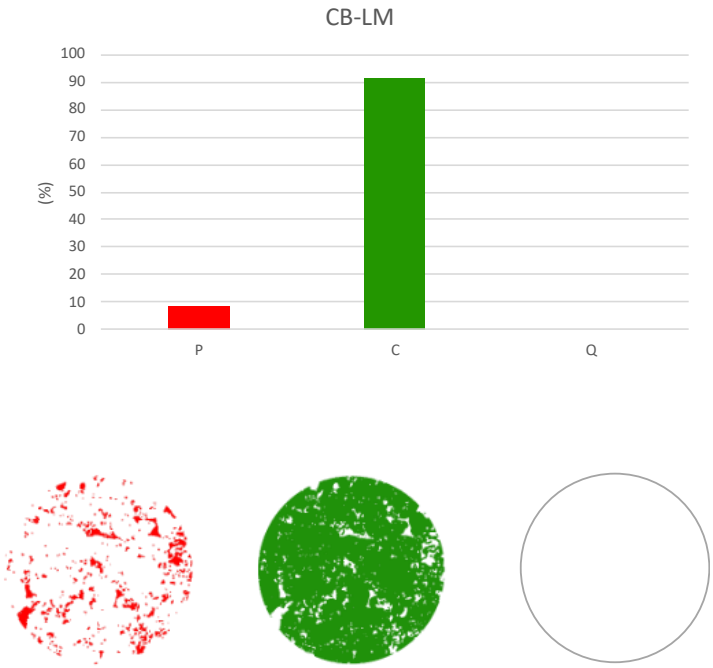

Figure 10-6: information acquired from image processing techniques on total porosity (P), carbonate minerals (C) and quartz (Q) for CB-LM.

10.1.4 Crema Fiorito Biocalcarenite

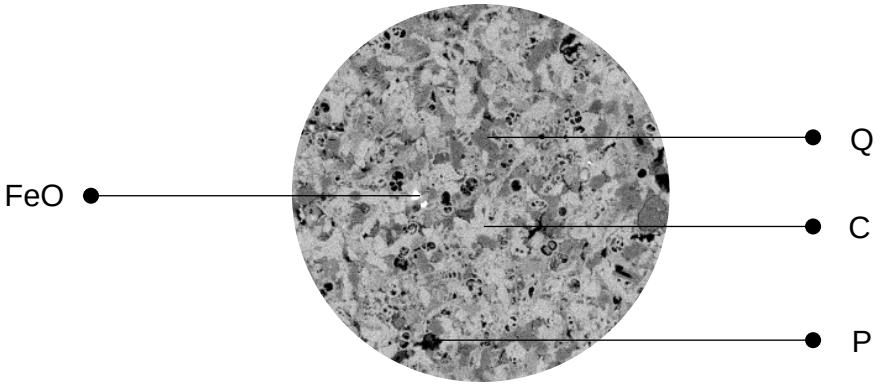

Figure 10-7: slice of the stack of images acquired from XCT scan data of CF-BC

The carbonate fraction (C) represents the major component of the sample and is homogeneously distributed across the section (figure 10-7). Carbonates are combined to a minor fraction of silicate minerals (Q), which occupy about 25% of the sample's total volume (figure 10-8). Iron oxides (FeO) are present in low concentrations. The pore fraction is composed of circular pores with an average dimension of 0.002 mm, with bigger pores measuring 0.27 mm. The identification of a relatively low amount of porosity suggests the predominance of micropores, which were not detected by X-ray µCT data. For this reason, the pores interconnection could not be modelled, preventing the acquisition of information about the sample permeability.

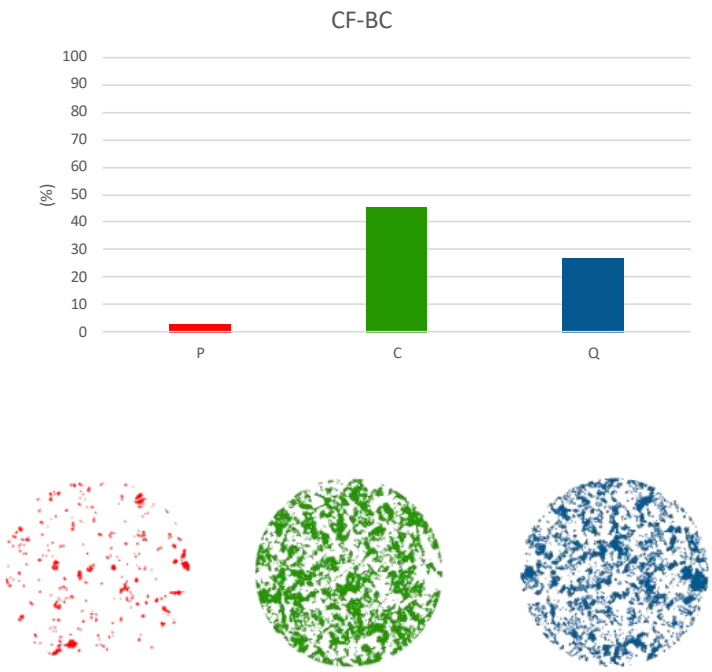

Figure 10-8: information acquired from image processing techniques on total porosity (P), carbonate minerals (C) and quartz (Q) for CF-BC.

10.1.5 Dunhouse sandstone

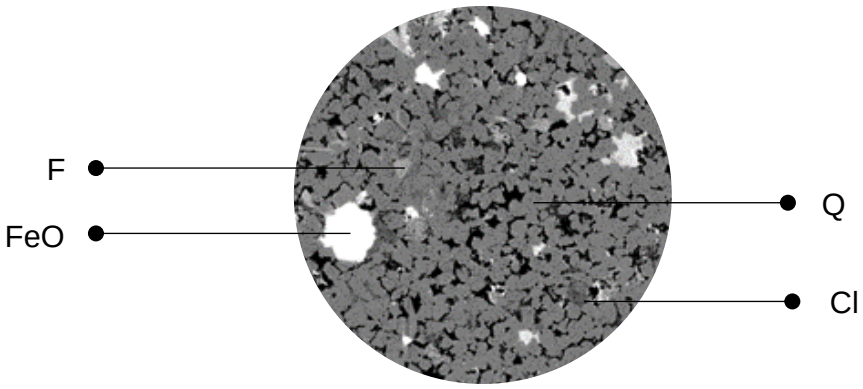

Figure 10-9: slice of the stack of images acquired from XCT scan data of DH-SS

The sample displays a fine grained and well sorted clastic fraction, mainly composed by quartz (Q) (figure 10-9). Iron oxides (FeO) are present in substantial amounts, giving the stone its distinct colour. Feldspars (F) and pore filling clays (Cl) are also identifiable from the sample's section. The pore fraction (P) consists of pores with an average dimension of 0.077 mm, with larger pores measuring 0.80 mm. The modelling of the pore fraction displayed a moderately connected structure, with about 60% of the total pores being connected (figure 10-10). The stone pore network has a tortuosity factor of 1.98, and a permeabily of 1.86 μm^2.

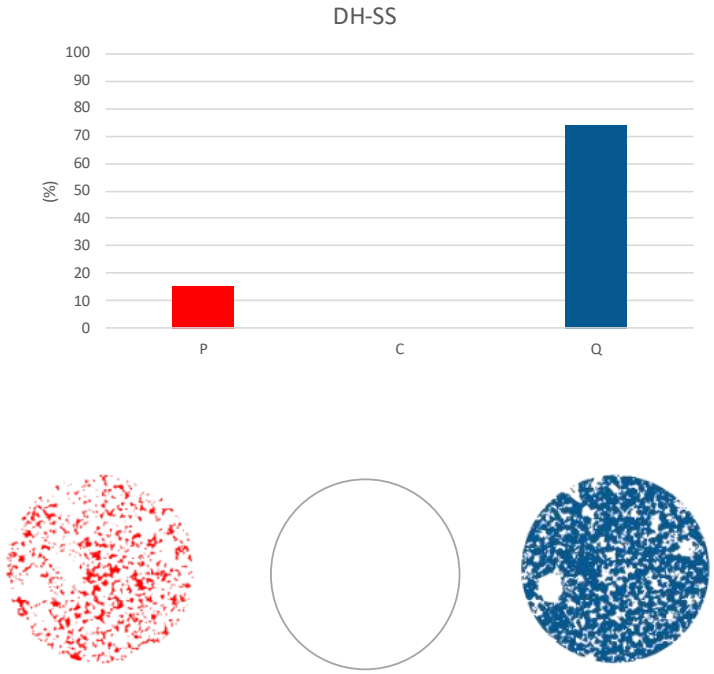

Figure 10-10: information acquired from image processing techniques on total porosity (P), carbonate minerals (C) and quartz (Q) for DH-SS.

10.1.6 Drumhead sandstone

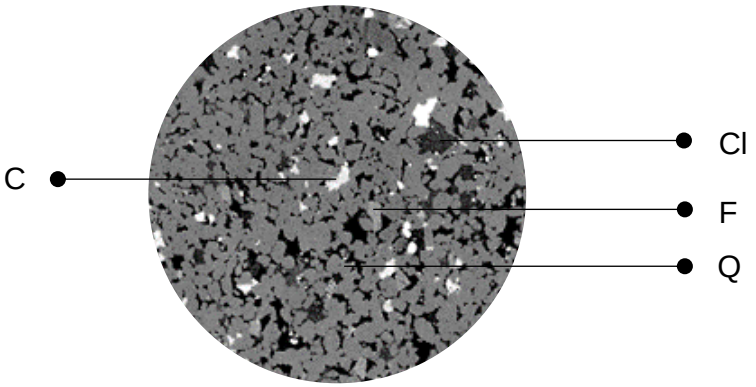

Figure 10-11: slice of the stack of images acquired from XCT scan data of DM-SS

The sample displays fine to medium grained moderately well sorted clasts (figure 10-11). Quartz (Q) grains represent the major component of the clastic fraction, followed by a small percentage of feldspars (F). Iron oxides (FeO) are relatively frequent and homogeneously distributed across the section. A small percentage of pore-filling clays (Cl) and carbonate minerals (C) form part of the stone intergranular components. The stone is highly porous, with a total porosity (P) occupying over 19% of the stone total volume (figure 10-12). The pores have an average diameter of 0.1 mm, with larger pores measuring 0.67 mm. The pore structure presents a high level of interconnection, with about 95% of the pores being interconnected. The tortuosity factor of the stone is 1.6 and the stone permeability is 1.68 μm^2.

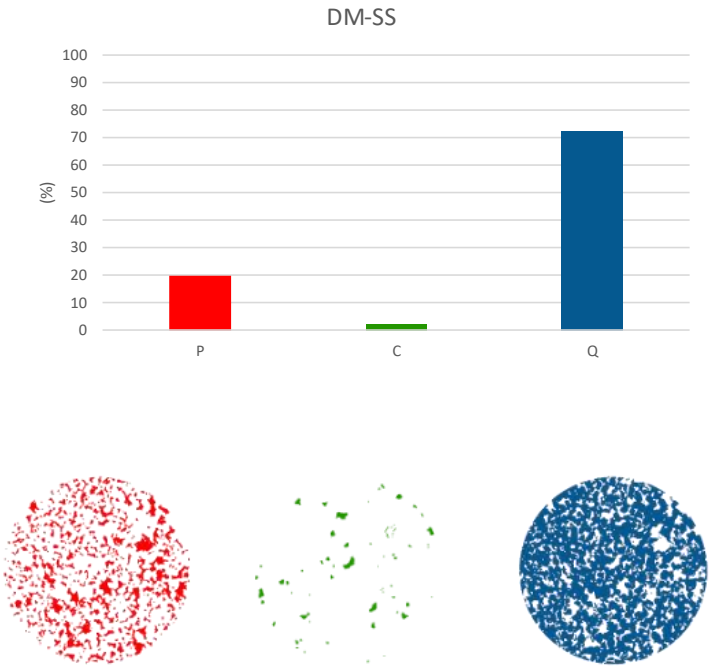

Figure 10-12: information acquired from image processing techniques on total porosity (P), carbonate minerals (C) and quartz (Q) for DM-SS.

10.1.7 Grigio Perla calcarenite

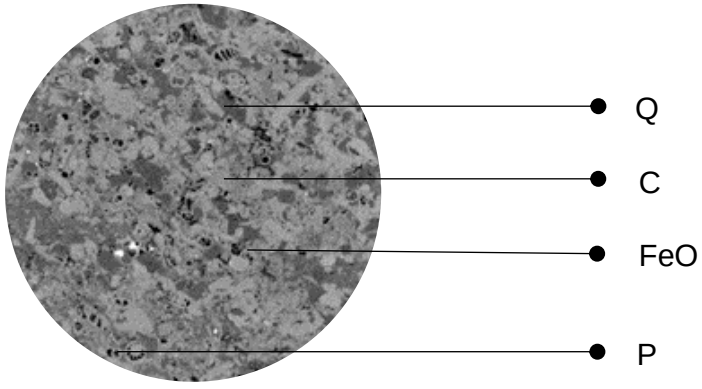

Figure 10-13: slice of the stack of images acquired from XCT scan data of GP-CA

The stone mineral composition presents a major carbonate component, followed by a minor percentage of quartz (figure 10-13). A small concentration of iron oxides is present. The measurable pore fraction is low. However, as in the case of CF-BC, this is probably caused by a prevalence of micropores, not detectable at the resolution achievable by the X-ray µCT analysis (figure 10-14). The average size of the visible pores is 0.051 mm, with the bigger pores measuring 0.32 mm. The sample permeability cannot be assessed, due to the impossibility of establishing the level of interconnections of the pore network.

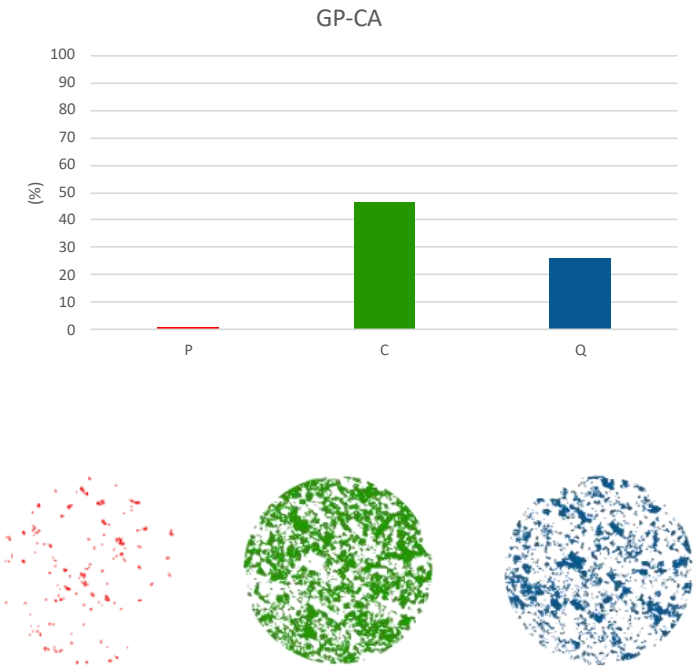

Figure 10-14: information acquired from image processing techniques on total porosity (P), carbonate minerals (C) and quartz (Q) for GP-CA

10.1.8 Pietra Serena sandstone

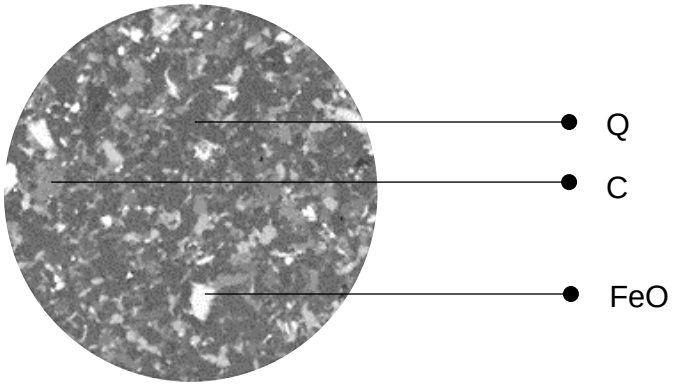

Figure 10-15: slice of the stack of images acquired from XCT scan data of PT-SS

The stone has a fine grained clastic fraction, mainly composed of quartz (figure 10-15). The cement fraction consists of carbonate minerals, which constitute over 12% of the stone intergranular fraction. Porosity is not visible from the X-ray µCT data, as it consists exclusively of micropores, whose dimension is beyond the limit of detection at the X-ray µCT resolution. As a result, total porosity values, the characteristics of the pore network and the sample permeability could not be determined (figure 10-16).

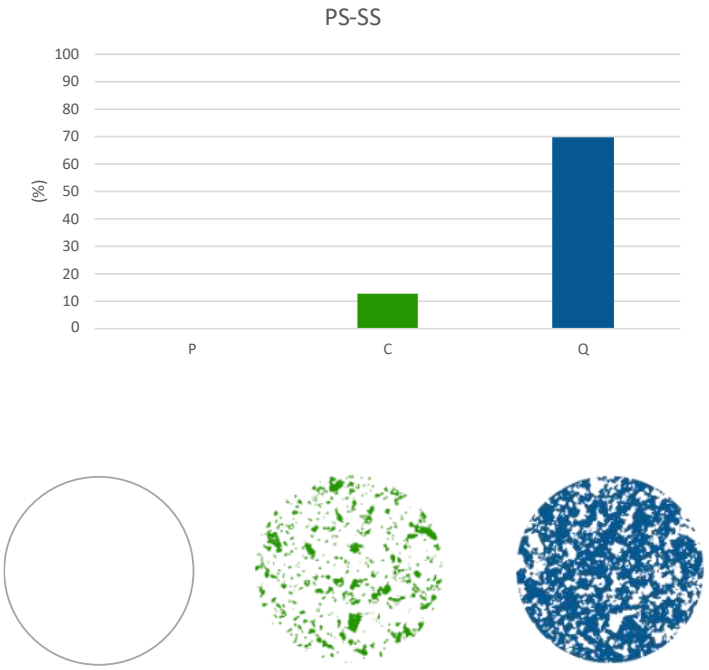

Figure 10-16: information acquired from image processing techniques on total porosity (P), carbonate minerals (C) and quartz (Q) for PS-SS.

10.1.9 Pietra Serena Extradura sandstone

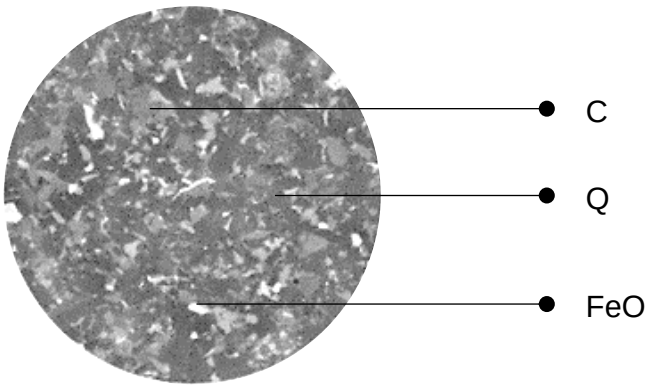

Figure 10-17: slice of the stack of images acquired from XCT scan data of PSX-SS

The sample composition is similar to that of PS-SS (figure 10-17). It is mainly composed of quartz (Q) and contains a high concentration of carbonate minerals (C), occupying about 15% of the sample volume (figure 10-18). Iron oxides are relatively common and homogeneously distributed across the sample. As with PS-SS, the pore fraction consists of micropores, which prevent the quantification of the total volume and characteristics of the network structure.

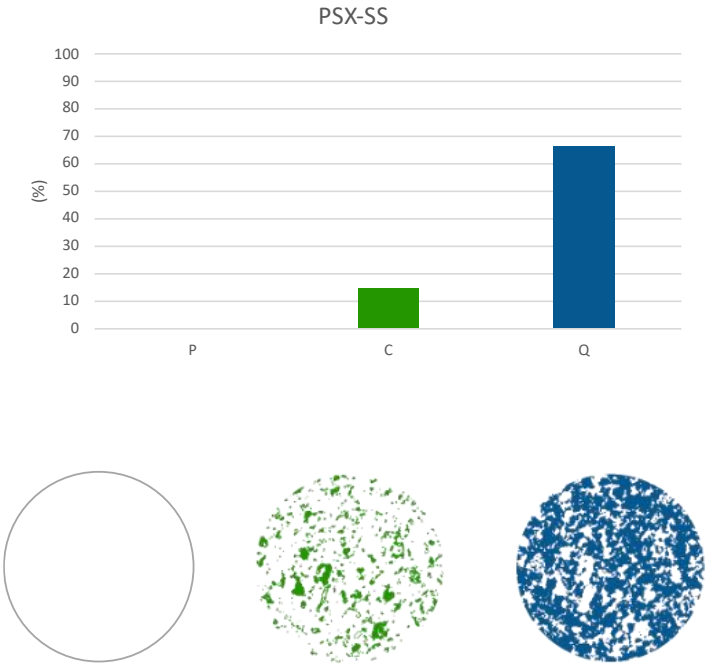

Figure 10-18: information acquired from image processing techniques on total porosity (P), carbonate minerals (C) and quartz (Q) for PSX-SS.

10.1.10 Pitairlie sandstone

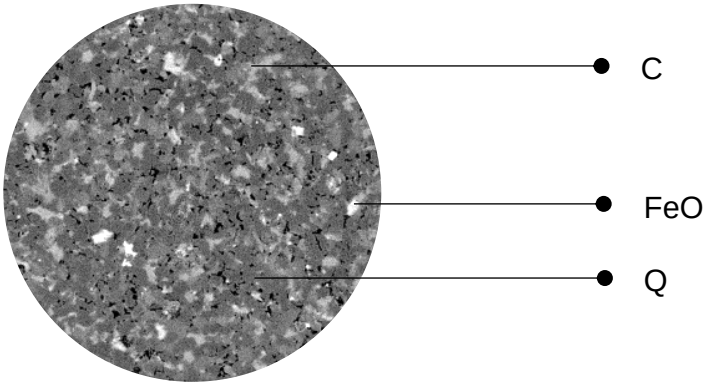

Figure 10-19: slice of the stack of images acquired from XCT scan data of PT-SS

The stone consists of a fine grained well sorted clastic fraction, mainly consisting of quartz (Q) (figure 10-19). Grains are bonded by carbonate cement, which occupy the intergranular fraction of the sample. The stone is characterized by low porosity (figure 10-20). The pores are relatively small, with an average size of 0.034 mm. Bigger pores measure about 0.17 mm. The level of interconnection could not be determined.

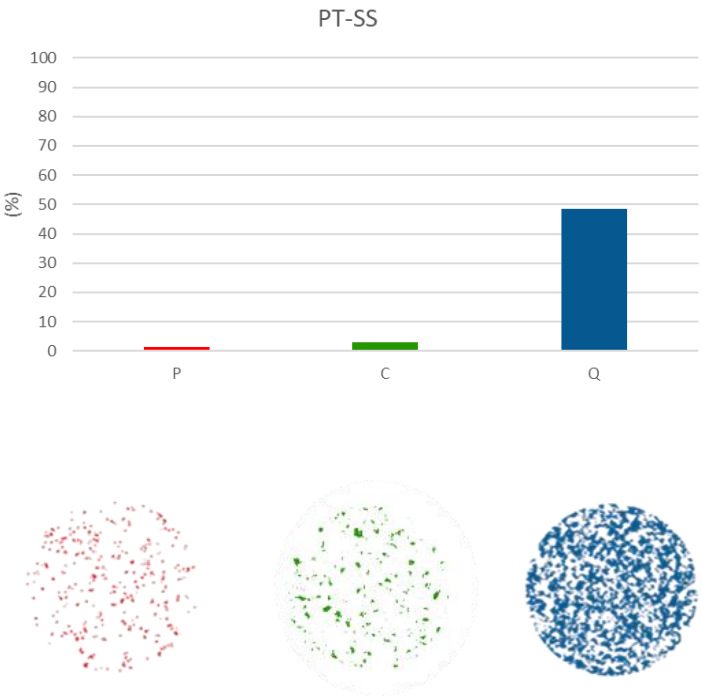

Figure 10-20: information acquired from image processing techniques on total porosity (P), carbonate minerals (C) and quartz (Q) for PT-SS.

10.2 List of Dose-Response and Damage functions

Table 10.20-1: dose-response functions

Study	Type of stone	Dose-response function
(Mansfeld, 1980)	White Cherokee Marble	$\mathbf{Log\ V(t) = 2.807 - 0.507 \log t - 0.005\ TS + 0.006\ S0_2 + 0.004\ H_2S + 0.010\ O_3 + 0.003\ TSP - 0.013\ S0_4 - 0.025\ NO_3}$ TS: total sulphur; TSP: total suspended particulate; t: time; H_2S: hydrogen sulphide concentration; O_3: ozone concentration ; SO_2: sulphur dioxide concentration ; NO_3: nitrogen dioxide concentration

(Reddy et al., 1989)	Vermont Marble	$\mathbf{Surface\ recession = 0.03 + [0.12 \cdot (H^+)]}$ Surface recession (μm per rainfall event); H+: hydrogen ion deposition (mmol m^2)
(Lipftert et al., 1989)	Generic calcite	$\mathbf{L = 18.8 \cdot Rn + 0.016 \cdot [H^+] \cdot Rn + 0.18\ (V_{dS}\ [SO_2] + V_{dN}[HNO_3])}$ L: recession rate per metre of precipitation (μm year $^{-1}$); Rn(m): yearly precipitation (m); V_{dS} and V_{dN}: SO_2 and NO_3 deposition velocity (cm s^{-1}); H+: hydrogen ions concentration (μmol l^{-1}); 18.8: intercept term based on solubility of calcite at 330 ppm CO_2
(Livingstone, 1992)	Generic calcite	$\mathbf{\Delta[Ca^{2+}] = \Delta[SO_4^{2-}] + \{10^{-11.6}(1/\gamma r0[H+]_{r0} + 1/\gamma 0[H^+]_0) - 1/2[H^+]_{r0} - [H^+]_0)\} + \{10^{-11.6}(1/\gamma 0[H^+]0 + 1/\gamma r[H^+]_r) - 1/2\ ([H^+]_0[H^+]_r)\}}$ $\Delta[Ca^{2+}]$ and $\Delta[SO_4^{2-}]$: difference in concentrations of Ca_2 and SO_4 ions (mol l^{-1}) between rainwater and runoff water; $[H^+]_0$: concentration of hydrogen ions in rainwater in the absence of anthropogenic pollutants ($10^{5.6}$); $[H^+]_r$: effective concentration of rain hydrogen ions; $[H^+]_{r0}$: concentration of hydrogen ions from the runoff; γ: coefficient of activity
(Webb et al., 1992)	Portland limestone	$\mathbf{g/m^2\ day = -0.162 + 0.0058\ SO^2 + 0.0666\ Rain + 638\ acid - 0.0026\ NO_2\ + 0.0155\ NO\ + 0.0007\ O_3}$ SO_2: sulphur dioxide concentration (ppb); Rain: amount of rainwater (mm day^{-1}); acid (mol m^{-2} day); NO_2: nitrogen dioxide concentration (ppb); NO: nitrogen oxide concentrations (ppb); O_3: ozone concentration (ppb)

(Baedecker et al., 1993)	Vermont Marble Indiana Limestone	$$Loss = \frac{0.16\,[1 - 0.015T + 0.0000922T^2]}{0.683} + 0.49[H^+]$$ Stone loss: mmol $\frac{Ca^{2+}}{L}$; T: temperature (°C); H+: hydrogen ions concentration (mol l^{-1})
(Butlin et al., 1995)	Portland Limestone Monks Park limestone White Mansfield Sandstone	$$\textbf{4 year surface recession (mm)} = 8.4 + 1.36(SO_2) + 0.0048\,(\textbf{Rainfall}) + 29(H^+)$$ SO_2: annual average concentration (mg m^3); rainfall: total rainfall (mm); H^+: rainfall acidity (mg $^{-2}$)
(Kucera and Fitz, 1995)	Portland limestone (1) Mansfield sandstone (2)	$$g/m^2\,(4 - \text{yrs}) = 34.4 + 5.96\,\text{Tow}\,[SO_2] + 388\,\text{rain}\,[H^+] \quad (1)$$ $$g/m^2\,(4 - \text{yrs}) = 29.2 + 6.24\,\text{Tow}\,[SO_2] + 480\,\text{rain}\,[H^+] \quad (2)$$ Tow: time of wetness (RH>80% , T>0°C, time fraction); SO2: concentration (µg/m^3); rain: amount of precipitation (m/year)
(Yerrapragata et al., 1996)	Carrara marble	$$\delta_m = 6.56 + 27.38H^+ + \frac{1.131 \cdot 10^{13} C_{SO_2}^{0.7} C_{NO_2}^{0.3}}{V} t$$ H^+: concentration of hydrogen ions in mmol l-1; CSO2 and CNO2: concentration of sulphur dioxide and nitrogen oxide in mol cm -3; t: time (years); V: rainwater (m)
(Mikhailov, 2001)	Portland limestone (1) White mansfeld sandstone (2a, 2b)	$$R = t^{0.96}(2.7\exp\{-0.018\,T\} + 0.019\,rain[H^+]) \quad (1)$$ $$R = t^{0.91}\left(2.0[SO_2]^{0.52} + 0.028\,Rain[H^+]\right) \quad T \le 10°C\ (2a)$$ $$R = t^{0.91}\left(2.0[SO_2]^{0.52}\exp\{-0.013(T - 10)\} + 0.028\,Rain[H^+]\right) \quad T \ge 10°C\ (2b)$$ t: time (years)(8 years range); T: air temperature (°C); rain: amount of rain (mm); H+: hydrogen ion concentration (mg/l); SO_2: sulphur dioxide concentration (µg/m^3)

(Tidblad et al., 2001)	Portland limestone (1) Mansfield sandstone (2)	$\mathbf{R = 2.7[SO_2]^{0.48}\exp\{f_{Pl}(T)\}t^{0.96} + 0.019Rain[H^+]t^{0.96}}$ (1) $\mathbf{R = 2.0[SO_2]^{0.52}\exp\{f_{Ms}(T)\}t^{0.91} + 0.028rain[H^+]t^{0.91}}$ (2) R: recession (μm); t: time (1-8 years); T: temperature; [SO_2]: concentration (μg/m^3); Rain: amount of rainfall (mm)
(Delalieux et al., 2002)	Massangis limestone	$\mathbf{\Delta Ca^{2+} = {0.015}/{rain}\,[-29 + 590\,rain + 800[H^+]rain + 5300\,SO_4^{2-}\,R + 5.5\,SO_2}$ ΔCa2+: Ca ion detachment (μm m_{rain}-1 yr-1); So_2 and SO_4^{2-} (μg m-3); rain (mm yr-1); R (mm): amount of rain
(Kucera et al., 2007)	Portland limestone	$\mathbf{R = 3.1 + t(0.85 + 0.0059Rh_{60}[SO_2] + 0.078Rh_{60}[HNO_3] + 0.054Rain[H^+] + 0.0258PM_{10})}$ R: surface recession (μm); t: time (years); Rh: relative humidity (%); SO_2: sulphur dioxide concentration (μg m^{-3}); NO_3: nitrogen dioxide concentration (μg m^{-3}); H^+: acidity of precipitation (mg l^{-1}); Rain: amount of precipitation (mm year); PM_{10}: particulate matter concentration (<10 μm) (μg m^{-3})

Table 10.20-2: damage functions and investigated processes.

Study	Decay Process	Damage function
(Mutlutürk et al., 2003)	Freeze-thaw Heating-Cooling	$\mathbf{I_n = I_0 e^{-\lambda n}}$ $\mathbf{N_{\frac{1}{2}} = \frac{Ln2}{\lambda} \approx \frac{0.693}{\lambda}}$ I_0: initial integrity of the rock; I_N: integrity of the rock after N cycles; λ: decay constant; N: number of cycles; $e^{-\lambda n}$: decay factor indicating the proportion of the remaining integrity after N cycles (I_N/I_0).
(Yavuz et al., 2006)	Freeze-Thaw Thermal shock	$\boldsymbol{V_{P\,(FT)} = 0.85\left(\frac{288.09 + 0.85\,V_{P0} - 7.53\,n}{0.85}\right)}$ $\boldsymbol{V_{P\,(HC)} = 0.84\left(\frac{442.27 + 0.84\,V_{P0} + 3.38n}{0.84}\right)}$ $\boldsymbol{UCS_{(FT)} = 0.81\left(\frac{5.78 + 0.81\,UCS_0 - 1.78n}{0.81}\right)}$ $\boldsymbol{UCS_{(HC)} = 0.83\left(\frac{4.11 + 0.83\,UCS_0 - 0.38n}{0.83}\right)}$ $\boldsymbol{SH_{(FT)} = 1.01\left(\frac{-3.69 + 1.01\,SH_0 + 0.28n}{1.01}\right)}$

		$SH_{(HC)} = 1.12\left(\frac{-6.57 + 1.12\,SH_0 + 0.17n}{1.12}\right)$ Vp: P-wave velocity (m/s); UCS: uniaxial compressive strength (MPa); SH: Schmidt hardness; *n*: porosity
(Bayram, F., 2012)	Freeze-Thaw	$UCS\,(\%loss) = -20.55 - 1.29\,IS + 2.13\,E - 3.90\,WA$ UCS: in uniaxial compressive strength (MPa); IS: impact strength (MPa); E: modulus of elasticity (GPa); WA: water absorption (%).
(Jamshidi et al., 2015)	Freeze-Thaw	$Bts = -1.215 - 0.343\,W_a + 1.008\,BTS_0$ $Bts = -0.595 - 0.125\,p_t + 0.973\,BTS_0$ $Is_{(50)} = -0.759 - 0.277\,W_a + 0.983\,Is_{(50)0}$ $Is_{(50)} = -0.430 - 0.095\,p_t + 0.957\,Is_{(50)0}$ $Vp = -832.194 - 13.382\,W_a + 1.097\,Vp_0$ $Vp = -55.027 - 27.28\,p_t + 0.954\,Vp_0$ W_a: water absorption; P_t: total porosity; BTS: Brazilian tensile strength (MPa); $Is_{(50)}$: point load index (50 mm sample diameter) (MPa); Vp: P-wave velocity (m/s).
(Ince and Fener, 2016)	Freeze-Thaw	$UCS\,(\%\,loss) = 39.91 + 42.25\,Vp - 12.50_{Is(50)} + 95.29\,p_d + 2.76\,I_{d4}$ UCS(%loss): % loss in uniaxial compressive strength; $Is_{(50)}$: point load strength index; Vp: P-wave velocity; p_d: dry density; I_{d4}: slake durability text index.
(Wang et al., 2016a)	Thermal shock	$\lambda\,UCS = 0.0067 + 0.1489e^{-0.01197\varepsilon}$

		$\lambda\ E_d = 0.0133 + 0.0642e^{-0.0127\varepsilon}$ $N_{1/2}\ (UCS) = -20.6 + 0.28\varepsilon$ $N_{1/2}\ (E_d) = 20.4 + 0.08\varepsilon$ λ: decay constant; $N_{1/2}$: half-life; UCS: uniaxial compressive strength; E_d: deformation modulus; ε: strain rate
(Wang et al., 2016b)	Freeze-Thaw	$\lambda(\varepsilon)_{UCS} = \begin{cases} 0.0257 & \varepsilon: 10^{-5}s^{-1} \\ 0.0298 + 0.19e^{-0.010\varepsilon} & 213\ s^{-1} < \varepsilon < 422s^{-1} \end{cases}$ $\lambda(\varepsilon)_{Ed} = \begin{cases} 0.0453 & \varepsilon: 10^{-5}s^{-1} \\ 0.0387 + 0.21e^{-0.013\varepsilon} & 213\ s^{-1} < \varepsilon < 422s^{-1} \end{cases}$ $N_{\frac{1}{2}UCS} = \begin{cases} 27 & \varepsilon: 10^{-5}s^{-1} \\ 18.0 - 44.5\ e^{-0.011\varepsilon} & 213\ s^{-1} < \varepsilon < 422s^{-1} \end{cases}$ $N_{\frac{1}{2}Ed} = \begin{cases} 15.3 & \varepsilon: 10^{-5}s^{-1} \\ 25.5 - 36.44\ e^{-0.005\varepsilon} & 213\ s^{-1} < \varepsilon < 422s^{-1} \end{cases}$ λ(ε): decay constant as a function of strain rate; $N_{1/2}$: half-life; UCS: uniaxial compressive strength; E_d: deformation modulus.
(Amirkiyaei et al., 2021)	Freeze-Thaw	$UCS_{25} = 2.3587e^{(0.6695292 + 0.0004356vp0 - 0.0515508n)}$ $UCS_{25} = 0.106\ Vp_0 - 587.773$ **(low-porous stone)** $UCS_{25} = 0.022\ Vp_0 - 79.067$ **(medium-porous stone)** $UCS_{25} = 0.012\ Vp_0 - 26.288$ **(high-porous stone)** UCS: uniaxial compressive strength (25 cycles); Vp_0: P-wave velocity before exposure.

(Jamshidi et al., 2021)	Freeze-Thaw	$\boldsymbol{UCS_{60} = 0.1972\ pmpp_{ucs} + 70.906}$ $\boldsymbol{BTS_{60} = 0.1981\ pmpp_{bts} + 5.3819}$ $\mathbf{Pmpp}\left(\frac{\mathbf{n}}{\mathbf{mm}}\right) = \frac{(\mathbf{isi\ x\ iqfi})}{\left(\frac{\mathbf{mgs_i + mgs_{f-t}}}{\mathbf{2}}\right)}$ PMPP: petro-mechanical parameter; $IS_{initial}$: initial strength of sample as UCS or BTS before F-T cycles (N/mm^2); IQF: quartz-feldspar index before F-T cycles; $MGS_{initial}$: index of mean grain size of samples before F-T cycles; MGS F-T: index of mean grain size of samples after F-T cycles; UCS_{60}: uniaxial compressive strength after 60 cycles; BTS_{60}: Brazilian tensile strength after 60 cycles.